UNIVERSITY OF OKLAHOMA

GRADUATE COLLEGE

INCLUSIVE CHARGED KAON PRODUCTION FROM B MESONS IN $\Upsilon(4S)$ DECAYS

A DISSERTATION

SUBMITTED TO THE GRADUATE FACULTY

in partial fulfillment of the requirements for the

degree of

DOCTOR OF PHILOSOPHY

By

Stephen Joseph Richichi
Norman, Oklahoma

2000

UMI Number: 9964766

INCLUSIVE CHARGED KAON
PRODUCTION FROM B MESONS
IN $\Upsilon(4S)$ DECAYS

A DISSERTATION APPROVED FOR THE
DEPARTMENT OF PHYSICS AND ASTRONOMY

BY

Patrick Louis Skubic

Patrick Skubic (*Chair*)

Ronald Kantowski

Ronald Kantowski

Philip Gutierrez

Bruce Mason

Bruce A. Mason

Patrick McCann

Pat McCann

Patrick McCann

Acknowledgments

This work would not exist but for the direct and indirect efforts of many people. It would take a work of equal volume to give proper credit to all concerned, but I will make my best attempt in a reasonable amount of space.

Firstly, I wish to thank my Thesis Advisor, Professor Patrick L. Skubic, who took me under his wing many years ago. His personal and professional support over the years have been greatly appreciated. His physics insights have been invaluable to this difficult analysis, and his patience was more than reasonable when results weren't always as forthcoming as they should have been. I am also grateful to Dr. George Kalbfleisch and the rest of the OUHEP community for providing the resources through our DOE grant which allowed me to move to Cornell to complete this research.

I owe a great debt of gratitude to Professor John Furneaux, who as OU's Graduate Recruitment Chair allowed me to plead my case with a less than outstanding undergraduate record. He agreed to give me a chance to prove myself by allowing me to take my first graduate level physics class (*Quantum Mechanics I* at my own expense, my performance in which allowed me to enter the Graduate Physics Program at OU on a conditional basis. I am grateful to Professor Bruce Mason, instructor of said physics class, whose support, encouragement and dedication to his teaching craft enabled me to perform in the top half of that class after not having touched a physics textbook for (*AHEM!*) more than a few years. I asked him to serve on my Ph.D. Advisory Committee for these reasons. I also wish to thank the rest of my Ph.D. Advisory Committee: Physics Professor Ron Kantowski and Electrical Engineering Professor Patrick McCann for their insights both in and out of the classroom, and Physics Professor Philip Gutierrez for helping me with topics for my first High

Energy Physics Seminar presentations.

I am grateful to my office mates and class mates at OU for making the days a little brighter, especially (but not limited to): Joseph Howard, Scott McCartney, Chris Stockdale, Tommy Ericson, Terry Downard, Jim Snyder Francesca Boffi and Jackie Milingo. I will always fondly remember the times we spent working impossible homework problems in our course work, as well as the Marathon Qualifier Study Sessions we endured together. Many thanks to the gracious ladies of the Physics Office - Grettie Bondy, Linda Christie and Danette Miller Lloyd - both for their camaraderie and their fine attention to numerous administrative details during my graduate school years.

I am grateful to the inhabitants of the offices of the Cornell Catholic Community (CCC) for giving me a home away from home when I first moved to Cornell, and for affording me many opportunities to serve where my particular talents were needed. Special thanks go to: CCC Director Fr. Michael Mahler, for presiding at my wedding; and to Sr. Margaret Brogden, for being "*The* **Hand of GOD** *in our Midst*". I am also grateful to the past and present members of the CCC Graduate Forum, many of whom I hope will be lifelong friends, for providing many stimulating moral and intellectual discussions on a variety of topics of mutual interest.

I am grateful to the many faces of CESR and CLEO at Cornell whose commitment to excellence made possible the data for this research. Most particularly, I am grateful to Professor Ron Poling of the University of Minnesota, who as Spokesperson gave me the opportunity to contribute to the CLEO Experiment in a significant way by encouraging me to become Data Reconstruction Manager for the re-processing of all CLEO II data sets, the now-infamous *RECOMPRESS*. Although the project was much more intense than I could have suspected and indeed seemed to last forever, I

would most probably still do it again for the experimental perspective I have gained. The round of applause I received after making a presentation of the project at a CLEO meeting made it all worthwhile. I am especially grateful for the superior efforts of the overworked and under-appreciated members of the Computer Group at Wilson Lab (especially Selden Ball and Josef Schmidt) for all of their support during that massive project.

I am greatly appreciative of the work of my CLEO Paper Committee: *Chair* Jean Roy (Colorado), Jim Alexander (Cornell), Andy Foland (Cornell) and Akhtar Mahmood (Albany, UTPanAm) for helping to guide this analysis to its presentation before the CLEO collaboration and ultimately, to its publication. I am also grateful to past and present B Hadronic PTA[1] chairs Giancarlo Moneti and Roy Briere and Analysis Coordinators Frank Wüerthwein and David Jaffe for their useful guidance on this analysis.

I am very grateful for the love, support and encouragement of my family, both nuclear *(pun intended!)* and extended. I wish to especially acknowledge the contributions that my mother, Rosemarie Guzzone Richichi, and my grandfather, Paul Richichi from Palermo, Sicily — both of whom passed away during my time in graduate school — have made in my life. I am also most grateful to Dr. Bijan Nemati for his personal and professional support during much of my graduate school tenure. Bijan has taught me much about how to be a research scientist. He also helped me through the difficult time of dealing with the death of my mother by providing some much-needed spiritual counseling. Bijan has become my Brother in more ways than one and I will always treasure his friendship.

[1] *Physics Topic Association.*

Dedication

Ultimately, this work would not exist but for the love and support of my wonderful wife, *Suzanne*. Our collaboration on the RECOMPRESS brought us much closer than either of us could have anticipated. I will always be grateful for her immensely significant contributions to that project, but more for the difference she has made in my life outside of the lab (*i.e.*, I now <u>have</u> one). Her *Patience*, *Wisdom*, *Understanding* and *"Tough Love"* have given me the strength and confidence that I needed to bring this work to completion and to move on to bigger and better things in my career. I certainly couldn't have done it without her, and so I therefore dedicate this work to her.

Thank You, *SUZANNE*,
for being the Light of my Life!!

"Anyone else would have been long gone, packed it up and headed back home. And not a soul would blame you after what I put you through,

Yea, anyone else would have gone insane, called the game on account of rain. Anyone else, anyone else, anyone but you!"

— **Collin Raye**

"Anyone Else"

Contents

List of Figures

List of Tables

Chapter 1

Introduction

Our human nature has always led us to ponder the fundamental questions of existence. Since people first looked up at the stars, they have often wondered about the structure of matter in the universe, from cells to galaxies and everywhere in between. Many branches of science have evolved to explore the answers to the following questions, on many different levels: *"What is the universe made of?"*, *"What mechanisms give form and structure to matter?"* Pursuit of these questions has had profound implications on our everyday lives, has been largely responsible for our current level of technology, and has contributed to both our global awareness and societal maturity.

High Energy Particle Physics deals with the basic interactions of matter and energy on the most fundamental level. Such interactions ultimately have implications from electronics to cosmology. Increasing energy scales (and thus decreasing distance scales) have enabled us to probe these interactions with greater precision than ever before. We are now at the point where we are able to make measurements that will soon reveal whether current theory is adequate to describe observed phenomena, or whether new physics needs to be "invented" to account for its behavior. This work, which is a small contribution to that task, is an attempt to measure inclusive properties of charged kaons from B meson decays at the $\Upsilon(4S)$ resonance peak. Such measurements must necessarily be made with high precision, and thus will help to make clear the accuracy of measurements of much rarer processes involving such particles.

In this chapter, we discuss some of the theoretical framework of High Energy Physics (HEP), briefly reviewing the Standard Model and the formalism of the interactions it describes. In Section 1.3, we review some of the particular aspects of the physics of B meson decay which are of interest to this analysis, as well as some basic properties of charged kaons. In Chapter 2, we discuss the experimental setup which provided the data for this research, giving attention to the particle identification (PID) hardware which plays a crucial role in this analysis. We will also briefly discuss some relevant details of the experimental trigger and data acquisition. Chapter 3 deals with data reconstruction, on which the author spent a significant amount of time as a Service Task to the CLEO Collaboration. Some basic aspects of track reconstruction will be described. The relevant aspects of PID calibration will also be covered in some detail. Chapter 4 begins the description of how we performed the analysis in this dissertation. Chapter 5 presents our results and Chapter 6 contains some concluding remarks.

1.1 The Standard Model

1.1.1 Quarks, Leptons and Gauge Bosons

The great success of High Energy Physics thus far is the *Standard Model.* This model encapsulates our present understanding of the interactions between the particles which comprise matter and the mediators of the fundamental forces, and is consistent with all presently observed phenomena to date. Quarks and leptons are the fundamental matter-building components. Each are grouped by pairs (or doublets) into three so-called generations. Both quarks and leptons are point-like, spin-1/2 particles called *fermions*. Some basic properties of quarks and leptons appear in Table 1.1 and Table 1.2, respectively [1]. Note that the determination of the light quark masses (u, d, s) is no easy task, so the values listed give approximate ranges of the so-called "current-quark" masses. The values listed for c and b are derived from charmonium ($c\bar{c}$), bottomonium ($b\bar{b}$), D meson ($c\bar{q}$, $q\bar{c}$), and B meson ($b\bar{q}$, $q\bar{b}$) masses.

Quarks and leptons also have other properties described by different quantum numbers. Quarks have Baryon Number $B = 1/3$ and Lepton Number $L = 0$, whereas all leptons have $B = 0$ and $L = 1$. In fact, each lepton generation has its own distinct Lepton Family Number, L_ℓ, where $\ell = e$, μ, τ. Each of the quarks and leptons also has an antimatter counterpart which has the same mass and spin, but the opposite signs for its electric charge and other quantum numbers.

The charge carriers of the fundamental forces of the Standard Model are spin-1 particles which are called *gauge bosons*. The photon (γ) mediates the electromagnetic interaction. The charged and neutral vector bosons ($W^\pm$ and Z^0) mediate the weak nuclear interaction. The $W^\pm$ governs the conversion of a charged lepton into its neutrino through the charged weak current. The $W^\pm$ also governs the flavor change of quarks, as detailed in the next section. The Z^0 governs the scattering of leptons and quarks through the neutral weak current. Gluons (g) mediate the strong nuclear interaction between quarks, thereby allowing quarks to change *color*. Because they also carry the *color* charge, gluons can couple to themselves as well as to quarks. This makes *QCD* a non-Abelian theory.

Characteristics of the fundamental forces which are incorporated into the Standard Model are listed in Table 1.3. Note that gravity, whose gauge boson is the as-yet-undiscovered spin-2 *graviton, (G)*, is not included in the Standard Model. The relative strengths of the strong, electromagnetic, weak and gravitational couplings

Table 1.1: Summary of quark properties. The three generations are separated by horizontal lines.

Quark	Name	Charge (e)	Mass (GeV/c^2)	*Flavor*[1]
d	down	$-1/3$	$0.003 - 0.009$	$I_3 = -1/2$
u	up	$+2/3$	$0.015 - 0.005$	$I_3 = +1/2$
s	strange	$-1/3$	$0.060 - 0.170$	$S = -1$
c	charm	$+2/3$	$1.10 - 1.40$	$C = +1$
b	beauty	$-1/3$	$4.10 - 4.40$	$B = -1$
t	top	$+2/3$	174 ± 5	$T = +1$

[1] I_3 is the third component of isospin, and S, C, B, and T are strangeness, charm, bottom, and top numbers, respectively.

Table 1.2: Summary of lepton properties. The three generations are separated by horizontal lines.

Lepton	Name	Charge (e)	Mass (MeV/c^2)	Lifetime (sec)
e	Electron	-1	0.511	stable
ν_e	e Neutrino	0	$< 15 \times 10^{-6}$	stable
μ	Muon	-1	105.658	2.197×10^{-6}
ν_μ	μ Neutrino	0	< 0.17	stable
τ	Tau	-1	1,777	2.90×10^{-13}
ν_τ	τ Neutrino	0	< 18	stable

are roughly: 10, 10^{-2}, 10^{-13} and 10^{-42}, respectively. Gravitational interactions may thus effectively be neglected in the subatomic domain.

All quarks and charged leptons are subject to the electromagnetic interaction. Both quarks and leptons are subject to the weak interaction, but only quarks (and gluons, which also carry *color*) are subject to the strong interaction. Things actually get a bit more complicated than that, but first a discussion of the formalisms of the different interactions is in order. Further details on the development of the Standard Model and interaction formalisms of the underlying theories may be found in the following texts: [2, 3].

1.1.2 Formalisms of the Interactions

Each of the fundamental forces of the Standard Model has its own gauge theory, which describes its behavior on the particles which are subject to its interaction.

Table 1.3: Properties of the four mediators of the electro-weak and strong interactions.

Mediator	Mass (GeV/c^2)	Spin	Interaction
Photon (γ)	0	1	Electromagnetic
$W^{\pm}$	80.41 ± 0.10	1	Weak
Z^0	91.187 ± 0.007	1	Weak
8 Gluons (g)	0	1	Strong

These interactions may be classified, using the notations of group theory, according to the symmetries they represent.

Quantum Chromodynamics (*QCD*) describes the interactions of the strong force between quarks and gluons. This interaction is described in terms of a *color* charge on the quark, which is historical nomenclature and has nothing to do with optical properties. Convention has named these color charges *red*, *green* and *blue* (complete with their anticolor counterparts for antimatter), and they represent an exact symmetry of the group $SU(3)$. The high-strength, short-range nature of the strong interaction prohibits individual quarks from being observed. Quarks rather manifest themselves as bound states of either quark-antiquark pairs called *mesons* or three-quark bundles known as *baryons*. Mesons and baryons together are collectively known as *hadrons*. Because no hadron has ever been observed to carry color, it is believed that all hadrons observed in nature must be a color singlet. That is to say, each of the quarks in a baryon must be a different color, whereas the color of the quark in a meson is the anticolor of the antiquark.

The theory of Glashow, Weinberg and Salam [4] describes the electro-weak interaction in terms of weak isospin and weak hypercharge (Y), whose underlying symmetry group is $SU(2)_L \otimes U(1)_Y$. The subscript "L" will be explained in the next section. Isospin is completely analogous to the spin-1/2 theory of angular momentum, except that isospin represents a vector in abstract "isospin space". This notion is exploited to represent the proton and neutron as two distinct isospin states of a single particle, the *nucleon*. Isospin is conserved in all strong interactions if the strong force is invariant under rotations in isospin space. To date, no strong interaction process has ever been observed that violates isospin conservation. Hypercharge is the higher generational property of a quark (i.e., *charm*, *strangeness*, *bottom*, or *top*). It is related to electric charge, Q (in units of e) and the third component of isospin, I_3, according to:

$$Q = I_3 + \frac{1}{2} Y \tag{1.1}$$

This is where things start to get complicated. For leptons undergoing weak processes, coupling to the $W^{\pm}$ occurs strictly within a generation. That is, $\ell^- \rightarrow \nu_\ell + W^-$, where $\ell = e, \mu, \tau$. In fact this is one of the observed conservation laws, that Lepton Family Number is not violated in particle reactions. In other words, for every charged lepton type produced, the corresponding antineutrino will also be produced.

For quarks this is not true, as cross-generational coupling can indeed occur in weak processes. This happens because the weak eigenstates of the quarks are not the same as the strong eigenstates of the quarks, but rather superpositions of them. By convention, this mixing is taken to occur in the $1/3\,e$ members of each generation (namely d, s, b) and is described by the Cabibbo-Kobayashi-Maskawa [5] or CKM matrix:

$$\begin{pmatrix} d' \\ s' \\ b' \end{pmatrix} = \begin{pmatrix} V_{ud} & V_{us} & V_{ub} \\ V_{cd} & V_{cs} & V_{cb} \\ V_{td} & V_{ts} & V_{tb} \end{pmatrix} \begin{pmatrix} d \\ s \\ b \end{pmatrix} \tag{1.2}$$

The element V_{ij} describes the coupling strength of the quark mass eigenstate i to the quark mass eigenstate j by the charged weak current.

Assuming exactly three generations of quarks, experimental data gives limits on the magnitudes of the individual elements of the CKM matrix (at the 90% confidence level) as:

$$\begin{pmatrix} 0.9745 \text{ to } 0.9760 & 0.217 \text{ to } 0.224 & 0.0018 \text{ to } 0.0045 \\ 0.217 \text{ to } 0.224 & 0.9737 \text{ to } 0.9753 & 0.036 \text{ to } 0.042 \\ 0.004 \text{ to } 0.013 & 0.035 \text{ to } 0.042 & 0.9991 \text{ to } 0.9994 \end{pmatrix} \tag{1.3}$$

If the CKM matrix was the 3x3 Identity Matrix, then there would be no mixing at all between quark generations. The closeness of the diagonal elements to unity indicates that quarks preferentially **do** couple within their own generation. Inclusive decays of B mesons to K mesons necessarily involve cross-generational couplings from either $b \to c \to s$ or $b \to s$ directly.

The ranges shown above, however, are for measurements of the individual matrix elements. The constraints of unitarity also connect the various matrix elements, so choosing a specific value for one element limits the range of others. The CKM matrix is required to be unitary ($U^{-1} = \tilde{U}^*$) in order to conserve probability. This requirement is usually expressed as:

$$V_{ud} V_{ub}^* + V_{cd} V_{cb}^* + V_{td} V_{tb}^* = 0. \tag{1.4}$$

This limits the number of free parameters in the matrix elements to only four: three real angles (α, β, γ) and one complex phase (δ). These four parameters also define the so-called "Unitarity Triangle", which is a geometrical representation of this equation in the complex plane. It is this complex phase δ which gives rise to the phenomenon of *CP Violation*.

1.2 CP Violation

CP Violation in the neutral B meson system is a current "Hot Topic" in HEP. While this inclusive analysis doesn't directly involve CP-violating decays, it is a topic worth mentioning for the sake of completeness. Searches for 2-body, CP-violating decays with a highly energetic kaon or pion track may be able to make use of some of the results presented in this dissertation.

As mentioned previously, many quantities are found to be conserved in all particle reactions observed thus far. Chief among these are: *Electric Charge*, *Baryon Number* and *Lepton Family Number*. Two other quantities were also thought to be absolutely conserved: *Charge Conjugation, C* and *Parity, P*.

The action of the C operator is to change a particle into its antiparticle. This has the effect of reversing "internal" quantum numbers - like Charge, Baryon Number and Lepton Number - while not affecting properties like spin, mass, energy or momentum.

Parity conservation refers to the possibility of the "mirror image" of a given process to occur. In practice, this refers to *inversions* about the origin rather than *reflections* about an arbitrarily oriented mirror axis. For particles, this introduces the concept of *helicity*, which is the orientation of a particle's spin relative to its momentum. If a particle's spin is in the direction of its momentum, it has helicity $+1$ (sometimes called *"right-handed"*). If its spin is opposite its momentum, it has helicity -1 (*"left-handed"*). For a massive particle, boosting to a reference frame that reverses the direction of its momentum will also reverse its helicity. For neutrinos (and other massless particles), however, helicity is a Lorentz-invariant quantity. It was soon discovered experimentally that all neutrinos were left-handed and all antineutrinos were right-handed [6, 7]. Thus parity was found to be "Maximally Violated" for weak processes, although it is still a valid symmetry for strong and electromagnetic processes. A consequence of this fact is that only left-handed charged leptons (and thus only right-handed charged antileptons) are subject to the weak interaction. This explains the subscript *"L"* in the electroweak symmetry group term above.

Because parity was found to be maximally violated for neutrinos, it became clear that the charge conjugate of any interaction containing neutrinos (*i. e.*, weak processes) could not exist. It was then presumed that the combined operator CP would again be an absolutely conserved quantity. This operator turns a left-handed particle into its right-handed antiparticle, thus restoring Charge(-Parity) Conjugation as a valid symmetry for interactions containing neutrinos.

This CP operation has unusual consequences in the context of neutral mesons containing a higher generation quark (s, c, b). Gell-Mann and Pais [8] first noted that the neutral kaon (K^0) could turn into its antiparticle $(\overline{K^0})$, thus changing its strangeness from $+1$ to -1. These neutral mass eigenstates can then be combined to form (normalized) eigenstates of CP, which are:

$$|K_1>=(\frac{1}{\sqrt{2}})(|K^0>-|\overline{K^0}> \qquad |K_2>=(\frac{1}{\sqrt{2}})(|K^0>+|\overline{K^0}> \tag{1.5}$$

such that:

$$CP\,|K_1>=|K_1> \qquad CP\,|K_2>=-\,|K_2> \tag{1.6}$$

This meant that K_1 could only decay into a $CP=+1$ state (like two pions) and K_2 only into a $CP=-1$ state (like three pions), if CP was conserved. The two states have different lifetimes, and the long-lived state was discovered by Lederman [9] in 1956 at Brookhaven.

All was well and good until 1964, when Cronin and Fitch [10] discovered 45 two-pion events out of 22,700 decays at the end of a neutral kaon beam 57 feet long, well after the short-lived state should have completely decayed. This implied that the long-lived state was in fact composed of a small amount of K_1, and not an eigenstate of CP after all. That is:

$$|K_L>=\frac{1}{\sqrt{1+|\varepsilon|^2}}(|K_2>+\varepsilon\,|K_1>) \tag{1.7}$$

where ε is a measure of the amount of CP violation in the neutral kaon system; its magnitude is experimentally found to be about 2.3×10^{-3}.

Although neutrinos maximally violate parity because they are <u>**all**</u> left-handed, this phenomenon was nevertheless easily incorporated into the electroweak theory *because* it was such a stark effect. Indeed, there was already a theory to account for this effect, which nobody took seriously until well after the discovery of the existence of the neutrino. Weyl [11] had developed the theory of massless spin-1/2 particles, demonstrating their fixed "handedness", shortly after Dirac introduced his equation in 1929. Pauli rejected this theory after postulating the existence of the neutrino in 1931, however, because Weyl's theory violated parity conservation. Weyl's theory was finally vindicated in 1957, after parity was indeed found to be violated in Cobalt 60 β decay [12].

The minimal effect of CP Violation in neutral meson systems may in fact be a mechanism for explaining the dominance of matter over antimatter in the early universe, and is still one of the outstanding issues to be easily explained by the Standard Model. This was the motivation for constructing the asymmetric B Factories at *BaBar* and *BELLE*: to explore the phenomenom of CP Violation in the neutral B meson system, where the effect is expected to be greater because of the larger mass difference between the CP eigenstates of the neutral B meson, whose lifetime difference is almost negligible.

1.3 B Meson Physics

B mesons provide a rich laboratory for testing the predictions of the Standard Model. The lifetime of mesons containing one b quark is about 3 times that of their charmed counterparts (which contain one c quark). This allows them to travel a bit further than charmed mesons before decaying, which helps to resolve track ambiguities and thereby reduces background in the event. The heavy quark content opens up many more decay possibilities, as well. Table 1.4 lists some properties of B mesons. Note that this dissertation only deals with B mesons which also contain either a u-type or a d-type quark.

Table 1.4: Summary of B meson properties. The horizontal lines separate by quark flavor.

Meson Name	Quark Content	Mass (MeV/c^2)	Lifetime (ps)
B^+, B^-	$u\bar{b}$, $b\bar{u}$	5278.9 ± 1.8	1.65 ± 0.04
B^0, $\overline{B^0}$	$d\bar{b}$, $b\bar{d}$	5279.1 ± 1.8	1.56 ± 0.04
B_s^0, $\overline{B_s^0}$	$s\bar{b}$, $b\bar{s}$	5369.3 ± 2.0	1.54 ± 0.07

1.3.1 The Υ Resonances

There is also a bound state of $b\bar{b}$ called the Υ system, which displays several resonances where the cross section — essentially, the production rate — for $e^+e^- \to$ *hadrons* is enriched. These resonances are enhancements above the *continuum* cross section which exists at all energies. Table 1.5 lists some properties of the first four Υ resonances. Figure 1.1 shows a CESR energy scan detailing the structure of the Υ resonances.

Table 1.5: Summary of the Υ family of resonances.

Resonance	Mass (GeV/c^2)	Full Width (keV)
$\Upsilon(1S)$	9.46037 ± 0.00021	52.5 ± 1.8
$\Upsilon(2S)$	10.02330 ± 0.00031	44 ± 7
$\Upsilon(3S)$	10.3553 ± 0.0005	26.3 ± 3.5
$\Upsilon(4S)$	10.5800 ± 0.0035	10 ± 4 MeV

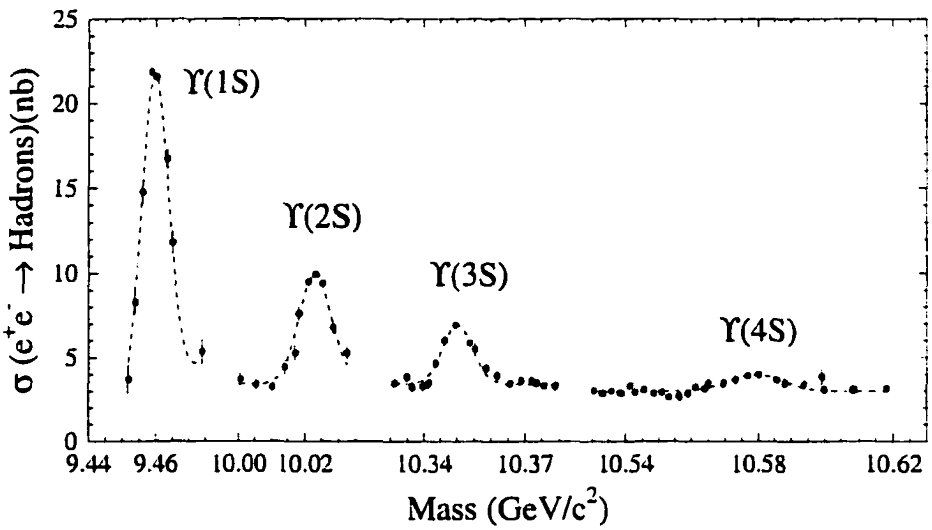

Figure 1.1: The four Υ resonances observed at CESR energies. Note the discontinuous horizontal scale.

It is at the fourth such resonance, a broad state called the $\Upsilon(4S)$, that the energy threshold for B^+B^- or $B^0\overline{B^0}$ production is first exceeded. This means that B mesons produced at the $\Upsilon(4S)$ are essentially at rest. In practice, the amount of kinetic energy that the B mesons retain from the e^+e^- collision <u>can</u> be measured, it is just not significant compared to the masses of the B mesons themselves. Below the $\Upsilon(4S)$ resonance, there is NO possibility for the $b\bar{b}$ pair to form B mesons. The lower resonances must therefore decay to other particles containing only u , d , s or c quarks. CLEO takes advantage of this phenomena to isolate events that can only come from B meson decays, as detailed in Chapter 4. Figure 1.2 shows some possible decay mechanisms of the Υ resonances.

1.3.2 Exclusive and Inclusive B Meson Decays

B mesons typically decay into 2 or more other particles. Figure 1.3 shows some possible decay mechanisms of B Mesons. The diagrams in Figures 1.2 and 1.3 are known as *Feynman diagrams*. They are actually a complex shorthand notation with specific rules governing each line or vertex. Each particular line or vertex represents a contribution to the calculation of the matrix amplitude of a given reaction. The amplitude squared is proportional to the decay rate. Further discussion of the Feynman Rules for calculating matrix amplitudes may be found in [13], for instance.

Sometimes, we wish to identify all of the particles coming from a given decay type. Those decays where all of the decay particles are identified are called *Exclusive Decays*. These decays can tell us much about particular aspects of the Standard

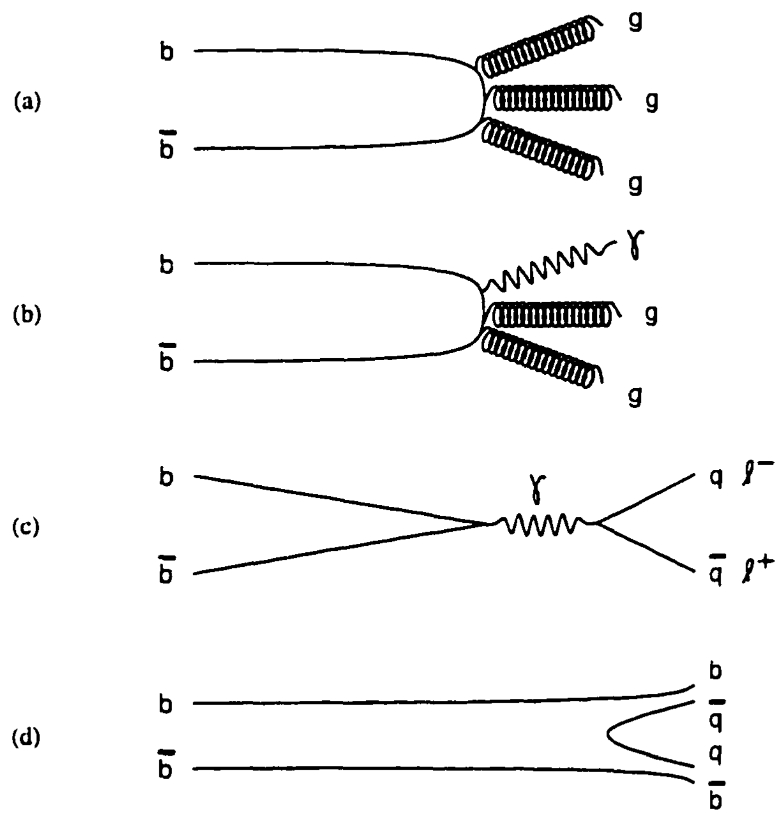

Figure 1.2: Possible decay mechanisms of the Υ resonances. Figures (a) through (c) show how the $\Upsilon(1S)$ through $\Upsilon(3S)$ resonances can decay via annihilation of the b and $\bar{b}$ quarks, and (d) shows how B mesons are formed in $\Upsilon(4S)$ decay.

Model in which we are interested. Measuring the branching ratio (the likelihood of a given decay to occur) of a certain exclusive process confirms the validity of the theory which predicts a certain rate for a given reaction, based on its matrix amplitude calculation according to the Feynman Rules. CLEO takes advantage of both its well-known beam energy and its energy resolution to reconstruct such exclusive decays with greatly reduced backgrounds. A concise explanation of this technique may be found in [14]. Figure 1.4 shows an invariant mass plot for the B meson, as reconstructed from one particular type of exclusive decay.

Sometimes, we only wish to identify one or two of all of the particles which have resulted from a given decay type. Those decays where only the particles of interest are identified are called *Inclusive Decays*. In Figure 1.3, anytime a generic quark labeled q occurs, instead of a particular quark like u or d, this is an example of an inclusive decay. There we are only interested in the decay of the b quark without regard for the other quark which is along for the ride, the so-called "spectator" quark.

In the particular case of charged kaons, there are a number of reasons which make

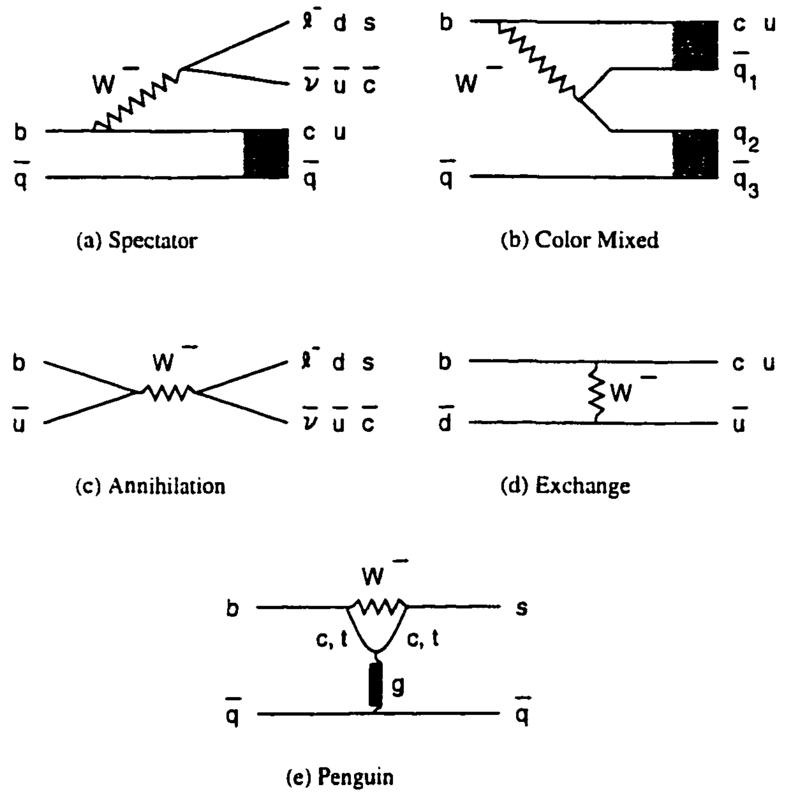

Figure 1.3: Decay mechanisms of the B meson, shown in the form of quark-level Feynman diagrams: (a) External W-emission ("Spectator"), (b) Internal W-emission ("Color Mixed"), (c) Annihilation, (d) W-Exchange, and (e) gluonic "Penguin."

accurate inclusive measurements of these particles from B meson decays desirable. There is great theoretical interest in a precise determination of the $b \to s\,g$ branching ratio. Enhanced $b \to s\,g$ from B decays would lead to increased kaon multiplicities, as well as decreases in the semi-leptonic branching ratio, $\mathcal{B}_\ell(B)$, and charm multiplicity, η_c. Kaon counting from B decays can tell us how much of the charmless b decay width (obtained from charm counting) is due to $b \to s$ transitions [15]. Precision measurements of light hadronic spectra (π, K, p) will yield global information on B decays and enable one to better estimate backgrounds from rare (possibly CP-violating) processes. A comparison of the observed charged light hadron momentum spectra with MC will lead to improvements in future MC generators [16]. This analysis should also promote a better understanding of PID device characteristics and systematics in CLEO II.

The most recently published values of pion, kaon and proton multiplicities at the $\Upsilon(4S)$ are listed in Table 1.6 [1]. The ultimate goal of this analysis was to update these numbers. We also intend to extract the branching fractions $\mathcal{B}(B \to K^\pm X)$, $\mathcal{B}(B \to \pi^\pm X)$, and $\mathcal{B}(B \to p,\bar{p}X)$. A future goal for a publication is to also ob-

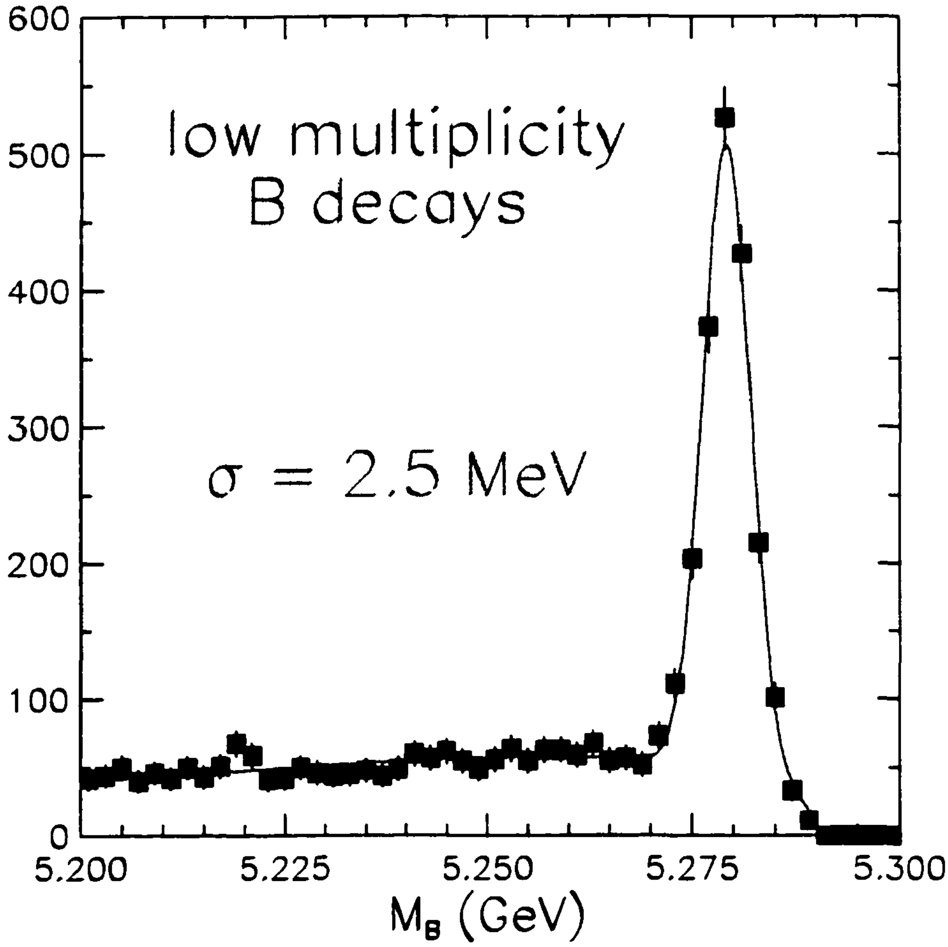

Figure 1.4: An invariant mass plot for the B meson.

tain the individual charged kaon contributions, $\mathcal{B}(B \to K^+X)$ and $\mathcal{B}(B \to K^-X)$. Currently published values for these branching fractions are listed in Table 1.7 [1]. CLEO has also published the above branching ratios, including kaon-lepton correlations [17]. Those results were obtained using the original CLEO I detector and are many years out of date, so updating these numbers is desirable to the collaboration.

1.4 Properties of Charged Light Hadrons

We conclude this chapter by briefly reviewing some of the properties of charged light hadrons: *i.e.*, pions, kaons and protons. Table 1.8 lists some properties of these particles. Because charged light hadrons are extremely long-lived compared to

Table 1.6: Average multiplicities in hadronic e^+e^- annihilation events at the $\Upsilon(4S)$. (PDG 98)

$\pi^\pm$	6.6 ± 0.2
$K^\pm$	0.90 ± 0.04
$p, \bar{p}$	0.253 ± 0.016

Table 1.7: Kaon branching fractions in $\Upsilon(4S)$ events. (PDG 98)

$\mathcal{B}(B \to K^\pm X)$	$(78.9 \pm 2.5)\%$
$\mathcal{B}(B \to K^+ X)$	$(66 \pm 5)\%$
$\mathcal{B}(B \to K^- X)$	$(13 \pm 4)\%$

B mesons, they survive long enough to leave tracks in the tracking chambers and signals in the rest of the detector components. The challenge for this analysis, then, is to identify these tracks as kaons, pions or protons as unambiguously as possible, using the available PID devices: namely, Specific Ionization, (dE/dx), and Time-of-Flight, (ToF). Many other analyses make loose PID cuts on a track, assuming that it is a kaon or pion for example, then reconstruct more massive particles by fitting to a resonant mass peak on top of a combinatorial background. The loose PID cut serves to reduce this background with a minimal loss of signal.

Table 1.8: Summary of charged light hadron properties.

Meson Name	Quark Content	Mass (MeV/c^2)	Lifetime ($sec.$)
π^+, π^-	$u\bar{d}$, $d\bar{u}$	139.56995 ± 0.00035	$(2.6033 \pm 0.0005) \times 10^{-8}$
K^+, K^-	$u\bar{s}$, $s\bar{u}$	493.677 ± 0.016	$(1.2386 \pm 0.0024) \times 10^{-8}$
p, $\bar{p}$	uud, $\overline{uud}$	938.27231 ± 0.00028	$> 1.6 \times 10^{25}$ $years$

Since charged light hadrons are primarily observed particles, however, this technique is not available for this analysis. We are thus forced to employ our PID systems in a different way to identify charged kaons at various momenta. We plot PID analysis variables for data as a function of momentum. We then fit these PID shapes using samples of known particles from data and Monte Carlo as control shapes, in order to extract particle yields for each device as a function of momentum. This technique will be elaborated in Chapter 4.

Chapter 2

Experimental Setup

The experimental data used for this dissertation was taken at Cornell University's Wilson Synchrotron Laboratory, home of the Cornell Electron Storage Ring (CESR) and the CLEO Detector[1] Both CESR and CLEO have undergone several major upgrades over the years, in order to remain competitive in the HEP field.

This chapter details the CLEO II Detector configuration [18], which was in operation from December 1989 until April 1995. This was when both CESR and CLEO were shutdown for several months, to accomodate the installation of a smaller radius beam pipe and the Silicon Vertex Detector (SVX). With the SVX installed, this became known as the CLEO II.V Detector configuration. As of this writing, the CLEO III Detector is being installed and commissioned, along with an upgraded CESR III Interaction Region. The CLEO III Detector features: a new even smaller radius beam pipe; a four-layer SVX; a completely new Drift Chamber; and a Ring-Imaging Cherenkov (RICH) Detector for PID.

2.1 The Cornell Electron Storage Ring

The Cornell Electron Storage Ring [19] began construction in 1977 and began operating in 1979. It has a circumference of 768 meters and is located ten meters below an athletic field on the Cornell University campus. Its purpose is to provide electron-positron (e^+e^-) collisions at energies between 9 and 11 GeV, the energy range of the Υ states. The resulting matter-antimatter annihilations convert the available energy into new and exotic states of matter, which are studied with the aid of the CLEO Detector. Figure 2.1 shows a schematic of the various components of CESR.

[1]To the best of the author's knowledge, *"CLEO"* is not an acronym for anything. Rather, this name for the detector was chosen because it was the perfect companion to CESR, pronounced *"Caesar"*.

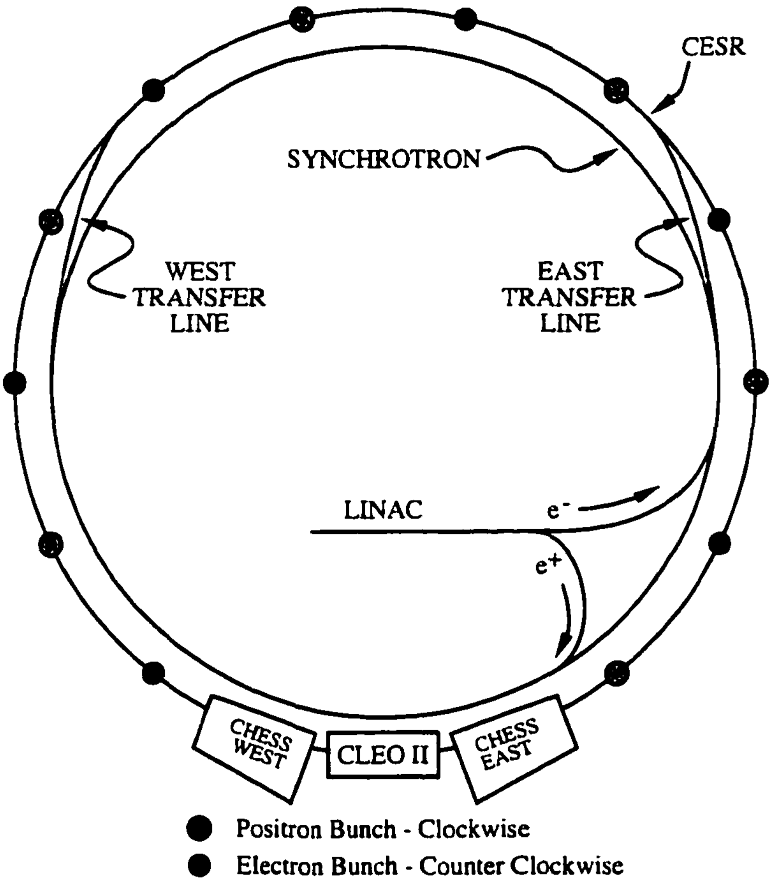

Figure 2.1: Schematic of the various CESR components.

2.1.1 LinAc and Synchrotron

CESR creates these electron and positron beams used for collisions in a *linear accelerator* (LinAc) and accelerates them to high energies in the *synchrotron*, as follows: In the LinAc, electrons are "boiled" off of a heated filament and accelerated through a vacuum pipe 30 meters long. Under the influence of a microwave electric field, they are accelerated up to an energy of about 300 MeV, before being injected into the synchrotron. Positrons are created by placing a tungsten target in the path of the electron beam, after it reaches an energy of about 140 MeV. This creates showers of electrons, positrons and X-rays. The positrons are separated, then focused and accelerated up to about 200 MeV before being injected into the synchrotron in the opposite direction. Positrons are typically injected first, then electrons, for CESR *fills* during HEP running.

In the synchrotron, a series of bending magnets keeps the particle beams separated from each other in the same beam pipe and moving in the circular orbit. the counter-rotating beams (electrons counterclockwise, positrons clockwise) are accelerated up to an energy of about 5 GeV. This occurs after about 4000 orbits, which only takes about a hundredth of a second. The beams are then transferred to the *storage ring*. To achieve the desired beam currents in the storage ring, the acceleration process is repeated about 60 times in ten minutes, first for positrons then for electrons. When they have achieved this energy, the particles are moving at 99.9999995% of the speed of light.

2.1.2 Storage Ring and Interaction Region

While the electrons and positrons spend very little time in the synchrotron, they must coast in the storage ring for much longer periods. This requires both precision placement of magnetic fields and rigid vacuum standards. Complex arrays of powerful quadrupole and sextuple magnets serve to precisely bend and focus the beams as they travel around the ring, with their currents often set to an accuracy of 0.01%. The vacuum chamber and its connections are made of a metal that can be heated to 150° C to "bake out" the air in the chamber. This reduces the pressure in the chamber to about a billionth of the value of atmospheric pressure.

The particles radiate a beam of 0.5 MW X-Rays as *synchrotron radiation* as they travel around the storage ring, losing about 1 MeV per turn. The Cornell High Energy Synchrotron Source (CHESS) Facility makes use of these X-Ray beams for research in a wide variety of scientific applications, including: Physics, Chemistry, Biology, and Environmental and Materials Sciences[2]. This energy lost to synchrotron radiation is returned to the particles by superconducting radio-frequency (SRF) cavities placed around the ring, which operate at a frequency of 500 MHz.

Electrons and positrons travel about the storage ring at about 390 kHz in complicated "pretzel orbits", with 9 approximately evenly spaced bunch trains of two bunches of electrons each colliding with 18 similarly spaced bunches of positrons traveling in the opposite direction. There are as many as 1.5×10^{11} particles in each bunch, and the size of a bunch is about 1.1 mm wide, 0.1 mm high and about 1.0 cm long. Electrostatic separators are used to prevent the beams from colliding at the beam intersection points other than the *interaction region*. As mentioned above, precision magnets manage to keep the beams apart elsewhere in the ring. As they approach the interaction region, however, the beams are re-focused to pass through each other. This results in the collisions which produce decay particles of interest to be studied by the CLEO Detector. The beams are allowed to collide until they lose a significant fraction of their currents. The beams are then dumped and electrons and positrons are re-injected into the storage ring. A typical CESR fill lasted from 60 to 75 minutes, depending upon beam conditions and the needs of the experimenters at CHESS. This time period is what defines a "data run" in CLEO.

[2] As of this writing, CHESS is in the process of constructing an additional experimental line in order to accommodate the number of researchers seeking to use this state-of-the art X-Ray facility.

2.2 The CLEO II Detector

The CLEO II Detector is an all-purpose, solenoidal collider detector with excellent charged and neutral particle detection capabilities. It stands about six meters square, contains about 900 metric tons of iron, and consists of about 25,000 individual readout elements for the various detector components[3]. The detector components consist of: a central detector region (CD), containing three layers of tracking chambers covering different radii (PT, VD, DR); a time-of-flight system (TF); a CsI crystal calorimeter (CC); and a muon identification system (MU), which is housed within the iron of the magnet flux return yoke. The CLEO II Detector is shown in side view and end view in Figure 2.2 and Figure 2.3, respectively.

All of the detector elements except the muon chambers are surrounded by a 30 ton, superconducting Cu-NbTi coil of radius 1.5 meters, which contains 650 turns and produces a 1.5 Tesla magnetic field in the $-z$ direction (the direction of the electron beam). This axial magnetic field is nearly uniform out to a radius of 100 cm from the beam line. The superconducting coil of the magnet is cooled by a liquid helium refrigeration system.

Particles which are created in e^+e^- collisions first pass through a thin-walled, low mass beam pipe. This beryllium pipe separates the vacuum of the storage ring from the gas system of the detector. It has a radius of 3.5 cm, a thickness of 0.5 mm and a length of 33 cm. To reduce the unwanted background from synchrotron radiation, a silver layer of 20 microns and a nickel layer less than 1 micron are plated inside the beam pipe. Heavy particles like D and B mesons decay well within the beam pipe, so only their decay products will survive long enough to reach the other components of the detector. The thinness of the pipe and its low atomic mass serve to reduce the effects of multiple scattering.

The detector elements relevant to this analysis are briefly described in the following sections. Further details may be found in the published reference [18].

2.2.1 The Tracking Chambers

Particles emerging from the beam pipe then pass through the three concentric, cylindrical layers of the central detector (CD): the precision tracking layer (PT), the vertex detector (VD), and the main drift chamber (DR). The three chambers were filled with Argon-Ethane gas in equal mixture, which would ionize in the wake of a charged particle's trajectory, due to the electric field produced by the high voltage wires. This phenomenon is the basis for both track reconstruction and dE/dx measurement, which will be covered in greater detail in sections 3.1.2 and 3.8.1, respectively.

[3]The addition of the SVX *doubled* the number of readout channels for CLEO II.V data!

The Precision Tracking Layer

The PT was designed to facilitate precise transverse momentum (P_t) measurements near the interaction point[4]. This especially applies to particles with P_t less than 90 MeV/c, which can only cross seven layers of the DR. The PT extends 22.5 cm in either direction along the beam pipe, and radially from 4.7 cm to 7.2 cm. It is composed of six layers of nested aluminized Mylar tubes which function as cathodes, with 64 tubes in each layer. The tubes are slightly larger in each layer (from 2.2 cm to 3.5 cm) and are staggered by half a cell, to accommodate the requirement that each tube be in contact with all adjacent tubes. This configuration also provided stability and internal alignment for this device. Each tube contains an axial wire (functioning as an anode), which means that longitudinal measurements are not possible with this device. A high voltage of about 1500 V was applied across each wire in the tube.

In 1992, DME (DiMethyl Ether) was substituted for the Argon-Ethane gas in the PT, improving the $r - \phi$ position resolution from 100 microns to 60 microns. The PT was replaced by the SVX in the CLEO II.V Detector, which makes further resolution improvements in $r-\phi$, and also allows precision z measurements near the interaction point.

The Vertex Detector

The VD extends 35 cm in either direction along the beam pipe, and radially from 8.4 cm to 16.0 cm, in ten layers. It is composed of 2272 aluminum field wires and 800 nickel-chrome sense wires, with three field wires for each sense wire arranged to form small hexagonal cells. The inner five layers each contain 64 cells and the outer five layers each contain 96 cells. The Argon-Ethane gas is run at a pressure of 20 psi to allow higher operating voltages and allow for more ionization. A small amount of water vapor added to the gas mixture helps to reduce the amount of organic compound which can build up on the wires.

Segmented cathode strips of 76 micron Mylar sheets with 8 micron aluminum foil bonded on both sides shape the field cage of the inner and outer surfaces of this device. Each Mylar sheet covers one-half of the active length of the chamber and 1/8 of the azimuth. Reading out the anode wires at both ends, a *Charge Division* method can be used to achieve a z position measurement. The more of the charge that is collected at one end, the closer the track is to that end. The ratio of charge measured at either end of the highly resistive sense wire gives a measure of the z position of the track near that wire. Figure 2.4 shows the wire layout in the PT and the VD.

[4] *Interaction Point* really means the center of the interaction region, within the limits of the positional uncertainties of the well-known beam spot.

The Main Drift Chamber

The DR extends 95 cm in either direction along the beam pipe and radially from 17.5 cm to 95.0 cm. It consists of 36240 field wires and 12240 sense wires strung between two aluminum endplates and support rings. They are arranged in 51 layers of nearly equal size rectangular (slightly trapezoidal) cells, with three field wires for each sense wire. Three to five axial layers alternate with stereo layers to form layer groups, each layer within a group having an equal number of wires. To achieve nearly equal cell sizes, there are a different number of wires for each layer group. Figure 2.5 shows the layout of wires and cells at either end of the CLEO II Drift Chamber.

Sense wires are arranged in 40 axial layers. These axial layers provide position measurements in the azimuthal ($r-\phi$) direction, momentum transverse to the beam, and the radial distance of closest approach of a track's extrapolation to the beam line. There are also 11 stereo layers, whose sense wires are at an angle of about 5° with respect to the beam axis. These stereo layers alternate with every three layers of axial wires up to layer 40, which begins the region where there are five axial layers between stereo layers at the outermost part of the drift chamber. The stereo layers, along with the cathode strips, allow for the measurement of a particle's z position as it passes through the chamber. The stereo layers also provide information on the polar angle, momentum in the longitudinal direction, and the longitudinal distance from the interaction point to the track's extrapolation to the beam axis.

The sense wires are 20 micron diameter gold-plated tungsten under a tension of 50 grams. Field wires in layers 1 to 40 are 110 micron diameter gold-plated aluminum under a tension of 170 grams. The remaining layers of field wires are made of 110 micron gold-plated copper-beryllium under a tension of 270 grams. This introduces extra material which reduces tracking resolution, but this effect is minimal at the larger radii.

Similar to the VD, the field cage is again shaped by cathode strips in the inner and outer surfaces. These cathode segments are made of 188 micron Mylar sheets with 25 micron aluminum foil bonded to one side. There are 16 (8) azimuthal sections on the inner (outer) cathode, with each section covering 6 (48) wires. This reduces the confusion of cathode signals correlated to different sense wires. Each cathode segment is about 1 cm in the beam direction, which means that the image charge of the avalanche at the wire is spread over three cathode pads.

For the parameters of the CLEO Detector, transverse momentum resolution in the tracking chambers is given by the formula:

$$\left(\frac{\delta p_t}{p_t}\right)^2 = (0.0011\, p_t)^2 + (0.0067)^2 \tag{2.1}$$

where p_t is the transverse momentum in GeV/c, and the constant term is due to multiple scattering. For $p_t = 5.280$ GeV/c, the resolution, δp_t, is about 47 MeV/c.

The angular resolutions for the reaction $e^+e^- \rightarrow \mu^+\mu^-$ are about 1 mrad in ϕ and about 4 mrad in θ. This difference in angular resolutions arises from the fact that fewer measurements can be made with the stereo layers compared to the axial layers.

2.2.2 Particle Identification (PID) Hardware

The CLEO Detector employs two separate means of *Particle Identification (PID)*, based upon devices which are named for two different phenomena. The two phenomena (and devices) are *Specific Ionization Energy Loss*, (dE/dx) and *Time-of-Flight*, (ToF). The hardware components of these two devices are described below. The effectiveness of each device depends upon momentum and a few other factors. A brief explanation of the phenomena involved follows, but will also be pursued in section 3.8, where PID calibration is explained in greater detail.

Specific Ionization Energy Loss, dE/dx

The 49 inner layers of the main drift chamber also serve as a dE/dx device. The innermost and outermost layers are not used because of the edge effects of the electrostatic field. Charged particles crossing the DR cells leave ionization "hits", which will produce signal pulses in the sense wires. The amount of charge measured along the particle's trajectory will be an indication of its amount of energy loss.

A charged particle with velocity $\beta \equiv v/c$ will lose energy as a function of distance according to the Bethe-Bloch formula for ionization energy loss:

$$-\frac{dE}{dX} = Kz^2\frac{Z}{A\beta^2}\left[\frac{1}{2} - ln\frac{2m_e\beta^2\gamma^2T_{max}}{I^2} - \beta^2 - \frac{\delta}{2}\right] \tag{2.2}$$

where:

T_{max} is the maximum kinetic energy a free electron can gain in one collision,

Z and A are the atomic number and mass (in g/mol) of the medium, respectively,

I is the mean excitation energy in eV,

ze is the charge on the particle,

γ is the relativistic velocity factor, $1/\sqrt{1-\beta^2}$,

$K = 4\pi N_A\, r_e^2\, m_e\, c^2$,

r_e above is the classical electron radius, $e^2/4\pi\epsilon_0 m_e c^2$, and

δ is a density effect correction.

A truncated mean of the ionization distribution is taken as the best estimator of dE/dx. The truncated mean is used to reduce the effects of noise and of the large Landau tail in the distribution. These reductions are achieved by dropping 5% of the lowest pulse heights (1-2 hits) and 40% of the highest pulse heights, respectively [20]. To optimize dE/dx resolution, several effects are corrected for. They are listed below, along with a brief explanation of their effects on dE/dx:

1. *Dip Angle Saturation* - Tracks nearly perpendicular cause electric shielding which reduces collected charge for that track. Measured charge depends on polar angle.
2. *Drift Distance* - Amount of charge reaching wire in allowed readout time depends on distance electrons drift from track to wire, which depends on electric field shape within cell.
3. *Entrance Angle* - Drift distance distribution depends on angle of track into cell in $r - \phi$ plane.
4. *Axial-Stereo Layer* - axial and stereo cells have different electric field shapes. Drift distance distribution depends on layer type.

For a track with 40 or more good dE/dx hits, the following resolutions have been achieved: 6.2% for Bhabhas and 7.1 % for minimum-ionizing pions.

Time of Flight, ToF

The TF system in CLEO is used as a primary trigger, as well as a means of PID. The trigger system will be explained in section 2.2.5. The TF system contains both barrel and endcap counters. The barrel TF system is located immediately outside the central drift chamber and is fastened by straps to the inner surface of the crystal mounting assembly. Each of the 64 barrel counters consist of a scintillator which is 279.4 cm long, 10 cm wide and 5 cm high, connected to a lightpipe and a photomultiplier tube (PMT), using an epoxy with the desired optical properties. The scintillator material, Bicron BC-408, was chosen for its fast decay time (2.1 ns) and long attenuation length (2.5 m). The lightpipe is made of UVT lucite bent at a 17° angle. The barrel counters cover the polar angle region from 36° to 144°, which is about 81% of 4π. Figure 2.6 shows two views of a barrel TF counter.

The 28 endcap TF counters are wedge-shaped pieces of the same scintillator material, mounted on the endcap calorimeters. Each counter is a trapezoidal sector of thickness 4.5 cm, covering the radial range from 25.9 cm to 89.0 cm at a longitudinal distance of 117.5 cm from the interaction point. The small end of the wedge extends into a 45° prism shape to avoid the need for gluing on a separate piece. The PMTs are glued directly onto the square face of the prism, at right angles to the length of the scintillator counters. The two endcap counters cover the polar angle regions from 15° to 36° on the east and from 144° to 165° on the west, which is about 16% of 4π. Figure 2.7 shows the layout of the TF endcap counters and PMT addresses.

The momentum of a track is measured from its curvature in the drift chamber. Measurement of the "time" to reach the scintillation counters then determines its velocity. Along with the independent measurement of the momentum from the CD, this then gives a means of particle identification by constraining the particle's mass.

Each PMT signal has two time to pulse height converters and a circuit which records the integrated charge in the signal pulse in the readout electronics. Each time channel also has a discriminator which determines the time the measurement began from the signal pulse. The stop signal for this time measurement comes from the rf frequency of CESR and is directly related to the time of a beam collision. The resolution of the TF system ranges from 120 ps to 250 ps, with an average of 170 ps. Compare this to the CESR crossing time, which is a few hundred nanoseconds.

2.2.3 Crystal Calorimeter

The CC consists of 7800 thallium-doped cesium iodide (CsI) crystals, approximately 5 cm square by 30 cm long. The 30 cm length of crystal is about 16 radiation lengths[5], which assures very little energy leaks out the back of the crystal. The central barrel region ($45° < \theta < 135°$) covers 71% of the solid angle and has the least amount of material in front of it, improving the energy resolution. The 6144 barrel crystals are trapezoidal in cross-section and slightly tapered along their length. The barrel crystals are oriented to point nearly toward the interaction point in 48 rows along the z-direction, as seen in Figure 2.2. This prevents losses in solid angle coverage. Photons arriving from the interaction point strike crystal faces in the barrel at nearly normal incidences.

Endcap crystals are rectangular in cross section at 5 cm per side, with the same length as the barrel crystals. There are 828 crystals mounted on each endcap in a four-fold symmetric pattern. There is much more detector material, including endplates and readout electronics, in front of the endcap calorimeters. This reduces the resolution of these devices.

The crystal material was chosen to allow precision measurements for photons from 15-5000 MeV in a highly segmented, large-volume shower detector at a 1 meter radius in a 1.5 T magnetic field. The desirable properties of CsI include: high light output, low hygroscopicity (capacity to absorb moisture), an emission spectrum that is well matched to photodiodes, plasticity and resistance to cracking, ease of machining, high density (4.51 g/cm^3), short radiation length (3.8 cm) and good thermal stability near room temperature. The size of the crystals was chosen to attain adequate position and energy resolution while keeping total costs (including support structures and readout components) reasonable. Nitrogen flows over the crystals keeping them dry, and humidity and temperature are constantly monitored.

Four photodiodes mounted at the rear of each crystal convert the scintillation light into electrical signals, which are each passed first to a preamplifier then to a mixer/shaper card that sums the four outputs and shapes the signal to be input to the ADC. Shower reconstruction in the calorimeter begins with the formation of clusters from individual hits. Electrons (and photons) typically lose almost all of their energy in such showers in a highly localized region. Hadrons typically lose much less of their energy than electrons in a more disperse pattern through nuclear interactions in the CC. These are two of the ways that the CC can distinguish electrons

[5] *Radiation Length* (X_0) is defined as the distance over which an electron's energy is reduced by a factor of $1/e$ (natural logarithm base, in this case, not electron charge).

from hadrons, by the ratio of their energy in a shower compared to their momentum from the drift chamber and by the localization of their shower shapes.

2.2.4 Muon Identification System

The muon chambers take advantage of the fact that muons are highly penetrating particles, That is, they interact very little with matter and can thus travel large distances. The goals of the design of the MU system were: maximum solid angle coverage, low probability of a hadron being misidentified as a muon (fake rate), reliability and ease of operation. Space limitations restrict the coverage of the muon chambers to the polar angle region $30° < \theta < 150°$, which covers 85% of the solid angle.

The MU system is placed outside the magnet coil, between several layers of iron. The first iron layer also serves as the magnet's flux return. The iron depths at which the counters are embedded are: 36, 72 and 108 cm, corresponding to 3, 5 and 7 nuclear interaction lengths (λ_i), respectively. These iron layers stop most other types of particles, although some hadronic tracks penetrate enough to be misidentified as a muon. Such lepton fake rates (including hadrons misidentified as electrons in the CC) have been studied in detail [21, 22]. We will use the results of such studies in our consideration of systematic errors.

The muon counters themselves are "plastic streamer counters", which operate as proportional chambers, under a voltage of 2500 V in a 50:50 Argon-Ethane mixture. Figure 2.8 shows the dimensions of an individual muon counter composed of eight separate chambers. A 50 micron diameter silver-plated Cu-Be wire serves as the anode in each counter, and a graphite coating on three sides of the counter serves as the cathode. External copper pickup strips measure a coordinate orthogonal to the one measured by the anode.

The muon counters are grouped into *superlayers*, which are 3-layer groupings of 20, 25, 29 or 24 counters for the inner, middle, outer and endcap superlayers, respectively. The geometrical inefficiency of a single layer is removed by having two slightly staggered layers. The third layer allows for noise reduction and also provides redundancy in case of malfunction of some counters. A muon superlayer is shown in Figure 2.9.

Muon identification is achieved by associating track hits from the CD with hits in all layers of the muon chambers. Tracks that are muon candidates are assigned the depth of the outermost chamber that records a hit. If a track does not penetrate further than expected according to track extrapolation, it is considered a non-muon. It is considered a bad quality muon candidate if it does not record a hit in each of the layers below the maximum depth. Further details of the maintenance and calibration of the muon identification system may be found elsewhere [23].

2.2.5 Timing, Trigger and Data Acquisition (DAQ)

The CLEO timing system handles the enabling, disabling and resetting of the various detector elements, and also provides gates and strobes properly timed to the crossing of the beams in CESR. CESR communicates its timing information to CLEO, which allows CLEO to decide when to trigger the readout of the detector. The crossing rate for the bunches of electrons and positrons in CESR is 2.8 MHz, while the rate of interesting events is typically about 10-20 Hz. It is therefore not possible to record the result of each and every beam crossing. The CLEO trigger system strives to maintain a balance between deciding when to write out an "interesting" event and reducing the "dead-time" in the detector (when no further events can be recorded).

The CLEO trigger is described in detail elsewhere [24]. A series of hardware requirements must be met on three levels before precious "live-time" will be sacrificed to read out an event. A final, software trigger program further determines what events are worthy of being written from disk to tape.

Different levels of the trigger system use different criteria. The following detector information is used by each level of the trigger system, the process of which is briefly described below:

1. **L0**: use TF, VD and CC.
2. **L1**: after L0 met, use VD, DR, TF, CC.
3. **L2**: after L1 met, use DR and VD.
4. LVL3: on-line software filtering for writing from disk to tape.

L0 is the fastest trigger and is thus the first trigger to select events. L0 accepts information from TF, VD and CC to select events. L0 attempts to reduce the 2.8 MHz beam-crossing frequency to a rate on the order of about 20 kHz.

After an L0 trigger has registered, all detector gating is disabled and a search is made for an L1 trigger requirement. L1 uses information from CD, CC and TF, for events which passed the L0 trigger. It takes about 1.0 μs for an event to arrive at the L1 circuitry. This causes about 2% dead time after an L0 trigger has fired. If an L1 trigger is not satisfied, the system is reset and detector gating resumes. The goal of the L1 trigger is to reduce the event rate to about 25-50 Hz.

The L2 trigger uses information from DR and VD to evaluate incoming events, after an L1 trigger has fired. It takes about 50 times longer than an L1 trigger to write out an event, about 50 μs. L2 would typically fire at about 10-20 Hz, depending upon CESR running conditions. When an L2 trigger had fired, the CLEO-II data acquisition (DAQ) system would write all of the information gathered by the crates from the various detector components onto disk.

The CLEO DAQ system consists of the crates from the component subsystems, plus "link boards" and VME processors [25]. These serve to build the raw data event every time an L2 trigger signal is passed. A number of multi-channel boards in each detector subsystem's crate perform charge integration on capacitors, or time-to-charge conversion with capacitors on the raw data stored there. Control boards in each crate then perform the following tasks:

1. compare analog signal level to a threshold, to select "hit" channels (*data sparsification*)
2. ADC digitization;
3. electronics pedestal subtraction;
4. gain correction;
5. buffering of data, until:
6. trigger signal initiates VME readout of crate buffers.

"Link boards" connect the various sub-detector crates to the VME crate, which directs the data traffic and creates the raw data event from the accumulated signals in the various detector components. This crate of VME processors directs transfer of data from the crate controllers of the individual detector subsystems into VME global memory, builds the event by constructing the ZEBRA[6] banks for all the subsystems, then transfers the event to the CPU running LVL3. The DAQ system for CLEO II consisted of 34 crates for the detector subsystems, 4 VME processors and 10 link boards. A schematic of the CLEO II DAQ system is shown in Figure 2.10.

Further filtering is employed with software when events passing L2 triggers are logged to disk, then dumped to tape. LVL3 is the software trigger program which further discards some unwanted events for tape storage. For instance, only a predetermined percentage of Bhabha events will be written to tape. Another task of the LVL3 trigger software is to kill "beam wall" events, which make up about 45% of the events which passed an L2 trigger. A fraction of "random trigger" events (about 1/8) is also kept in order to verify that what the trigger system has thrown away really was uninteresting.

We conclude this chapter by summarizing the CLEO II Detector's properties in Table 2.1. Typical resolutions and material thicknesses out to the various detector elements are shown. Note that thicknesses are given in terms of percentage of radiation length, X_0.

[6] *ZEBRA* is a special format for storing raw HEP data. It was developed by CERN.

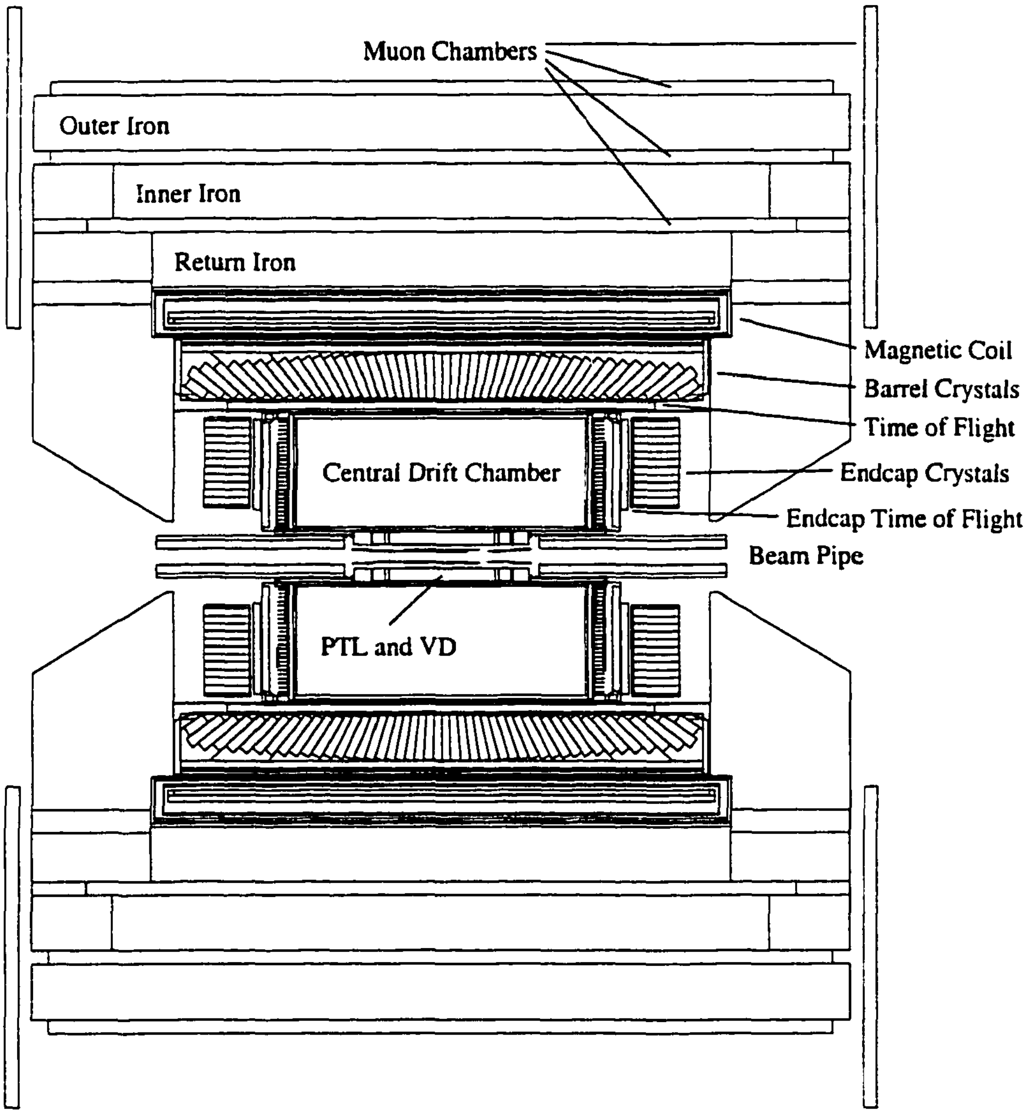

Figure 2.2: Side View of the CLEO II Detector, showing the various detector components.

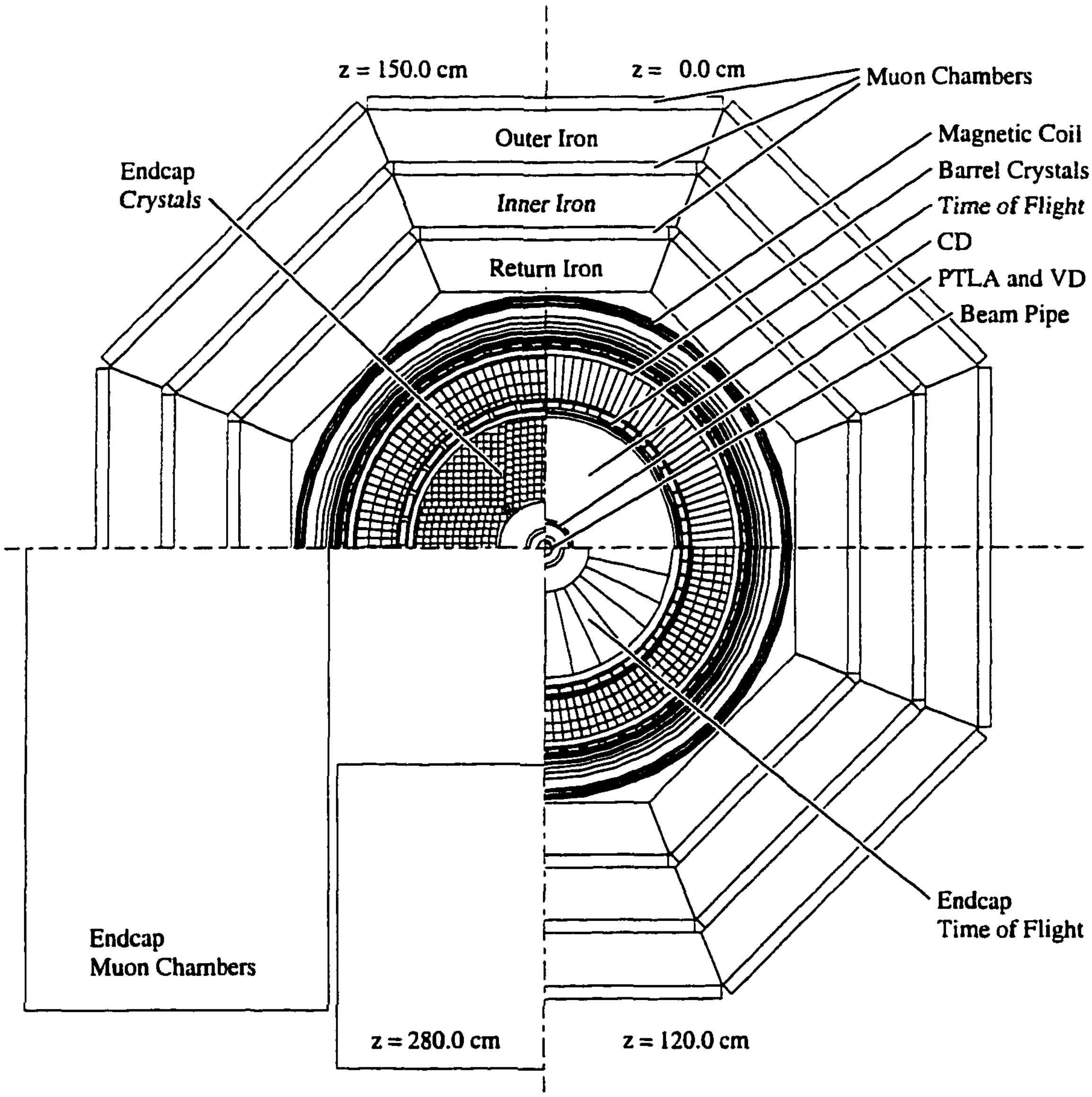

Figure 2.3: End View of the CLEO II Detector. Three quadrants show the various endcap detector components, which are located at different z values.

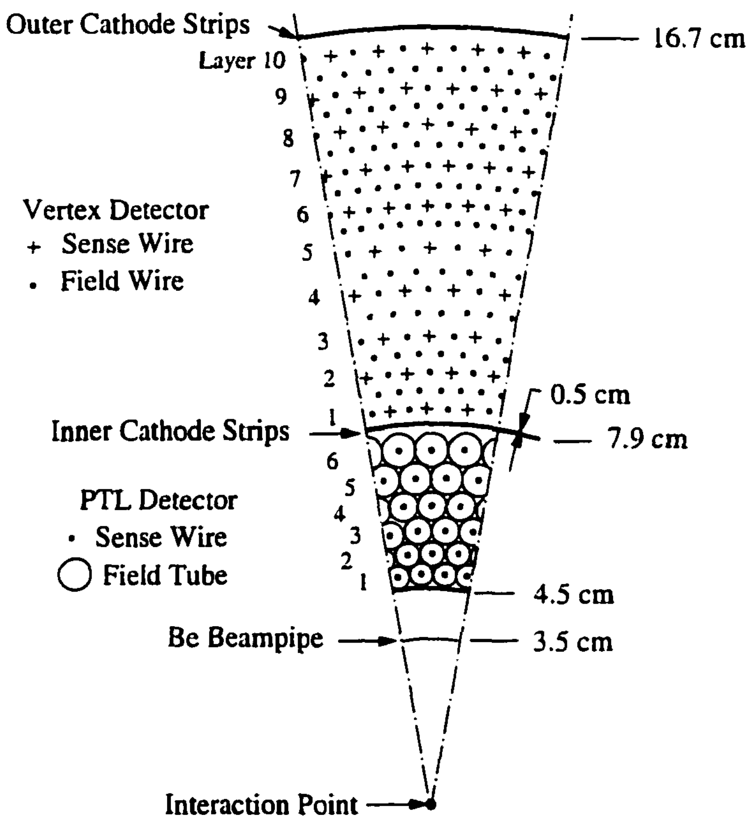

Figure 2.4: Wire Layouts for the PT and the VD, showing the relative positions of field and sense wires in the VD and sense wires and field cages of the PT.

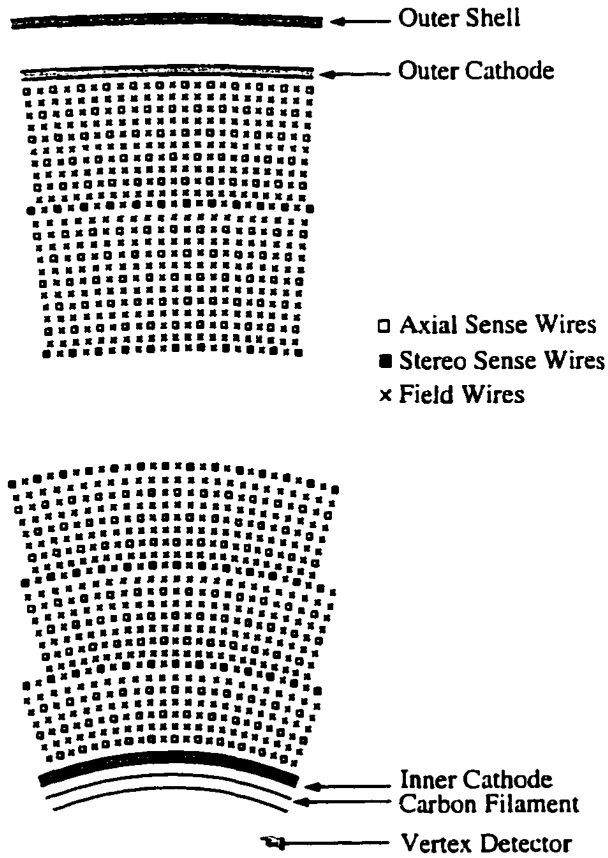

Figure 2.5: Wire Layouts for both ends of the DR, showing the relative positions of field wires and axial and stereo sense wires.

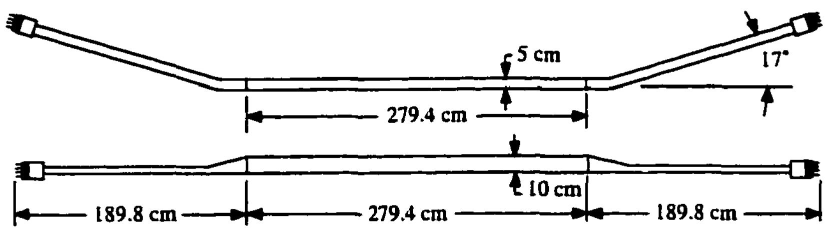

Figure 2.6: Two Views of a Barrel Time-of-Flight Counter.

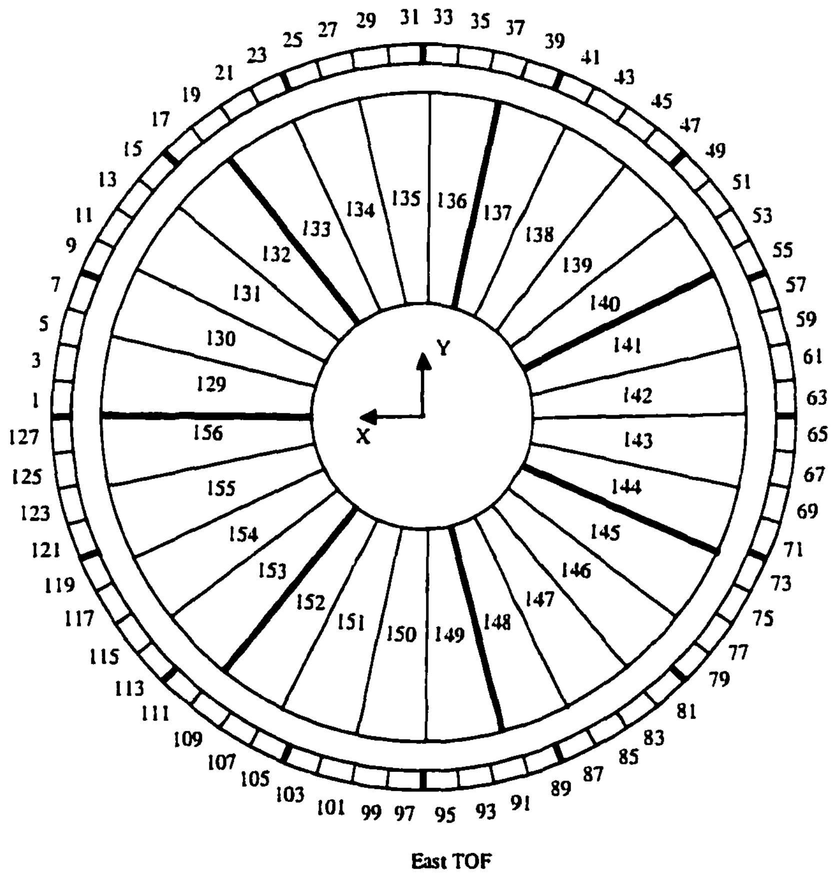

Figure 2.7: Layout of the East Endcap Time-of-Flight Counters. PMT addresses for the barrel counters can be seen surrounding the endcap counters. PMT addresses for barrel counters on the east side are odd integers, those on the west side of the same counter are the next even integer. West endcap addresses range from 157 to 184.

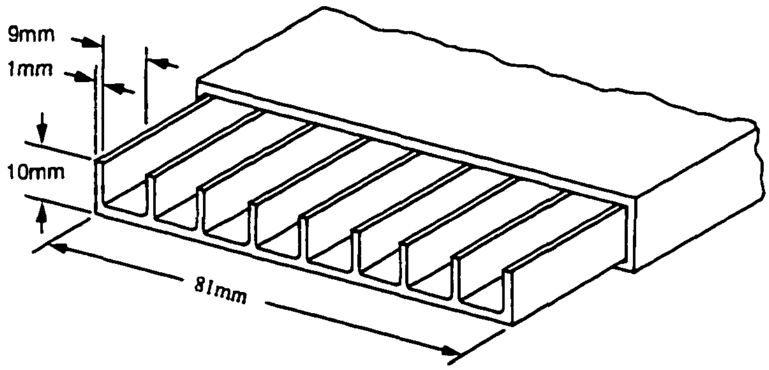

Figure 2.8: Cross-section of a muon streamer counter.

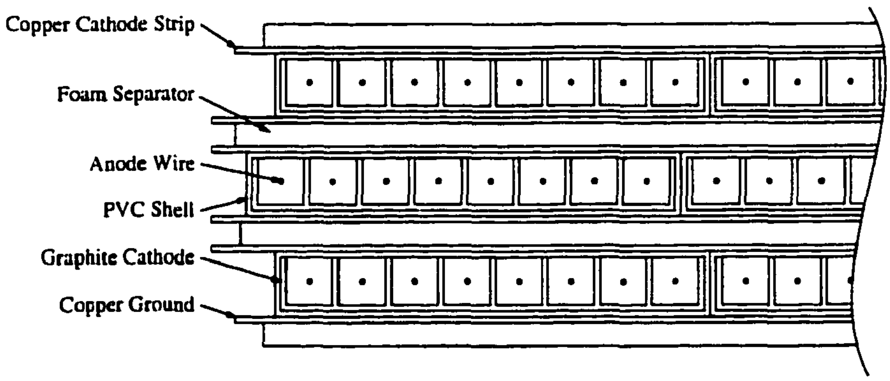

Figure 2.9: Cross-Section of a muon superlayer.

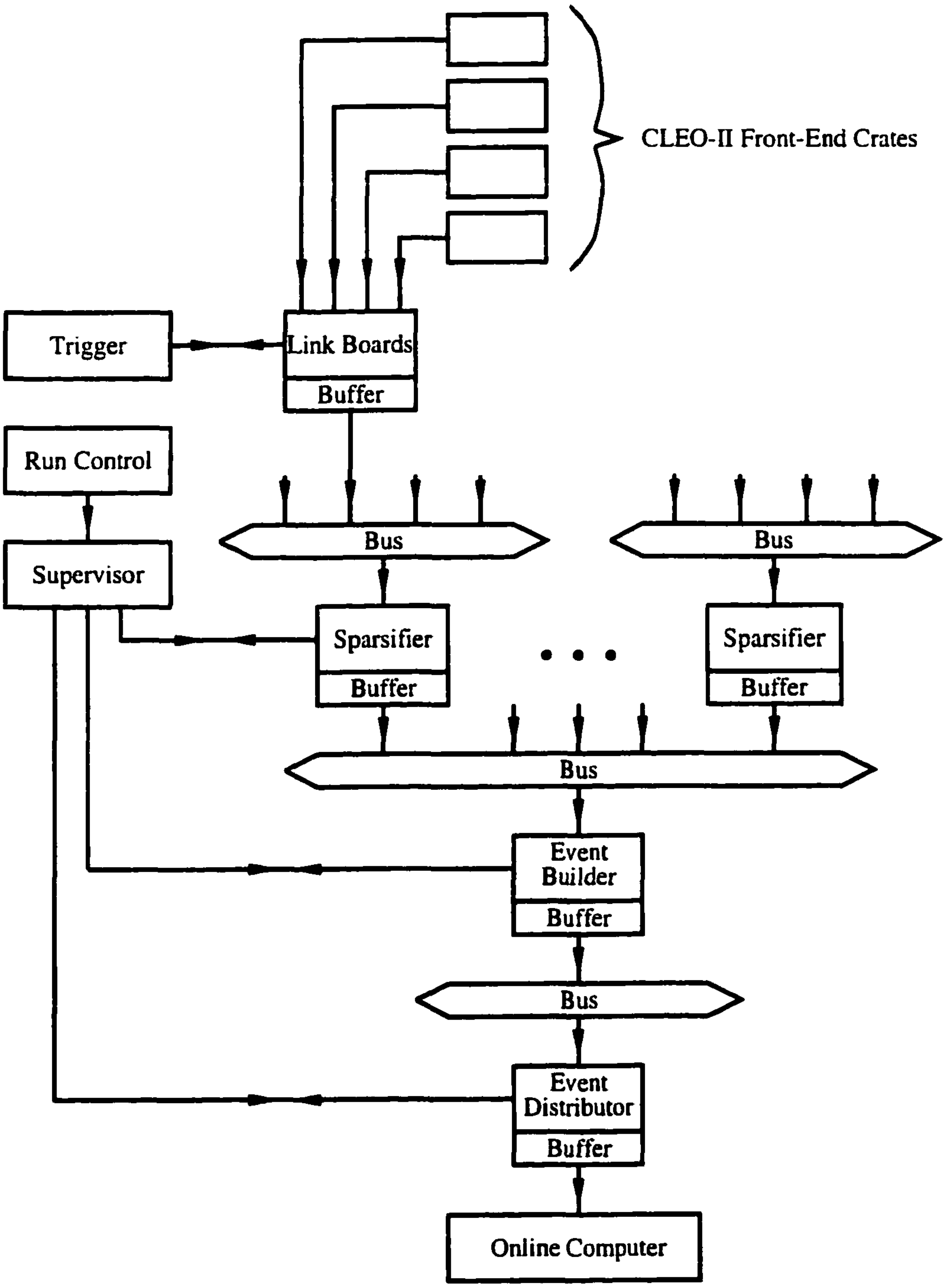

Figure 2.10: The CLEO II Data Acquisition System.

Table 2.1: Achieved resolutions in various elements of the CLEO-II Detector.

Detector Element	Resolution	Material in Front (% X_0)
PTL	100 μm ($r-\phi$ plane) no longitudinal measurements	0.46
VD	150 μm ($r-\phi$ plane) 750 μm (z-direction)	1.38
DR	110 μm ($r-\phi$ plane - axial) 130 μm ($r-\phi$ plane - stereo)	2.51
All Drift Chambers	$(\delta p_t/p_t)^2 = (.0011\,p_t)^2 + (.0067)^2$ $\sigma_\phi = 1\,mrad$ $\sigma_\theta = 4\,mrad$	
Ionization Loss	6.2% (5 GeV Bhabha electrons) 7.1% (minimum ionizing pions)	
Time-of-Flight	139 ps (5 GeV Bhabha electrons) 154 ps (minimum ionizing pions)	2.93
Barrel CsI Calorimeter	$\delta E/E[\%] = 0.35\,E^{-0.75} + 1.9 - 0.1\,E$ $\sigma_\phi = 2.8\,E^{-0.5} + 1.9$ $\sigma_\theta = 0.8\,\sigma_\phi \sin(\theta)$	18.0
Endcap CsI Calorimeter	$\delta E/E[\%] = 0.26\,E^{-1} + 2.5$ $\sigma_\phi = 3.7\,E^{-0.5} + 7.3$ $\sigma_\theta = 1.4\,E^{-0.5} + 5.6$	
Muon Chambers	2.4 cm (counters) 2.8 - 5 cm (strips)	Covers $\sim$ 7 nuclear absorption lengths

Chapter 3

Event Reconstruction

This dissertation utilizes data which was recorded between November 1990 and October 1994. Each *dataset* was originally processed shortly after being recorded. This was known as the "Original Compress" of these datasets. Section 3.3 describes naming conventions for CLEO datasets.

This same data was then re-processed between June 1996 and July 1997, using new calibration constants and track reconstruction code, including a Kalman Filter. This re-processed data is thus known as "*RECOMPRESS*" Data. The *RECOMPRESS Project* was undertaken to take advantage of the many gains that had been made in characterizing and calibrating the detector over the years, and to provide a uniformly processed, consistent dataset (which was also compatible with the format of CLEO II.V data). Appendix A contains a summary of RECOMPRESS datasets, and Appendix B contains a list of RECOMPRESS Full-ROAR and Skim DLTs[1] created by the author during this massive project.

This chapter details information relating to the Data Reconstruction Process which is known in CLEO as PASS2[2], with particular regard to processing RECOMPRESS data. Much of this chapter is taken from an uncirculated CLEO document which was heavily revised by the author [26]. The author served as Data Reconstruction Manager (affectionately referred to as *"PASS2 Guru"*) during the RECOMPRESS as a Service Job to the CLEO Collaboration. As part of his training prior to the start of the RECOMPRESS, the author also managed the Original Compress of about one-fifth of the total CLEO II $4S$ dataset (4sC-4sG) which had been taken between June 1994 and April 1995 (this was when the shutdown for the installation of the Silicon Vertex Detector began). This span of time also included a $1S$ and a $2S$ dataset, for which the author also managed both the Original Compress and the RECOMPRESS.

The RECOMPRESS Run Plan began by re-processing the 4sC-4sG datasets in dataset order, then proceeded in reverse dataset order beginning with 4sB down to

[1] *Digital Linear Tape* is a magnetic storage media with cartridge dimensions measuring 10.5 cm square by 3 cm high. DLT technology is patented by *Quantum Corporation*.

[2] The on-line calibration and monitoring process during data-taking is known as PASS1.

4s1. The lower resonance datasets were also re-processed, usually when there was a gap in the readiness of calibration constants for the next $4S$ dataset.

3.1 The PASS2 Process

3.1.1 Overview

PASS2's task is to transform raw data collected during CLEO runs into a format which can be readily analyzed by CLEO collaborators. Raw data such as drift time and pulse height information from the tracking chambers (and other analog-to-digital data), is read in and the $e^+ e^-$ event which triggered the readout of this information is reconstructed. To do this, PASS2 runs two separate CLEVER jobs to produce two different output formats. "CLEVER" is sort of a mnemonic for CLeo EVEnt Reconstruction.[3]

In the first CLEVER job, a set of *processors* is employed to actually reconstruct the event. These processors (linked software packages) include: `DUET` [27], which transforms wire hits into charged tracks; `CCFC` [28] and `XBAL` [29], which group energy deposits in the calorimeter into clusters of showers; and `KNVF` [30], which uses kinematic information provided by `DUET` to identify displaced track vertices (secondary vertices) in an event. In all, some 20+ processors are employed to fill the ROAR data banks that catalogue the key features of each event. The tracking banks were extensively re-written for the RECOMPRESS. Excellent documentation of the RECOMPRESS tracking banks may be found in [31, 32, 33]. By far the most important and the most CPU-intensive processor is `DUET`. About 80% of the CPU-time during PASS2 is spent on this single processor. With the RECOMPRESS, `DUET` also includes the actions of a Kalman Filter (also known as a Billoir Fitter), which properly takes into account the phenomena of multiple scattering and energy loss as a track is transported through different materials under different mass hypotheses.

The output from the first CLEVER job, as well as the raw data input, are stored in a special data format called *ZEBRA*, which was developed by CERN. The size of a *ZEBRA*-formatted file produced by this CLEVER job will usually exceed that of the input file by a factor of about 2.1.[4] Whether it's some historical artifact or somebody's peculiar sense of irony, the PASS2 process is nevertheless referred to as a "*COMPRESS*" of the raw data.

The second CLEVER job takes the output from the first CLEVER job (which includes all of the ROAR data banks and most of the raw data) and essentially just trims off the raw data piece, leaving only the ROAR data banks.[5] Output from this second CLEVER job is referred to as *Full-ROAR* data; *Full* because it

[3]Then again, CLEVER has also been accused of being a one-word oxymoron. *Take your pick!*

[4]For CLEO II.V data, this factor was about 4.3. Output FZX files were gzip'ed as written to save on disk space.

[5]Beginning with the 4sC, **RAW** data from the CD has also been stored on Full-ROAR DLTs.

contains data from ALL the events in a run, and *ROAR* referring to the data format in which this information is stored. A couple of additional processors are also run during the second CLEVER job, including: **TRKM** [37], a program to flag "good" and "bad" tracks, and **EVCL** [38], a program to classify an event according to its physics characteristics. The primary function of the second CLEVER job, however, is the conversion of *ZEBRA* formatted data (*.*fzx*) into *ROAR* format (*.*rp*) through the action of the **MAKR** (MAKe Roar) processor.

3.1.2 Track Reconstruction

The major advancement of the RECOMPRESS was the introduction of a Kalman Filter to the track reconstruction process. As mentioned in section 3.1.1, the Kalman Filter correctly takes into account the phenomena of multiple scattering and energy loss as a charged particle is transported along a track, either through different materials or under different mass hypotheses. Documentation on the Kalman Filter as it pertains to CLEO may be found in the following documents [34, 35, 36].

Many of the dE/dx corrections listed in section 2.2.2 were also used to improve tracking calibration in the RECOMPRESS. Other tracking calibration improvements included trapezoidal corrections to the drift chamber cells and z-dependent drift functions.

The quantities of interest to physics analyses are the components of a track's momentum (evaluated at the point of closest approach to the beam spot) and its energy, which is dependent upon the mass hypothesis of the track. These are related to the fundamental quantities which can be measured by a solenoidal detector with an axial magnetic field, such as the CLEO Detector [40].

The motion of a charged particle will be a helix, which can be described by five track parameters (c, ϕ_0, d_0, λ, z_0) measured with respect to a reference point (x_r, y_r, z_r), usually the beam spot. Assuming the magnetic field is oriented in the $+z$ direction, these five track parameters are:

- $c \equiv 1/(2R)$ - where R is the radius of curvature of the track,
- ϕ_0 - the azimuthal angle of the track at the point of closest approach to the reference point,
- d_0 - the signed distance of closest approach to the reference point,
- $\lambda \equiv \cot\theta$ - where θ is the polar angle from the $+z$ axis, and
- z_0 - the z position at the point of closest approach to the reference point in the $x - y$ plane.

These five canonical track parameters can be related to the fundamental physics quantities of energy and momentum through the following relations:

$$p_x = \frac{a}{2c}\cos\phi_0$$

$$\begin{aligned}
p_y &= \frac{a}{2c}\sin\phi_0 \\
p_z &= \frac{a}{2c}\lambda \\
E &= \sqrt{(a/2c)^2(1+\lambda^2)+m^2} \\
x &= x_r - d_0\sin\phi_0 \\
y &= y_r + d_0\cos\phi_0 \\
z &= z_r + z_0
\end{aligned} \tag{3.1}$$

where:

$a = -0.299792458\,Bq$, with B in Tesla and q in units of e, and
$(x,\ y,\ z)$ is the position at which the track has this momentum and energy.

Tracks from charged particles are found using a two step process. First, detector measurements are run through pattern recognition algorithms to identify those likely to have come from a single track. These measurements are then statistically fit using the maximum likelihood method to determine the most probable set of track parameters that are consistent with these measurements. The least squares method is used to fit the track parameters and estimate their errors.

The effects of multiple scattering and energy loss, however, serve to complicate the helical trajectory of the charged particle. The previously used general least squares method would simultaneously fit all the measurements. The Kalman Filter method improves on this previous fitting technique by picking up measurements along the trajectory and incorporating them into the fit one at a time. The iterative nature of this new algorithm takes these effects into account better than the global method of general least squares. The (extremely) gory details of track fitting, including formulas for multiple scattering and energy loss, can be found in [41].

CLEO writes out six alternative mass hypotheses: electron, muon, pion, kaon and proton (e, μ, π, K and p) hypotheses at the point of closest approach to the z-axis, and the π hypothesis at the outer-most CD hit used in the track fit. This last hypothesis, the so-called "pion-out" hypothesis, was to be used for dE/dx calculations through the DEDR processor. An unfortunate *feature*[6] of the tracking code stored the proton hypothesis at the outer-most CD hit ("proton-out" hypothesis) instead. This was not discovered until well after skimming was complete and the RECOMPRESS data had been released to the Collaboration, but it still needed to be fixed. Section 3.7 discusses the details of this dE/dx-fixing process for RECOMPRESS skim data in ROAR format.

3.1.3 The RECOMPRESS Farm Hardware

The RECOMPRESS Farm was an isolated network of CPUs, disks and DLT drives dedicated to addressing the needs of PASS2 processing. Much of the RECOMPRESS

[6]CLEO code contains no "**bugs**", only *features!*

Farm has since been dismantled and re-appropriated for other tasks, including the processing of CLEO II.V raw data and production of CLEO II.V MC. This section will therefore briefly describe the chief hardware components of the RECOMPRESS Farm, without regard to the specific machines or device names which were used during this project.

The Staging Node was connected to a 9 GB staging disk and a DLT drive. The *Stager* script had to be run on this node, as this was where the staging disk and *cl.fzx* input DLT drive were attached.

There were 6-9 alpha CPUs on each of three *legs* of the PASS2 RECOMPRESS Farm, each of which can function as a *Player* (PASS2 Processor). (Some machines were borrowed from the Nile Project [39] and others from the MC Production Farms at Minnesota and, eventually, Florida.) Each Player had its own 3-4 GB local disk on which it did its processing. These machines processed different runs in parallel, independently of each other. The logic of distributing the players into three legs was to better control I/O traffic on the farm during processing.

The Dumping Node was connected to: a 9 GB FZX dumping disk, a 9 GB ROAR holding disk, a 4 GB congealed ROAR dump disk, a congealed ROAR dump DLT drive and a dump FZX DLT drive. The *Congealer* and *Dump_** scripts had to be run on the dumping node, as this was where the congeal and dump disks and output DLT drives were attached.

The Staging, Dumping and Player's local disks were all auto-mounted and exported to the other PASS2 machines. They were accessible from any of the other PASS2 machines by using the syntax `/nfs/`*node_name*`/disk1` for the local disk of the desired CPU (and also through soft links). A schematic of the RECOMPRESS Farm hardware is shown in Figure 3.1.

3.2 Processing Scripts

PASS2 processing is accomplished through a suite of `UNIX` *Shell Scripts* which run on a cluster of CPUs, the PASS2 Farm. Raw data stored on DLT is dumped onto the staging disk, then moved to the local disk of a PLAYER where *ZEBRA* and *ROAR* output is generated by its CPU. Eventually the processed data files are moved to the dump disks, from which they are dumped to DLT.[7] The scripts which do this are separated by the various tasks which must be performed. A flowchart of the RECOMPRESS PASS2 process is shown in Figure 3.2.

3.2.1 STAGER

Raw data recorded at CLEO II run time was stored on $4\,mm$ tapes, typically five or six runs to a tape. Runs from these $4\,mm$ tapes have since been copied to DLT,

[7]ROAR data was dumped *after* it was congealed by $4\,mm$ tape number.

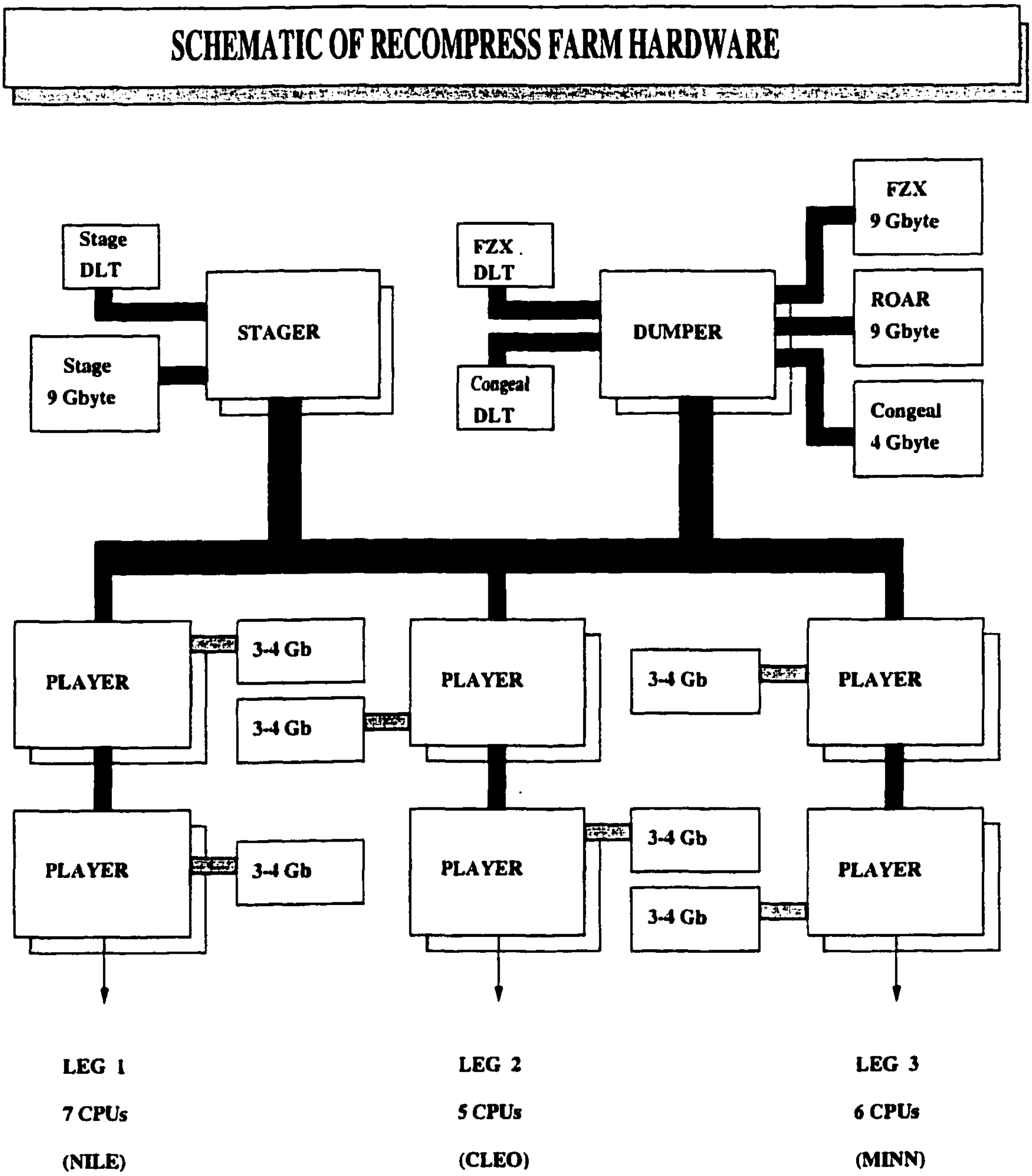

Figure 3.1: The PASS2 RECOMPRESS Farm. The Player CPUs performed the actual *ZEBRA* and *ROAR* processing on their local disks, while the Stager and Dumper were dedicated to moving input and output onto and off of the farm, respectively. (See the description in the text.)

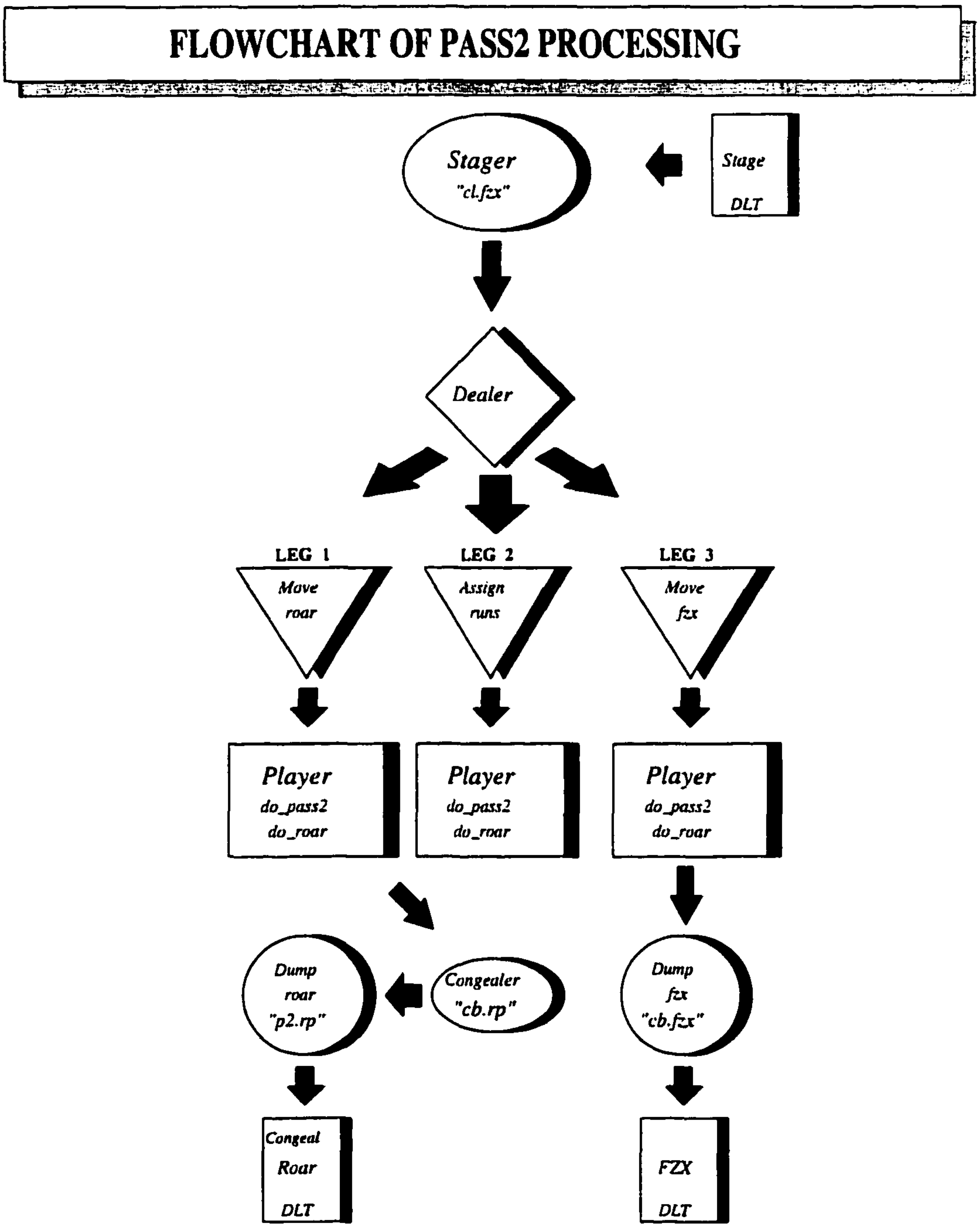

Figure 3.2: Flowchart of PASS2 Processing on the RECOMPRESS Farm. The *Player* scripts performed the actual *ZEBRA* and *ROAR* processing. The *Dealer* managed I/O traffic control on each leg through the *Assign* and *Move_** scripts. The *Stager* and *Dump_** scripts were dedicated to moving input and output files onto and off of the farm, respectively. (See the description in the text.)

each of which can hold about 10 $4\,mm$ tapes' worth of data.[8] The STAGER writes the input *ZEBRA* file of each data run which has an entry in *cleoiirun.fil*[9] from DLT to the staging disk on the PASS2 Farm.

Files are staged one run at a time, until the staging disk reaches its assigned quota. When its disk quota is reached, the STAGER sleeps for an hour and then wakes up to repeat the staging process when there is again room on the staging disk. An input *ZEBRA* file is called the "*cl.fzx*" file for a run.

3.2.2 DEALER

PLAYERs (PASS2 CPUs) must be assigned runs to process after determining that output can safely be generated without the risk of filling up that PLAYER's local disk. *ZEBRA* and *ROAR* output must be moved to the output disks to be congealed (*ROAR* data only) and dumped to DLT in order to make room on the local disk to process the next run assigned. These actions are performed by three sub-scripts which are managed by the DEALER. These sub-scripts are:

1. *Assign_runs_to_players*,
2. *Move_fzx_to_Dump_fzx*, and
3. *Move_roar_to_Congealer*.

As dictated by the DEALER, each sub-script above performs its task on all currently eligible PLAYERs hanging on one of the three legs of the farm. By communicating with each sub-script through a series of "*key-files*" (empty file-pointers created or `touched` by these different sub-scripts), these three sub-scripts are managed by the DEALER.

The PLAYERs submit request key-files, thus asking for assignments. The *Assign* sub-script above, after determining that the necessary conditions exist, answers with corresponding response key-files. The PLAYER scripts run in infinite loops; checking their disk space, submitting requests, receiving assignments, moving input runs to their local disk, processing those runs, and pausing (`sleeping`) in the interim.

The DEALER itself touches one of three different key-files, `SCRIPT_NAME_LEG_#`, one for each sub-script. These key-files indicate which sub-script is running on which leg. When finished with its individual task, each sub-script will rename its own key-file to `SCRIPT_NAME_FINISHED`, in order to tell the DEALER that the sub-script has done all that it can do at that time for all PLAYERs on that leg. The DEALER then cyclically re-shuffles these three other sub-scripts between the three legs of the RECOMPRESS Farm, after detecting and deleting each of the "`*_FINISHED`" key-files that each sub-script above had previously renamed.

[8]With the advent of CLEO II.V data-taking, raw data was recorded directly onto DLT.

[9]A text file which contains status information for all CLEO II runs. It gives the run energy, number of events and $4\,mm$ tape number. It also distinguishes between data and calibration runs, for example.

3.2.3 PLAYER

A PLAYER with enough local disk space will submit a request for a run. The PLAYER communicates to the *Assign* sub-script that it is ready to receive an input *cl.fzx* file by touching the key-file, ~/com/SPACE/*Feedme_leg#_playernode*, where *playernode* is the hostname of the Player CPU. The *Assign* sub-script will detect and delete this key-file, then tell the PLAYER which *cl.fzx* file to move to its own disk for processing. It does this by appending a *cl.fzx* file on the staging disk with the suffix "*_assigned_playernode*".

The PLAYER will then copy this file to its own disk (renaming it without the suffix) and then use this completely moved *cl.fzx* file to run the first CLEVER job by calling the sub-script '*do_pass2*', thus producing a *ZEBRA* output file for that run, "*cb.fzx*". The PLAYER will then use that *ZEBRA* output file as the input for the second CLEVER job by calling the sub-script '*do_roar*', which produces the *ROAR* output file for that run, "*cb.rp*".

After successfully creating the *cb.rp* file, a PLAYER will remove its corresponding *cl.fzx* file, thus freeing up disk space for the next run to be moved to its disk when assigned. The PLAYER will also rename the output files to signal to the *Move_** sub-scripts that they are ready to be moved to the output disks. The *cb.fzx* file is appended with the suffix "*_move_me*", and the *cb.rp* with the suffix "*_done.rp*". During normal PASS2 operation, several PLAYERs will independently process runs in parallel on the three separate legs.

3.2.4 DUMP_FZX

After a *cb.fzx* file has been created from the first CLEVER job, the PLAYER appends its name with the suffix "*_roarprocessing*" to indicate its status of ROAR processing. After the ROAR job is complete, the *cb.fzx* file is again renamed. The PLAYER re-appends the *cb.fzx* file with the suffix "*_move_me*" to indicate that it is finished with ROAR processing and ready to move to the FZX dump disk. The *Move_fzx* sub-script detects this "*_move_me*" file and moves it to the FZX output disk, renaming it without the suffix.

Runs were dumped in run number order, the same order in which they were staged. To accomplish this, DUMP_FZX called the sub-script '*wait_for_fzx*', which looked for the next file from the current 4 *mm* tape. When the next run was found on the FZX output disk, DUMP_FZX would dump it to the FZX output *cb*-tape in the dump FZX DLT drive. Output FZX files were then deleted from the FZX output disk after successfully being dumped to DLT.

Prior to the Original Compress of the 4sC dataset, PASS2 maintained a 1:1 correspondence between the number of input *cl*-tapes and output *cb*-tapes in 4 *mm* format, with the same set of runs for each tape. After the 4sC, however, PASS2 began dumping *cb.fzx* output to DLT. In addition to far greater reliability (in so far as PASS2's experience has gone), one DLT can hold as much data as *ten* 4 *mm* tapes. This accordingly reduces the number of times a *Computer Batch Operator* must answer tape mount requests, and thus the number of times the wrong tape can inadvertently be mounted in the wrong drive.

Because of the more complete ROAR information available, the *cb.fzx* DLTs were eventually determined to be of limited usefulness. (They were really only needed for the raw CD hits by folks working on the detector simulation for Monte Carlo. The raw CD hits were now available in ROAR format for all RECOMPRESS datasets.) They had thus become a tremendous waste of resources for *Computer Operations* to continue copying, checking and storing these DLTs. Beginning with the RECOMPRESS 4sA dataset, then, PASS2 stopped dumping *cb.fzx* files to DLT.[10] This required the introduction of a new sub-script, *Remove_fzx_files*, to replace the *Move_fzx* sub-script detailed above. This *Remove* sub-script would just remove a *cb.fzx* file from the PLAYER's local disk once ROAR processing was done, instead of moving it to the FZX dump disk. This sub-script was also controlled by the DEALER with the same key-files described above. This new sub-script had the effect of significantly speeding up production, since dumping the large FZX files was the most time-consuming I/O portion of traffic control on the RECOMPRESS Farm.

3.2.5 CONGEALER

The PLAYERs produced a *cb.fzx* file and a *cb.rp* file for each *cl.fzx* file on DLT which has an entry in *cleoiirun.fil*. While processing, the *cb.rp* file had the suffix "*_roarprocessing.rp*". When finished, it was renamed with the suffix "*_done.rp*". This indicates that it was ready to be moved to the ROAR output disk by the *Move_roar* sub-script. The *Move_roar* sub-script moved the next "*_done.rp*" file to the ROAR holding disk, renaming it without the suffix.

The CONGEALER waited for all of the *cb.rp* files from the next $4\,mm$ tape by calling the sub-script '*wait_for_ror*', which sequentially searches the ROAR holding disk for all of the necessary files. After all these files had been moved to the ROAR holding disk (or the script "timed out" waiting for one or more of all the files), the CONGEALER took the individual *cb.rp* files corresponding to all the runs on a $4\,mm$ tape and *congealed* them into a *single p2.rp* file on the congeal output disk. The *cb.rp* files for the individual runs were then deleted from the ROAR holding disk by the CONGEALER after successfully creating this single congealed ROAR file. Congealed ROAR files have the format,

$$\texttt{p2\_\{1st\_run\_of\_4mm\#\}} - \texttt{\{last\_run\_of\_4mm\#\}\_\{dataset\}.rp}\,.$$

This is what constituted the Full-ROAR data for a $4\,mm$ tape's worth of runs.

[10]This was one of *Suzanne*'s more significant contributions to the project, successfully convincing the *CLEO Software Coordinator* of the need to eliminate the writing of these *cb.fzx* DLTs.

3.2.6 DUMP_ROAR

DUMP_ROAR writes congealed *p2.rp* files from the congeal output disk to a Full-ROAR DLT in the dump ROAR DLT drive. Congealed ROAR files were then deleted from the congeal output disk after successfully being dumped to DLT. For a given dataset, we should have as many congealed *p2.rp files* as we do input 4 *mm tapes.* Full-ROAR RECOMPRESS DLTs have the naming convention,

{`dataset`}`_FR`{*2-digit tape_number*}

(i.e., `4sG_FR01` for the first DLT of 4sG).

After all the runs for a dataset have gone through the above procedures, additional work must be done by the PASS2 crew, namely *Gold-Plating* and *Skimming.* These steps will be elaborated later, stay tuned to this PASS2 Channel for details.

3.3 Processing a New Dataset

In this and in subsequent sections, we use the notation 4sX_Y in place of a specific dataset and version number. For those not familiar with the CLEO II dataset naming conventions, 4sX refers to the X'th distinct period (since CLEO II first started recording events in 1989) when CESR ran on the $\Upsilon(4S)$ resonance. A distinct period has usually been defined as the set of runs recorded between the times when the pole magnets near the end-caps were opened for hardware maintenance. Because a six-character limitation on tape names was enforced by the data-taking operating system, datasets after 4s9 were given single-letter names (4sA, 4sB, *etc.*) [42]. This limitation has since been lifted, but the practice has continued through CLEO II.V data-taking for consistency.

The suffix _Y has had a few different meanings depending upon the dataset. Usually, it referred to the number of times a dataset had been processed (compressed). For example, the 4s7_1 which has only been compressed once, or the 4s5_2 which was done *after* a serious (and unfortunately subtle) bug in the `VFND` code forced PASS2 to process that dataset a second time. On other occasions, this suffix has been used to designate the version number of the reconstruction code used, such as the 4s4_6 or the earlier 4s2_5. Since the 4s5, however, the practice has been to use this suffix to describe the number of times a dataset has been compressed (sometimes called the *iteration* of the dataset).

For consistency in the RECOMPRESS, the author chose to use the iteration number "_2" for all datasets except 4s5, 4s6 and 4sC. These three datasets were identified with iteration number "_2" in their Original Compresses, thus their RECOMPRESS iteration number was incremented to be "_3".

It is worth mentioning here that there is nothing in any of the PASS2 scripts that depends upon running on the 4S resonance. One could always substitute the appropriate resonance number to process lower energy datasets, as necessary, using similar naming conventions as above. It is highly unlikely that the CLEO Collaboration will record any more data on the lower Υ resonances, however, unless there is a clamor from a significant (or at least highly vocal) part of the collaboration (and the B-Factories at both *BaBar* and *BELLE* blow up).

3.3.1 Setting Up a New Dataset

Before a new dataset could be processed, a new directory structure must be created, necessary files copied into the proper areas, and the appropriate soft links created. This included, but was not limited to:

- creating a new *bin_4sX_Y* area for executables
- creating a new *com_4sX* area for scripts
- creating a new *log_com_4sX_Y* area for log files
- creating a new *ccon_4sX_Y* area for constants files
- creating a new *runfil_4sX_Y* area for library files
- creating a new *com* soft link for the scripts
- creating a new *bin* soft link for the scripts
- creating a new *ccon* soft link for the scripts
- copying up-to-date calibration constants files
- copying up-to-date library files
- copying a new *pass2* executable

The author's most significant contribution to the *PASS2 Legacy* was to automate much of the setup and startup processes, with just a few new Shell Scripts.

To setup a new dataset directory structure, simply execute the command (from `/home/cmprs2`)[11]:

- ~/Setup_new_set *newset new_iteration oldset old_iteration*

This script created the new *com* and *bin* areas and set up the directory structure needed for running the PASS2 scripts on the RECOMPRESS Farm, including the necessary soft links. Each soft link should be verified. That is, make sure each link points to an *existing* file or directory.

The above script also copied most of the other files needed for PASS2 processing into the ~ */com* and ~ */bin* areas, from these areas of the previous dataset.

The *Setup_new_set* script also moved the necessary constants files from the previous constants area into the new pass2 constants area in order to conserve disk space. It also made the appropriate soft links in that area. It was the *PASS2 Guru*'s responsibility to obtain more current constants files from the public CLEO constants area, when necessary.

The *Setup* script copied a new *pass2* executable into the *bin* area for the new dataset, as well as the *congeal* executable from the previous dataset.

[11]CMPRS2 is the UNIX account name for the *RECOMPRESS PASS2 Guru*.

3.3.2 Generating Tape Lists

New tape lists would also need to be created for the *Dump_fzx* and *Congealer* scripts, otherwise they would exit immediately. To do this, execute the *PERL*[12] Script *generate_tape_list* in `~/cmprs3_Util/` and follow the prompts given there.

The new dataset should now be ready for processing to begin.

3.3.3 Starting the PASS2 Scripts

Pre-run Checklist

Several areas must be examined before starting the PASS2 process (or *re-starting* in the case of occasional disasters!). Any left-over or pre-existing key-files corresponding to tapes or runs which are about to be requested or processed must be deleted.

The scripts *Check_new_set* and *Clean_new_set* would, respectively, check for or remove any and all key-files which exist. These scripts would also check for or remove **ALL** *fzx* and *rp* files from **ALL** of the PASS2 INPUT/OUTPUT and PLAYER disks, and check for or remove the tape log files and tape list files, as well.

To check for or remove all existing key-files, *fzx* and *rp* files, tape log files and tape list files, execute the respective commands (from `/home/cmprs2`):

- ~/Check_new_set *newset* (*to Check*)
- ~/Clean_new_set *newset* (*to Remove*)

Most importantly, it was necessary to regenerate the tape lists for *Congealer* and *Dump_fzx* before *re-starting* the dataset.

PASS2 Start-Up Scripts

A number of Start-Up Shell Scripts were written to ease the burden of starting a new dataset. Prior to configuring this automated procedure, the *PASS2 Guru* had to tediously start every processing script manually. This meant logging in to each Player CPU in turn, in order to start the *Player* script on that node.

The script *~/Start_Players* would execute the commands for starting the *Stager* and all available *Player*s (remotely via `rsh` commands, after defining the proper environment variables). One had to make sure that the unavailable *Player*s were commented out in this script before it was used. To start the *Stager* and all available *Players* remotely, execute the command (from `/home/cmprs2`):

- ~/Start_Players *newset first_tape last_tape*

[12] *PERL* has been said to stand for *Pathologically Eclectic Rubbish Lister*.

The script *~/Start_Output* would execute the appropriate commands for starting the *Dealer* and its sub-scripts (*Assign*, *Move_**), the *Congealer* and the *Dump_** scripts on the dump node. To start up all these scripts, execute the command (from `/home/cmprs2`):

- ~/Start_Output *newset [first_tape_fzx] first_tape_ror*

3.4 PASS2 Monitoring during Processing

Despite the automation of the processing scripts, PASS2 still requires the presence of an observant and diligent person to periodically examine the system. Said person must regularly monitor the log files for all of the data processing scripts mentioned in section 3.2 to ensure that things are still progressing smoothly. During processing, several diagnostic and monitoring scripts could be used to check for executable errors, bad input or output files or DLTs, etc.

3.4.1 Diagnostic Scripts

Three handy diagnostic scripts which may assist in this monitoring job are described below and could be run from the *com* area on any PASS2 CPU:

1. *Trouble_check.scr*
2. *Super_stat.scr*
3. *Check_tapelogs.scr*

Trouble_check.scr would check disk space usage on all of the input and output disks, as well as the *log* and *home* areas (no disk should be more than 95% full). This script would also look for existing *key-files*, as mentioned in the previous sections.

Super_stat.scr lists which files are on which disks, which PLAYER is running on which file, and whether the PLAYER is doing the **pass2** or **roar** job (indicated by a '**p**' or an '**r**'). An immediate sign of trouble is if the number of **p**'s plus the number of **r**'s on the PLAYER disks does not equal the number of PLAYERs currently processing runs. An input file that failed to successfully produce ROAR output with the correct number of events from *cleoiirun.fil* would be identified as a *mismatch*. *Super_stat.scr* also looks for these problem files (indicated by the tag "`_MISMATCH`" in the filename).

Check_tapelogs.scr would report when the latest input DLT was staged, as well as when the last *fzx* and *rp* files were dumped to DLT.

3.4.2 Monitoring Scripts

A number of other scripts could also be turned on which would monitor log files, mismatches, nodes, etc. These scripts were meant to *assist*, **not take the place of**, the observant and diligent *PASS2 Guru*. They would send an alert *via e-mail* that something was amiss, but would do nothing to fix the problem. These scripts may be run from the *com* area of any PASS2 CPU, using the following commands:

1. Log_checker $4sX$ > & LOG_COM_DIR/Log_checker.log &
2. Mismatch_finder $4sX$ > & LOG_COM_DIR/Mismatch_finder.log &
3. Node_checker > & LOG_COM_DIR/Node_checker.log &

3.5 Gold-Plating A Dataset

Given the complexity and scale of the many levels of data reconstruction code for the RECOMPRESS, it is amazing to realize that all but a few of the CLEO data runs from a given dataset *were* processed in this automated environment. Well over 90% of the input *cl.fzx* files of a dataset would be processed with no trouble. Both *ZEBRA* and *ROAR* output would be generated with the correct number of events processed. The output files would then be moved, congealed (ROAR), and dumped to DLT.

Occasionally, things did go wrong for various reasons, though, and a run would fail to process the correct number of events. These runs were flagged as "`MISMATCHes`" by the processing scripts, and had to be investigated as to the cause. A mismatch file's ROAR output would not be congealed or dumped, and it had to be fixed by hand. The process of fixing problem data runs in PASS2 is known as "*gold-plating*" the dataset.

When a mismatch occurred, the *cl.fzx* input file and any output files generated were each renamed with the flag "`EVENT_MISMATCH`" or "`SIZE_MISMATCH`" in the filenames, depending upon the nature of the mismatch. Consequently, **ALL** of these flagged files would remain on the PLAYER's local disk and would not be moved by the scripts. Until these mismatches were removed or otherwise resolved, the PLAYER may not have had enough disk space to request more runs. If a large number of mismatches remained on the PLAYER disks, this would seriously diminish the processing power of the RECOMPRESS Farm.

When a mismatch occurred, a first step was to check that PLAYER's log file to determine what went wrong. The next step would be to consult the log files for the first CLEVER job (*pass*2 job) and the second CLEVER job (*roar* job) for that run. All problem files had to be fixed before a dataset's skims could be released to the collaboration for analysis.

Typically, a half dozen or so runs from a dataset would fail to run to completion, depending upon the total number of runs in the dataset. There may have been any number of reasons for a failure. Problems that have most commonly occurred during

RECOMPRESS PASS2 processing are listed below, along with the preliminary steps to take in order to be able to fix them.

1. **MISSING CONSTANTS** - Contact the *Constants Librarian* and/or *Constants Makers* for file update(s).
2. **CODE CRASH** - Run the *pass2* executable in debug mode using **dbx** to get a traceback to show to code makers.
3. **HARDWARE FAILURE** - Contact *Selden Ball* or *Joe Schmidt* for a diagnosis of the problem.
4. **WRONG NUMBER OF EVENTS** - Consult CLEO Log Books to verify the event difference from *cleoiirun.fil*.

All mismatch jobs had to be fixed before DLTs could be certified by *Brian Heltsley* (BKH) and analysis-ready skims subsequently generated. The certification process checks the *luminosity*, and also verifies that Full-ROAR DLTs have no missing or duplicate data runs. Luminosity in HEP experiments is the number of particles in the beam per unit time per unit area. With the cross-section, it is a measure of the data-taking event rate.

In the first three cases above, either the pass2 job, the roar job, or more probably both, would have to be re-run. In the last case, also consulting with the CLEO II Run Manager of that time or with *David Kreinick* (DLK) would soon verify that the number of events which were processed by PASS2 **WAS** the correct number of events for that run. For the earliest datasets, even CLEO II Logfiles on *microfiche* were consulted with DLK's help! PASS2 would then send e-mail to RUNINF[13], advising the *PASS1 Guru* to update *cleoiirun.fil* with the actual number of events which were processed by PASS2 for that run.

Gold-Plating Scripts

A number of scripts may be used to facilitate the gold-plating process. Procedures for fixing problem runs are outlined below. The gold-plating steps which follow presume that the above steps identifying the reasons for a crash and correcting the reason(s) for that problem run's crashing were already taken. That is to say, new constants files or new executables were copied to the proper directories, or an input file was recovered from a failed disk (perhaps re-dumped from DLT).

Run the script *4sx_comd_scrpt*, with the appropriate arguments, on each mismatch *cl.fzx* file. This script would in turn call the processing scripts '*do_pass2_single*' and '*do_roar_single*' to produce both an output *cb.fzx* file and an output *cb.rp* file. The *do_*_single* scripts were also run individually, when necessary. The output *cb.fzx* file could be deleted after the *cb.rp* file was verified to be correct. The input *cl.fzx* file could also be deleted once the output files were produced correctly.

[13] RUNINF is the UNIX account name for the *PASS1 Guru*.

The next step was to fix the Full-ROAR DLT. Sometimes the *wait_for_ror* subscript mentioned in section 3.2.5 would exceed its allowed time limit while waiting for a file which had already been flagged as a `MISMATCH`. In these cases, the *Congealer* would just `congeal` all of the other files from that 4 *mm* tape without the missing file. The `MISMATCH` *cb.rp* file would thus have to be re-congealed with the remaining runs of that 4 *mm* tape in the correct run order, and then inserted into the proper location of the appropriate Full-ROAR DLT. The sections below outline this procedure.

Re-Congealing Fixed ROAR Files

Determine which Full-ROAR DLT contains the adjacent runs in the mis-congealed ROAR file(s). The `UNIX` tape command, `mt -f` *tape_device_name* `fsf`, may need to be used to fast-forward to the correct file location on the DLT first.

Then copy these file(s) to disk using the `dd` command syntax with block size (`bs`) 32400, as follows:

`dd if=`*tape_device_name* `of=`*disk_path/file_name* `bs=32400`

Consulting the *Dump_roar* log file and checking the number of blocks written to DLT for that file would verify that the correct file was dumped.

Then fix the corresponding file, as follows: If the mismatch run fits in the middle of the mis-congealed ROAR file, use the `congeal` executable twice to *bite* the mis-congealed ROAR file into the appropriate pieces. Put all of the runs **before** the mismatch in one file, and all of the runs **after** the mismatch in another file. Then use `congeal` once again to patch the pieces together in the proper run order. If the mismatch run belongs at the beginning or the end of the mis-congealed file, just use the `congeal` executable to patch it to the correct end of the mis-congealed ROAR file.

There were several scripts which executed the appropriate commands for these gold-plating `congeal` jobs. Which one(s) to call and the order in which they were used depended upon where the fixed file fell in the mis-congealed ROAR file. These scripts were:

- **congeal_bite.scr** — bites off runs before or after location of missing file.
- **congeal_end.scr** — places fixed file at start or end of congeal rp file.
- **congeal_fix.scr** — fixes two bitten files with fixed file in proper run order.

All of these gold-plating scripts required the proper arguments and syntax to run properly. The scripts themselves were well-documented and could be consulted for their proper usage.

Once a fixed congealed ROAR file was on disk, PASS2 would inform the *Computer Operations Supervisor* where it was located and what file number on which Full-ROAR DLT it replaced (or was to be inserted as) so that the DLT could be repaired.

PASS2 adopted the following naming convention for a gold-plated file:

{Full-ROAR_tape_#}_{file#}_{replace/insert}.rp

i.e., 4sC_FR01_file5_replace.rp replaces file 5 of DLT 4sC_FR01.

Gold-Plating was by far the most time-consuming and labor-intensive part of the Service Job for the RECOMPRESS *PASS2 Guru*. For CLEO II.V data, runs were not congealed because of much larger file sizes per run (mostly due to the SVX). Also, because of the overhead on *Computer Operations* DLT resources, mismatch runs were no longer patched to DLTs in run number order; they were merely written at the end of a dataset's DLTs. All valid data runs were still processed, despite any problems that may have occurred during the running of the scripts. Sadly, this did not make life much easier for the *CLEO II.V Pass2 Guru*, (PASS25), because the hazards of processing the more complicated SVX data easily outweighed these modest gold-plating gains.

3.6 Re-ROAR

The RECOMPRESS Project was a very intensive re-writing of massive amounts of code, requiring the time and effort of literally dozens of people (over many months, if not *years*.). The interplay between all these software packages was not trivial, to say the least. A number of delays occurred before the project was begun, because people were always figuring out how to do things better. Finally, the CLEO *Powers-That-Be* decided that the project must begin, and we would produce the best data possible.

Because of his intensive responsibilities as *CLEO Librarian* prior to and during the RECOMPRESS (and parallel deployment of the SVX code), however, Florida Graduate Student (and fellow Service Task Slave) *Craig Prescott* was delayed in making the final modifications to KNVF, which was a significant improvement in performance over the existing vertex finder, VFND. A comparison of the performance of the two vertex finders is documented in [47].

It was thus decided that, after all the RECOMPRESS datasets had been processed, a separate DRIVER[14] job would further process the Full-ROAR files, prior to skimming (which is detailed in the next section). This phase of the project became known as the *Re-ROAR* [43] of RECOMPRESS data, and is briefly reviewed here.

The NILE Farm was used for Official RECOMPRESS ROAR-Fixing and Skim Production. The Nile Farm at Cornell consists of six high-speed Digital Alpha WorkStations, with four DLT drives and about 100 GB of disk space attached to the various nodes.

ROAR-Fixing consisted of running the *Fixer* Shell Script (analogous to a PASS2 *Player* script) on each NILE node. This UNIX Shell Script moved a congealed ROAR

[14] DRIVER is CLEO's main ROAR analysis job environment, within which users compile, link and run their own analysis code.

File from the staging disk to a local fixer disk and then ran the following 2 executables in sequence:

1. *bmspot* - which produced updated beam positions in new **AFN** Files for each congealed ROAR file. Each congealed **AFN** file was then `split` into single-run **AFN** Files, which were then exported to:
2. *reroar* - which: fixed the "proton-out" bug, ran KNVF, cleaned up and re-wrote a bunch of ROAR fields (to make RECOMPRESS Data compatible with the format of CLEO II.V Data), re-did Cathode Clustering, and probably a bunch of other stuff which only *clib*[15] knows for sure.

The *Fixer* Script checked that all events were processed and also compared original ROAR and Re-ROAR file sizes, then moved the new single-run **AFN** files to the common **bpdir** directory for that dataset. These new **AFN** files were later copied to the official constants areas, to make the improved beam spot calculations available for user analyses.

3.7 Producing Skims for Physics Analysis

As mentioned in Chapter 2, the CLEO Trigger System decides when to write out an "interesting" event. Even so, we end up with many events on DLT which are not useful for physics analyses. Table 3.1 shows a typical breakdown of event types for a given data run.

The skim process serves to identify particular types of physics events which are of interest for physics analysis, based on different selection criteria. Event classification variables are filled by the EVCL processor during the second PASS2 CLEVER job. Note that the majority of events in Table 3.1 are classified as two-photon (~30%) and e pair (~33%). Electron pair events, arising from a process called *Bhabha scattering*, are useful (along with μ pair events) for calibrating the various detector components, thus producing the constants files needed for PASS2 processing. Hadronic events (CLASS 10) make up about 10% of the events in a given data run. Most physics analyses are interested in hadronic events. The skim process reduced the number of Full-ROAR DLTs for a RECOMPRESS dataset by anywhere from a factor of three up to an order of magnitude, depending upon the type of skim being produced.

Once a congealed ROAR File had been fixed on each NILE node, it was ready for skimming. The *Skimmer* Shell Script ran the *dskm* [44] executable, set with different *User Control Flags* [45], to sequentially produce the following skim formats *(Skim Cuts Used and ROAR Fields Written are indicated)*:

1. **FHD** - *Full-ROAR HaDron Skims*
   (KLGL.EQ.10 .OR. KLGL.EQ.11)
   ***ALL* ROAR Fields Written!**

[15] CLIB is the UNIX account name for the *CLEO Librarian*.

Table 3.1: Event Classification Types for a given CLEO data run containing 5818414 triggered Events.

ICLAS Number	Class Type	Cross Section	Number of Events	$jclas = 1$	$jclas = 2$	$jclas = 3$
1	Junk	8.595	823275	823275	0	0
2	Cosmic	0.261	24971	24971	0	0
3	Beam gas	2.171	207934	66595	141339	0
4	Two photon	18.142	1737752	462557	91970	1183225
5	e pair	20.049	1920395	1279741	571049	69605
6	μ pair	1.158	110950	75195	35755	0
7	γ pair	2.849	272897	176270	96627	0
8	$e\,e\,\gamma$	2.151	206042	178871	27171	0
9	Unknown	0.000	0	0	0	0
10	Hadronic	5.047	483390	404776	70472	8142
11	Had-badVtx	0.322	30808	6057	20068	4683

2. **HAD** - *Pared-Down Hadron Skims*
   `(KLGL.EQ.10 .OR. KLGL.EQ.11)`
   `TREL, TRMU, CDRH, TRHI, TRHT, CCEL, TFDT` **Fields Deleted!**
3. **TAU** - *Pared-Down Tau Skims*
   `LTSKM [46] .EQ. .TRUE.)`
   `TREL, TRMU, CDRH, TRHI, TRHT, CCEL, TFDT` **Fields Deleted!**
4. **2TK** - *Pared-Down 2-Track Skims*
   `(ETGL.LT.8.0) . AND. (NTRKCD.EQ.2 .OR. NCHGGL.EQ.2)`
   `.OR. IS_RAD_MU() .OR. KLGL.EQ.6`
   `TREL, TRMU, CDRH, TRHI, TRHT, CCEL, TFDT` **Fields Deleted!**
5. **4TK** - *Pared-Down 4-Track Skims*
   `(NTRKCD.EQ.4 .OR. NCHGGL.EQ.4)`
   `TREL, TRMU, CDRH, TRHI, TRHT, CCEL, TFDT` **Fields Deleted!**

The *Skimmer* script also echoed the number of events written for each skim type to its log file.

All of these different skim types were written to DLT, then copied by the *Computer Operations Supervisor* or the Computer Batch Operators. The **FHD** and **2TK** Skims were dumped *on-line* (during processing), since they were the largest skim files and there were only 4 DLT drives on the Nile Farm (1 for Full-ROAR Input, 1 for Fixed-ROAR Output, 2 for Skim Output). The other three skims were moved off to reserve disks during processing, in order to keep the local *Fixer* disks clear. They were then dumped *off-line*, after skimming of a dataset was complete.

After a fixed ROAR file had been skimmed, it was then dumped to a Fixed Full-ROAR **(FR)** DLT. BKH then certified luminosity and run number order for these **FR** DLTs. He also certified that all of the various skim type DLTs had no missing or duplicated runs.

A number of other UNIX Shell Scripts were also written, to manage I/O traffic on the *NILE Farm*. They are:

- *Nile_Stager*
- *Nile_Dealer*
- *Move_Skims*
- *Dump_Skims*
- *Dump_Fixed_Roar*

The name of each of the above Shell Scripts is indicative of its task. The **_Skims* Scripts accepted one of the five skim types above as an argument, in order to perform its task for each of the different skim formats. Many of these scripts became the basis for the suite of scripts used for CLEO II.V skimming.

A minor amount of gold-plating was also required to correctly fix and skim all of the events on all of the RECOMPRESS ROAR files on DLT. Sometimes the wrong number of events or wrong file size was flagged as a MISMATCH. Other times, adjacent files were deliberately copied to replace missing files, in order to keep the *Dump* scripts moving. These problems were mostly due to some unfortunate *features* of the Shell Scripts (and/or tape list files) themselves, for which the author chooses not to provide further detail. Suffice it to say that eventually all was made right on all Full-ROAR and Skim Tapes before releasing them to the collaboration, thanks largely to the superior efforts of the *Computer Operations Supervisor*.[16] The skim tapes were then released to the CLEO Collaboration (and the author breathed a huge sigh of relief!).

Re-dE/dx

As mentioned in section 3.1.1, all of the RECOMPRESS skims had incorrect dE/dx information. This was because the *reroar* executable did not re-run the dE/dx code after fixing the "proton-out" bug. The **FHD** DLTs were used to create a new set of **HAD** DLTs with correct dE/dx info, so-called **NEW_HAD** DLTs [48].

To fix the other skims, the Full-ROAR DLTs had to be re-skimmed, because the *pared-down* skim DLTs did not have the correct tracking parameters for the "pion-out" hypothesis stored, which were needed to recalculate dE/dx on the track-hit level. The so-called **NEW_TAU**, **NEW_2TK** and **NEW_4TK** skims were consequently re-written with **ALL** Full-ROAR fields during this process, so that they could be used to fix other problems without re-skimming (again). *Pared-down*

[16] who is now even more greatly appreciated as the author's *WIFE!*

TAU skim DLTs, labeled **RTAU**, were also recently produced in order to reduce the number of DLT mount requests for those doing tau physics analyses.

The Full-ROAR and **FHD** DLTs themselves were not fixed, however, because of the overhead on *Computer Operations* DLT resources. Those users who have a need to run on Full-ROAR or **FHD** data have been reminded of the necessity to run the dE/dx-fixing routine themselves in their analysis code.

3.8 PID Device Calibration

The PID device hardware of the CLEO II Detector has been described in detail in section 2.2.2. We concern ourselves here with providing a brief description of the calibration methods used to construct the variables which describe the performance of these systems with respect to physics analysis. Such calibrations are made using the above mentioned ROAR data in either Full-ROAR or skim formats.

3.8.1 dE/dx Calibration

As mentioned in section 2.2.2, a number of effects are corrected for to produce the best estimator of the ionization distribution. This truncated mean of pulse heights on the `DR` wires is known in CLEO as the variable `DE50DI`. The Santa Barbara (UCSB) CLEO Group has developed an improved calibration technique that converts this truncated mean into a fundamental quantity of specific ionization, I, that is only a function of $\beta\gamma$. This eliminates the systematic effects of curvature, $\cos\theta$, and gas gain saturation. Changes in atmospheric pressure and DR voltages can cause the gas gain to vary from run to run.

This new calibration procedure is outlined as follows. Further details may be found in [49]. We call this new calibration subroutine in our DRIVER analysis code for both data and Monte Carlo.

- The mean `DE50DI` for electrons is a function of $\cos\theta$ and curvature, although electrons above 100 MeV/c are expected to have a uniform ionization. Therefore, construct a function of $\cos\theta$, curvature, run number and bunch number that transforms `DE50DI` into a new variable $\mathrm{DE50_{elec}}$, chosen so that the mean value of $\mathrm{DE50_{elec}}$ is a constant for electrons.
- It is expected that particles with values of $\mathrm{DE50_{elec}}$ different from electrons will still exhibit a $\cos\theta$ dependence from gas gain saturation. Use protons, which have $\mathrm{DE50_{elec}}$ larger than the electrons, and pions and muons, which have $\mathrm{DE50_{elec}}$ smaller than the electrons to parameterize this effect. Then construct a variable I from $\mathrm{DE50_{elec}}$ and $\cos\theta$ where the mean value of I shows no $\cos\theta$ dependence.
- Parameterize the mean and width of the I distributions and use those parameterizations to construct the `SGXXDI` variables, which give the number of

standard deviations a track differs from the XX particle hypotheses, where XX = EL, MU, PI, KA, PR.

Figure 3.3 shows the specific ionization energy loss for different particles as a function of momentum. There is less than one sigma separation between pions and kaons from about 750 MeV/c to about 1.5 GeV/c. Above about 2.0 GeV/c, there is roughly a two sigma separation between them. For kaons and protons, there is one sigma separation or less above 1.2 GeV/c.

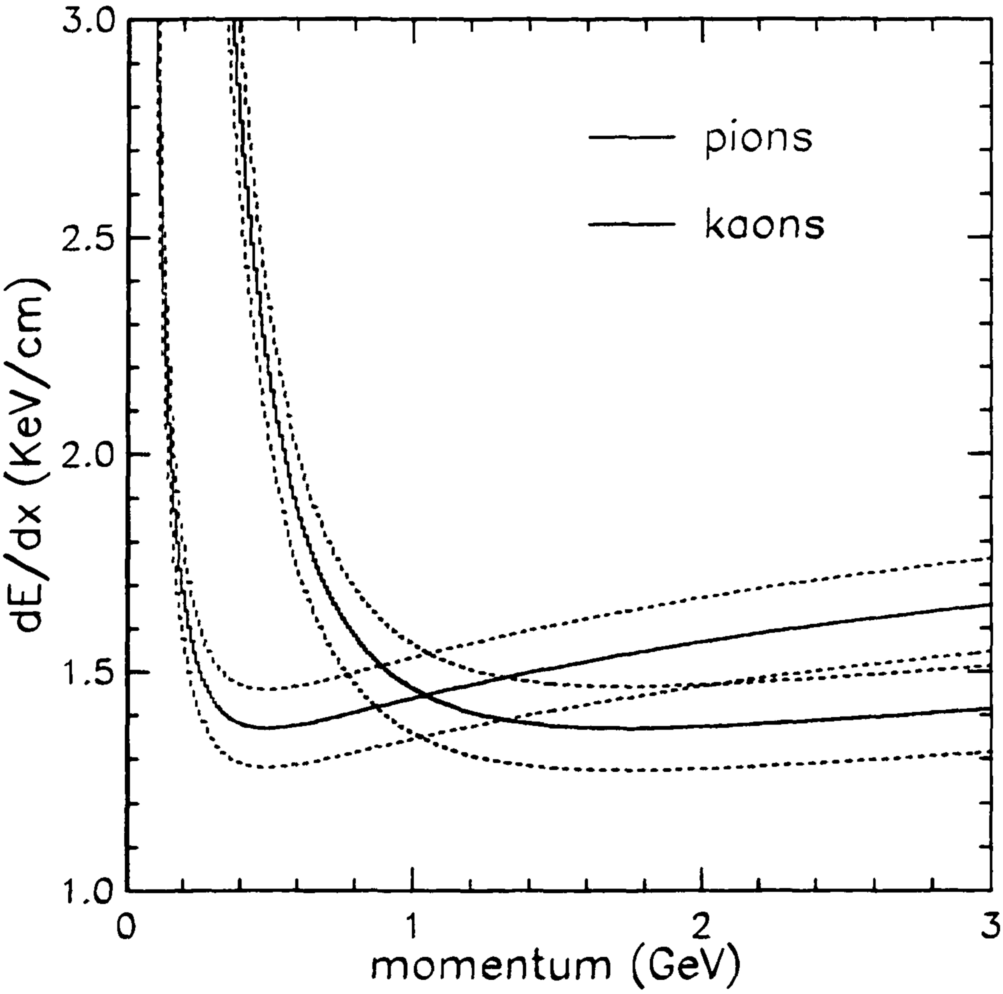

Figure 3.3: Energy loss versus momentum for various particles.

3.8.2 *ToF* Calibration

The time measured from a PMT is compared to the expected time, T_{ij}, using an expression of the form:

$$T_{ij} = T_{0j} + T_i + L_i/v_i + K_i/Q_j^n \qquad (3.2)$$

where:

T_{0j} is the calculated time for an electron to reach the scintillator from the interaction point,

T_i is a time offset constant for each channel,

L_j is the distance from the point where an electron crosses the scintillator to the end of the scintillator,

v_i is the velocity of signal propagation in the scintillator,

Q_j is the measured pulse height in TDC counts, and

K_i and n are parameters which depend upon pulse shape and time slewing in the discriminator.

T_i, v_i and K_i are taken as free parameters for each PMT, and the best values were determined by minimizing the difference between T_{mij} and T_{ij} using Bhabha calibration data. T_{mij} represents the time calculated from TDC counts for PMT i for event j, based on electronic calibration constants.

From these measured times, the expected time for a given hypothesis is then subtracted (giving `DTXXTF`). This result is then divided by the resolution for that measurement to give `SGXXTF` variables, which give the number of standard deviations a track differs from the `XX` particle hypotheses (with `XX` as above), according to its time-of-flight measurement. A number of effects are corrected for including: pulse height and z-dependence, momentum dependence and species dependence [50]. The relativistic velocity factor is also stored (as `BETATF`) in the ROAR common blocks. Figure 3.4 shows the distribution of $1/\beta$ (`1/BETATF`) for different particles as a function of momentum.

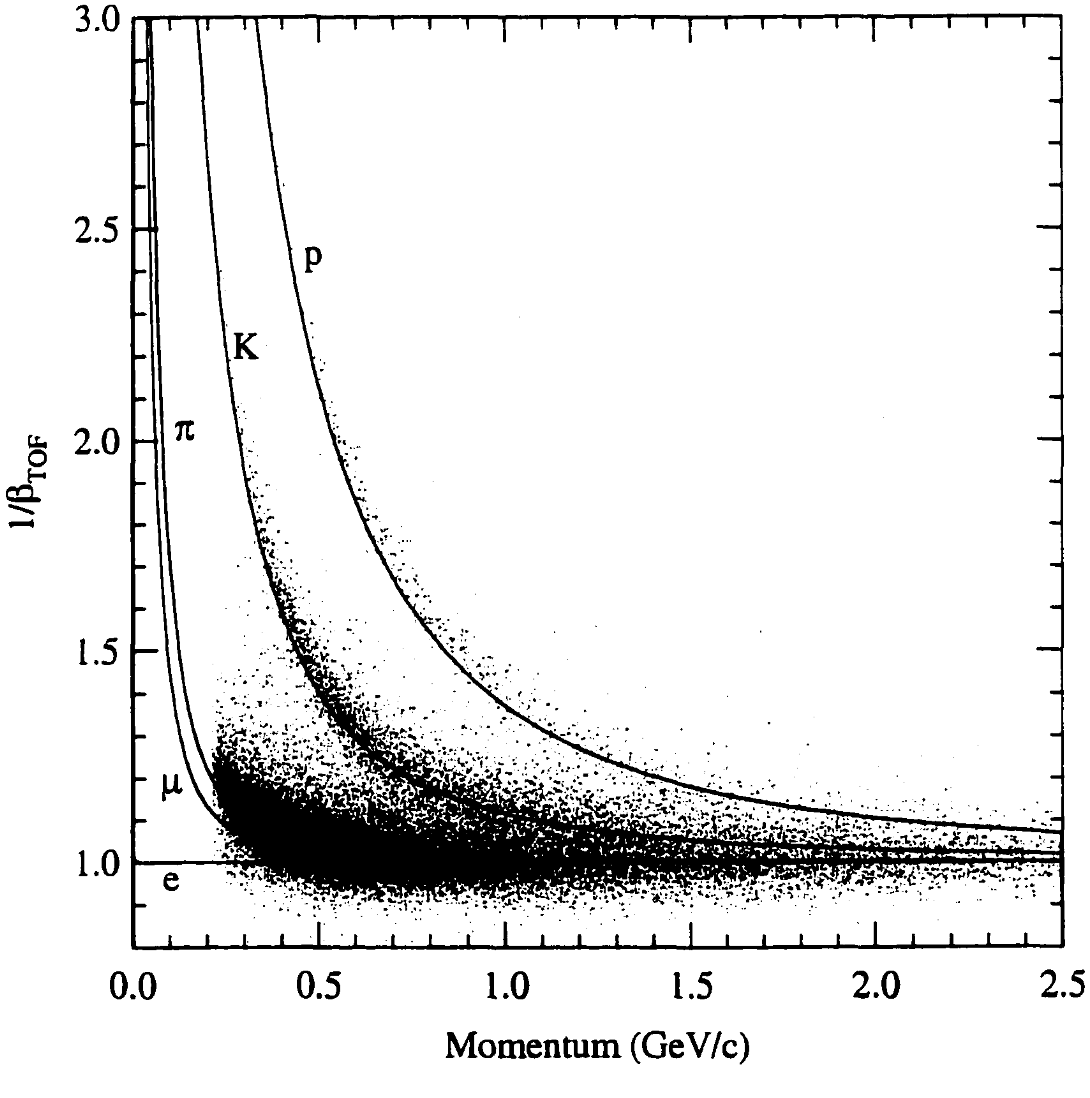

Figure 3.4: Distribution of $1/\beta$ versus momentum for various particles.

Chapter 4

Analysis Procedure

Once tracks have been reconstructed, the task of a physics analysis is to identify such tracks with specific particle species in order to characterize a particular physics event. To accomplish this, certain selection criteria are established that attempt to isolate the desired properties of the event without introducing too much of a selection bias. Understanding such selection biases is a measure of the *systematic error* of the analysis procedure employed. For measurements of relatively rare phenomena, the statistical errors will usually be much larger than any systematic error effects of the analysis procedure. Such measurements are thus *statistically-dominated.*

Unfortunately, that is not the case for this analysis. This dissertation documents our efforts to make precision measurements of properties related to charged kaons of all attainable momentum from B meson decays at the $\Upsilon(4S)$ resonance. Such measurements abound in statistics[1], therefore this analysis is a *systematics-dominated* analysis. We have chosen our data sample and refined our analysis procedure in order to minimize these systematic effects and thus produce the most meaningful measurements. The effects of these systematic errors will be examined in further detail in section 4.7.

The intent of this analysis is to use known samples of well-identified pions, kaons and protons from the above datasets to fit dE/dx and ToF PID distributions in the data, with both data and control shapes subject (as much as possible) to the same tracking and event shape cuts described below. From these PID fits, we extract the charged kaon yields for each PID device as a function of momentum. These momentum spectra are then used to compute branching fractions and multiplicities, as detailed in Chapter 5. Section 4.1 details our data sample and event selection cuts. Section 4.2 discusses the performance of the PID analysis variables we use as a function of momentum. Most of the details of this chapter were taken from an internal CLEO document which was written by the author and his thesis advisor [51].

Our analysis procedure is to perform a χ^2 fit for each momentum bin, using the

[1] To paraphrase Major Frank Burns of M*A*S*H fame, *"You can't swing a B meson in CLEO without hitting a charged kaon!"*

PID distribution histogramss for samples of well-identified pions, kaons and protons (as described above) as fitting functions. We will also need to include contributions from identified low-momentum leptons (electrons and muons). These so-called primary and secondary *Control Shapes* will be detailed in sections 4.3.2 through 4.3.6.

We have recently modified our procedure to perform a Maximum Likelihood fit for each momentum bin. In this case, We use the PID distributions for samples of well-identified pions, kaons and protons described above as inputs to the likelihood function. We use all five of these identically-binned control shape histograms themselves as probability distribution functions (PDFs), and construct our likelihood function to be maximized using `Minuit`. Our likelihood fit results below 800 MeV/care comparable to the results presented here. The Maximum Likelihood method should prove useful for simultaneously extracting pion and proton yields, as well as improve the fits at higher momenta where the statistics are lower in each bin. This new fitting method is detailed in Appendix D.

Our initial attempts to parameterize signal (*kaon*) and background (*pion, etc.*) shapes using different combinations of various Gaussian-type distribution functions and polynomial background functions in `Mn_Fit` seemed hopeless. `Minuit` is an interactive software package commonly used in analyzing HEP experimental data [52]. `Mn_Fit` is a wrapper package which accesses `Minuit` fitting routines and allows plotting of fit results. The CERN package `HBOOK` [54] is used to book and fill histograms for both our data and Monte Carlo samples.

We allow the overall normalizations for the primary control shapes (*pion, kaon* and *proton*) to float. Since each primary control shape contributes to different regions in each fit, there is essentially only one combination of the three primary shapes that will produce the best fit.

For the leptons (electrons and muons) which persist in our data shapes, we constrain their normalizations in the fits by fitting those tracks in the MC which pass the appropriate lepton ID cut (the complement of the corresponding lepton suppression cut) to those tracks in the data which pass that same lepton ID cut. This normalization method is necessary because electrons and muons tend to be distributed directly below one of the primary control shape distributions. Without constraining these secondary control shape distributions from leptons to match the data, a fit could return virtually any normalization for the primary control shapes. Attempting to ignore these lepton contributions altogether has resulted in horrendous looking fits to the data. This technique of computing lepton normalizations will be explained in further detail in section 4.4.1.

The real problem that persists in this analysis is the need for the inclusion of muons in many of our fits below 1.0 GeV/c, before our muon suppression cut is activated. It is difficult to obtain sufficient samples of well-identified leptons in the data below 1.0 GeV/c to use as PID control shapes. We are thus forced to rely on the MC to provide us with lepton control shapes. Fortunately, our PID distribution shapes for leptons appear to be reasonably well-modeled in the MC, as we will show in section 4.4.1.

We display our PID fits in section 4.4.2 and describe our extraction of raw yields in section 4.4.3. We discuss efficiency calculations in section 4.5. We use these efficiencies to correct our raw yields for acceptance of our selection criteria. Section 4.6 discusses a check of our analysis methods with Monte Carlo and section 4.7 discusses contributions to the systematic error from various sources.

4.1 Data Sample and Event Selection

The data sample for this analysis consists of the 4*s*2–4*s*D RECOMPRESS datasets. The total integrated luminosity of these datasets is about 4.0 fb^{-1}, with 2.7 fb^{-1} on the $\Upsilon(4S)$ resonance and 1.3 fb^{-1} about 60 MeV below the $\Upsilon(4S)$ resonance. This corresponds to roughly 2.86 *million* $B\overline{B}$ pairs. Integrated luminosity is measured in units of inverse area, where:

$$1\ barn\,(b) = 10^{-24}\ cm^2 \text{ and } 1\ fb^{-1} = 10^3\ pb^{-1} = 10^6\ nb^{-1} = 10^{15}\ b^{-1}. \tag{4.1}$$

The off resonance sample is used to subtract the effects of processes from the underlying *continuum* beneath the $\Upsilon(4S)$ resonance, leaving only events from $B\overline{B}$ decays. This *Continuum Subtraction* method is detailed in section 4.3.1.

These datasets were chosen because they appear to be the most consistent with respect to running conditions. The `VD` was broken and a quarter of it turned off, beginning with 4*s*E and continuing through 4*s*G. A vastly different version of the `DUET` reconstruction code was used for 4*s*1–4*s*4 track finding, but this was equalized with the RECOMPRESS. The 4*s*1 dataset also contains an energy scan searching for a B^* resonance above the $\Upsilon(4S)$ peak. Thus, we believe that the 4*s*2–4*s*D RECOMPRESS datasets are our best chance of understanding and extracting systematic errors in this analysis.

We make event selection cuts for hadronic skim (`CLASS 10`) data in these datasets as detailed below. CLEO physics analysis variables are described in Appendix C. All distance measurements (i.e., `DBKL, ZOKL`) are in meters. Where an analysis variable is dependent upon the Kalman hypothesis of the track fit (i.e., `XXKL`), we assume the kaon hypothesis.

We make the following event shape and track quality cuts for the data shapes only:

- `R2GL` < 0.35
- `KINCD` $= 0$
- `|DBKL|` ≤ 0.015

All other tracks used for control shapes have `KINCD` ≥ 0.

The parameter `R2GL` in CLEO is the ratio of the second to zero*th* Fox-Wolfram [55] moments, H_2/H_0, where both charged tracks in the central detector and shower energies deposited in the crystal calorimeter have been used in its determination. It is a measure of the "jettiness" (high R2GL) or "sphericity" (low R2GL) of the event. Continuum events are typically jetty, while $B\overline{B}$ events are much more isotropic in track distribution.

We impose the following track quality cuts on both the data shapes and the control shapes used to fit the data:

- TNG $= 0$
- |CZCD| ≤ 0.707 ($45° < \theta < 90°$, θ w.r.t. beam axis)
- |ZOKL| ≤ 0.050
- KALMAN_FIT
- .NOT. Z_ESCAPE
- .NOT. DREDGE
- IQALDI $= 1$ (to use dE/dx info)

The IQALDI $= 1$ cut is a quality flag which ensures that at least 10 dE/dx hits contribute to the truncated mean of the pulse height distribution on the drift chamber wires.

To minimize the contributions from electrons and muons in our fits, we require all tracks in these data to pass the following lepton suppression cuts, with momentum thresholds indicated:

- R2ELEC < 3.0 (above 0.4 GeV/c)
- DPTHMU < 3.0 (above 1.0 GeV/c)

In order to use ToF information, we impose the following additional cuts above 0.3 GeV/c:

* TFIDQL $= 0$
* TFSTAT $= 2$
* BETATF $\neq 0$

4.2 PID Device Performance

The PID device hardware of the CLEO II Detector has been described in detail in section 2.2.2. Calibration details were outlined in section 3.8. We concern ourselves here with extracting useful information from these devices by considering the variables which describe the performance of these systems with respect to physics analysis, notably as a function of momentum.

For dE/dx information, we consider the variable SGKADI. This is defined in CLEO as the difference between the measured and expected values of dE/dx for the kaon hypothesis divided by the resolution for that pulse height and number of dE/dx hits. This variable is thus represented in units of sigma. SGKADI is meant to be a Gaussian of unit width centered at zero for well-identified kaons. For other particles, SGKADI is meant to be a Gaussian displaced from zero. Figure 4.1 shows the distribution of SGKADI versus momentum for continuum-subtracted data in the 4s7 RECOMPRESS dataset. As momentum increases, the distinct peaks corresponding primarily to pions and kaons begin to merge.

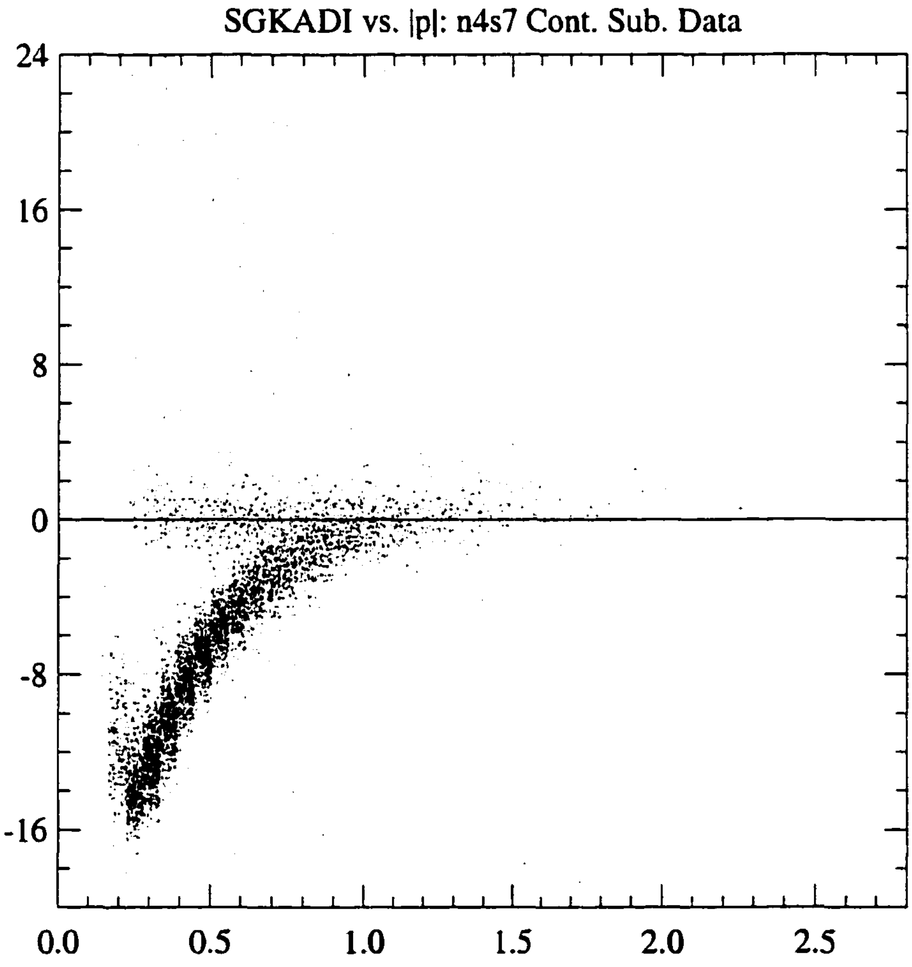

Figure 4.1: Distribution of SGKADI versus momentum for continuum-subtracted data in the 4s7 RECOMPRESS dataset.

For *ToF* information, we consider the variable SGKATF. This is defined in CLEO as the difference between the measured and expected times in nanoseconds (under the kaon hypothesis) for a charged track to reach the *ToF* scintillators, divided by the estimated resolution for that measurement. This variable is also represented in units of sigma and is again meant to be a Gaussian of unit width centered at zero for well-identified kaons. For other particles, SGKATF is meant to be displaced from zero. Figure 4.2 shows the distribution of SGKATF versus momentum for continuum-subtracted data in the 4s7 RECOMPRESS dataset. As momentum increases, the distinct peaks corresponding primarily to pions and kaons again begin to merge.

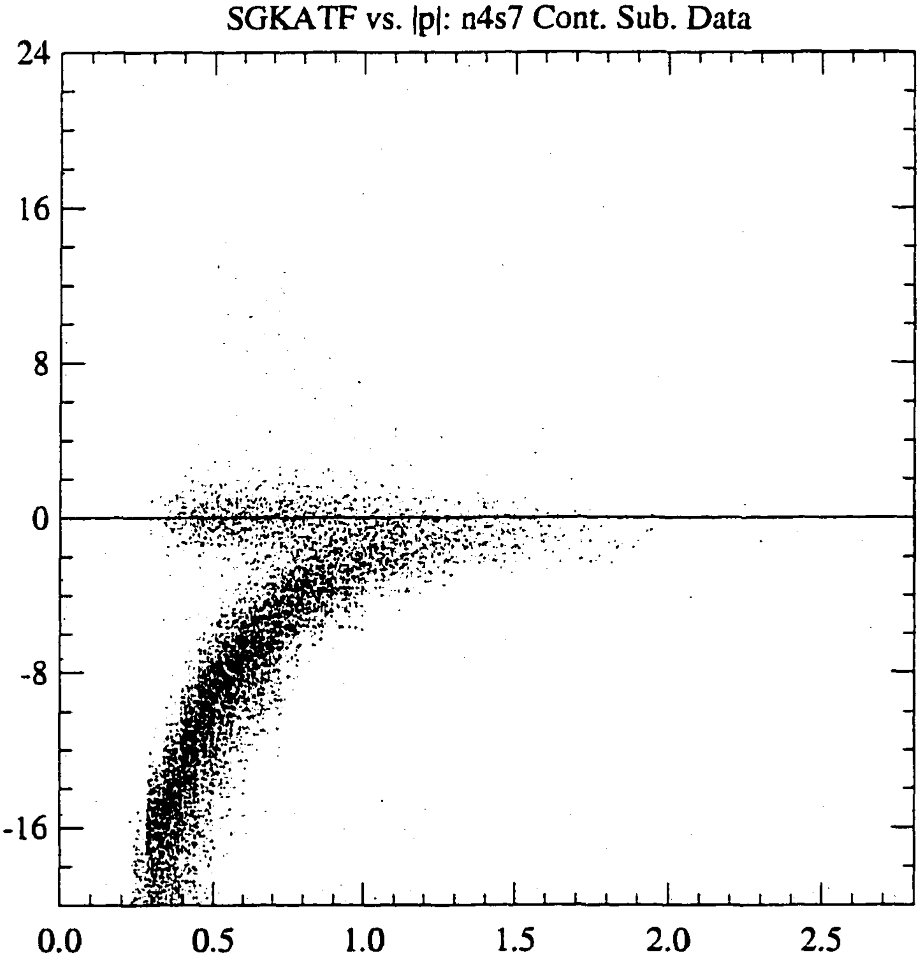

Figure 4.2: Distribution of SGKATF versus momentum for continuum-subtracted data in the 4s7 RECOMPRESS dataset.

4.3 Data and Control Shape PID Distributions

For our data shape histograms, We fill separate SGKADI and SGKATF histograms for both on resonance and continuum data from -20.0 to 24.0 in 440 bins. This allows for the contributions from the other primary shapes in our fits.

For our control shape histograms, we do not distinguish between resonance and continuum data when filling these PID histograms. We do, however, fill separate histograms for the *peak* and *sideband* regions of the invariant mass plot of the reconstructed particle used to obtain each control shape. We then subtract the sideband histogram from the peak histogram, after scaling for equal areas of the background shape. This *Sideband Subtraction* method allows us to obtain clean samples of the desired species types and is detailed in section 4.3.2.

The distributions of SGKADI and SGKATF for continuum-subtracted data are referred to as our *Data Shapes.* The distributions of SGKADI and SGKATF for each species type from sideband-subtracted data are referred to as our *Control Shapes.* We plot these PID variables from 0 to 800 MeV/c in 25 MeV/c bins, and from 0.8 to 2.8 GeV/c in 0.1 GeV/c bins. Because the *ToF* scintillators are located at about a meter from the interaction point, however, tracks with momentum below 0.3 GeV/c do not make it to the *ToF* system with a good enough signal quality to pass our *ToF* cuts. We therefore fill no *ToF* histograms below 0.3 GeV/c.

4.3.1 Continuum-Subtracted Data Shapes

For each PID distribution, we subtract the continuum histogram from the on resonance histogram for each momentum bin. We first scale the continuum histogram by the ratio of resonance to continuum luminosities and by the ratio of the average continuum beam energy squared to the average resonance beam energy squared, to get the continuum-subtracted histogram for that bin. For RECOMPRESS 4s2–4sD data, this scale factor is:

$$\begin{aligned}
K_{Scale}^{Total} &= K_{Scale}^{Lumi} \cdot K_{Scale}^{Energy} \\
&= \frac{\mathcal{L}_{On4s}^{4s2-D}}{\mathcal{L}_{Cont}^{4s2-D}} \cdot \frac{< E_{beam}^{Cont} >^2}{< E_{beam}^{On4S} >^2} \\
&= \frac{2.683\ fb^{-1}}{1.287\ fb^{-1}} \cdot \frac{(5.260\ \text{GeV})^2}{(5.289\ \text{GeV})^2} \\
&= 2.084 \cdot 0.989 \\
&= 2.061
\end{aligned} \tag{4.2}$$

The ratio of average beam energies squared accounts for the $\sim 1/s$ fall-off in $e^+ e^- \to q\bar{q}$ cross section below the $\Upsilon(4S)$, where $\sqrt{s} = 10.58$ GeV. The error on K_{Scale}^{Total}, notably due to the errors on luminosity and cross-section measurements, is considered as a source of systematic error on the number of $B\,\overline{B}$ pairs.

Figures 4.3–4.4 show plots of SGKADI for continuum-subtracted data from 200 MeV/c to 800 MeV/c, in 25 MeV/c momentum bins. Figures 4.5–4.6 show plots of SGKADI for continuum-subtracted data from 0.8 GeV/c to 2.6 GeV/c, in 0.1 GeV/c momentum bins. At low momenta, there are well separated negative and zero-centered peaks comprising chiefly pions and kaons, respectively. There are also residual electron and muon contributions from those leptons which either pass the suppression cuts detailed above or which are not suppressed at all below the momentum threshold for that cut. These peaks merge together as momentum increases and the discriminating power of this variable weakens. At higher momenta, The positive tail of the zero-centered pion+kaon peak also includes the contribution of electrons and protons, although the MC does not reflect this effect well for electrons.

Figures 4.7–4.8 show plots of SGKATF for continuum-subtracted data from 300 MeV/c to 800 MeV/c, in 25 MeV/c momentum bins. Figures 4.9–4.10 show plots of SGKATF for continuum-subtracted data from 0.8 GeV/c to 2.6 GeV/c, in 0.1 GeV/c momentum bins. At low momenta, there are again well separated negative and zero-centered peaks comprising chiefly pions and kaons, respectively. There are also residual electron and muon contributions from those leptons which either pass the suppression cuts detailed above or which are not suppressed at all below the momentum threshold for that cut. These peaks again merge together as momentum increases and the discriminating power of this variable weakens. Generally speaking, SGKATF has better discrimination as a function of momentum than SGKADI.

4.3.2 Pion Data Control Shapes ($K_s^0 \to \pi^+\pi^-$)

The dominant contribution to the fits for each PID device is from pions. We obtain charged pion control shapes by reconstructing $K_s^0 \to \pi^+\pi^-$, using the kinematic fit vertex finding package KNVF [30]. This package performs a vertex constrained fit of tracks originating from displaced vertices ("secondary vertices"), using the pion hypothesis for both tracks when reconstructing K_s^0. Both pion tracks for each K_s^0 candidate are subject to the same tracking cuts described earlier in section 4.1. The K_s^0 fit used to obtain the *ToF* pion control shapes also requires both tracks to pass the *ToF* cuts described in section 4.1.

To reduce background under the K_s^0 mass peak, we impose the following vertex quality cuts:

$$\begin{aligned} \chi^2_{vertex} &< 4\,, \\ Z_{miss} &< 1\text{ cm}\,, \\ |M_{\pi^+\pi^-} - M_\Lambda| &> 20\text{ MeV}/c^2 \end{aligned} \tag{4.3}$$

where:

χ^2_{vertex} is the χ^2 of the vertex fit,
Z_{miss} is the separation in z of the two tracks at their $r-\phi$ intersection, and
the Λ mass peak region, where a pion is mis-identified as a proton, is explicitly excluded.

We choose a pion track from each K_s^0 decay as follows: we require the track we select to be less than 1 cm from the interaction point in the $r-\phi$ plane, while simultaneously requiring the opposite pion track to be a *minimum* of 2 mm from the interaction point in the $r-\phi$ plane. Occasionally, this allows us to use both tracks from a given K_s^0 decay. This still leaves us with plenty of statistics, but reduces the effect of the displaced vertex of the K_s^0 decay in flight. In particular, the UCSB

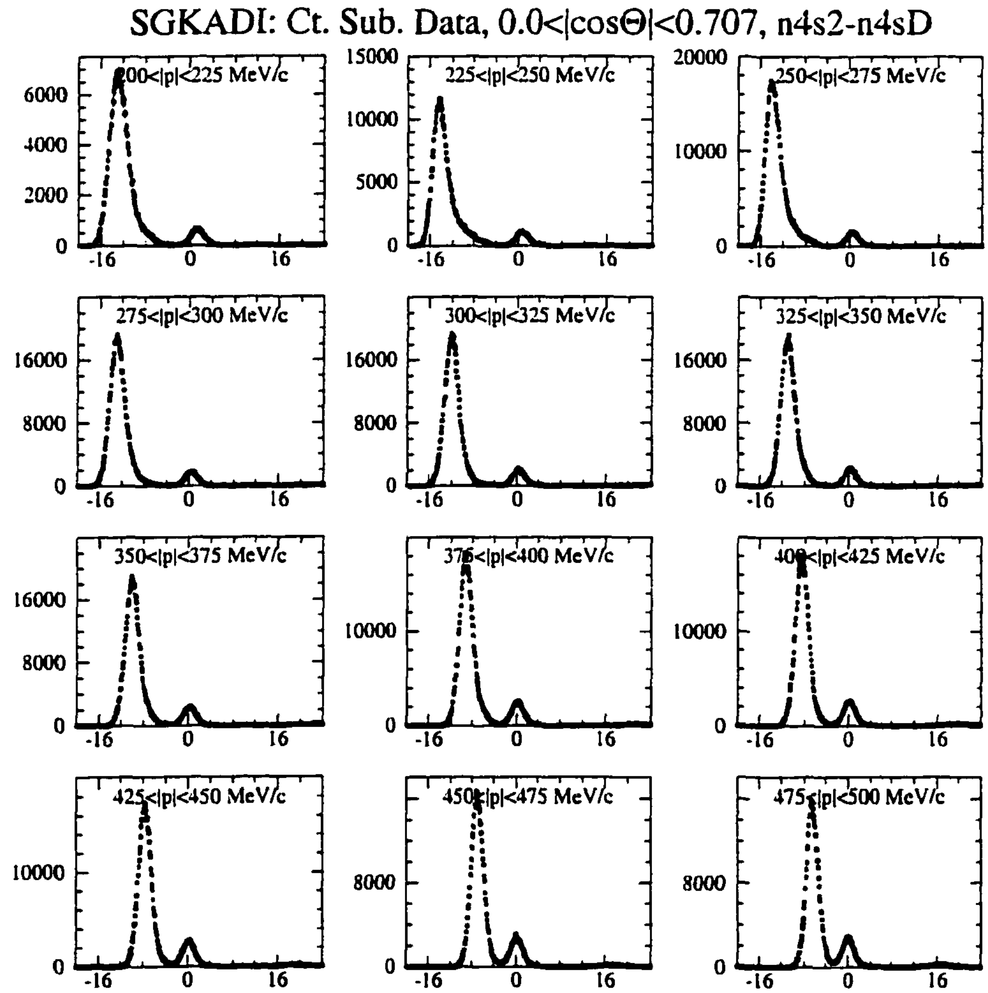

Figure 4.3: Plots of SGKADI from 200 MeV/c to 500 MeV/c in 25 MeV/c bins for continuum-subtracted data in the 4s2–4sD RECOMPRESS datasets, subject to the tracking and event shape cuts described in the text.

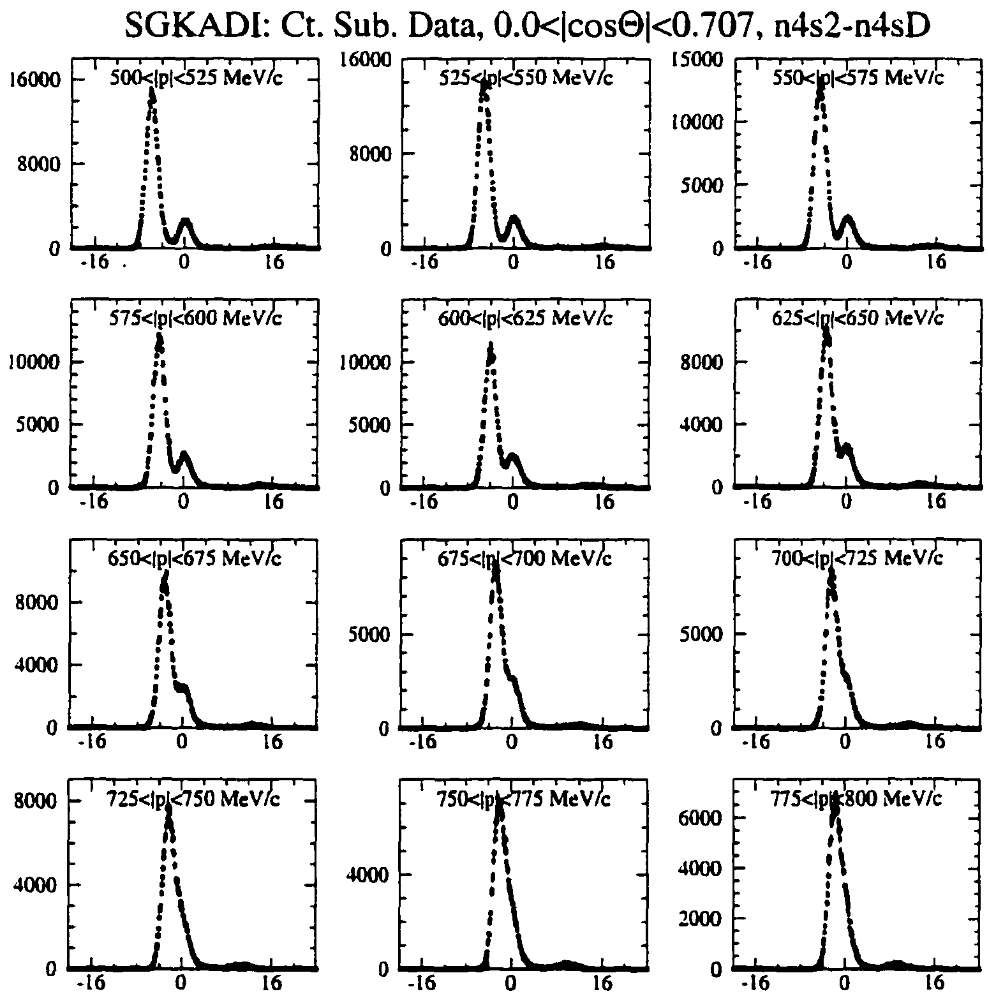

Figure 4.4: Plots of SGKADI from 500 MeV/c to 800 MeV/c in 25 MeV/c bins for continuum-subtracted data in the $4s2$–$4s$D RECOMPRESS datasets, subject to the tracking and event shape cuts described in the text.

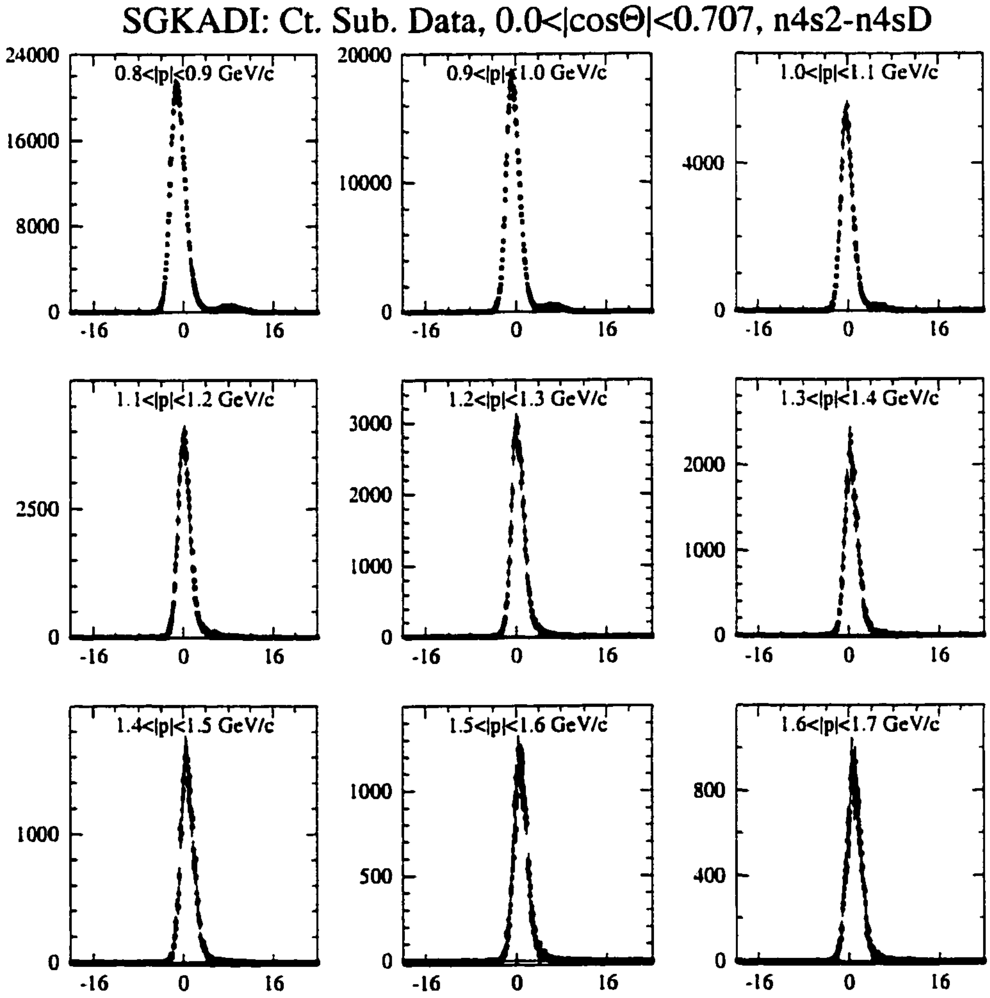

Figure 4.5: Plots of SGKADI from 0.8 GeV/c to 1.7 GeV/c in 0.1 GeV/c bins for continuum-subtracted data in the 4s2–4sD RECOMPRESS datasets, subject to the tracking and event shape cuts described in the text.

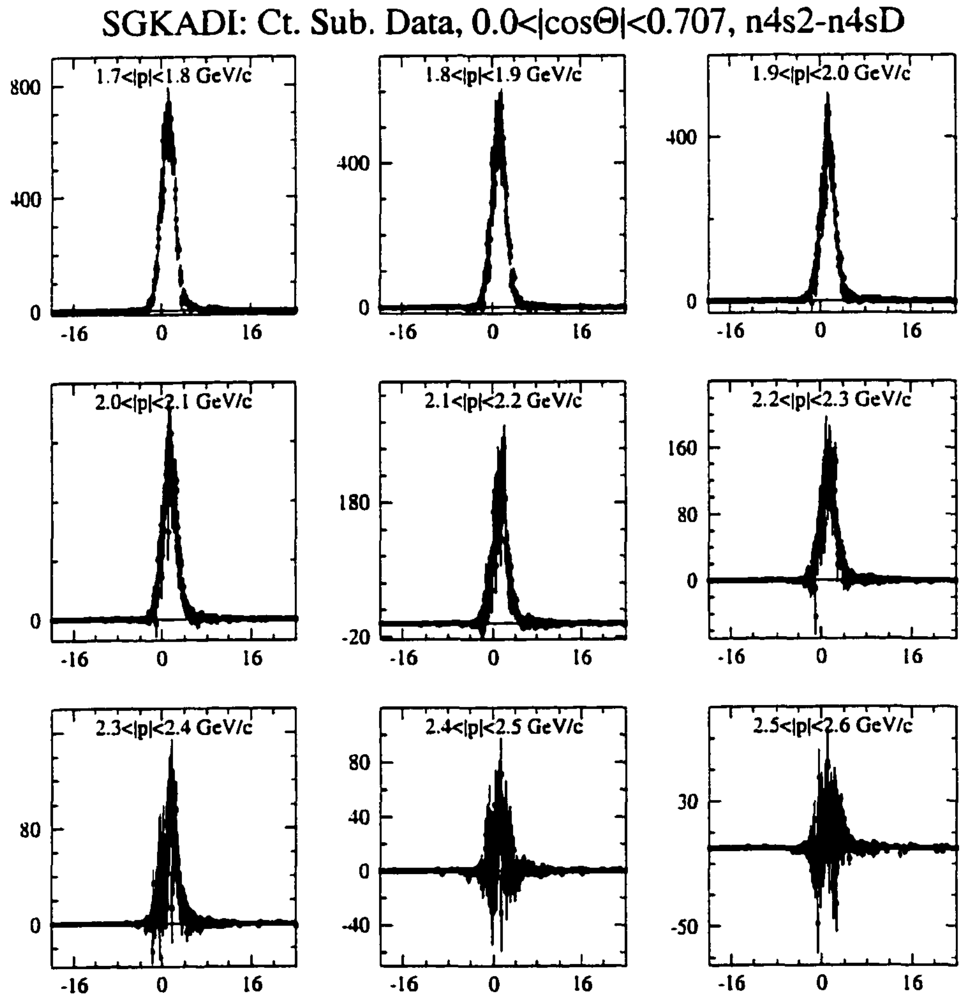

Figure 4.6: Plots of SGKADI from 1.7 GeV/c to 2.6 GeV/c in 0.1 GeV/c bins for continuum-subtracted data in the 4s2–4sD RECOMPRESS datasets, subject to the tracking and event shape cuts described in the text.

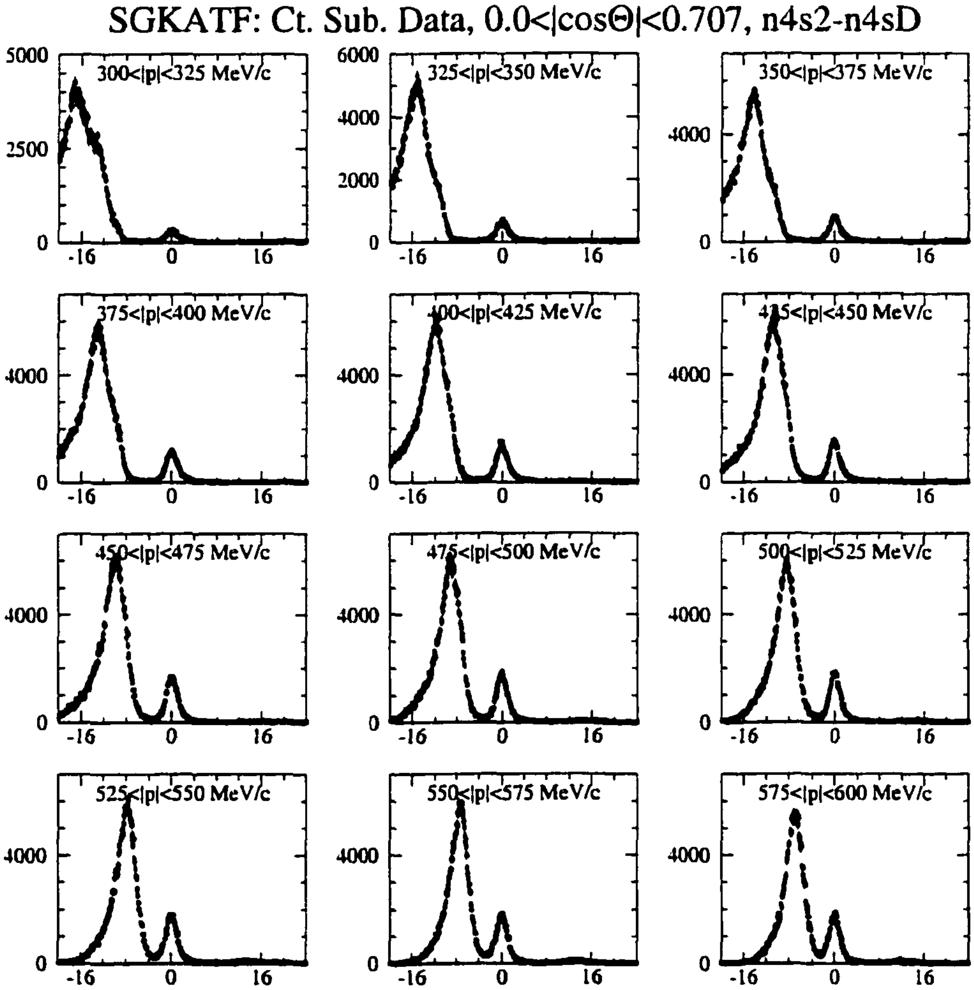

Figure 4.7: Plots of SGKATF from 300 MeV/c to 600 MeV/c in 25 MeV/c bins for continuum-subtracted data in the 4s2–4sD RECOMPRESS datasets, subject to the tracking, event shape *and ToF* cuts described in the text.

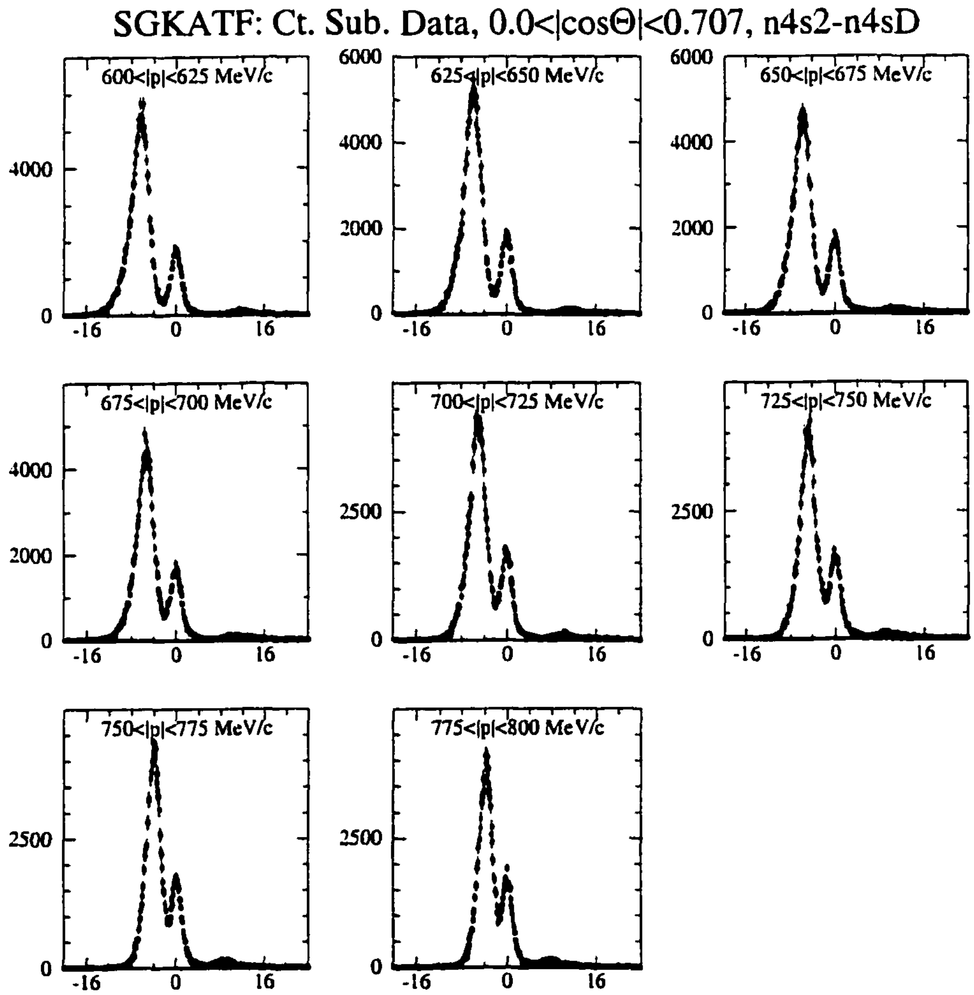

Figure 4.8: Plots of SGKATF from 600 MeV/c to 800 MeV/c in 25 MeV/c bins for continuum-subtracted data in the 4s2–4sD RECOMPRESS datasets, subject to the tracking, event shape *and ToF* cuts described in the text.

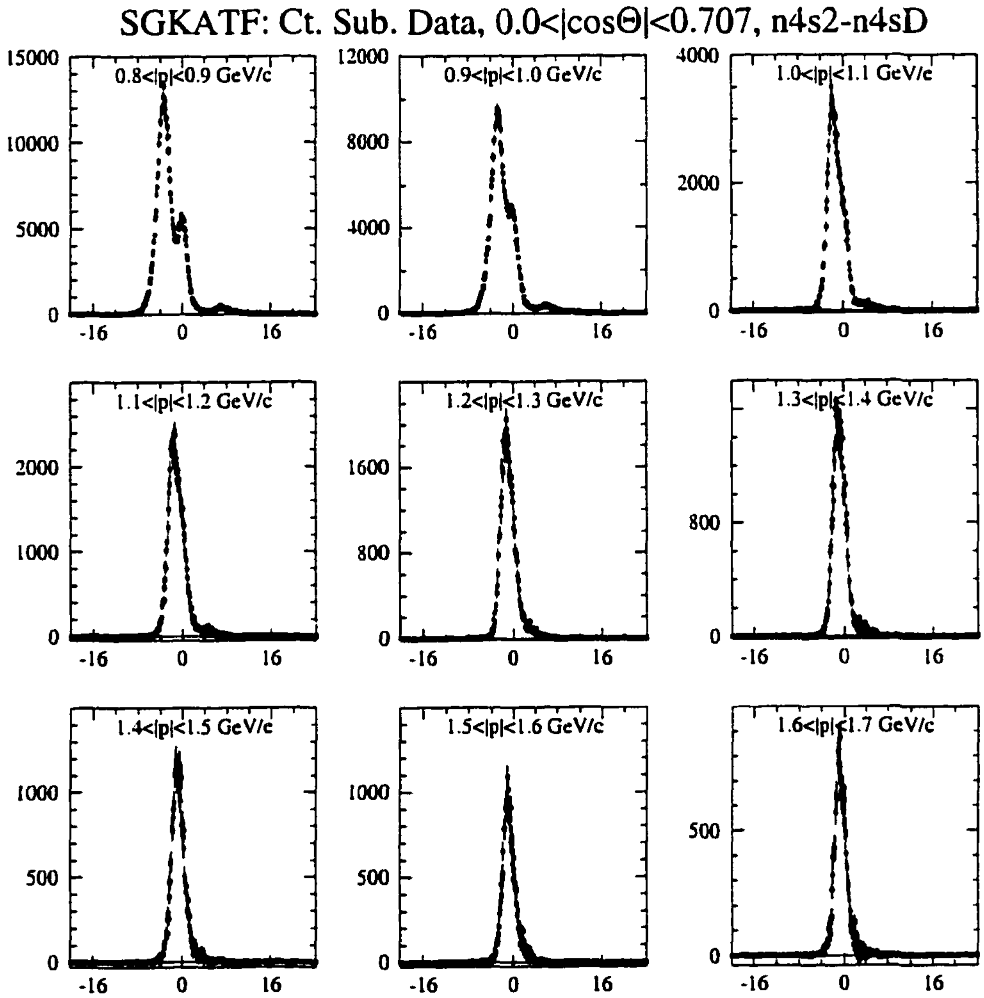

Figure 4.9: Plots of SGKADI from 0.8 GeV/c to 1.7 GeV/c in 0.1 GeV/c bins for continuum-subtracted data in the 4s2–4sD RECOMPRESS datasets, subject to the tracking, event shape *and ToF* cuts described in the text.

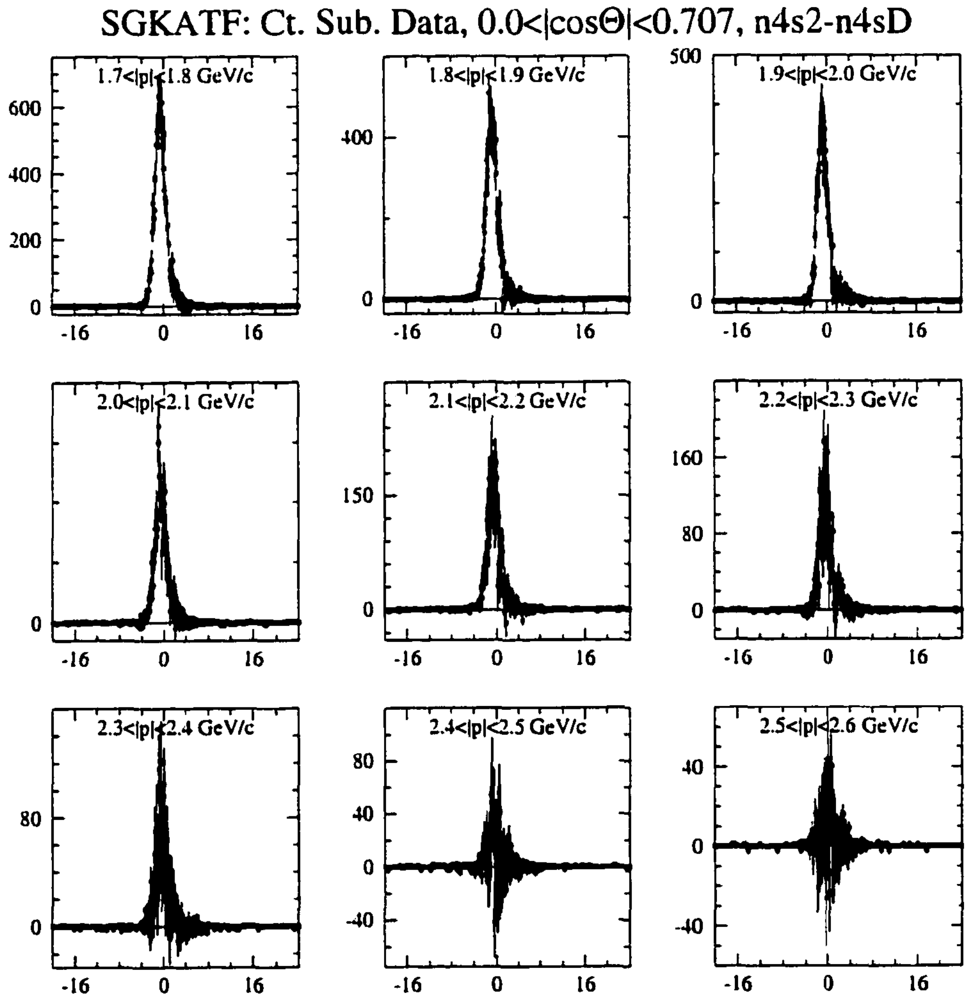

Figure 4.10: Plots of SGKADI from 1.7 GeV/c to 2.6 GeV/c in 0.1 GeV/c bins for continuum-subtracted data in the 4s2–4sD RECOMPRESS datasets, subject to the tracking, event shape *and ToF* cuts described in the text.

dE/dx calibration which assumes tracks come from the primary vertex is still valid. Since our criteria for selecting these pion tracks require the K_s^0 to decay within the beam pipe, the dE/dx measurements for these pion tracks will be nearly the same as if they had come from the beam spot themselves.

For each PID device, we plot the invariant mass of $\pi^+\pi^-$ combinations passing the tracking requirements listed in section 4.1 and fit the signal peak to a two-Gaussian shape. The means and widths of the two Gaussians are allowed to float about the nominal K_s^0 mass, 497.672 ± 0.031 MeV/c^2 [1]. We use a second-order Chebyshev polynomial to model the essentially flat background. We also plot PID distributions for each device for these peak and sideband regions, using the same momentum bins as was described earlier in this section for the data.

For K_s^0 mass fits used to obtain both dE/dx and ToF pion control shapes, we define peak plus low and high sideband regions for the K_s^0 sideband subtraction to be:

$$\begin{gathered} 0.490 < M_{\pi^+\pi^-}^{Peak} < 0.506 \text{ GeV}/c^2, \\ 0.474 < M_{\pi^+\pi^-}^{LoSB} < 0.482 \text{ GeV}/c^2 \ \text{ and } \ 0.514 < M_{\pi^+\pi^-}^{HiSB} < 0.522 \text{ GeV}/c^2. \end{gathered} \tag{4.4}$$

We integrate the background function for the K_s^0 mass fit for each device over these peak and sideband regions. For each device, we then divide the integration result for the peak region by the integration result for the sideband region to obtain the scale factor for the sideband subtraction for that device. The fractional error on the scale factor is taken to be the quadrature sum of the fractional errors on the integration of the background function over the peak and sideband regions. The absolute error on each integration result is taken to be the square root of that result. This results in scale factors of:

$$R_{K_s^0}^{dE/dx} = 1.0815 \pm 0.0035 \ \text{ and } \ R_{K_s^0}^{ToF} = 1.0954 \pm 0.0045\,, \tag{4.5}$$

respectively. The error on these K_s^0 scale factors, including the contributions from varying the vertex quality cuts listed above, are considered as a source of systematic error.

For each device, we scale the pion control shapes generated from the sideband region by the appropriate scale factor and subtract them from the control shapes generated from the peak region to obtain our sideband-subtracted pion control shapes for that device. Figure 4.11 shows the mass fit used for the K_s^0 sideband subtraction for dE/dx. Figures 4.12–4.13 show the resultant sideband-subtracted charged pion control shapes used for our dE/dx fits from 200 MeV/c to 800 MeV/c, in 25 MeV/c momentum bins. Figures 4.14–4.15 show the resultant sideband-subtracted charged pion control shapes used for our dE/dx fits from 0.8 GeV/c to 2.6 GeV/c, in 0.1 GeV/c momentum bins. Figure 4.16 shows the mass fit used for the K_s^0 sideband subtraction for ToF. Figures 4.17–4.18 show the resultant sideband-subtracted charged pion control shapes used for our ToF fits from 200 MeV/c to 800 MeV/c, in 25 MeV/c momentum bins. Figures 4.19–4.20 show the resultant sideband-subtracted charged pion control shapes used for our ToF fits from 0.8 GeV/c to 2.6 GeV/c, in 0.1 GeV/c momentum bins.

4.3.3 Kaon Data Control Shapes ($\phi \to K^+ K^-$)

For charged kaon shapes we reconstruct the decay $\phi \to K^+ K^-$, for which the branching ratio is $49.1 \pm 0.9\%$ [1]. Here again both kaon tracks for each ϕ candidate are subject to the same tracking cuts described earlier. The ϕ fit for ToF also requires both tracks from each candidate to pass our ToF cuts.

We use a convolution of a Gaussian of mean 1020 MeV/c^2 and a Breit-Wigner of fixed width $\Gamma = 4.43$ MeV/c^2 [1] to fit the observed signal shape. The Breit-Wigner signal shape of fixed width is used because the width of the ϕ is comparable to the mass resolution of the CLEO Detector. The kinematically disallowed region below 988 MeV/c^2 is excluded from the fit.

The phase space background is parameterized by a function of the form:

$$phibg\,(M) = Norm * (M - M_0)^{\alpha} e^{\beta(M-M_0)} \tag{4.6}$$

To reduce background in these $K^+ K^-$ combinations, we require a tight consistency cut for the opposite PID device. That is we require $|\mathtt{SGKATF}| < 2.5$ for dE/dx plots, and vice versa.

We select a kaon track from each ϕ decay by also requiring a *kaon level cut*, L_K, to be greater than 0.1 for the opposite kaon track from each ϕ candidate. This level cut is constructed by combining dE/dx and ToF information, when available, as follows: For each track, a combined probability is determined using the available SGXXYY information for each device, where YY = DI,TF. These probabilities, $P^i_{\chi^2}$ (where i is the mass hypothesis index corresponding to $i = \pi$, K, p), are obtained using *Ahren Sadoff*'s HADID routine. Using these probabilities, a normalized probability called an "ID Level", L_i, is evaluated for each track according to the formula [56]:

$$L_i \equiv \frac{P^i_{\chi^2}}{P^\pi_{\chi^2} + P^K_{\chi^2} + P^p_{\chi^2}} \tag{4.7}$$

A level cut greater than 0.1 thus constitutes a consistency cut for that particle species. This level cut reduces background under the ϕ peak by an order of magnitude while only reducing the ϕ signal by about 15%.

For both dE/dx and ToF fits, we define peak plus low and high sideband regions for the ϕ sideband subtraction to be:

$$\begin{gathered} 1.014 < M^{Peak}_{K^+K^-} < 1.026 \text{ GeV}/c^2, \\ 0.993 < M^{LoSB}_{K^+K^-} < 1.005 \text{ GeV}/c^2 \text{ and } 1.035 < M^{HiSB}_{K^+K^-} < 1.047 \text{ GeV}/c^2. \end{gathered} \tag{4.8}$$

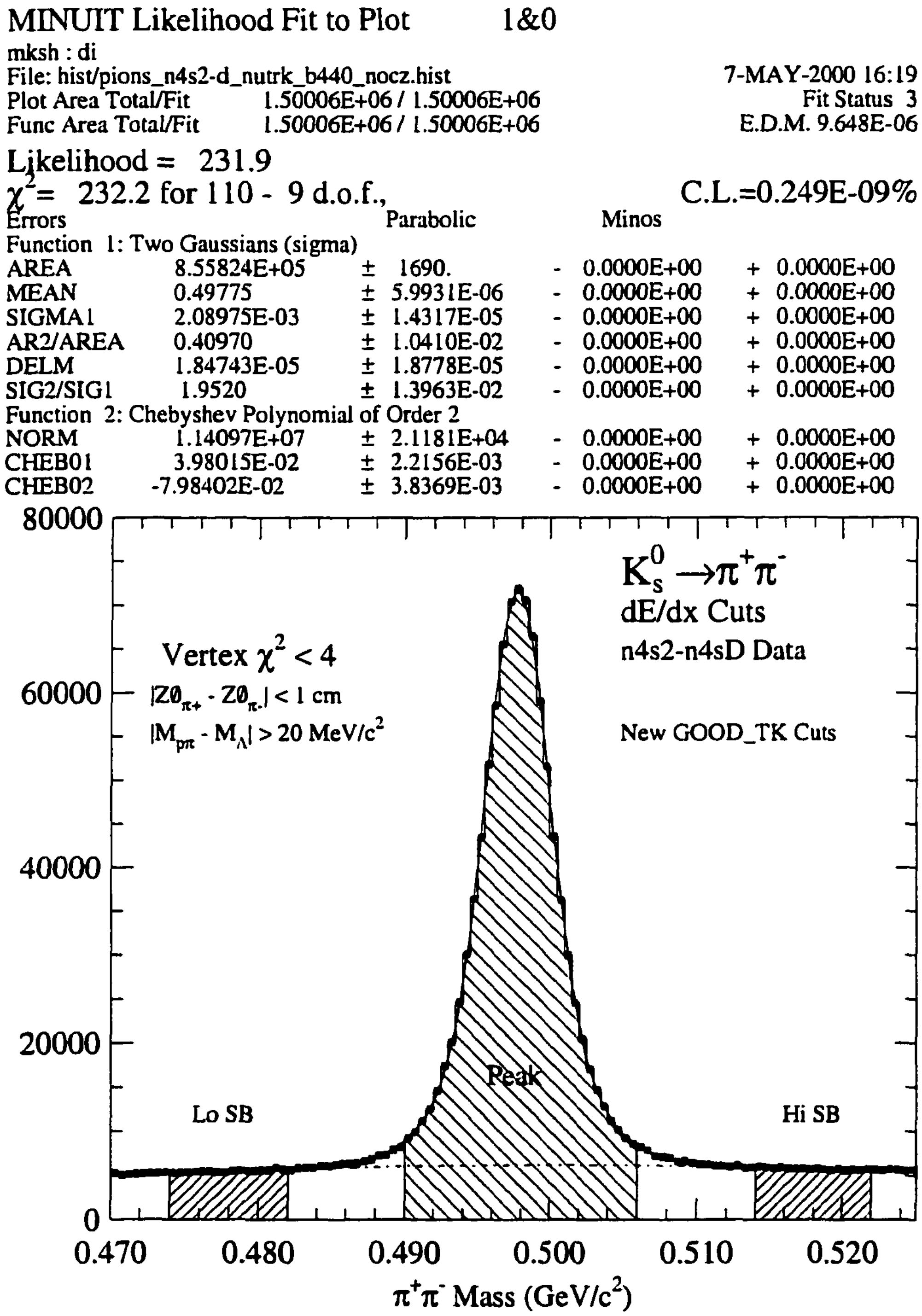

Figure 4.11: The invariant mass distribution for $\pi^+\pi^-$ combinations passing the tracking requirements described in the text. The light and dark shaded segments show the K_s^0 signal peak and sideband regions, respectively. This fit is used to obtain the charged pion control shapes for our dE/dx fits.

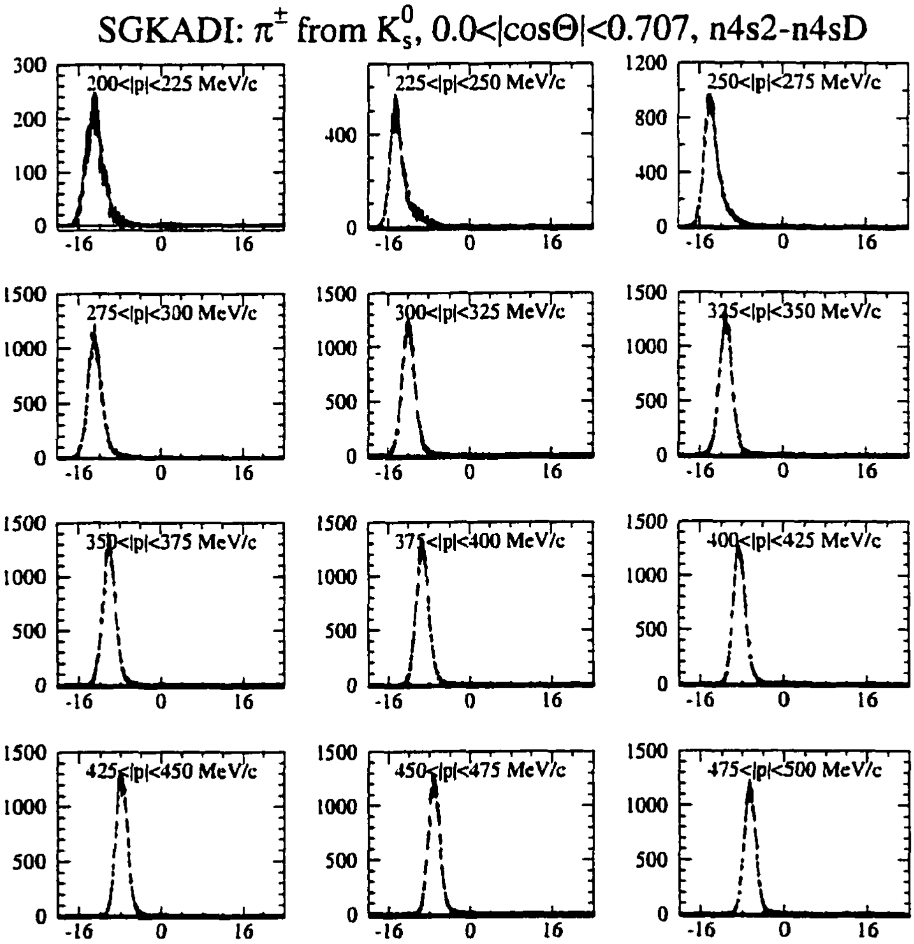

Figure 4.12: Plots of SGKADI from 200 MeV/c to 500 MeV/c, in 25 MeV/c bins for charged pions from K^0_s in the 4s2–4sD RECOMPRESS datasets.

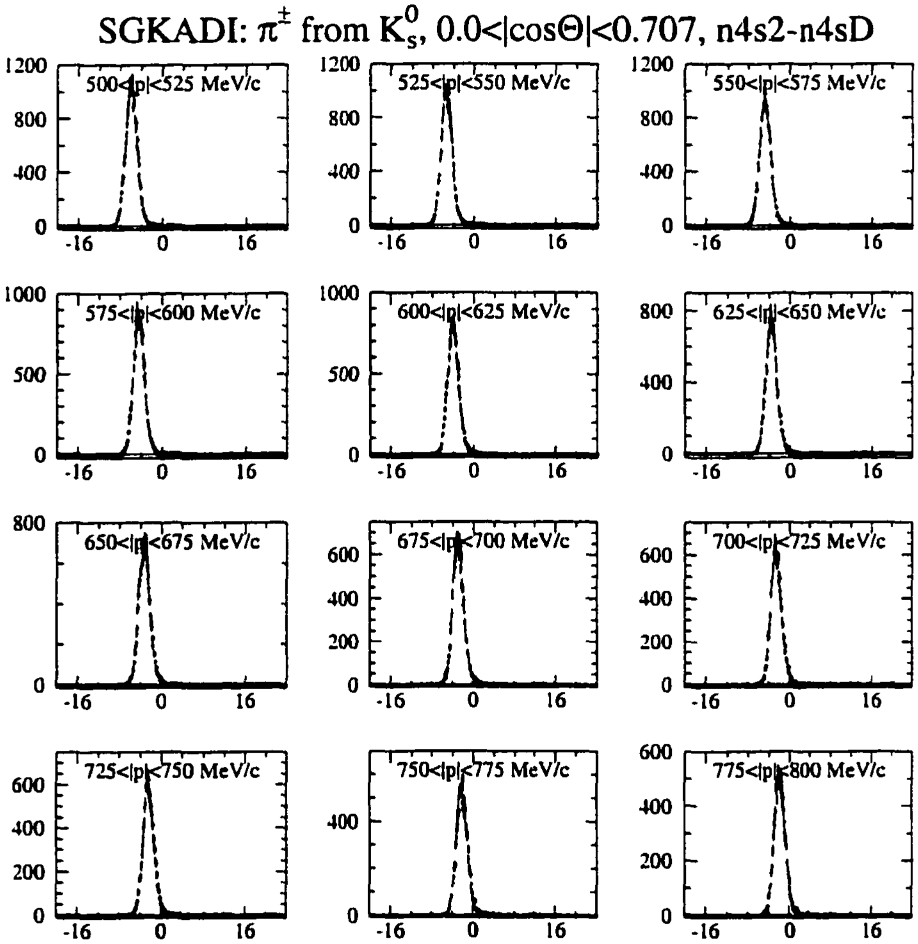

Figure 4.13: Plots of SGKADI from 500 MeV/c to 800 MeV/c, in 25 MeV/c bins for charged pions from K_s^0 in the $4s2$–$4s$D RECOMPRESS datasets.

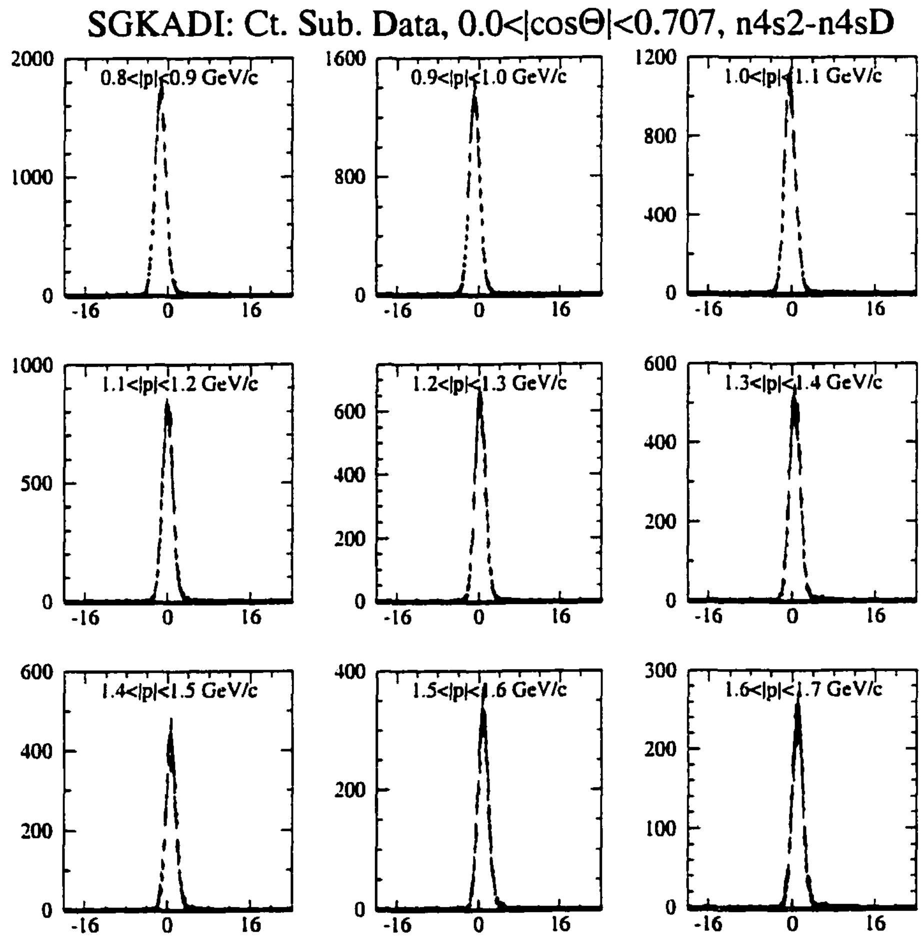

Figure 4.14: Plots of SGKADI from 0.8 GeV/c to 1.7 GeV/c, in 0.1 GeV/c bins for charged pions from K_s^0 in the 4s2–4sD RECOMPRESS datasets.

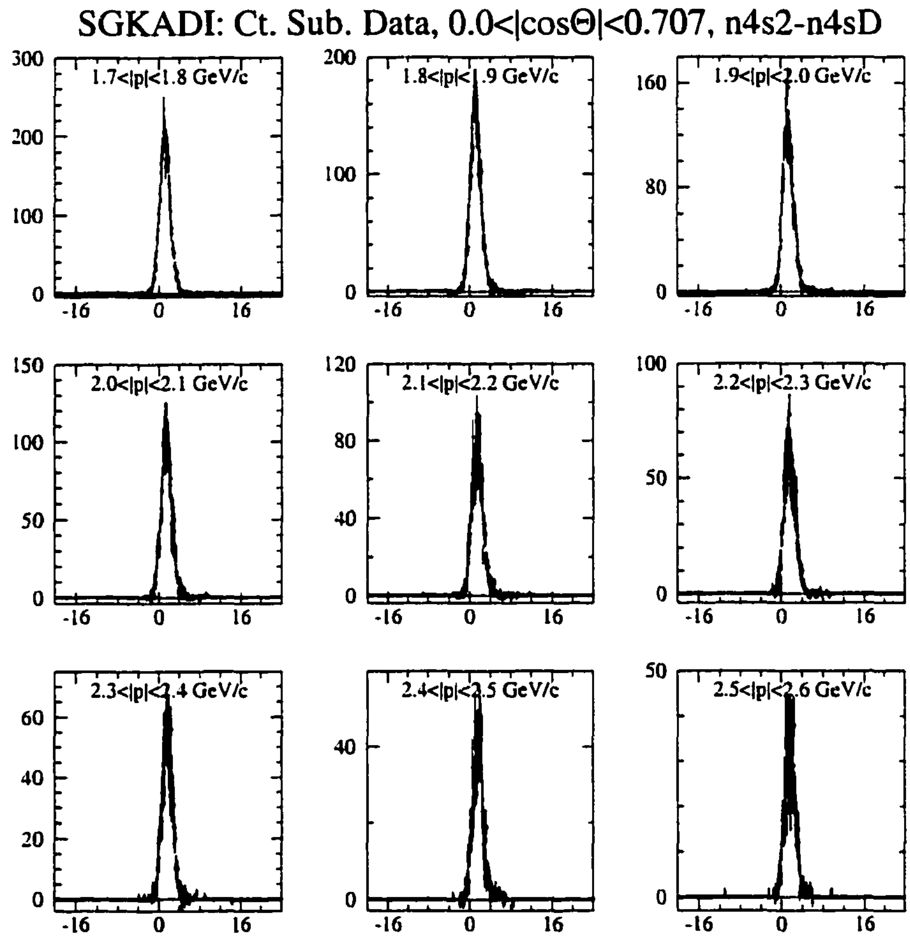

Figure 4.15: Plots of SGKADI from 1.7 GeV/c to 2.6 GeV/c, in 0.1 GeV/c bins for charged pions from K_s^0 in the $4s2$–$4s$D RECOMPRESS datasets.

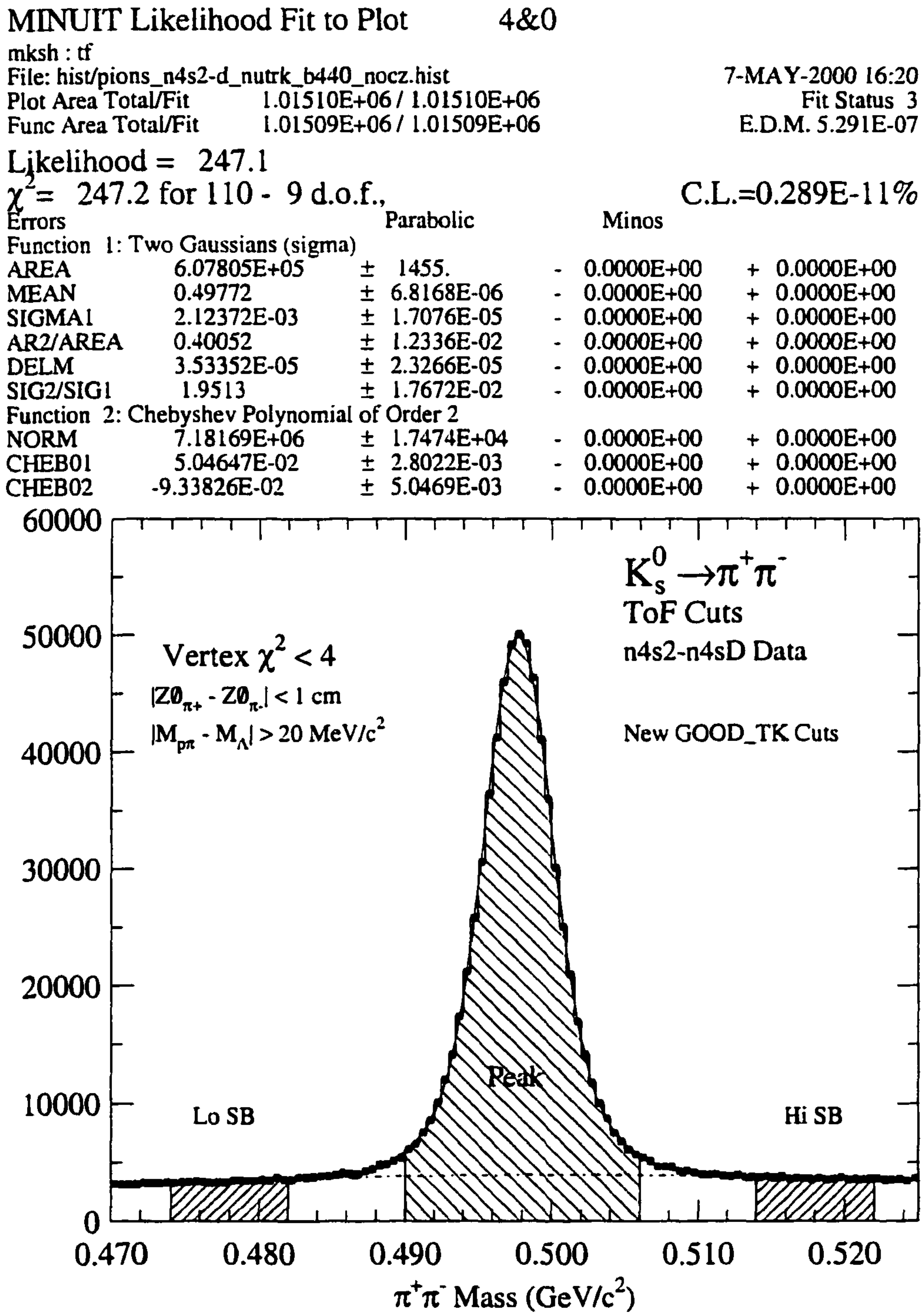

Figure 4.16: The invariant mass distribution for $\pi^+\pi^-$ combinations passing the tracking *and ToF* requirements described in the text. The light and dark shaded segments show the K^0_s signal peak and sideband regions, respectively. This fit is used to obtain the charged pion control shapes for our *ToF* fits.

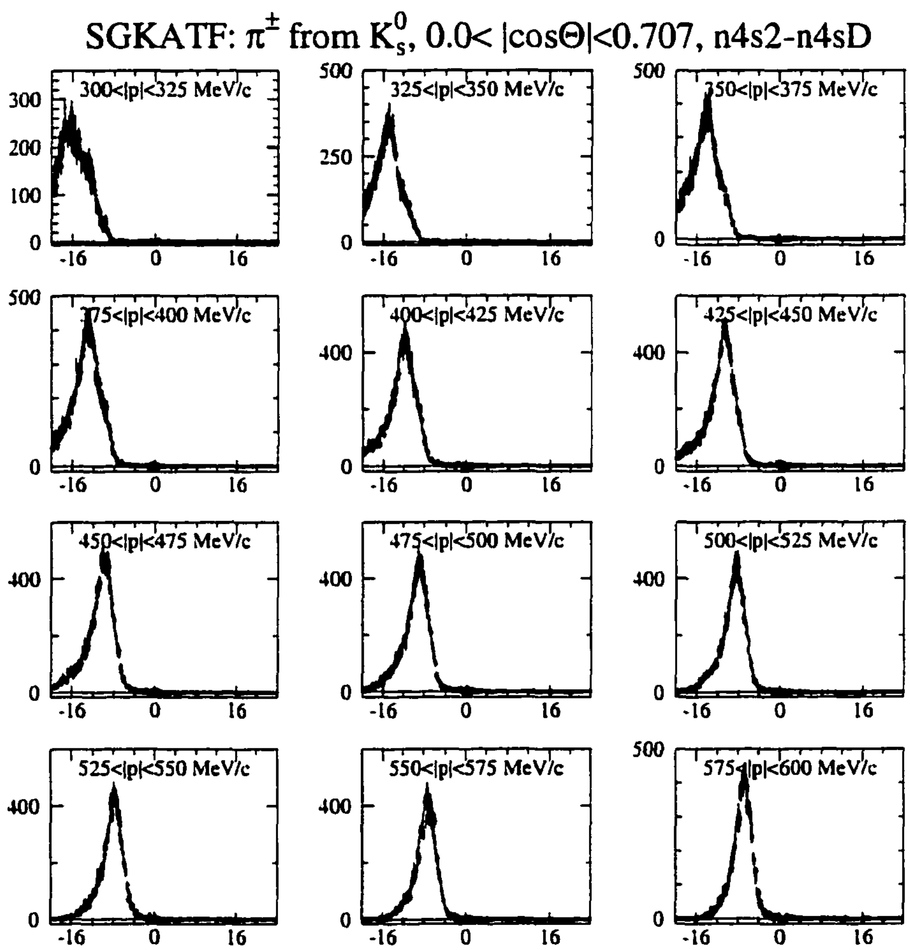

Figure 4.17: Plots of SGKATF from 300 MeV/c to 600 MeV/c, in 25 MeV/c bins for charged pions from K^0_s in the 4s2–4sD RECOMPRESS datasets.

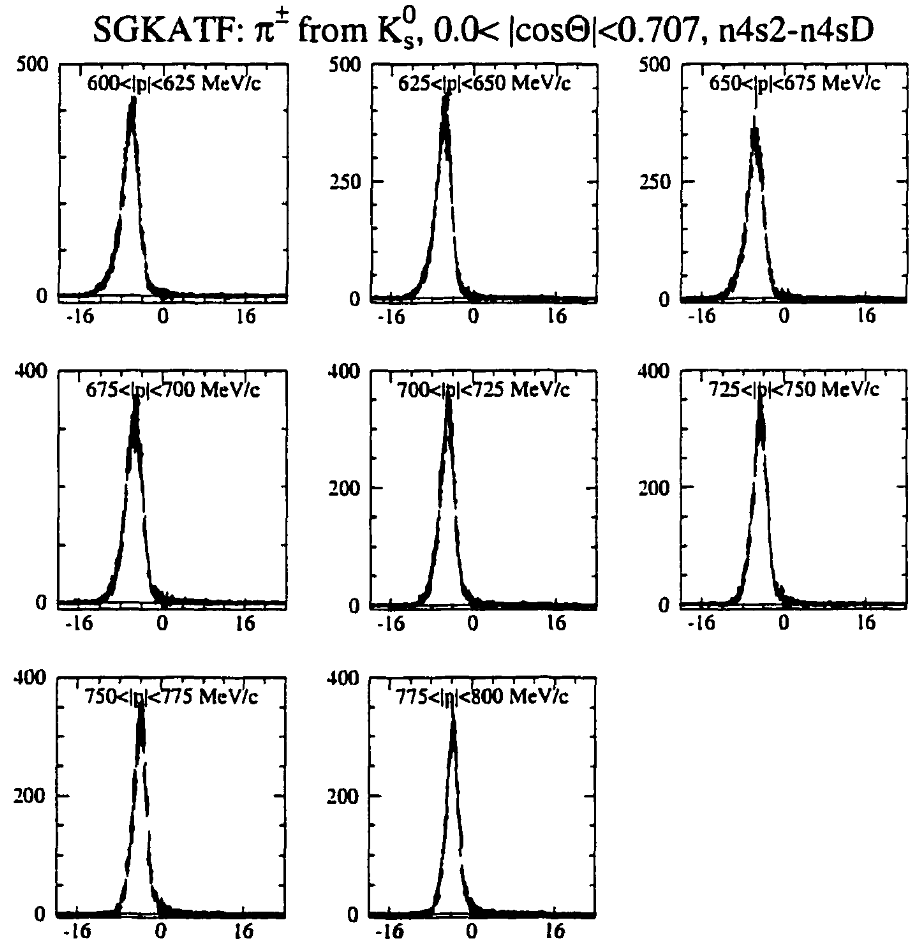

Figure 4.18: Plots of SGKATF from 600 MeV/c to 800 MeV/c, in 25 MeV/c bins for charged pions from K^0_s in the $4s2$–$4s$D RECOMPRESS datasets.

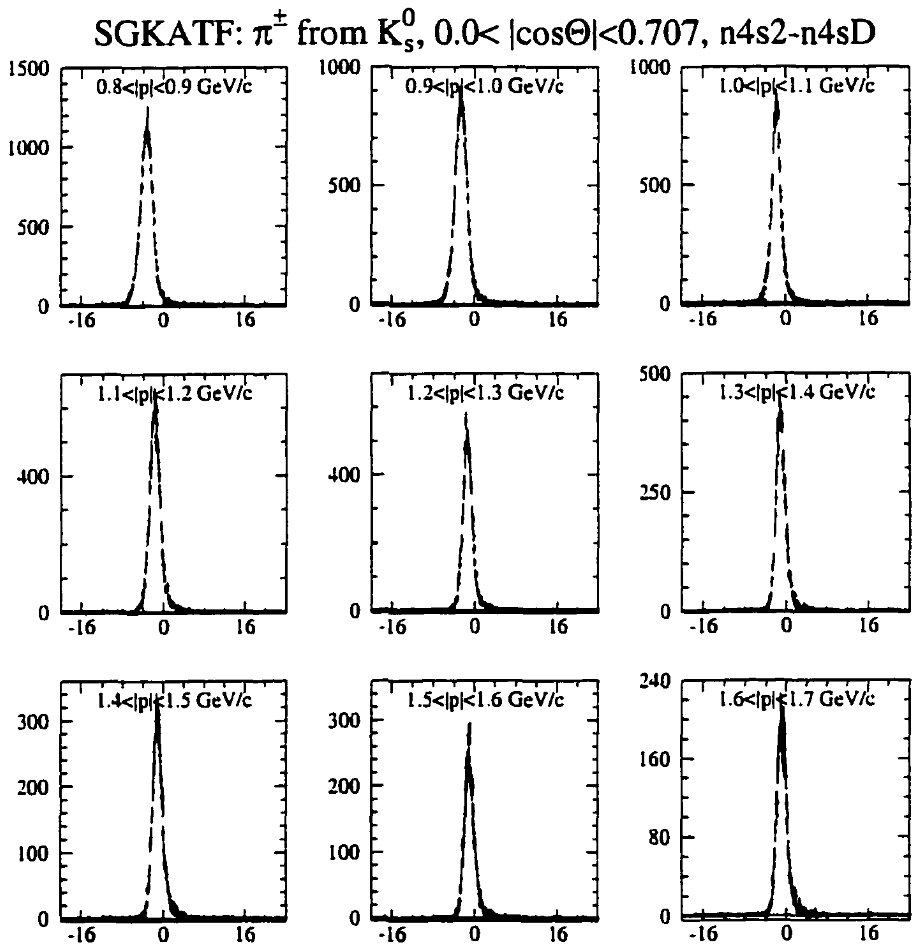

Figure 4.19: Plots of SGKATF from 0.8 GeV/c to 1.7 GeV/c, in 0.1 GeV/c bins for charged pions from K_s^0 in the 4s2–4sD RECOMPRESS datasets.

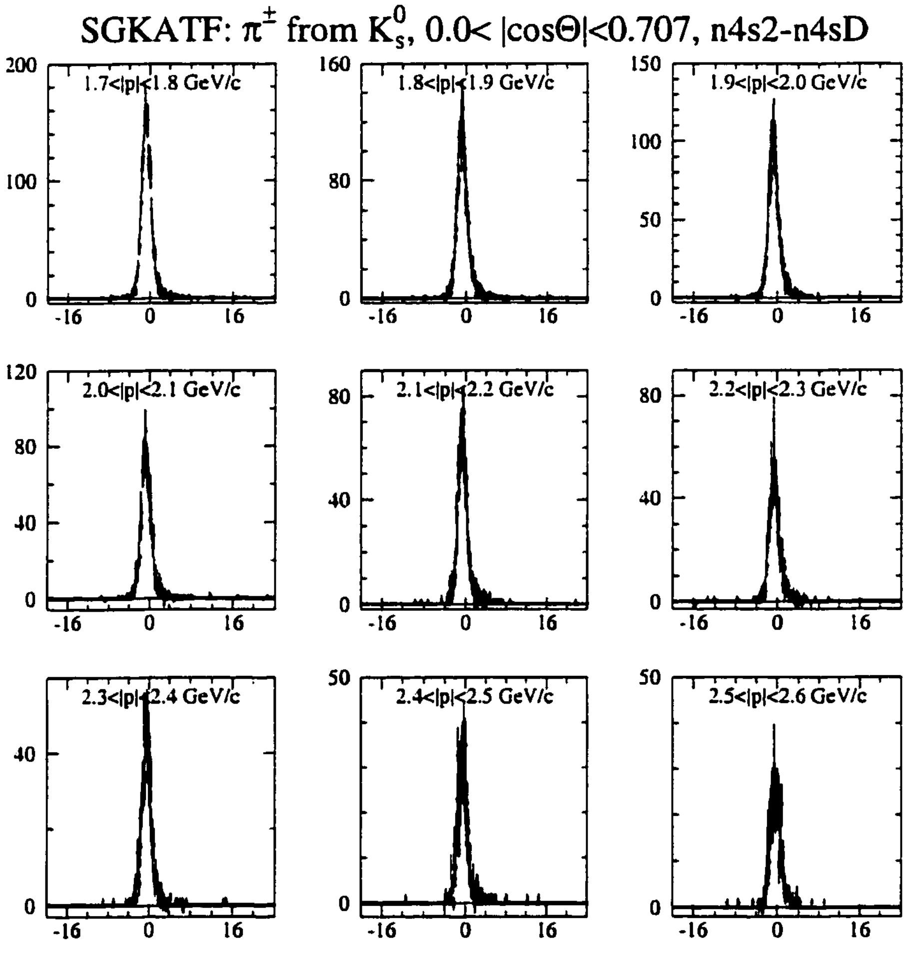

Figure 4.20: Plots of SGKATF from 1.7 GeV/c to 2.6 GeV/c, in 0.1 GeV/c bins for charged pions from K_s^0 in the 4s2–4sD RECOMPRESS datasets.

Integrating the background function over the ϕ peak and sideband regions (as detailed in the previous section) gives peak-to-sideband scale factors of:

$$R_{\phi}^{dE/dx} = 0.5746 \pm 0.0058 \text{ and } R_{\phi}^{ToF} = 0.5477 \pm 0.0073, \tag{4.9}$$

respectively.

Figure 4.21 shows the fit used for the ϕ sideband subtraction for dE/dx. Figures 4.22–4.23 show the resultant sideband-subtracted charged kaon control shapes used for our dE/dx fits from 200 MeV/c to 800 MeV/c, in 25 MeV/c momentum bins. Figures 4.24–4.25 show the resultant sideband-subtracted charged kaon control shapes used for our dE/dx fits from 0.8 GeV/c to 2.6 GeV/c, in 0.1 GeV/c momentum bins. Figure 4.26 shows the fit used for the ϕ sideband subtraction for ToF. Figures 4.27–4.28 show the resultant sideband-subtracted charged kaon control shapes used for our ToF fits from 200 MeV/c to 800 MeV/c, in 25 MeV/c momentum bins. Figures 4.29–4.30 show the resultant sideband-subtracted charged kaon control shapes used for our ToF fits from 0.8 GeV/c to 2.6 GeV/c, in 0.1 GeV/c momentum bins.

4.3.4 Proton Data Control Shapes ($\Lambda \to p\pi^-$)

The contribution of protons[2] to our PID fits is relatively small compared to pions. Despite the magnitude of their contribution, protons are still considered a primary control shape because they contribute to a distinct area of each PID fit. We obtain our proton control shapes by reconstructing $\Lambda \to p\pi^-$, with the proton track for each Λ candidate[3] subject to the same tracking cuts described earlier. The Λ mass peak used for obtaining the ToF shapes also requires the proton track to pass the ToF cuts described above. We obtain a clean sample of $\Lambda \to p\pi^-$ by making a (secondary) vertex identification cut (KINCD = 2) which greatly reduces background. For both dE/dx and ToF, we define the peak plus low and high sideband regions for the Λ sideband subtraction to be:

!

$$\begin{gathered} 1.112 < M_{p\pi}^{Peak} < 1.120 \text{ GeV}/c^2, \\ 1.101 < M_{p\pi}^{LoSB} < 1.108 \text{ GeV}/c^2 \text{ and } 1.124 < M_{p\pi}^{HiSB} < 1.131 \text{ GeV}/c^2. \end{gathered} \tag{4.10}$$

We extract our dE/dx and ToF proton shapes from these peak and sideband regions by performing a sideband subtraction as detailed in the previous sections. The resulting scale factors are:

$$R_{\Lambda}^{dE/dx} = 0.5462 \pm 0.0055 \text{ and } R_{\Lambda}^{ToF} = 0.5512 \pm 0.0048, \tag{4.11}$$

[2]Here *"proton"* refers to both p from Λ and $\bar{p}$ from $\bar{\Lambda}$.

[3]Unless otherwise specified, charge conjugate modes are implied throughout the entire discussion.

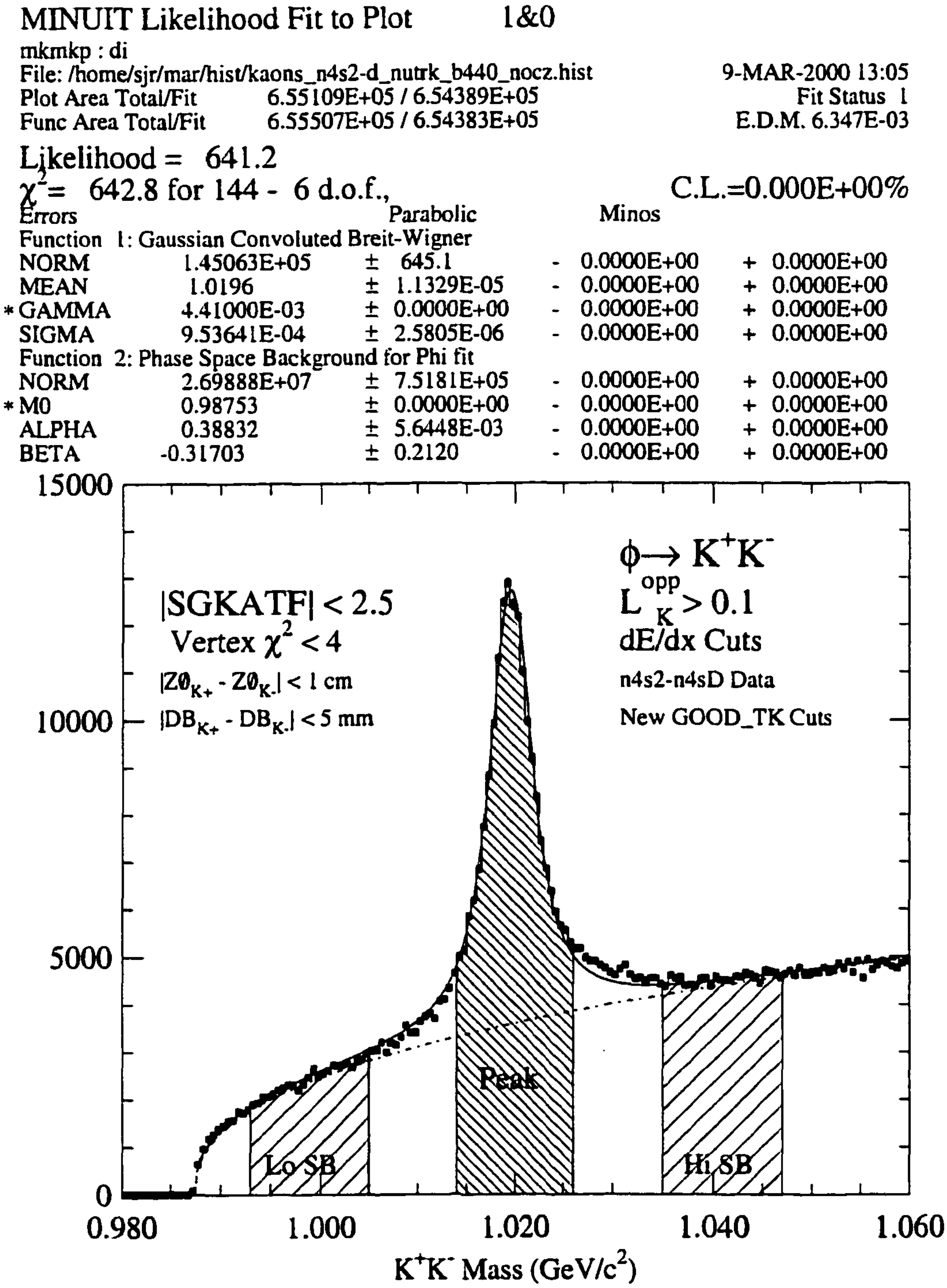

Figure 4.21: The invariant mass distribution for $K^+ K^-$ combinations passing the tracking requirements described in the text. The dark and light shaded segments show the signal and sideband regions, respectively. This fit is used for obtaining the dE/dx charged kaon control shapes.

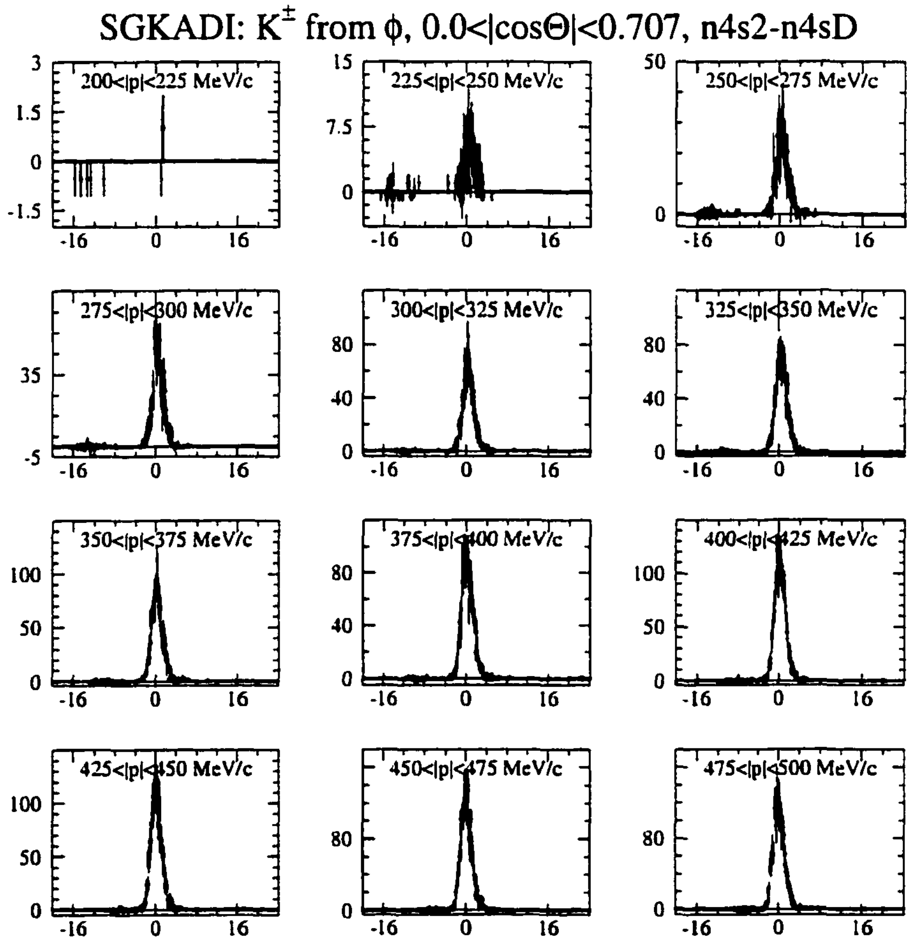

Figure 4.22: Plots of SGKADI from 200 MeV/c to 500 MeV/c, in 25 MeV/c bins for charged kaons from ϕ in the $4s2$–$4s$D RECOMPRESS datasets.

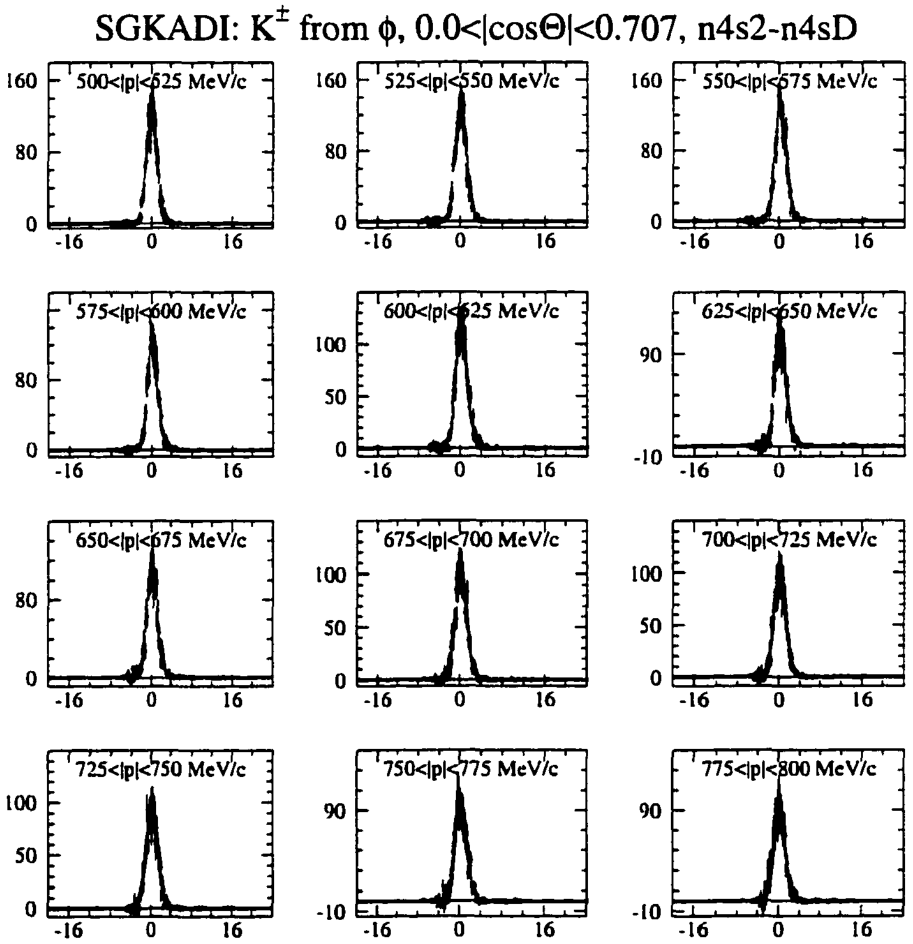

Figure 4.23: Plots of SGKADI from 500 MeV/c to 800 MeV/c, in 25 MeV/c bins for charged kaons from ϕ in the 4s2–4sD RECOMPRESS datasets.

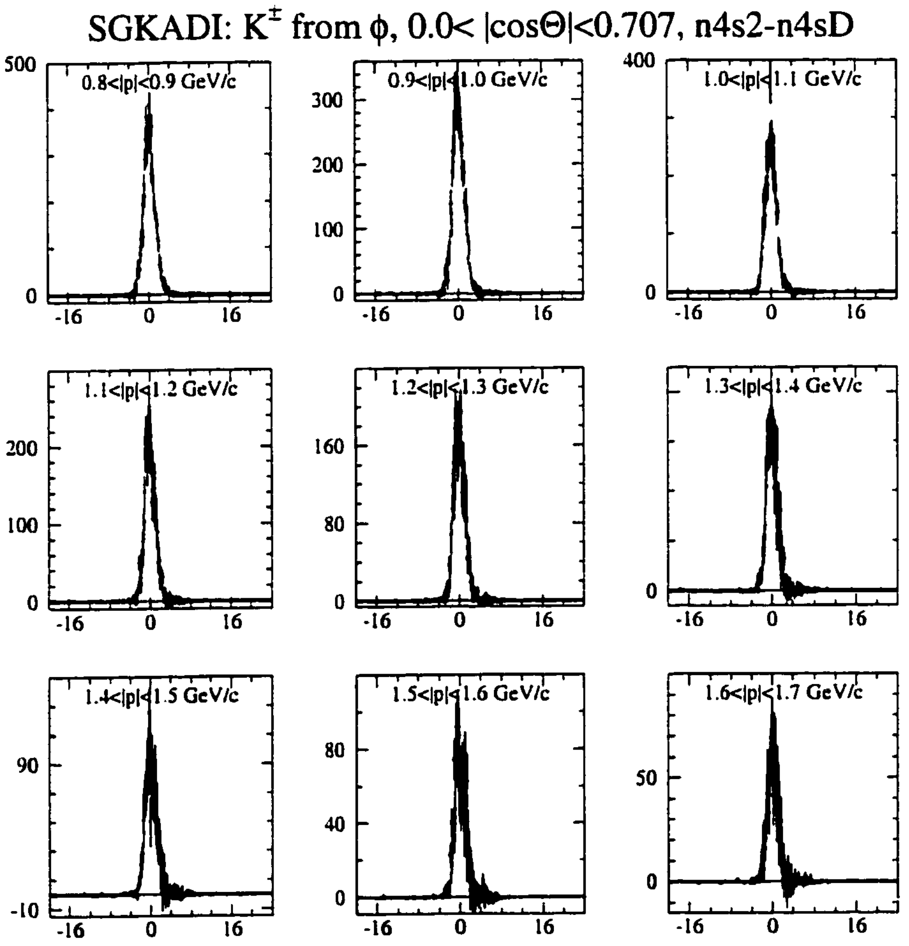

Figure 4.24: Plots of SGKADI from 0.8 GeV/c to 1.7 GeV/c, in 0.1 GeV/c bins for charged kaons from ϕ in the $4s2$–$4s$D RECOMPRESS datasets.

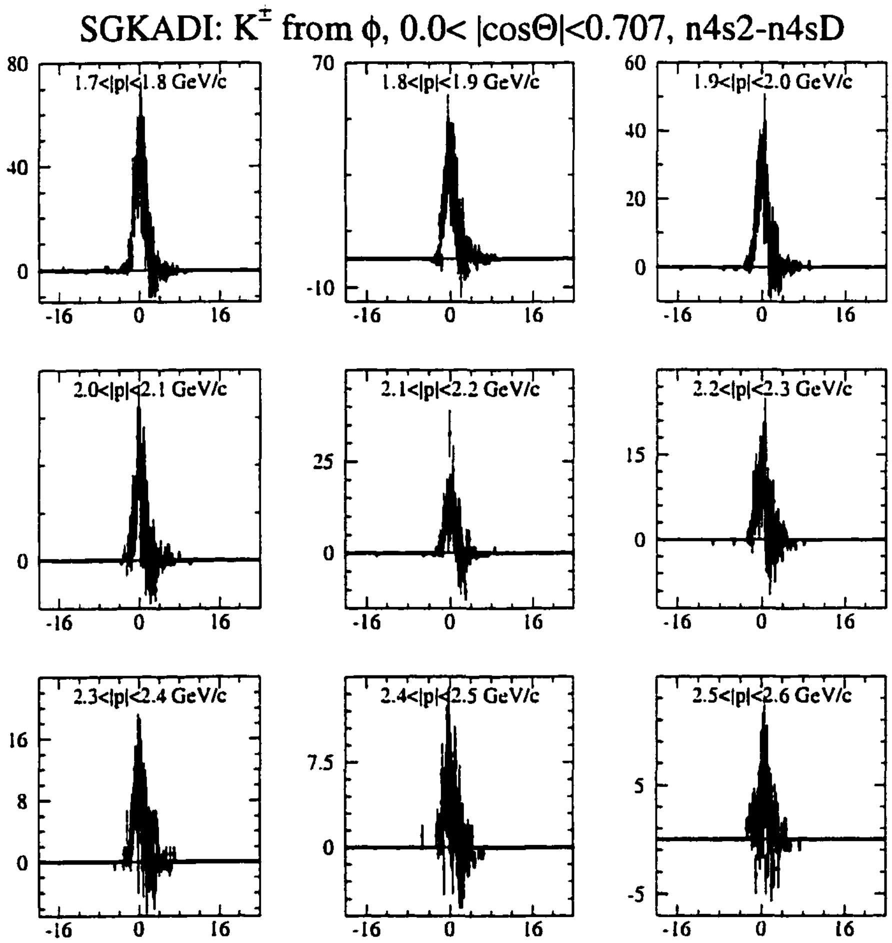

Figure 4.25: Plots of SGKADI from 1.7 GeV/c to 2.6 GeV/c, in 0.1 GeV/c bins for charged kaons from ϕ in the 4s2–4sD RECOMPRESS datasets.

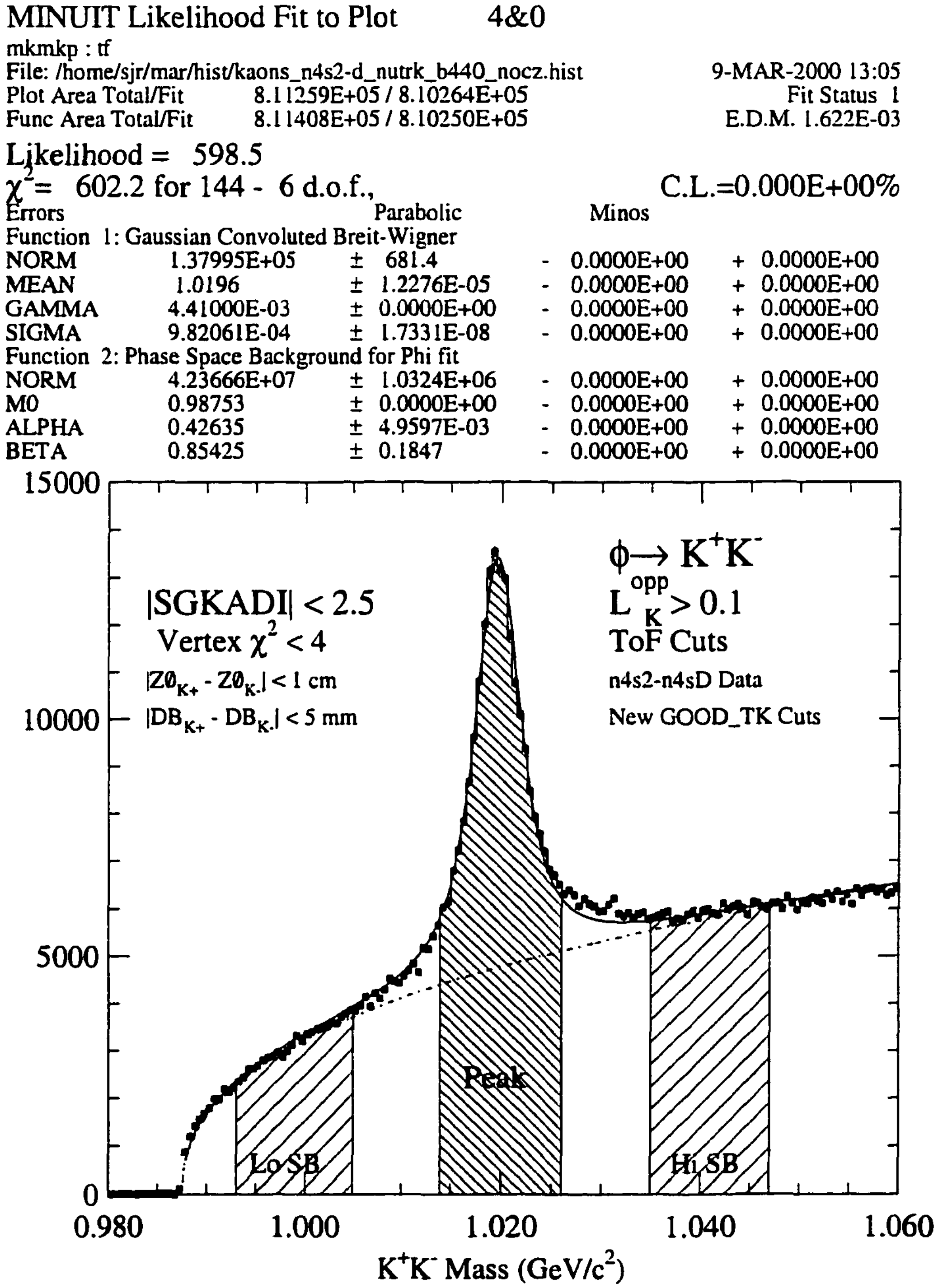

Figure 4.26: The invariant mass distribution for $K^+ K^-$ combinations passing the tracking *and ToF* requirements described in the text. The dark and light shaded segments show the signal and sideband regions, respectively. This fit is used for obtaining the *ToF* charged kaon control shapes.

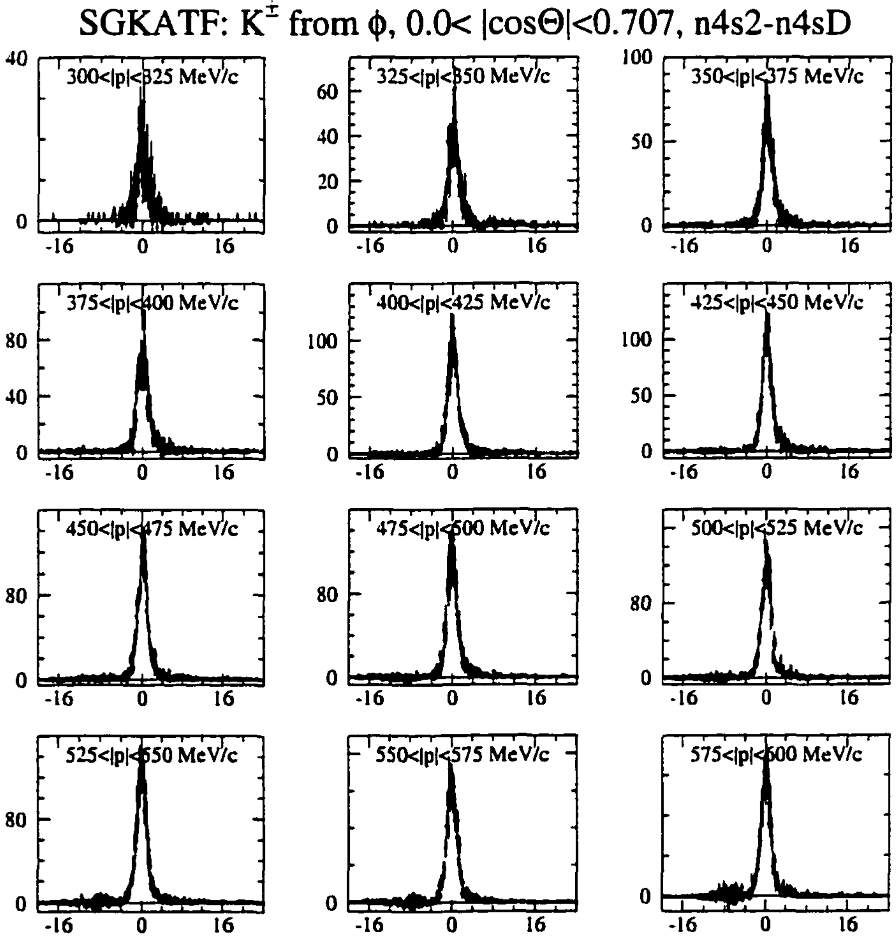

Figure 4.27: Plots of SGKATF from 300 MeV/c to 600 MeV/c, in 25 MeV/c bins for charged kaons from ϕ in the $4s2$–$4s$D RECOMPRESS datasets.

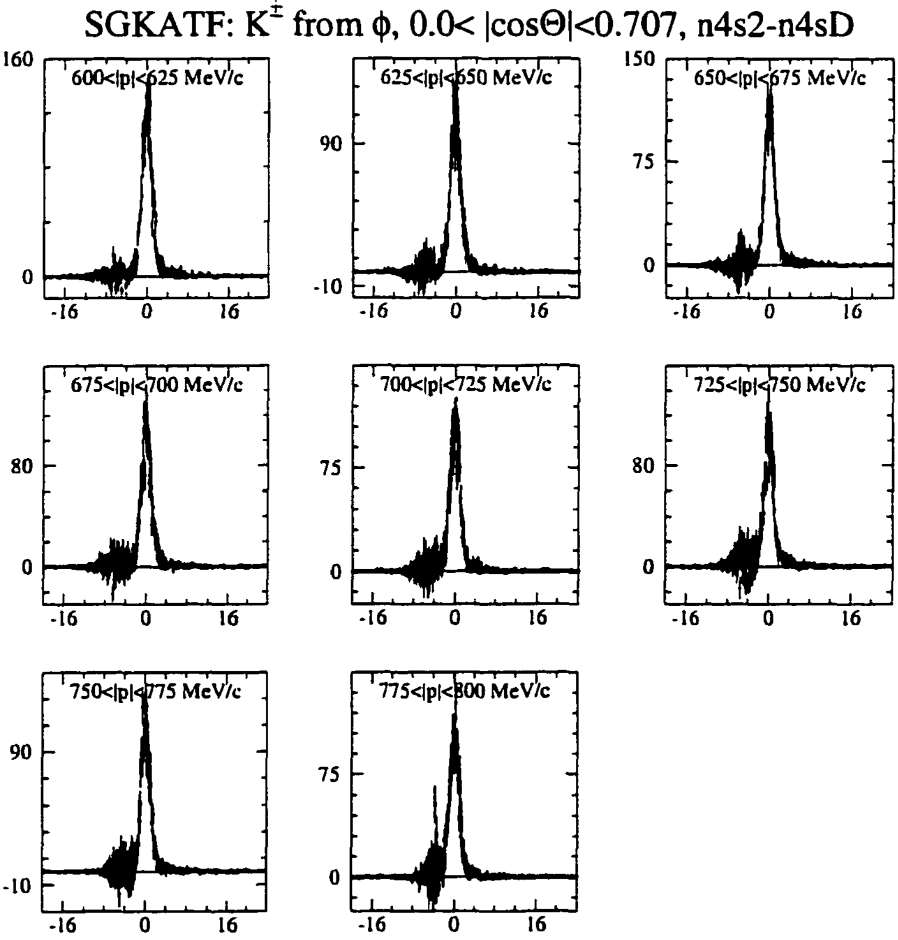

Figure 4.28: Plots of SGKATF from 600 MeV/c to 800 MeV/c, in 25 MeV/c bins for charged kaons from ϕ in the $4s2$-$4sD$ RECOMPRESS datasets.

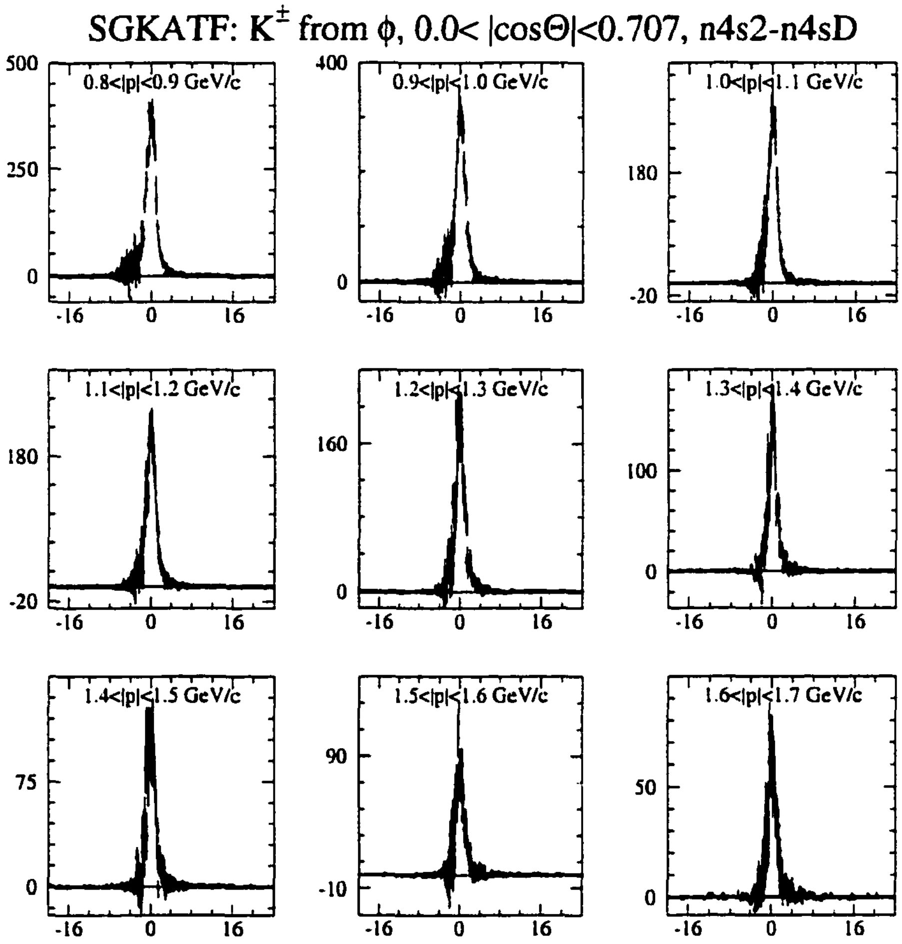

Figure 4.29: Plots of SGKATF from 0.8 GeV/c to 1.7 GeV/c, in 0.1 GeV/c bins for charged kaons from ϕ in the $4s2$–$4s$D RECOMPRESS datasets.

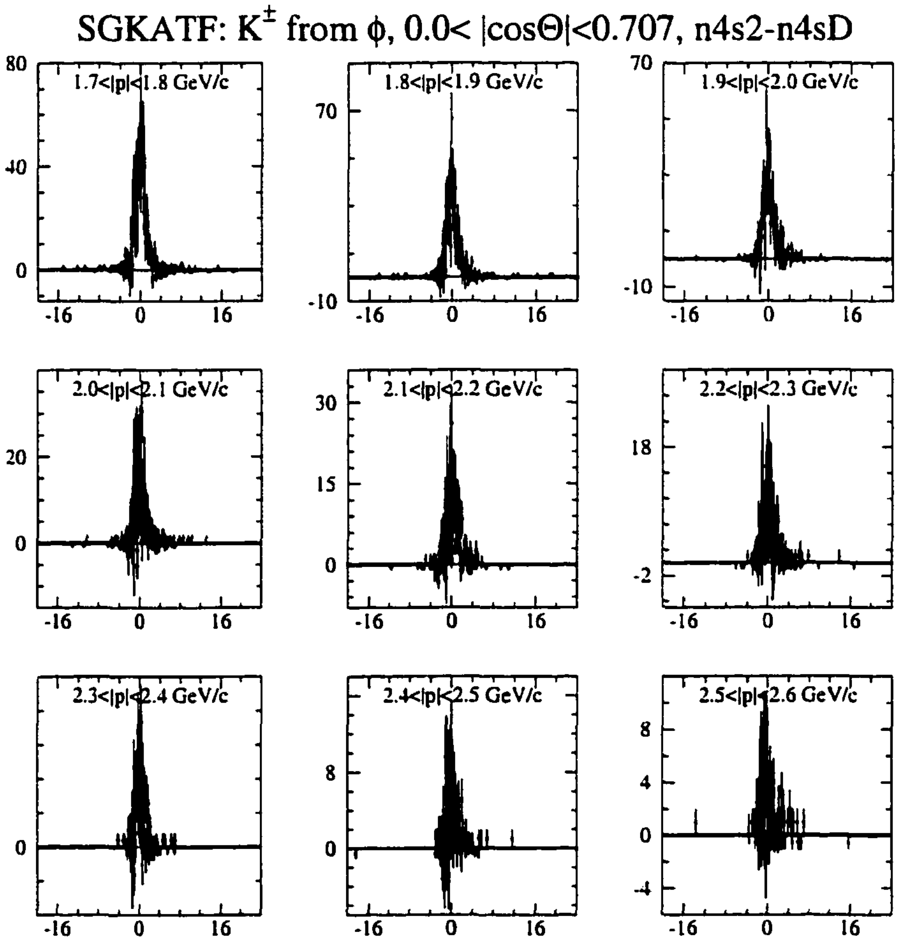

Figure 4.30: Plots of SGKATF from 1.7 GeV/c to 2.6 GeV/c, in 0.1 GeV/c bins for charged kaons from ϕ in the 4s2–4sD RECOMPRESS datasets.

respectively.

Figure 4.31 shows the fit used for the Λ sideband subtraction for dE/dx. Figures 4.32–4.33 show the resultant sideband-subtracted proton $(p, \overline{p})$ control shapes used for our dE/dx fits from 200 MeV/c to 800 MeV/c, in 25 MeV/c momentum bins. Figures 4.34–4.35 show the resultant sideband-subtracted proton $(p, \overline{p})$ control shapes used for our dE/dx fits from 0.8 GeV/c to 2.6 GeV/c, in 0.1 GeV/c momentum bins. Figure 4.36 shows the fit used for the Λ sideband subtraction for ToF. Figures 4.37–4.38 show the resultant sideband-subtracted proton $(p, \overline{p})$ control shapes used for our ToF fits from 200 MeV/c to 800 MeV/c, in 25 MeV/c momentum bins. Figures 4.39–4.40 show the resultant sideband-subtracted proton $(p, \overline{p})$ control shapes used for our ToF fits from 0.8 GeV/c to 2.6 GeV/c, in 0.1 GeV/c momentum bins.

4.3.5 Electron Data Control Shapes ($\gamma\gamma \to e^+ e^-$)

We obtain our lepton (electron and muon) shapes from the appropriate UCSB dE/dx Calibration (DIFIX) tapes. We use radiative Bhabha data (`SBDEDX_GGEE` DLTs) for electrons and radiative muon data (`SBDEDX_MUMUG` DLTs) for muons.

We process the RECOMPRESS `SBDEDX_GGEE` DIFIX DLTs through the same code which we used to process the data shapes. The electrons in the resulting file are thus subject to the same tracking and event shape cuts as the data. We then construct our electron control shapes for both dE/dx and ToFusing the same momentum bins as the data shapes. We generate comparable dE/dx and ToF shapes for $e^{\pm}$ from generic $B\overline{B}$ MC, as well. We compare the resultant control shapes from these $\gamma\gamma \to e^+ e^-$ data with those generated from MC in Figures 4.41–4.42 for dE/dx and Figures 4.43–4.44 for ToF.

There is some discrepancy in `SGKADI` distributions between electrons in the data and MC. This is especially true beginning around 400 MeV/c, where our electron suppression cut is activated. Electrons comprise a relatively small contribution to most of the fits above this momentum. We account for this discrepancy in our consideration of the systematic error on our lepton normalizations.

4.3.6 Muon Data Control Shapes ($\gamma\gamma \to \mu^+\mu^-\gamma$)

We also process the RECOMPRESS `SBDEDX_MUMUG` DIFIX DLTs through the same code which we used to process the data shapes. The muons in the resulting output file are thus subject to the same tracking and event shape cuts as the data. We again generate comparable dE/dx and ToF shapes for $\mu^{\pm}$ from generic $B\overline{B}$ MC, as well. We compare the resultant control shapes from these radiative muon data with those generated from MC in Figures 4.45–4.46 for dE/dx and Figures 4.47–4.48 for ToF. The reasonable agreement between data and MC for these PID distributions and the lack of a sufficient sample of well-identified, low momentum muons in the data leads us to use MC shapes for muons in both our dE/dx and ToF fits.

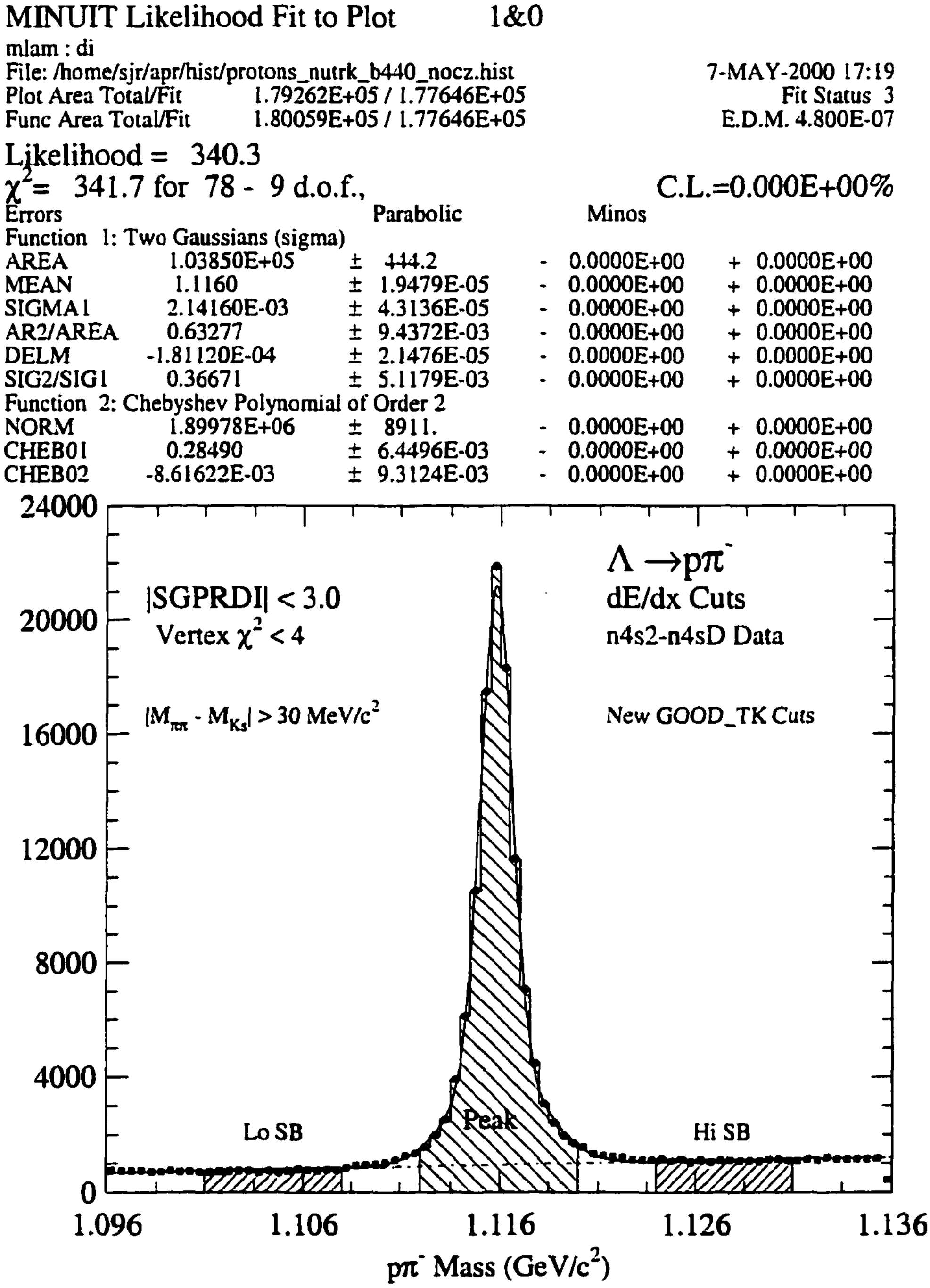

Figure 4.31: The invariant mass distribution for $p\pi$ combinations passing the tracking requirements described in the text. The dark and light shaded segments show the signal and sideband regions, respectively. This fit is used for obtaining the dE/dx proton $(p, \bar{p})$ control shapes.

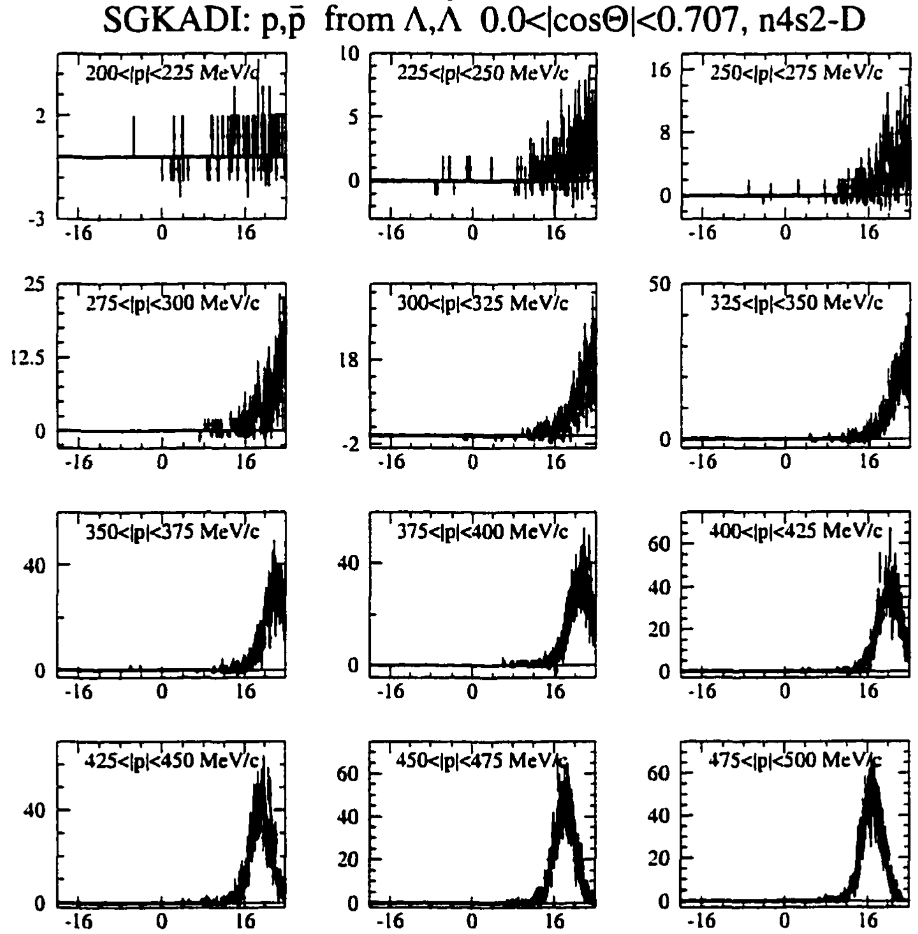

Figure 4.32: Plots of SGKADI from 200 MeV/c to 500 MeV/c, in 25 MeV/c bins for $p(\bar{p})$ from $\Lambda(\bar{\Lambda})$ in the $4s2$–$4s$D RECOMPRESS datasets.

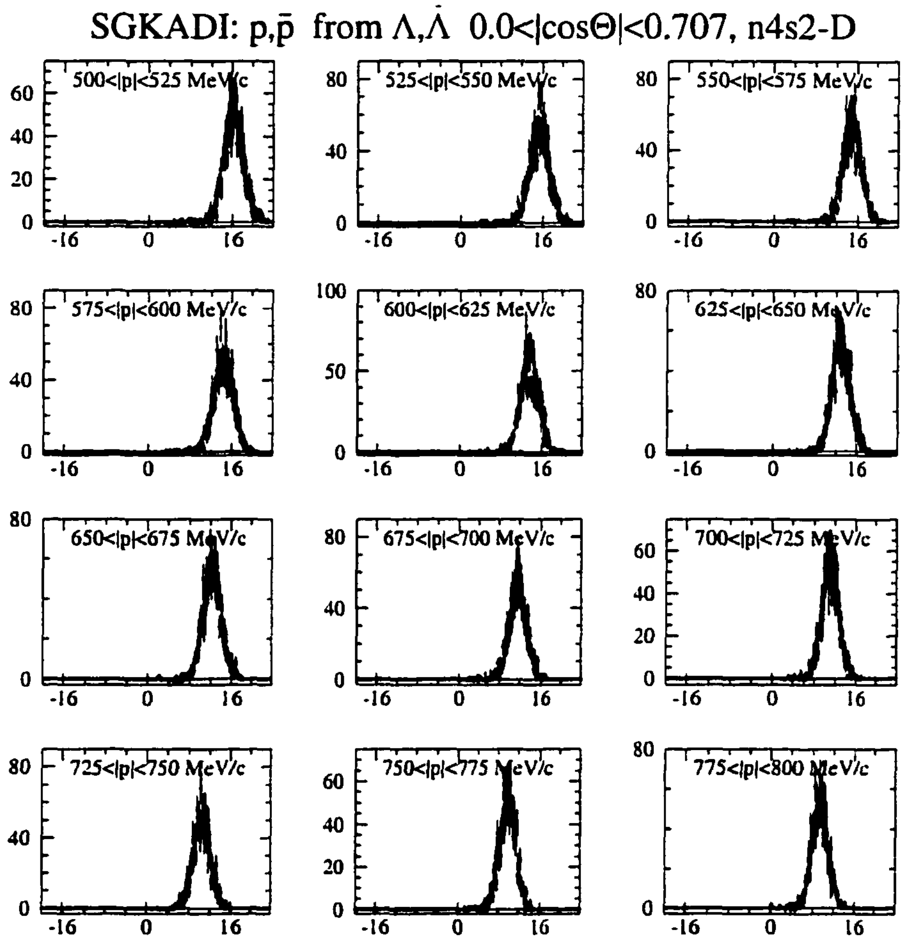

Figure 4.33: Plots of SGKADI from 500 MeV/c to 800 MeV/c, in 25 MeV/c bins for $p(\overline{p})$ from $\Lambda(\overline{\Lambda})$ in the 4s2–4sD RECOMPRESS datasets.

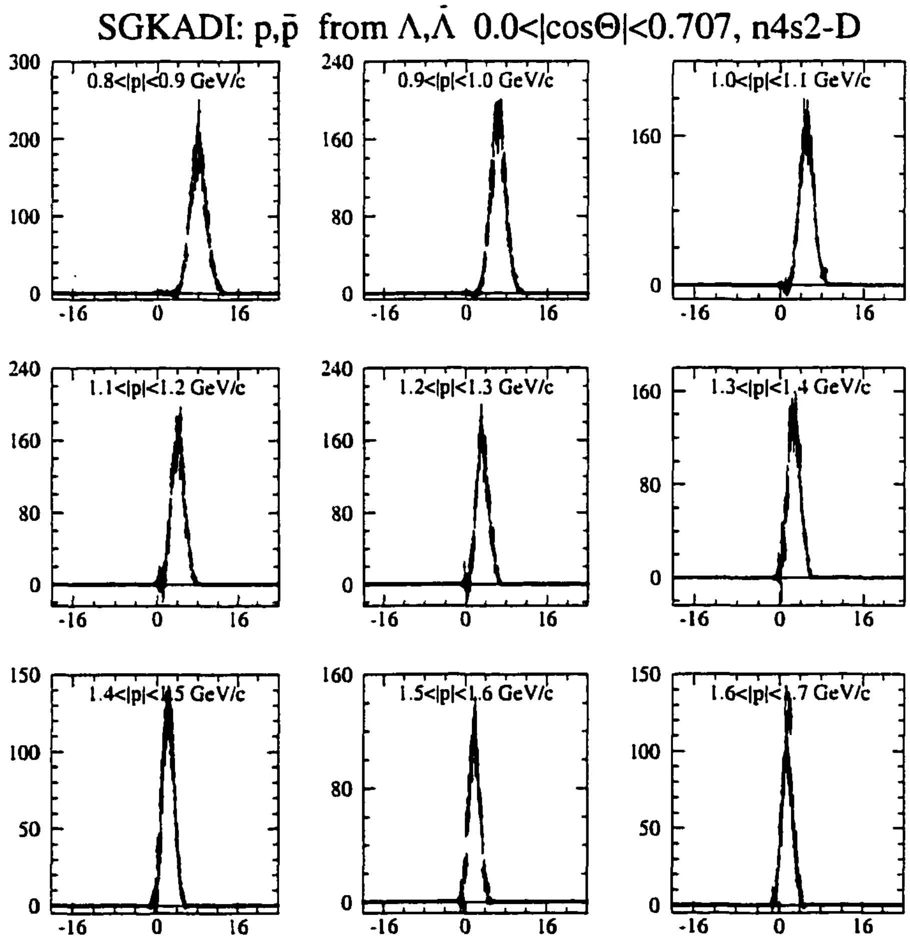

Figure 4.34: Plots of SGKADI from 0.8 GeV/c to 1.7 GeV/c, in 0.1 GeV/c bins for $p(\overline{p})$ from $\Lambda(\overline{\Lambda})$ in the $4s2$–$4s$D RECOMPRESS datasets.

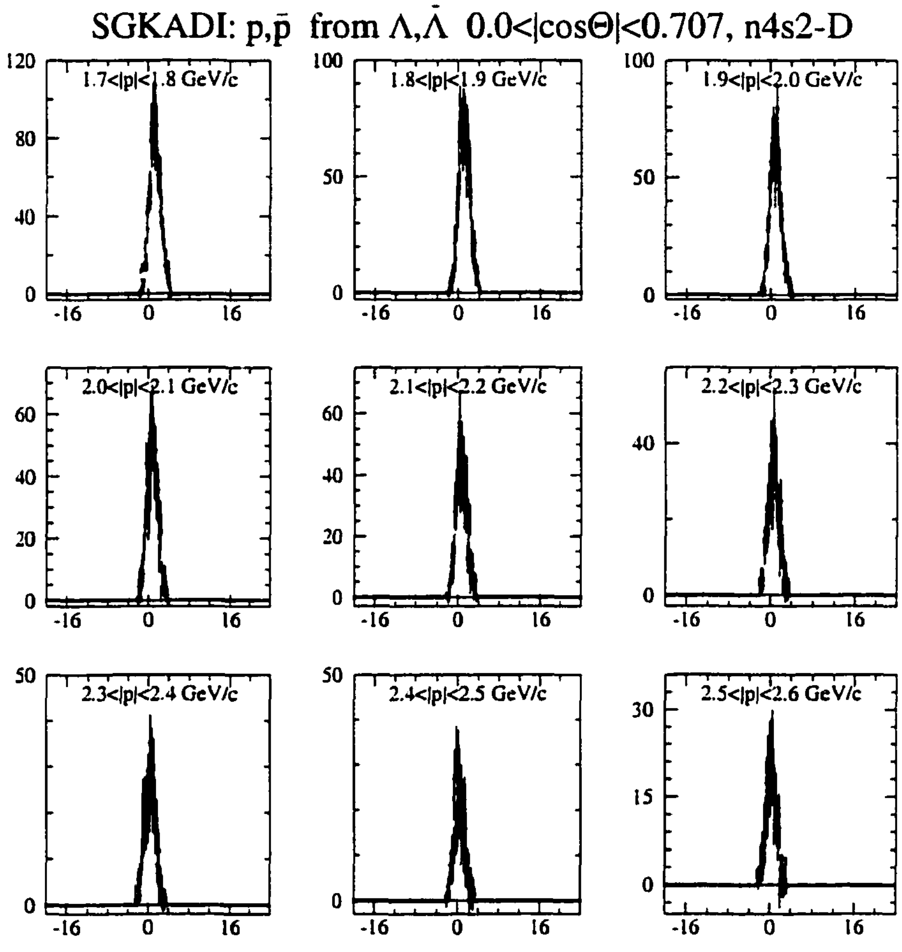

Figure 4.35: Plots of SGKADI from 1.7 GeV/c to 2.6 GeV/c, in 0.1 GeV/c bins for $p(\overline{p})$ from $\Lambda(\overline{\Lambda})$ in the $4s2$–$4s$D RECOMPRESS datasets.

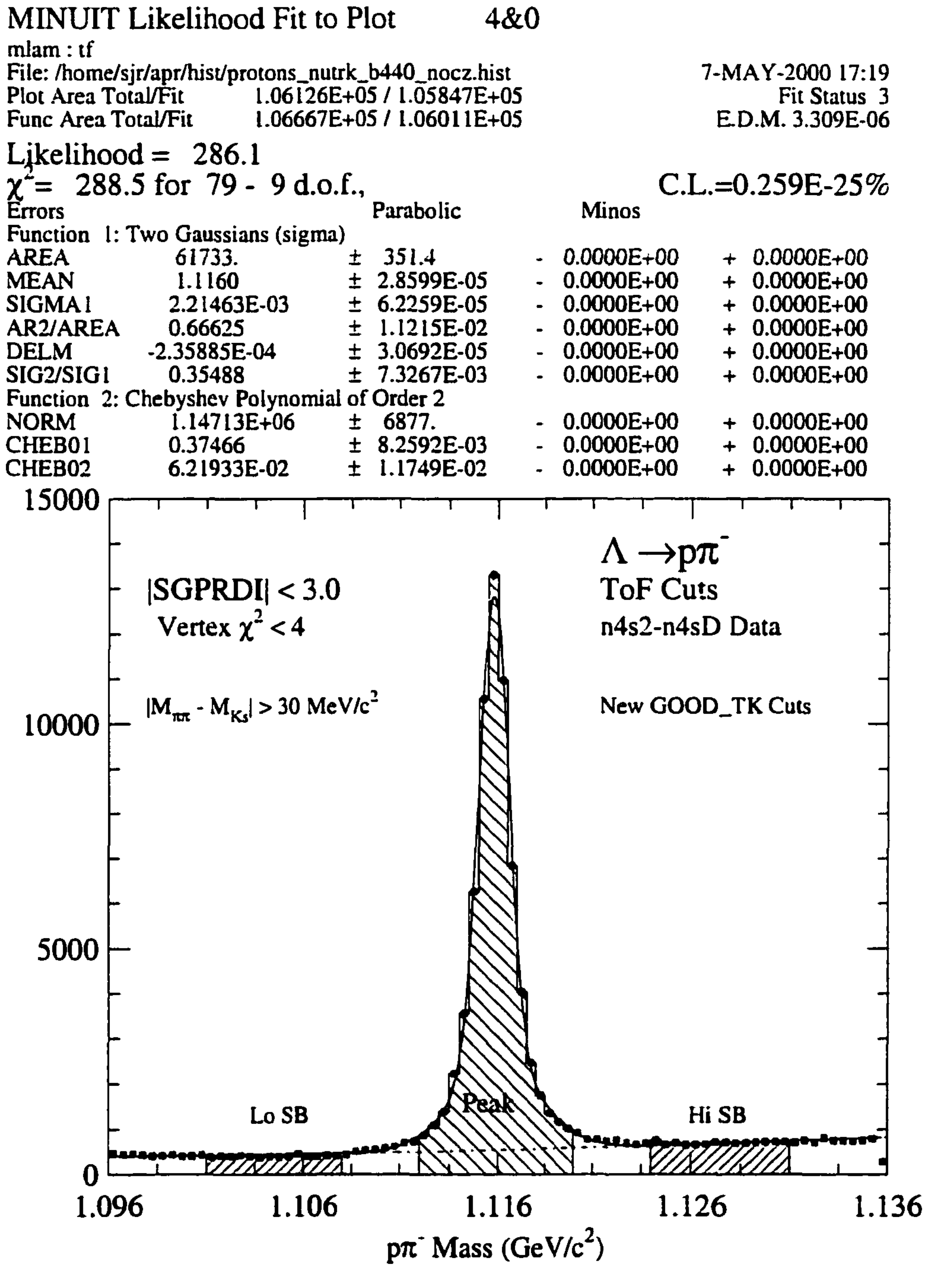

Figure 4.36: The invariant mass distribution for $p\pi$ combinations passing the tracking *and ToF* requirements described in the text. The dark and light shaded segments show the signal and sideband regions, respectively. This fit is used for obtaining the *ToF* proton $(p, \overline{p})$ control shapes.

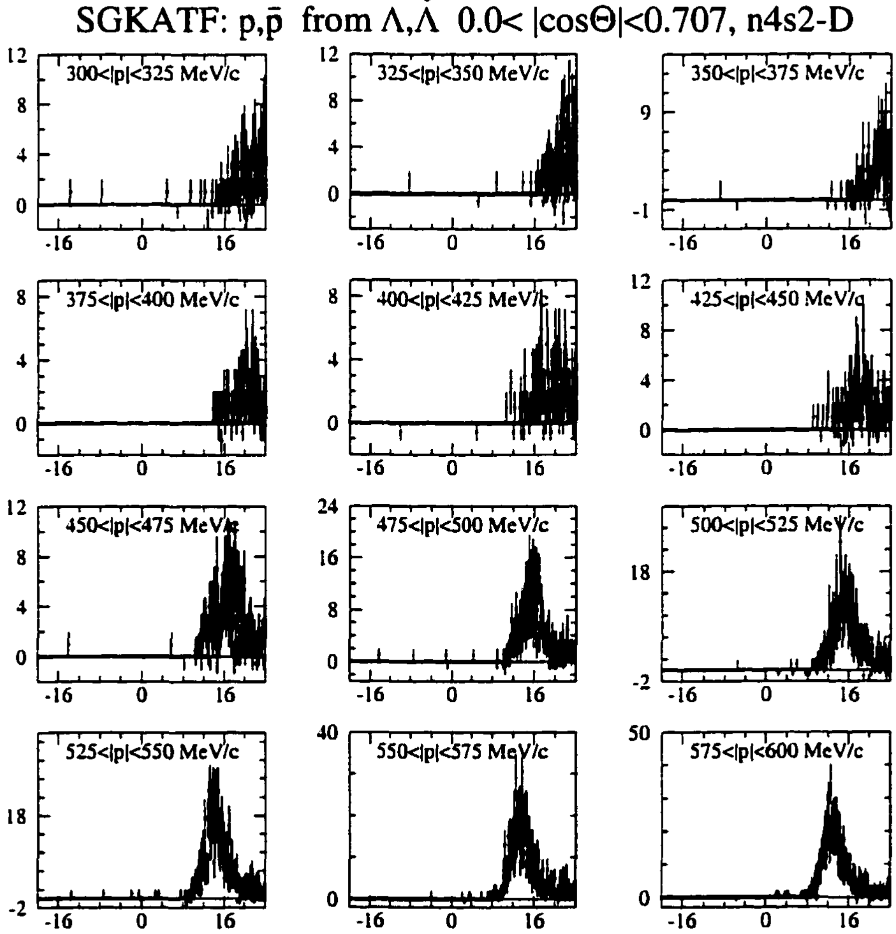

Figure 4.37: Plots of SGKATF from 200 MeV/c to 500 MeV/c, in 25 MeV/c bins for $p(\overline{p})$ from $\Lambda(\overline{\Lambda})$ in the $4s2$–$4s$D RECOMPRESS datasets.

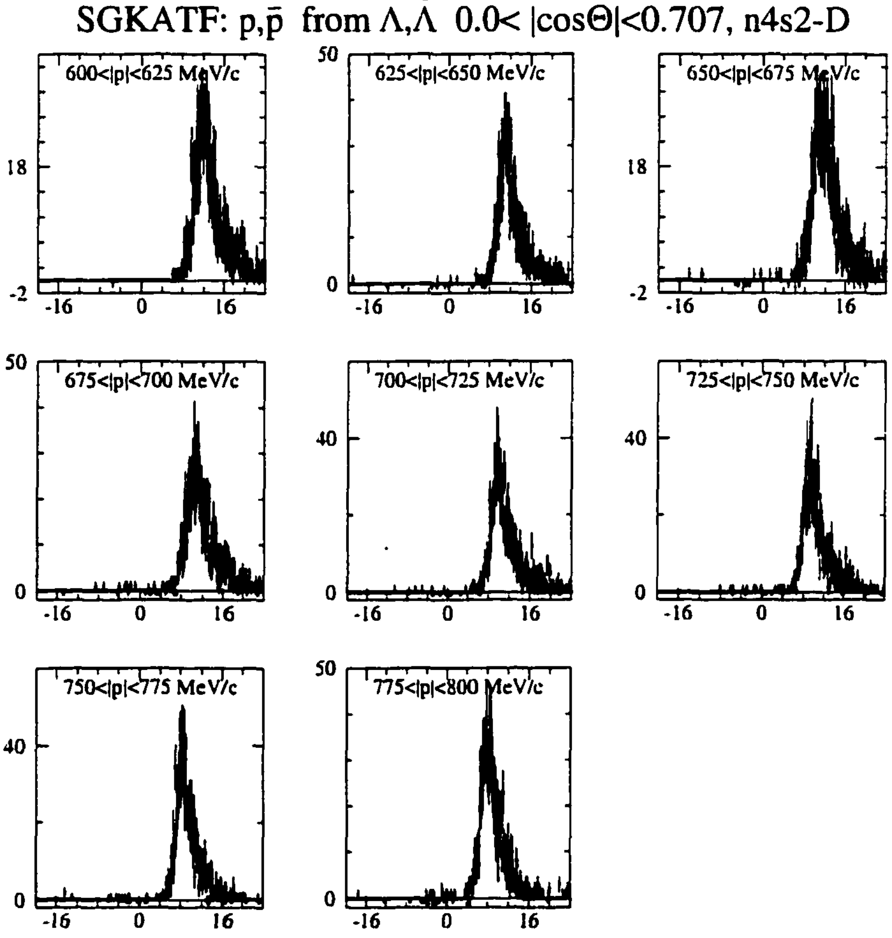

Figure 4.38: Plots of SGKATF from 500 MeV/c to 800 MeV/c, in 25 MeV/c bins for $p(\bar{p})$ from $\Lambda(\overline{\Lambda})$ in the 4s2–4sD RECOMPRESS datasets.

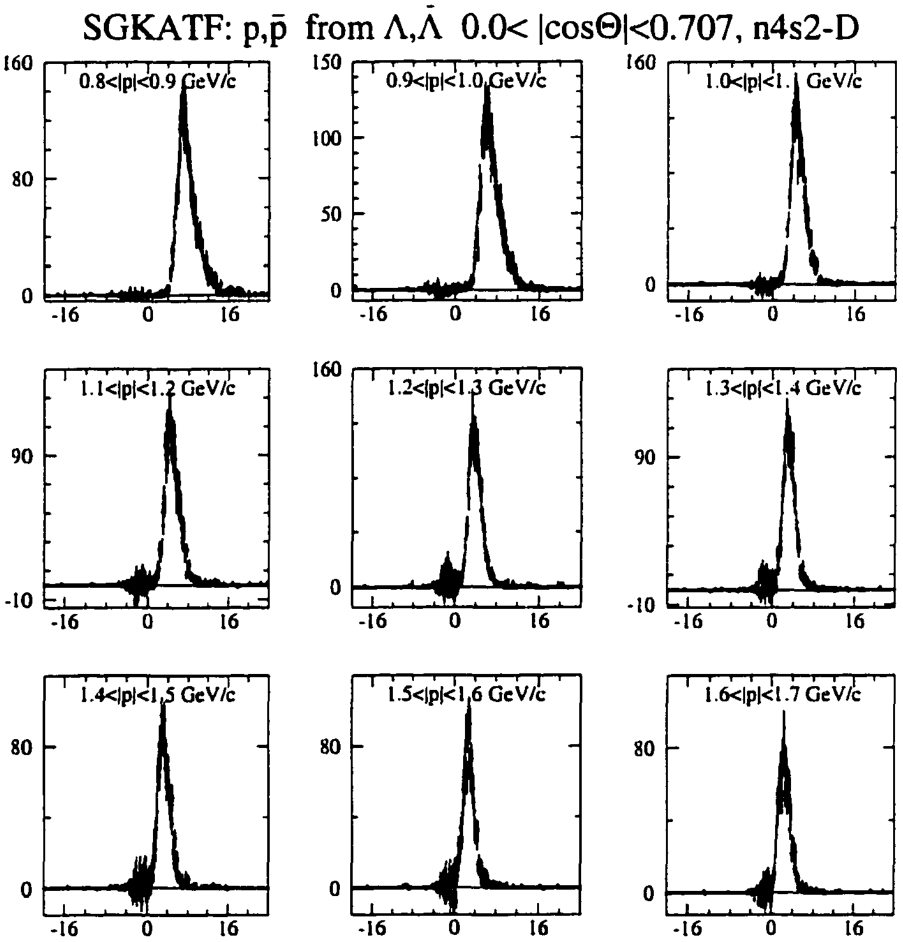

Figure 4.39: Plots of SGKATF from 0.8 GeV/c to 1.7 GeV/c, in 0.1 GeV/c bins for $p(\overline{p})$ from $\Lambda(\overline{\Lambda})$ in the 4s2–4sD RECOMPRESS datasets.

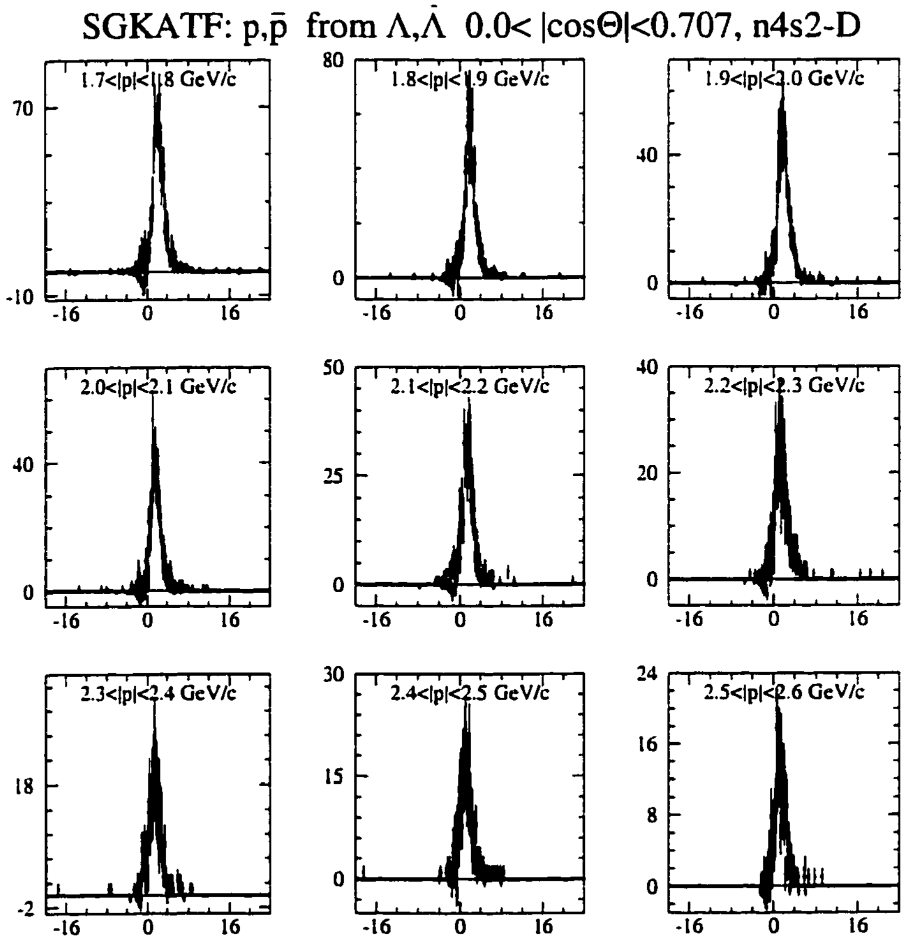

Figure 4.40: Plots of SGKATF from 1.7 GeV/c to 2.6 GeV/c, in 0.1 GeV/c bins for $p(\bar{p})$ from $\Lambda(\bar{\Lambda})$ in the 4s2–4sD RECOMPRESS datasets.

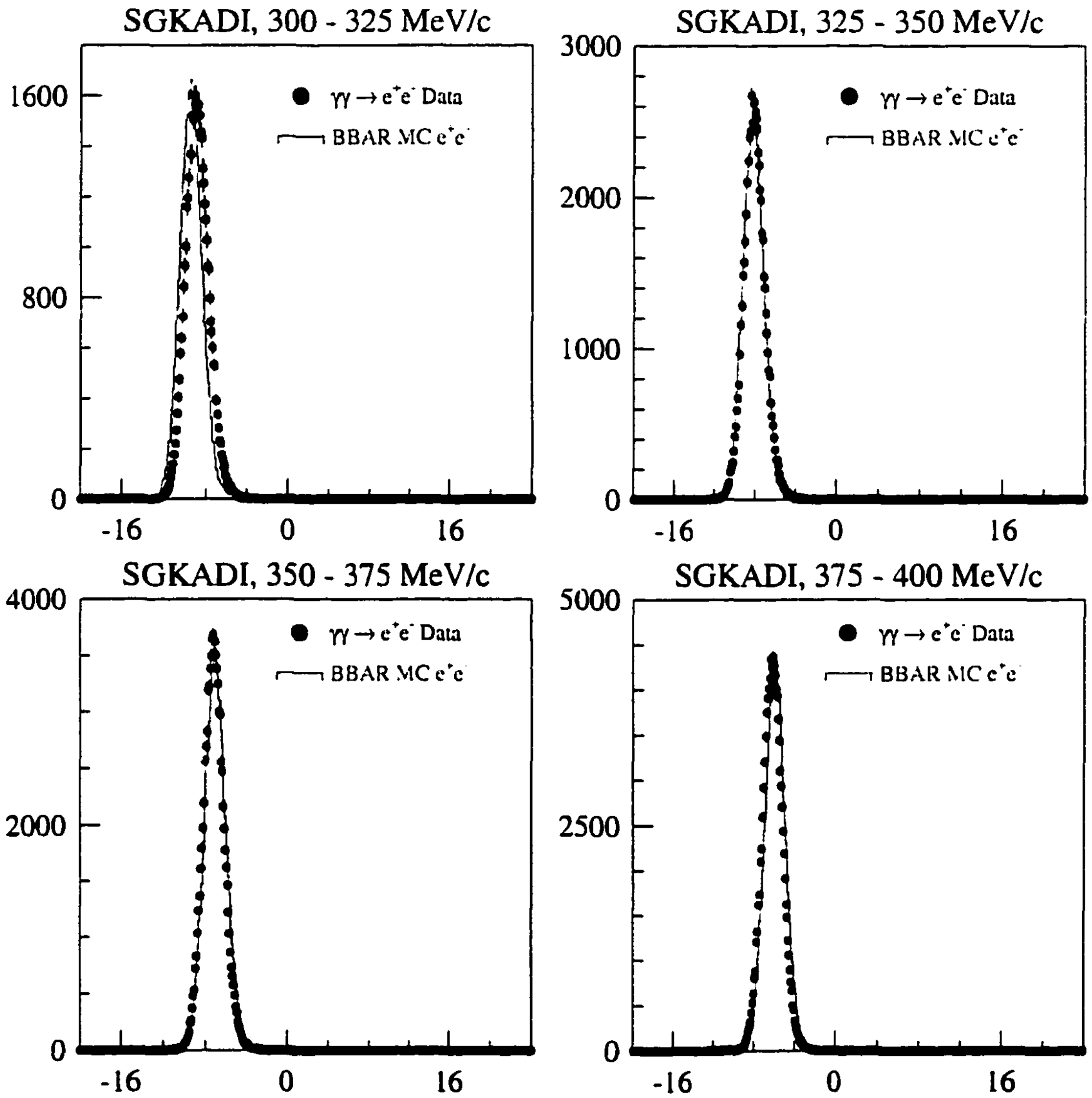

Figure 4.41: Plots of **SGKADI** from 300 MeV/c to 400 MeV/c, in 25 MeV/c bins for e^+e^- from radiative Bhabha data and $B\overline{B}$ Monte Carlo, subject to our tracking and event shape cuts. The MC plot is scaled to the area of the data plot.

Since the lepton contributions to the PID fits is relatively small, any discrepancy between our data and MC lepton shapes has a minimal effect on our fits. We account for this in our consideration of the systematic error contribution of our lepton normalizations in section 4.4.1.

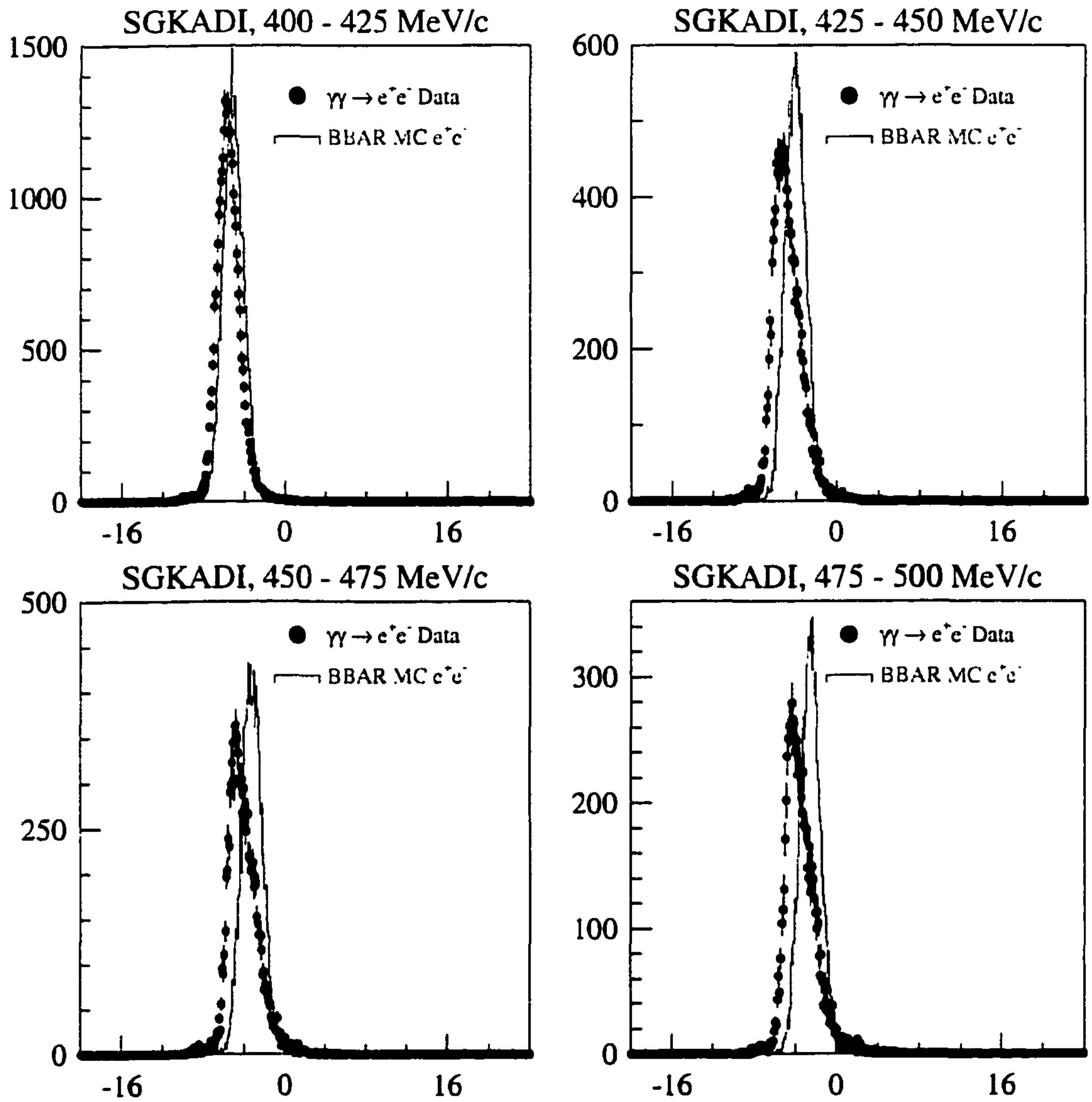

Figure 4.42: Plots of SGKADI from 400 MeV/c to 500 MeV/c, in 25 MeV/c bins for e^+e^- from radiative Bhabha data and $B\overline{B}$ Monte Carlo, subject to our tracking and event shape cuts. The MC plot is scaled to the area of the data plot.

4.4 Extraction of Signals

4.4.1 Lepton Normalizations

We determine the expected number of each lepton type in our fit for each momentum bin for each PID device as follows: we fit the number of MC tracks which pass each lepton ID cut (above the momentum threshold for that lepton suppression cut) to the number of tracks in the data which pass that same lepton ID cut. The lepton ID cut

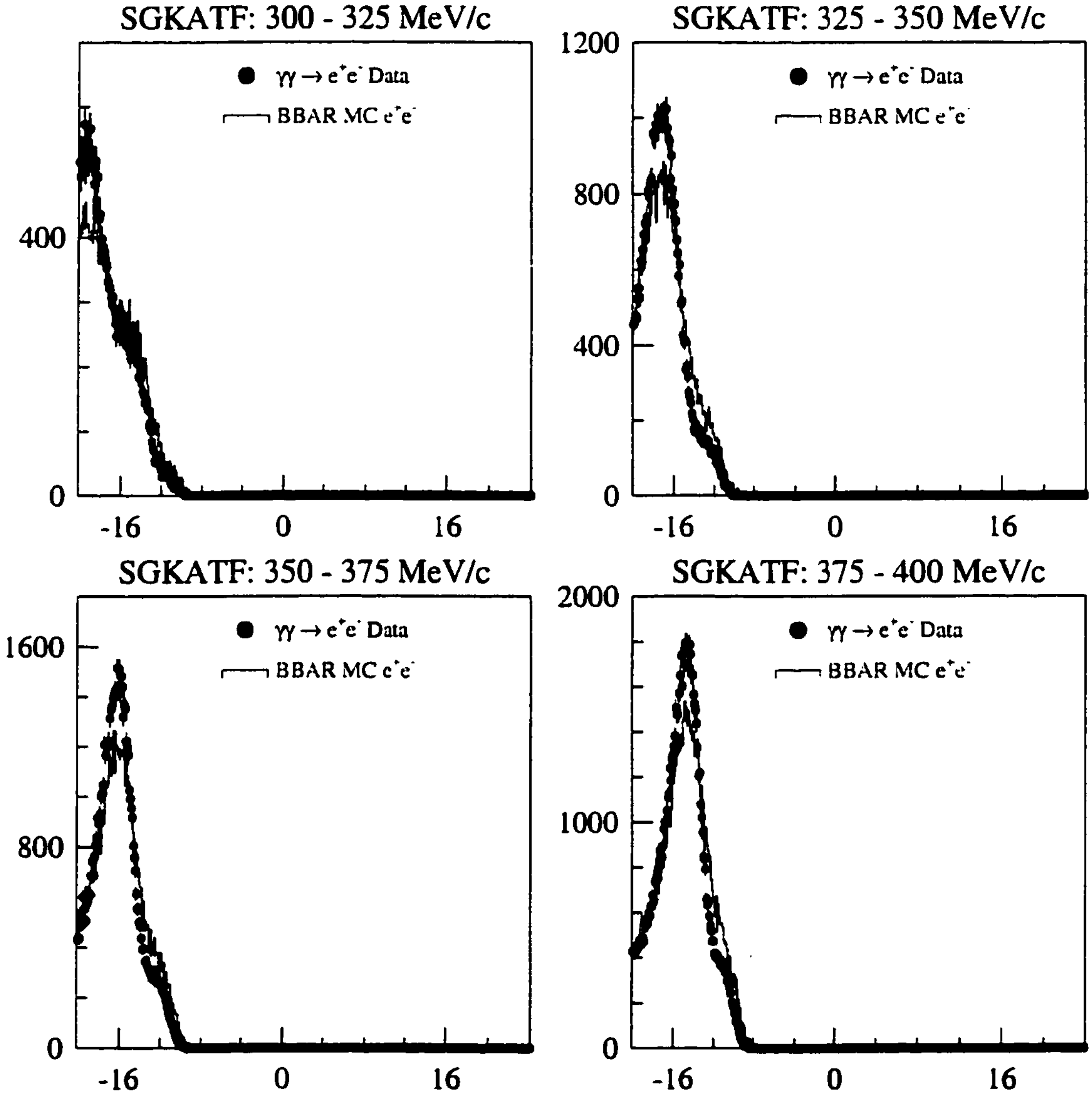

Figure 4.43: Plots of SGKATF from 300 MeV/c to 400 MeV/c, in 25 MeV/c bins for $e^+ e^-$ from radiative Bhabha data and $B\overline{B}$ Monte Carlo, subject to our tracking, event shape *and ToF* cuts. The MC plot is scaled to the area of the data plot.

is the inverse of the corresponding lepton suppression cut for each lepton type. We then use this resulting data-to-MC scale factor from the fit to set the normalization in each momentum bin for identified MC leptons which survive each of our lepton ID cuts. This is achieved by multiplying a momentum spectrum histogram for tagged electrons (muons) from the MC which pass our R2ELEC<3 (DPTHMU<3) cut with the data-to-MC scale factor from the appropriate lepton ID fit. The leptons used for the normalizations of our *ToF* fits are also required to pass our *ToF* cuts.

Figure 4.49 shows the MC fit to data for all tracks above 0.4 GeV/c which pass

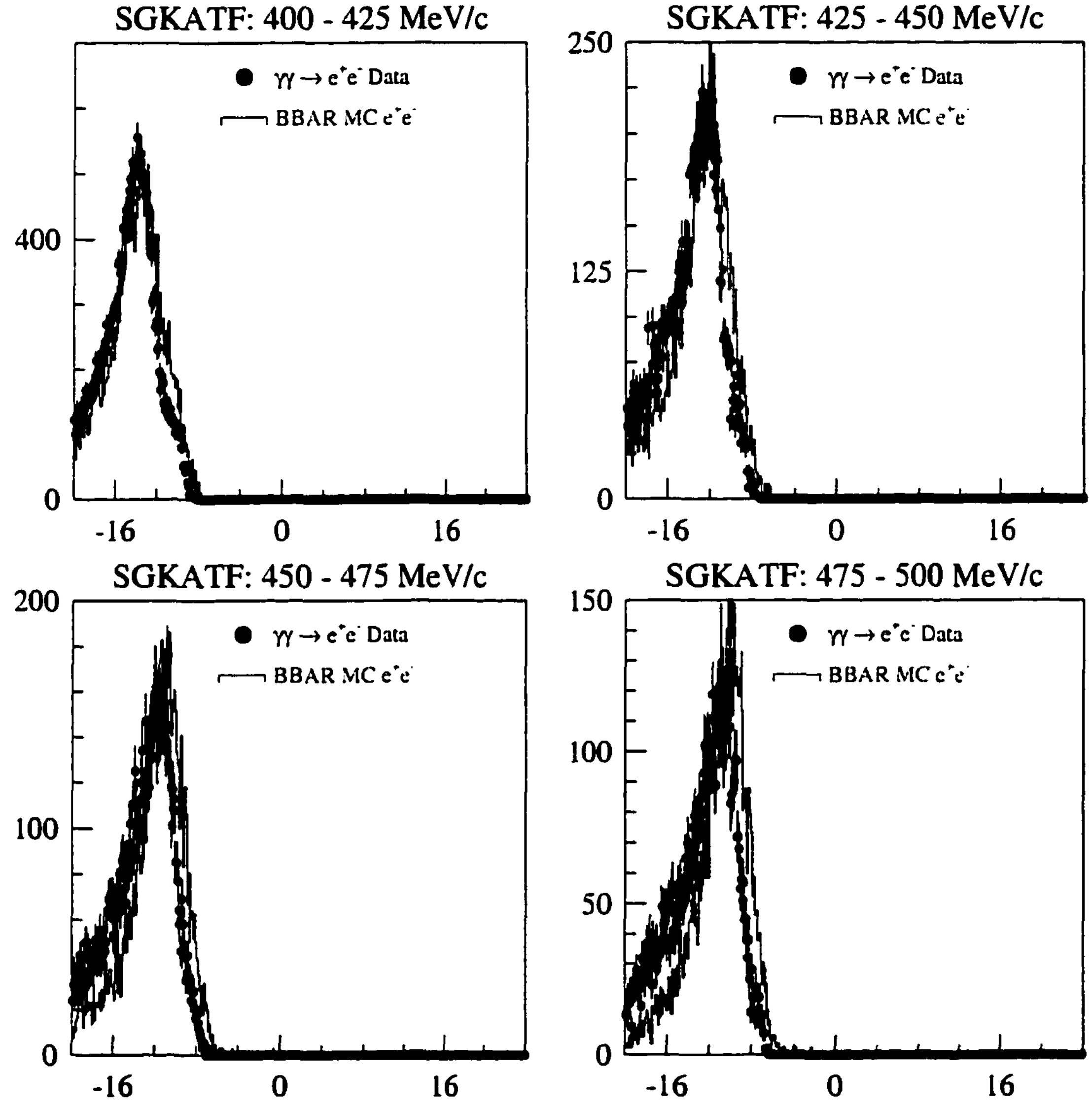

Figure 4.44: Plots of SGKATF from 400 MeV/c to 500 MeV/c, in 25 MeV/c bins for $e^+ e^-$ from radiative Bhabha data and $B\overline{B}$ Monte Carlo, subject to our tracking, event shape *and ToF* cuts. The MC plot is scaled to the area of the data plot.

R2ELEC>3, with and without our *ToF* cuts. Figure 4.50 shows the resulting scaled momentum spectra for electrons which survive our R2ELEC<3 cut, which is used for our dE/dx and *ToF* fits. Figure 4.51 shows the MC fit to data for all tracks above 1.0 GeV/c which pass DPTHMU>3, with and without our *ToF* cuts. Figure 4.52 shows the resulting scaled momentum spectra for muons which survive our DPTHMU<3 cut used for our dE/dx and *ToF* fits. Tables 4.1-4.2 list, for each momentum bin, the expected number of electrons and muons in the data which pass our lepton suppression cuts for each PID device, based on this method.

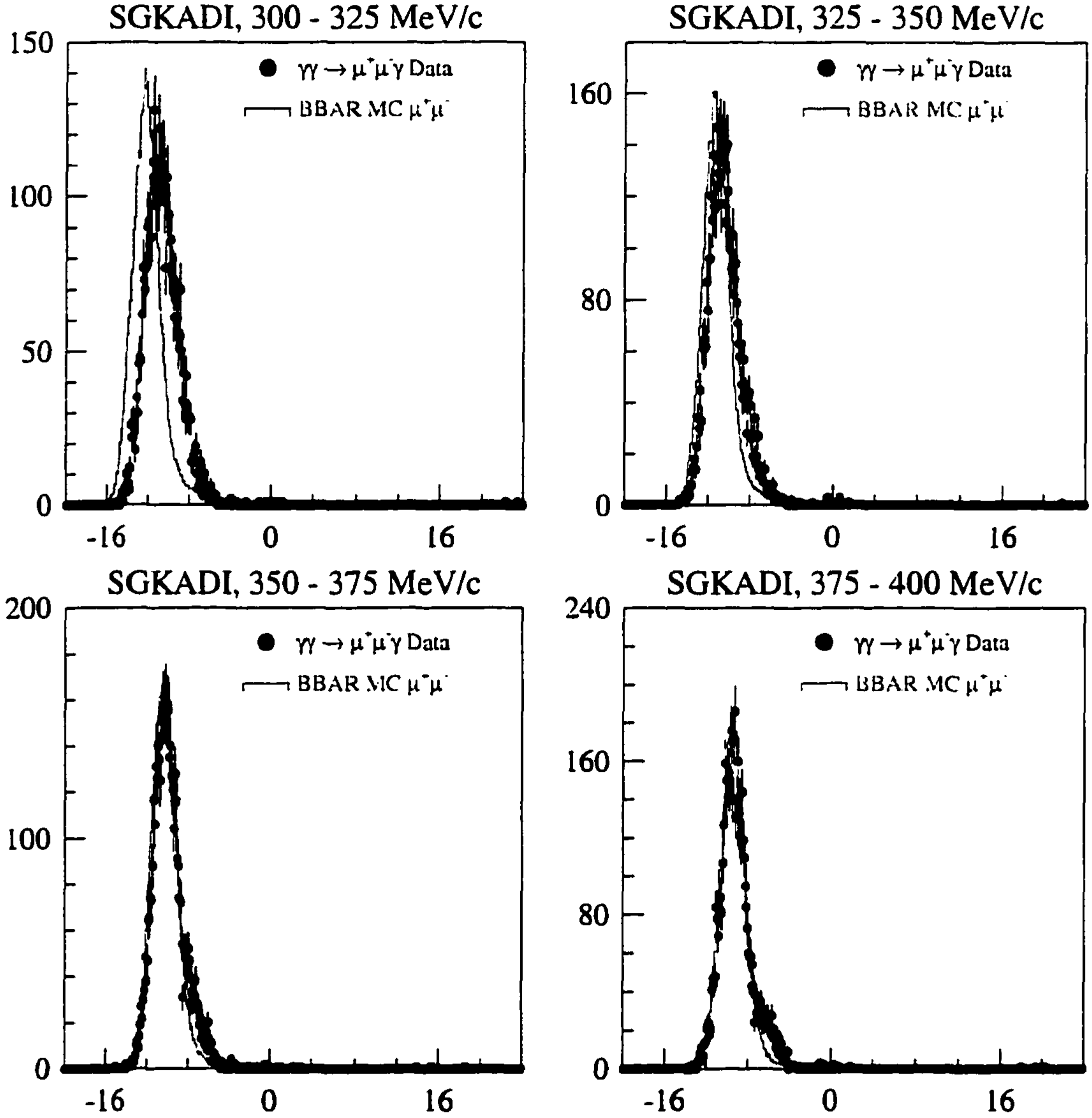

Figure 4.45: Plots of SGKADI from 300 MeV/c to 400 MeV/c, in 25 MeV/c bins for $\mu^+ \mu^-$ from radiative μ-pair data and $B\overline{B}$ Monte Carlo, subject to our tracking and event shape cuts. The MC plot is scaled to the area of the data plot.

We use these expected numbers of leptons to constrain the contribution of the corresponding lepton shape in each fit as follows: In each PID fit, we set the normalization scale factor for the lepton control shape histogram by setting it equal to the expected number of leptons for that momentum bin and PID device divided by the area of the input lepton shape histogram for that momentum bin and PID device. We set the error on this normalization scale factor to be the statistical error on the expected number of leptons and PID device for that momentum bin divided by the area of the lepton shape histogram for that momentum bin and PID device. We

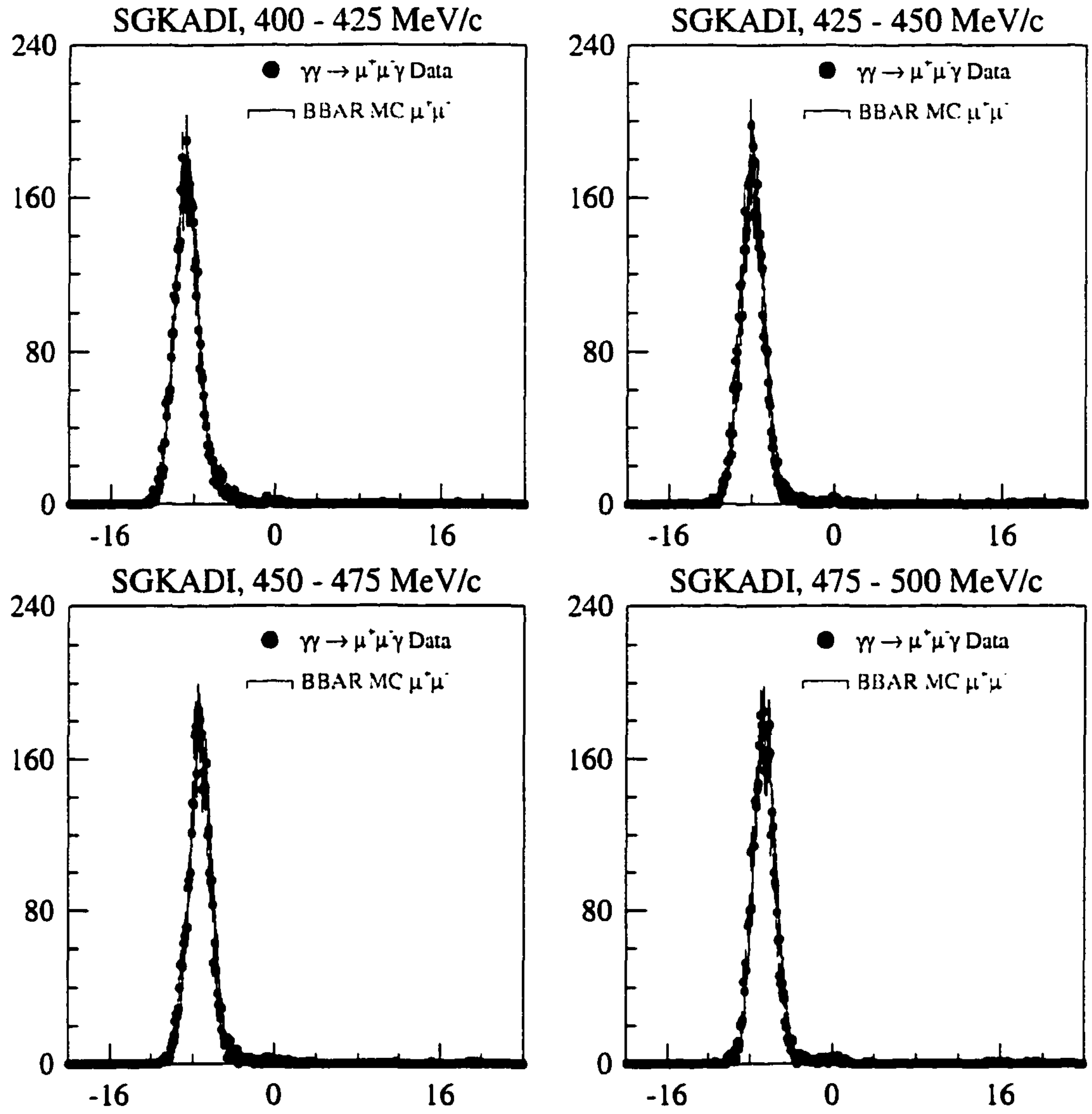

Figure 4.46: Plots of SGKADI from 400 MeV/c to 500 MeV/c, in 25 MeV/c bins for $\mu^+\mu^-$ from radiative μ-pair data and $B\overline{B}$ Monte Carlo, subject to our tracking and event shape cuts.

allow this normalization scale factor to vary within these statistical errors in Mn_Fit when performing each fit.

4.4.2 PID Data Fit Plots

This section discusses the plots which illustrate our PID fits to the data, using the control shapes described earlier. The contribution from the different control shapes

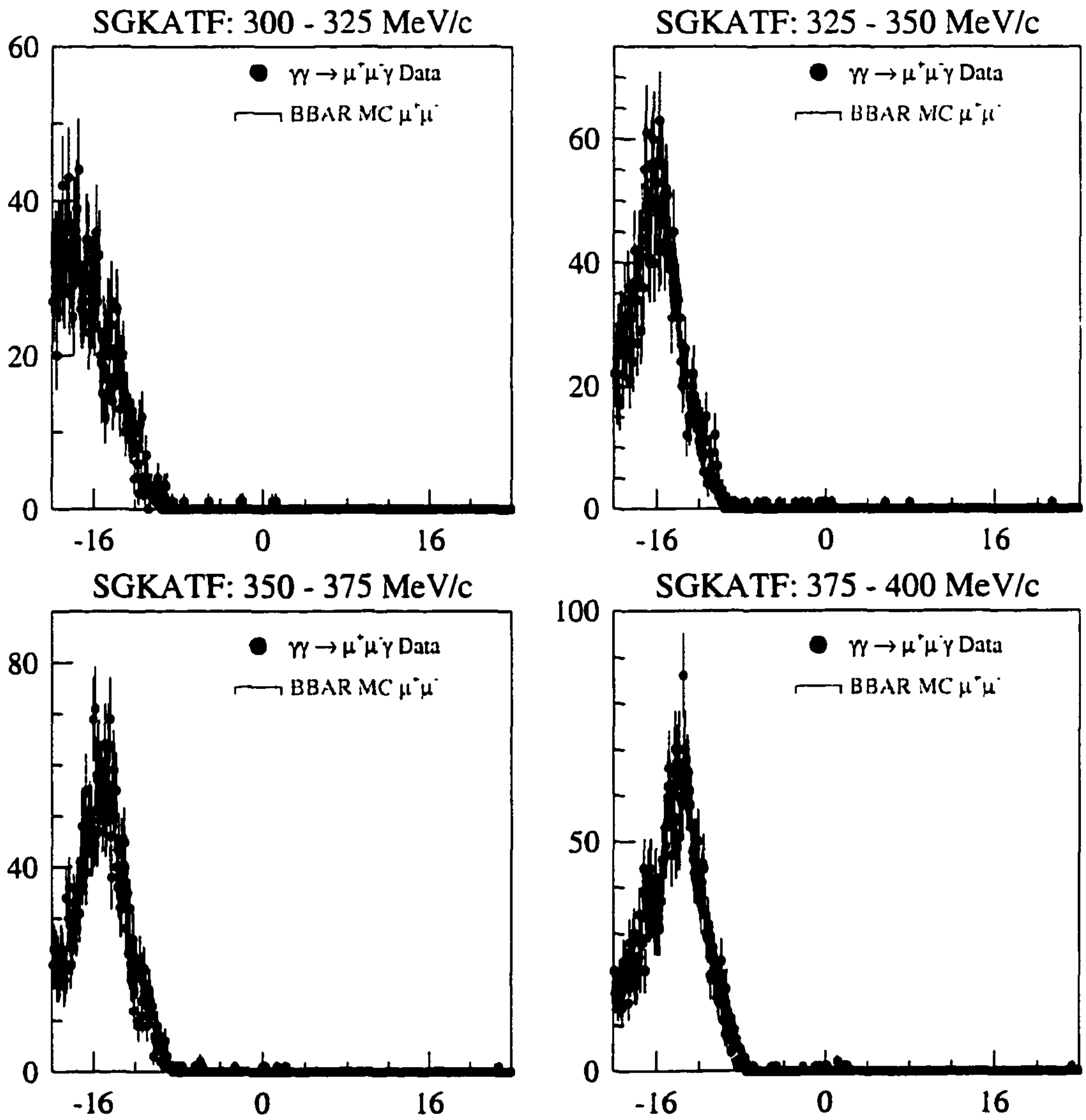

Figure 4.47: Plots of SGKATF from 300 MeV/c to 400 MeV/c, in 25 MeV/c bins for $\mu^+\mu^-$ from radiative μ-pair data and $B\overline{B}$ Monte Carlo, subject to our tracking and event shape cuts. The MC plot is scaled to the area of the data plot.

is highlighted in a different hatching (and color) on each plot. In each fit, the solid squares are the data and the solid black line is the fit to the data. There is reasonable agreement between the two in most areas of each plot, except in those dE/dx plots below 400 MeV/c. where our electrons are slightly overestimated in the fit. For this momentum range only (*i.e.*, below 400 MeV/c for dE/dx), kaon yields were obtained by counting the number of entries within the zero-centered peak.

Figures 4.53–4.58 show dE/dx fit results from 300 MeV/c to 1.2 GeV/c and Figures 4.59–4.64 show fit results for ToF from 300 MeV/c to 1.2 GeV/c.

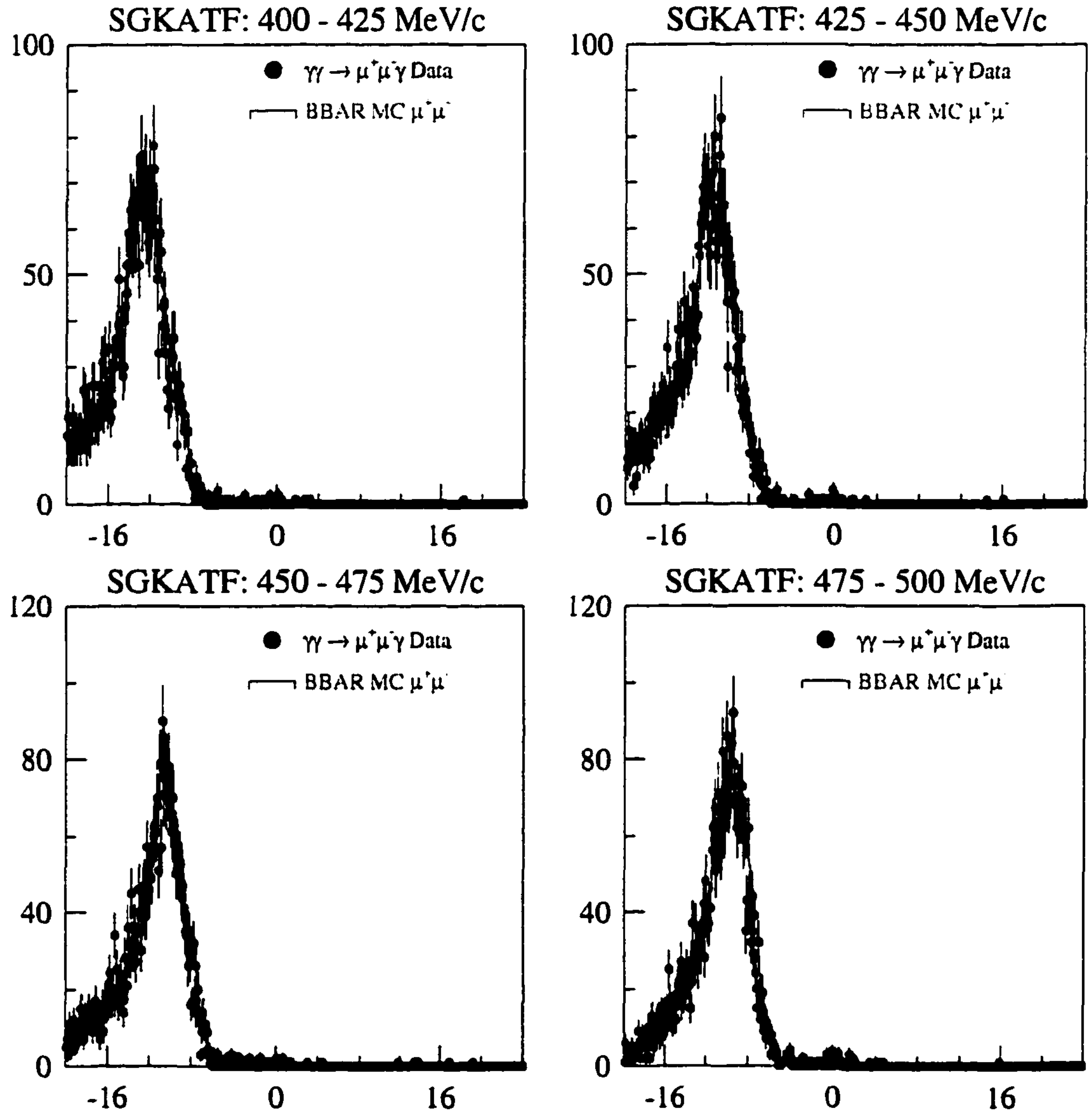

Figure 4.48: Plots of SGKATF from 400 MeV/c to 500 MeV/c, in 25 MeV/c bins for $\mu^+ \mu^-$ from radiative μ-pair data and $B\overline{B}$ Monte Carlo, subject to our tracking and event shape cuts. The MC plot is scaled to the area of the data plot.

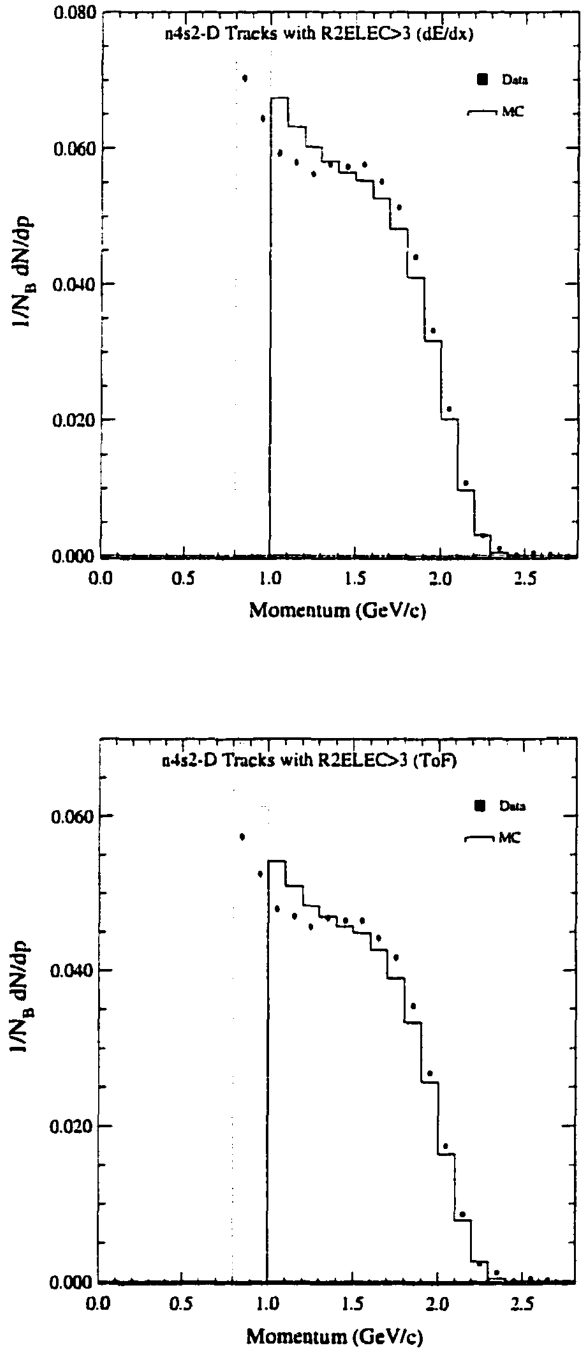

Figure 4.49: Fits of Monte Carlo tracks with R2ELEC>3 to data tracks with R2ELEC>3, subject to our tracking and event shape cuts. These fits are used to obtain the data-to-MC scale factors for electron normalizations. The top plot is used for dE/dx. The bottom plot is also subject to our *ToF* cuts and is thus used for *ToF*.

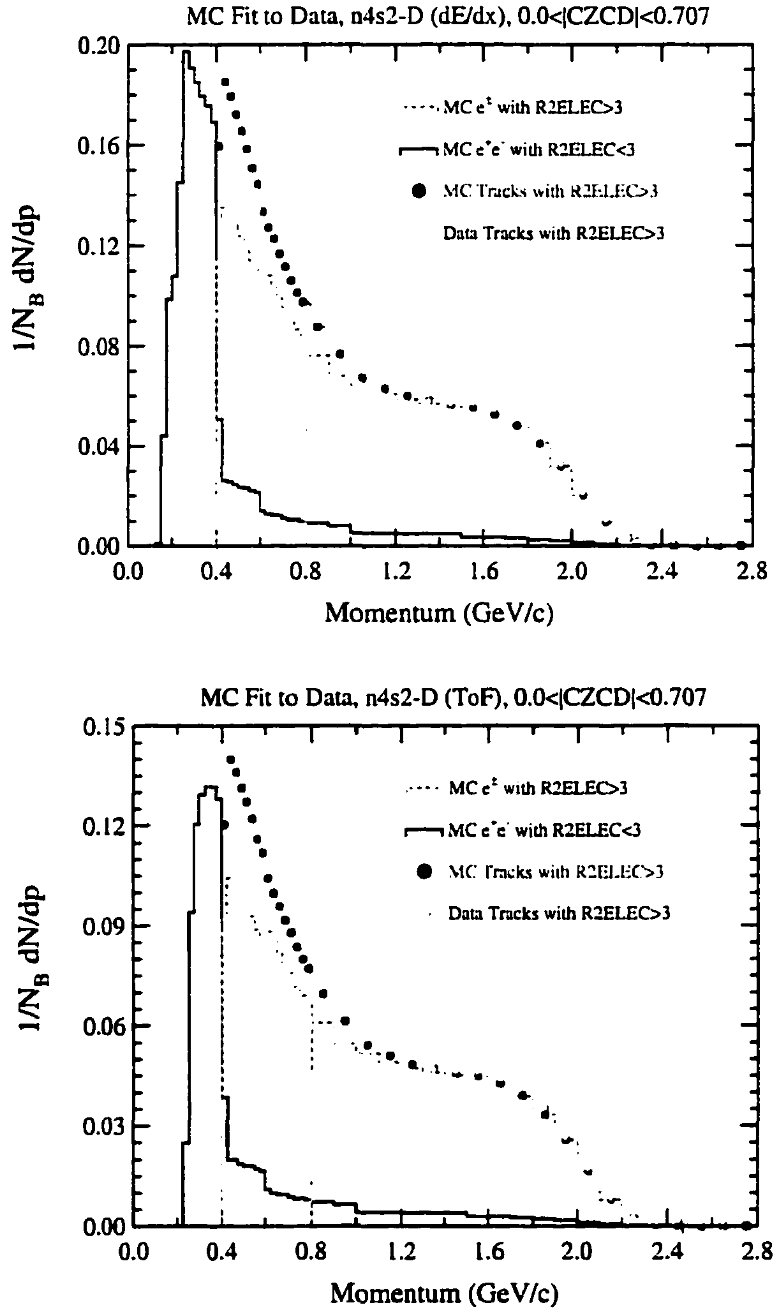

Figure 4.50: Scaled momentum spectra for Monte Carlo electrons, based on the scale factor obtained from R2ELEC>3 tracks fit to data. The solid line in the top plot shows the expected number of electrons in each momentum bin for our dE/dx fits and the bottom shows the same for ToF. These results are scaled by momentum bin width and the number of $B\overline{B}$ pairs.

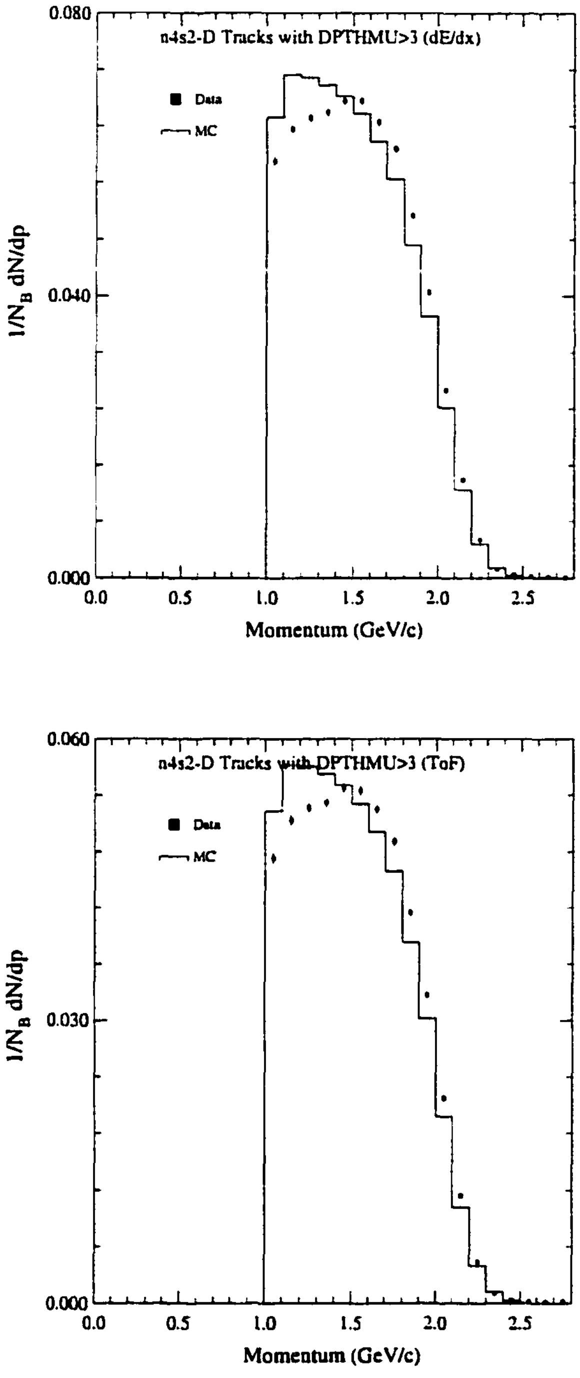

Figure 4.51: Fits of Monte Carlo tracks with DPTHMU>3 to data tracks with DPTHMU>3, subject to our tracking and event shape cuts. These fits are used to obtain the data-to-MC scale factors for muon normalizations. The top plot is used for dE/dx. The bottom plot is also subject to our ToF cuts and is thus used for ToF.

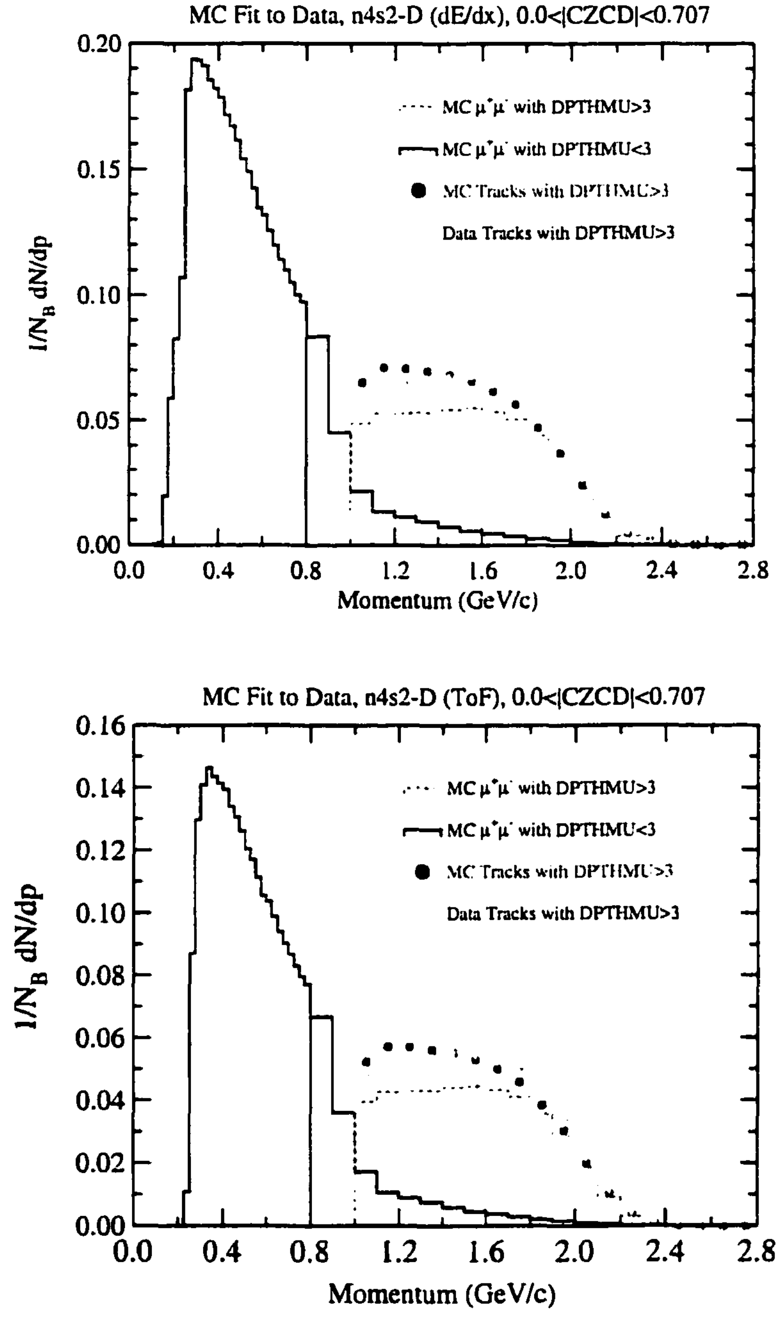

Figure 4.52: Scaled momentum spectra for Monte Carlo muons, based on the scale factor obtained from `DPTHMU`>3 MC tracks fit to data. The solid line in the top plot shows the expected number of muons in each momentum bin for our dE/dx fits and the bottom shows the same for ToF. These results are scaled by momentum bin width and the number of $B\overline{B}$ pairs.

Table 4.1: Expected numbers of electrons and muons which pass our lepton suppression cuts for each PID device, in 25 MeV/c momentum bins from 75–800 MeV/c.

Momentum (MeV/c)	N_e (dE/dx)	N_e (ToF)	N_μ (dE/dx)	N_μ (ToF)
75–100	8.2 ± 2.9	0.0 ± 0.0	3.0 ± 1.7	0.0 ± 0.0
100–125	43.9 ± 6.7	0.0 ± 0.0	36.1 ± 6.0	0.0 ± 0.0
125–150	335.1 ± 18.5	0.0 ± 0.0	292.8 ± 17.1	0.0 ± 0.0
150–175	14489.8 ± 121.7	0.0 ± 0.0	6457.3 ± 80.5	0.0 ± 0.0
175–200	32434.3 ± 182.0	0.0 ± 0.0	19415.1 ± 139.5	0.0 ± 0.0
200–225	35429.1 ± 190.3	0.0 ± 0.0	27180.2 ± 165.1	0.0 ± 0.0
225–250	47590.3 ± 220.5	8182.3 ± 90.4	35188.9 ± 187.9	3552.9 ± 58.7
250–275	64823.6 ± 257.4	30897.3 ± 175.7	59711.6 ± 244.7	28620.3 ± 166.7
275–300	62705.4 ± 253.1	39545.2 ± 198.8	63675.8 ± 252.7	42660.2 ± 203.5
300–325	60764.0 ± 249.2	42500.0 ± 206.0	63493.3 ± 252.3	46302.4 ± 212.0
325–350	58975.9 ± 245.5	43275.2 ± 207.9	62787.3 ± 250.9	48105.5 ± 216.1
350–375	57724.3 ± 242.9	43247.2 ± 207.8	60967.1 ± 247.3	47184.5 ± 214.0
375–400	55618.4 ± 238.4	42052.5 ± 205.0	59816.8 ± 244.9	46427.5 ± 212.3
400–425	16649.9 ± 130.4	12629.6 ± 112.3	58688.6 ± 242.6	45810.3 ± 210.9
425–450	8522.6 ± 93.3	6499.1 ± 80.6	56371.1 ± 237.8	43998.4 ± 206.6
450–475	8367.3 ± 92.5	6538.1 ± 80.8	54923.0 ± 234.7	42932.9 ± 204.1
475–500	8003.6 ± 90.4	6155.5 ± 78.4	53063.7 ± 230.7	41447.1 ± 200.6
500–525	7676.6 ± 88.6	5964.7 ± 77.2	50593.7 ± 225.3	39556.6 ± 195.9
525–550	7583.6 ± 88.0	5917.7 ± 76.9	48977.1 ± 221.6	38451.2 ± 193.2
550–575	7228.0 ± 85.9	5651.0 ± 75.1	46784.8 ± 216.6	36621.9 ± 188.5
575–600	6973.6 ± 84.4	5466.2 ± 73.9	44289.8 ± 210.8	34707.1 ± 183.5
600–625	4556.1 ± 68.2	3612.2 ± 60.1	43310.0 ± 208.4	34071.5 ± 181.8
625–650	4133.1 ± 65.0	3249.6 ± 57.0	41272.2 ± 203.4	32482.8 ± 177.5
650–675	3967.6 ± 63.7	3148.7 ± 56.1	39375.8 ± 198.7	30943.6 ± 173.3
675–700	3960.4 ± 63.6	3121.7 ± 55.8	37523.5 ± 194.0	29671.3 ± 169.7
700–725	3617.1 ± 60.8	2877.0 ± 53.6	36109.5 ± 190.3	28525.2 ± 166.4
725–750	3430.1 ± 59.2	2679.2 ± 51.7	34516.0 ± 186.0	27275.2 ± 162.7
750–775	3437.3 ± 59.3	2726.1 ± 52.2	32982.7 ± 181.9	26155.3 ± 159.3
775–800	3222.7 ± 57.4	2593.3 ± 50.9	31984.8 ± 179.1	25350.8 ± 156.9

Table 4.2: Expected numbers of electrons and muons which pass our lepton suppression cuts for each PID device, in 0.1 GeV/c momentum bins from 0.8–2.8 GeV/c.

Momentum (GeV/c)	N_e (dE/dx)	N_e (ToF)	N_μ (dE/dx)	N_μ (ToF)
0.8–0.9	11895.5 ± 110.2	9530.9 ± 97.6	109883.0 ± 332.0	87640.7 ± 291.6
0.9–1.0	10540.6 ± 103.8	8484.0 ± 92.1	59395.7 ± 244.1	47338.8 ± 214.3
1.0–1.1	6856.1 ± 83.7	5512.2 ± 74.2	28154.9 ± 168.0	22470.4 ± 147.7
1.1–1.2	6517.9 ± 81.6	5274.4 ± 72.6	17458.6 ± 132.3	13829.3 ± 115.8
1.2–1.3	6389.2 ± 80.8	5131.6 ± 71.6	14715.8 ± 121.5	11747.6 ± 106.8
1.3–1.4	6289.0 ± 80.2	5118.6 ± 71.5	12338.0 ± 111.2	9831.9 ± 97.7
1.4–1.5	6220.6 ± 79.7	5020.7 ± 70.8	9603.3 ± 98.1	7626.0 ± 86.0
1.5–1.6	4530.6 ± 68.0	3682.1 ± 60.6	7476.2 ± 86.6	5975.2 ± 76.1
1.6–1.7	4503.0 ± 67.8	3672.1 ± 60.6	6116.4 ± 78.3	4871.8 ± 68.8
1.7–1.8	4141.3 ± 65.0	3349.5 ± 57.8	4729.4 ± 68.9	3765.4 ± 60.5
1.8–1.9	3433.2 ± 59.2	2794.0 ± 52.8	3385.6 ± 58.3	2712.5 ± 51.3
1.9–2.0	2589.2 ± 51.4	2124.8 ± 46.1	2345.7 ± 48.5	1835.2 ± 42.2
2.0–2.1	1697.2 ± 41.6	1402.5 ± 37.4	1351.8 ± 36.8	1087.9 ± 32.5
2.1–2.2	833.8 ± 29.2	671.3 ± 25.9	680.9 ± 26.1	533.8 ± 22.8
2.2–2.3	281.0 ± 16.9	242.7 ± 15.6	255.7 ± 16.0	181.5 ± 13.3
2.3–2.4	40.9 ± 6.5	34.0 ± 5.8	77.2 ± 8.8	31.1 ± 5.5
2.4–2.5	9.2 ± 3.1	7.0 ± 2.6	32.1 ± 5.7	12.6 ± 3.5
2.5–2.6	3.1 ± 1.8	1.0 ± 1.0	32.1 ± 5.7	9.7 ± 3.1
2.6–2.7	4.1 ± 2.0	2.0 ± 1.4	24.1 ± 4.9	4.9 ± 2.2
2.7–2.8	0.0 ± 0.0	0.0 ± 0.0	28.1 ± 5.3	7.8 ± 2.7

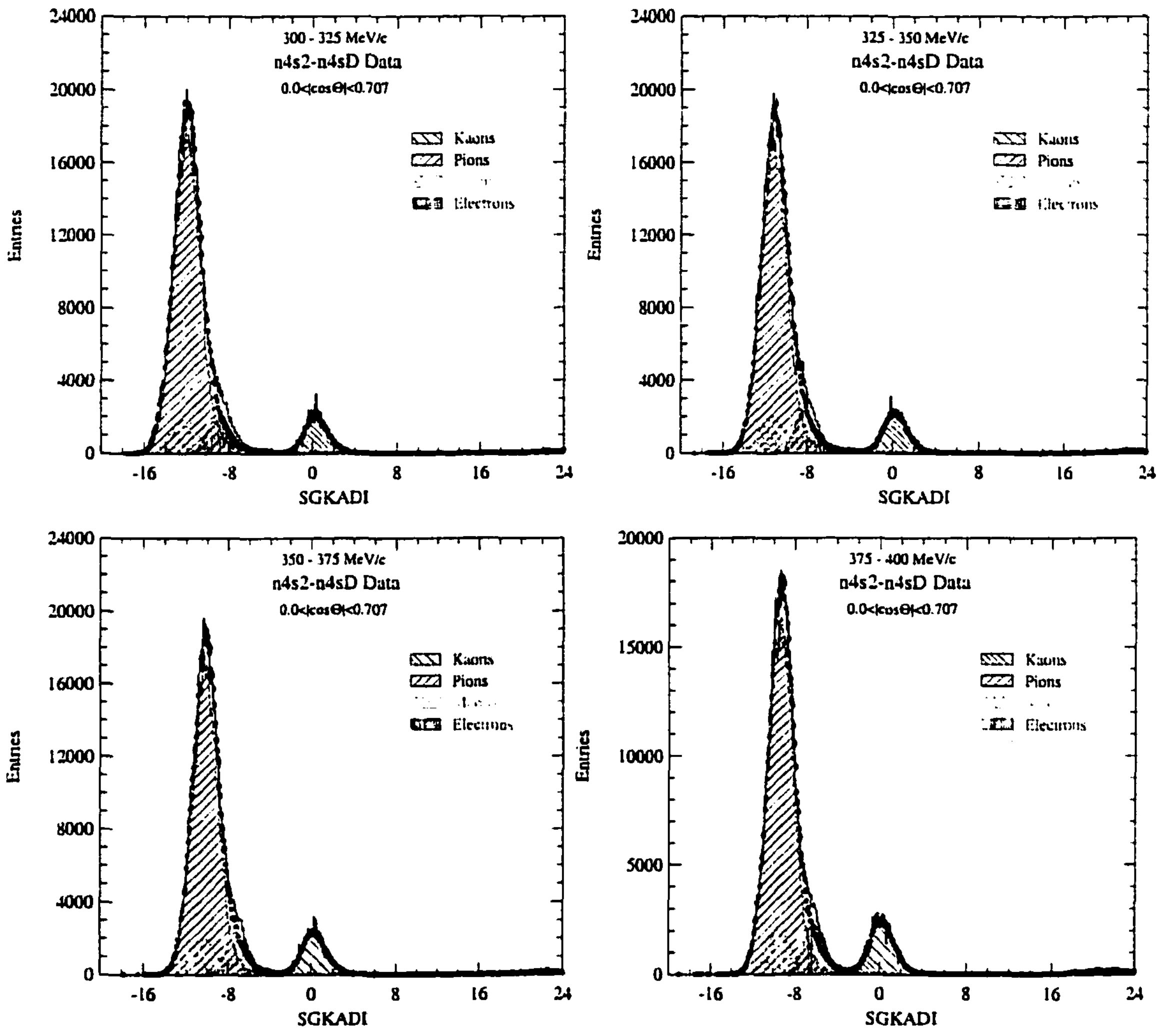

Figure 4.53: Fits to dE/dx data for 300–400 MeV/c in 25 MeV/c momentum bins, using control shapes described in the text as fitting functions. The solid line in each plot is the fit to the data (solid squares), with different hatchings representing the different control shape contributions. For this momentum range only, kaon yields were obtained by counting the number of entries within the zero-centered peak.

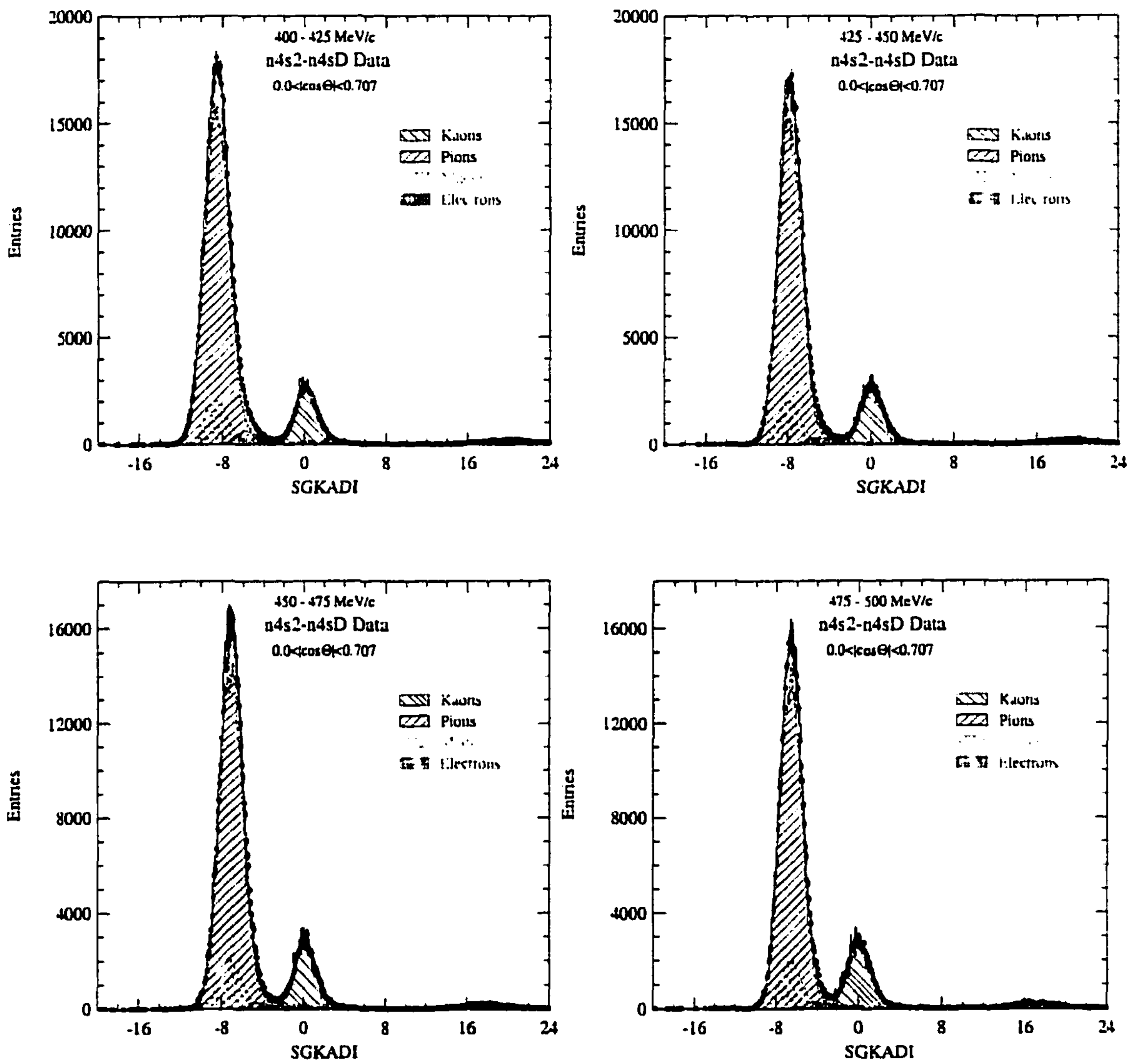

Figure 4.54: Fits to dE/dx data for 400–500 GeV/c in 25 MeV/c momentum bins, using control shapes described in the text as fitting functions. The solid line in each plot is the fit to the data (solid squares), with different hatchings representing the different control shape contributions.

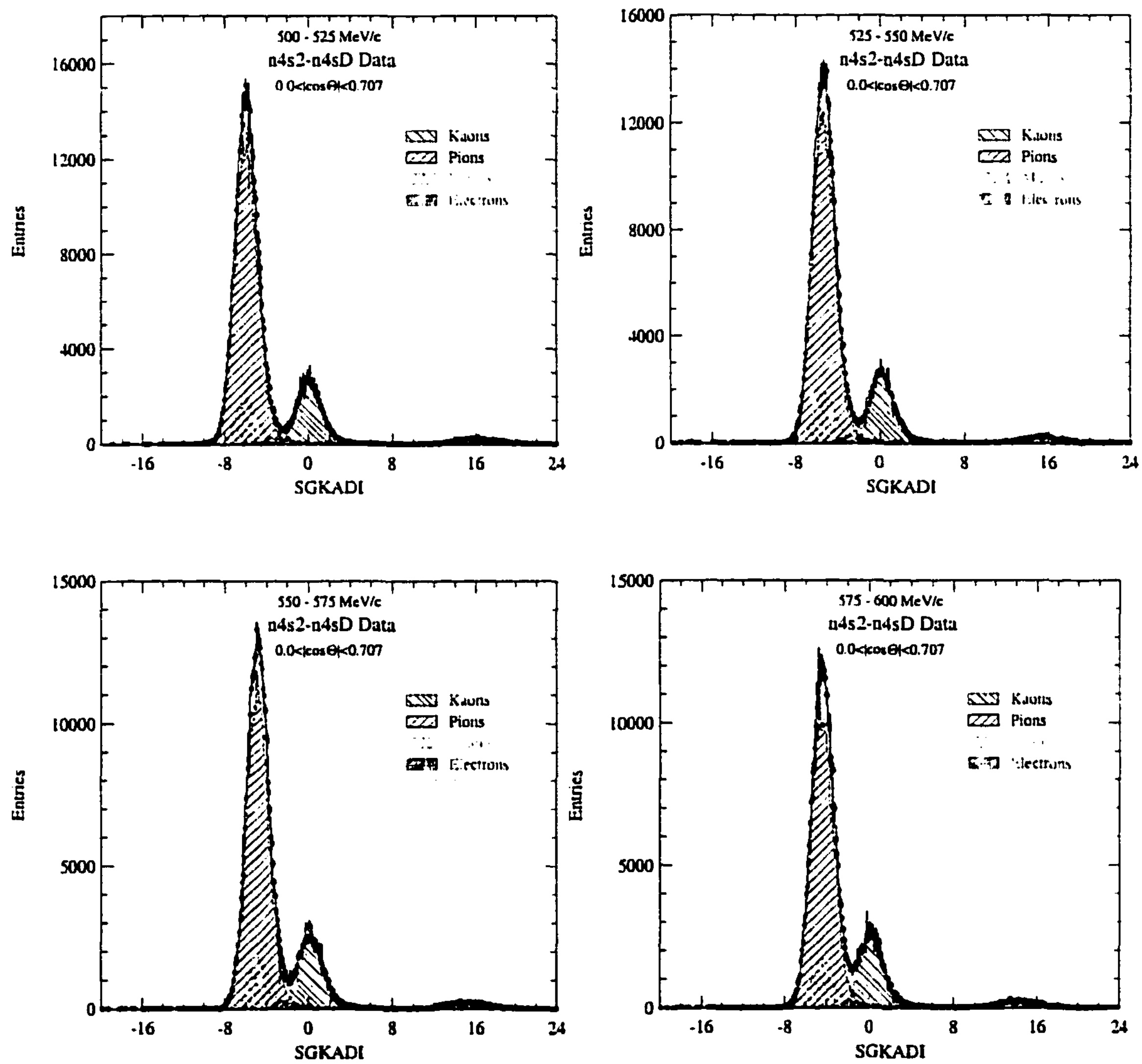

Figure 4.55: Fits to dE/dx data for 500–600 MeV/c in 25 MeV/c momentum bins, using control shapes described in the text as fitting functions. The solid line in each plot is the fit to the data (solid squares), with different hatchings representing the different control shape contributions.

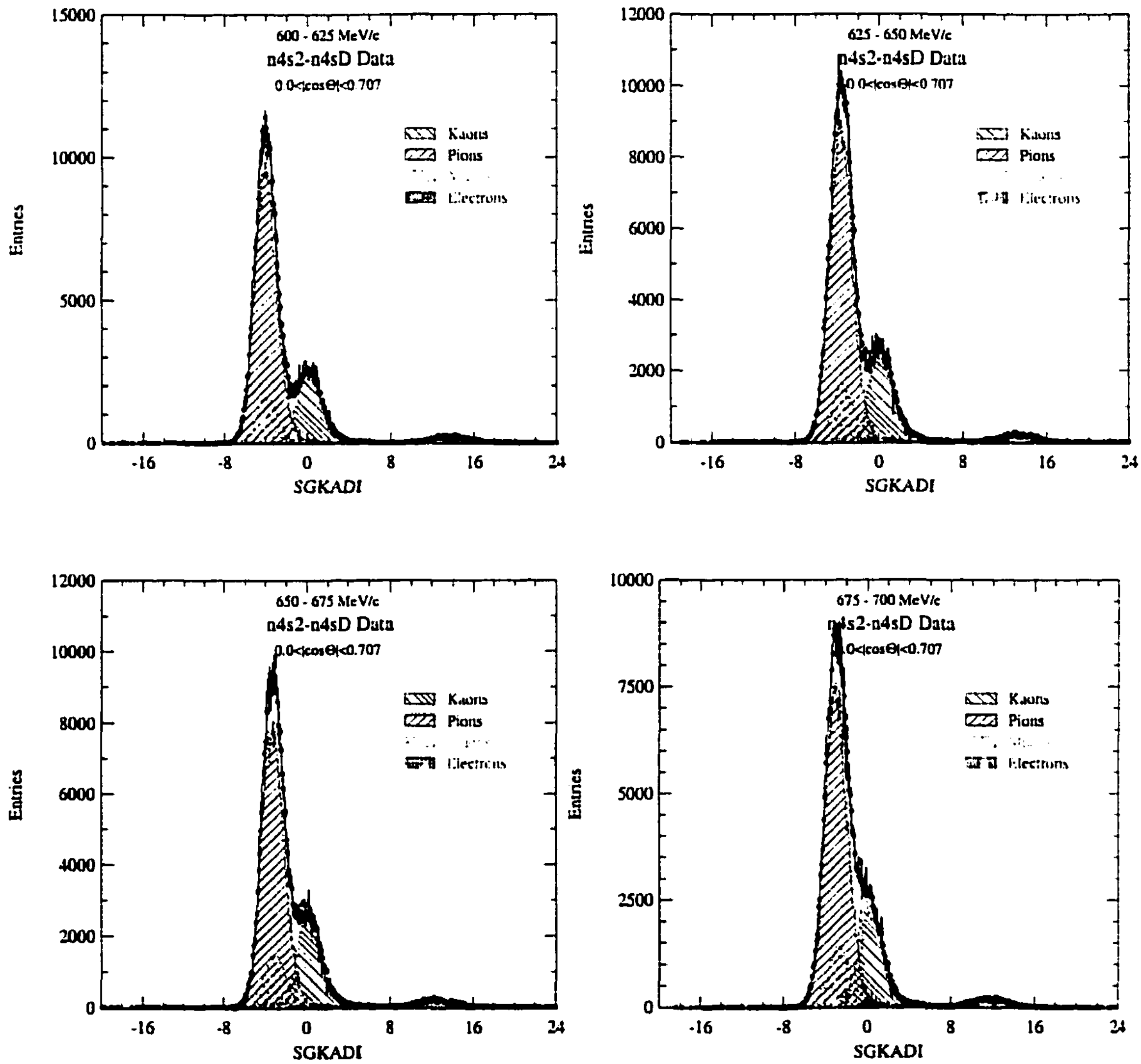

Figure 4.56: Fits to dE/dx data for 600–700 MeV/c in 25 MeV/c momentum bins, using control shapes described in the text as fitting functions. The solid line in each plot is the fit to the data (solid squares), with different hatchings representing the different control shape contributions.

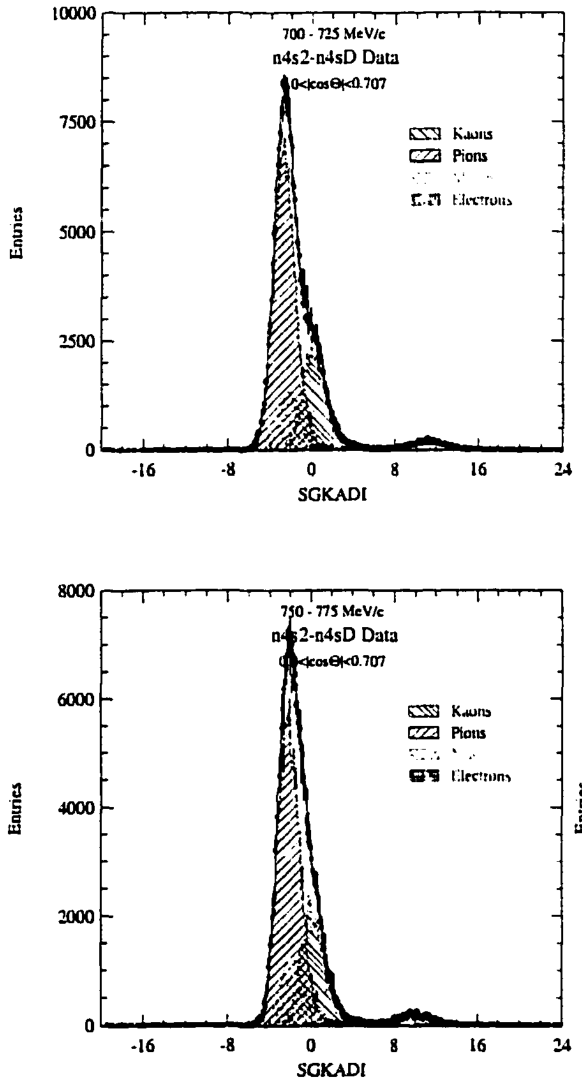

Figure 4.57: Fits to dE/dx data for 700–800 MeV/c in 25 MeV/c momentum bins, using control shapes described in the text as fitting functions. The solid line in each plot is the fit to the data (solid squares), with different hatchings representing the different control shape contributions.

4.4.3 Extraction of Raw Kaon Yields

For each momentum bin (above 400 MeV/c for dE/dx), we extract the raw kaon yield from each fit for each PID device as follows: In each momentum region, we book separate unbinned histograms for the extracted raw kaon yields for each PID

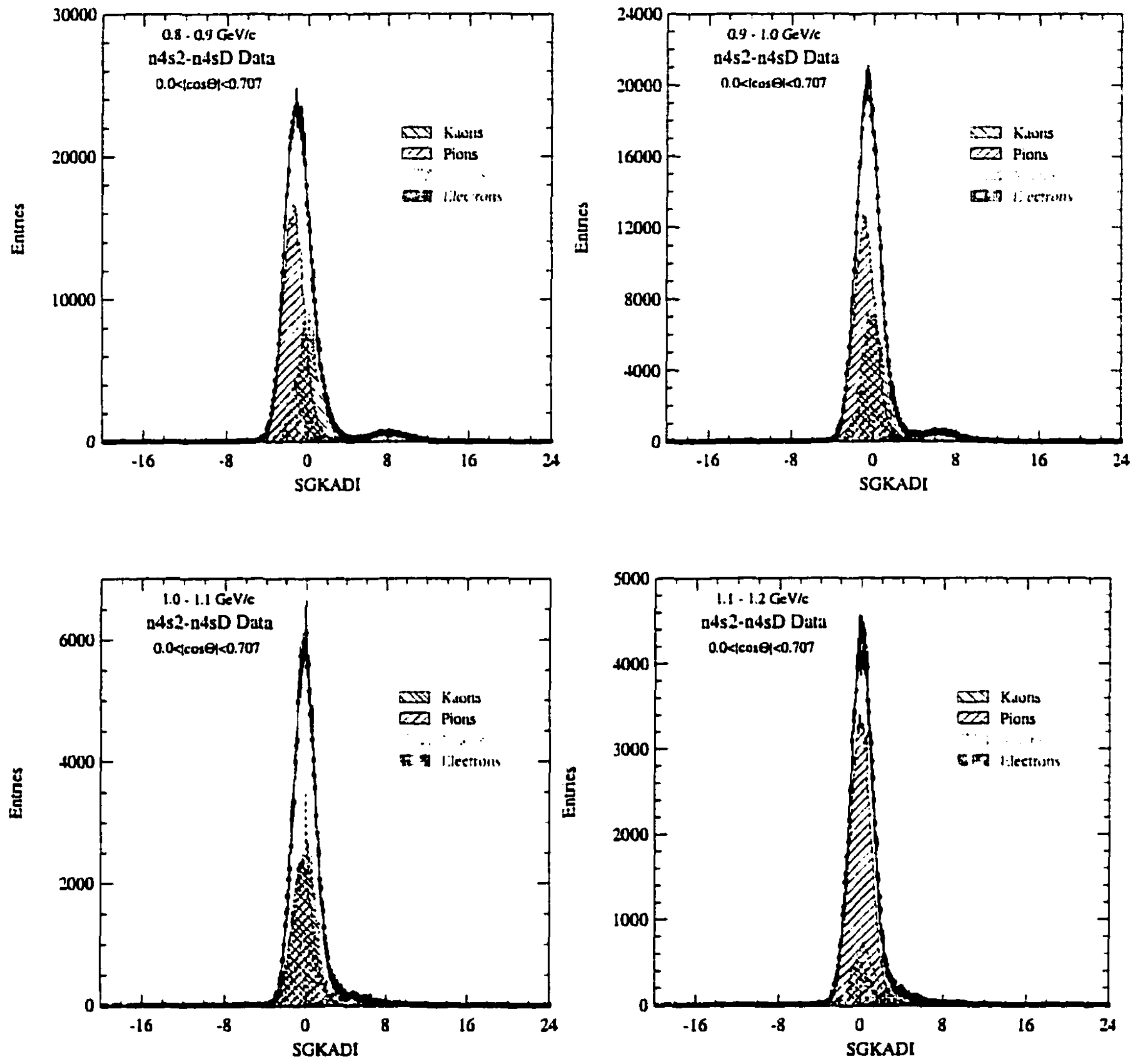

Figure 4.58: Fits to dE/dx data for 0.8–1.2 GeV/c in 0.1 GeV/c momentum bins, using control shapes described in the text as fitting functions. The solid line in each plot is the fit to the data (solid squares), with different hatchings representing the different control shape contributions.

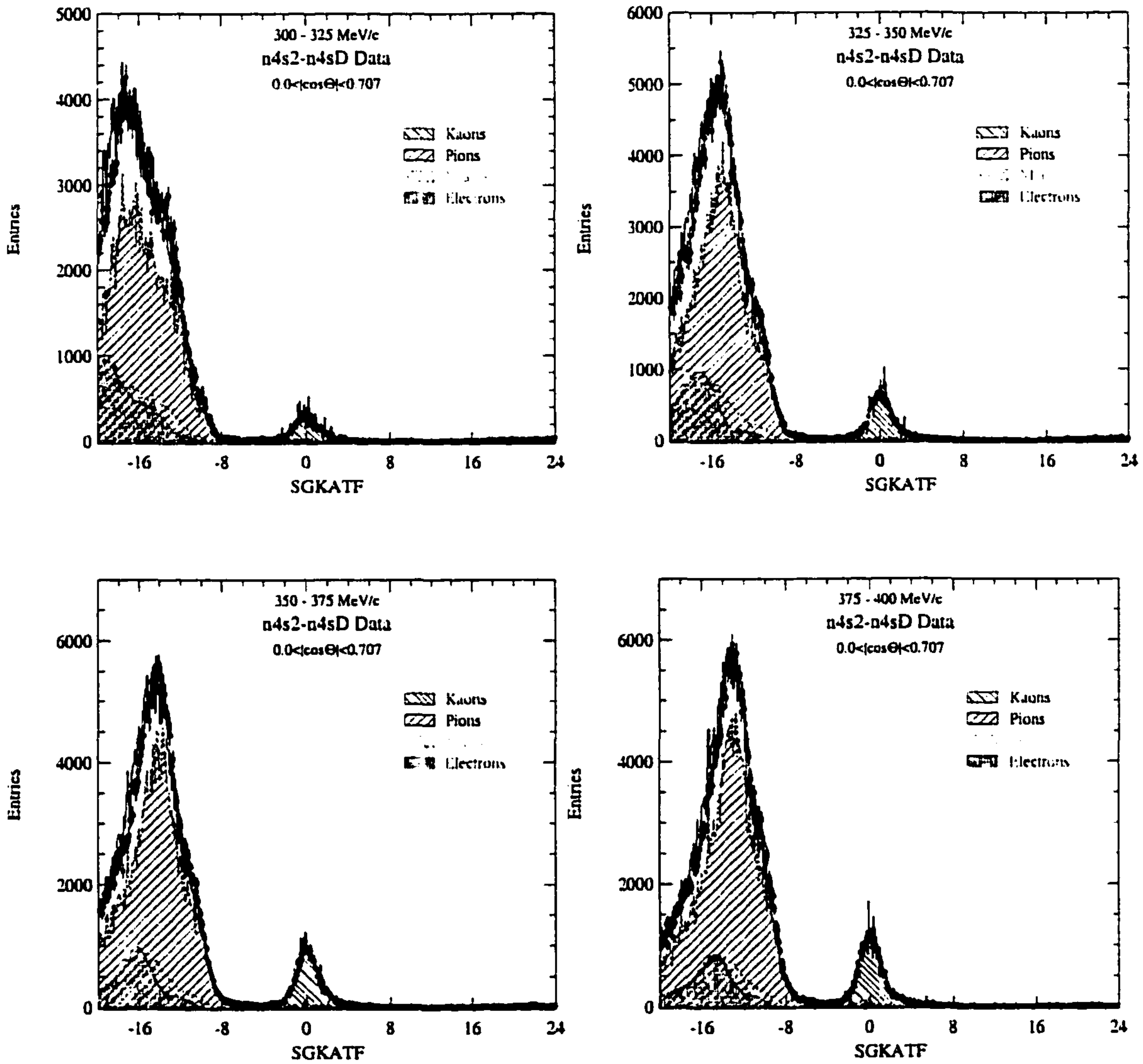

Figure 4.59: Fits to *ToF* data for 300–400 MeV/c in 25 MeV/c momentum bins, using control shapes described in the text as fitting functions. The solid line in each plot is the fit to the data (solid squares), with different hatchings representing the different control shape contributions.

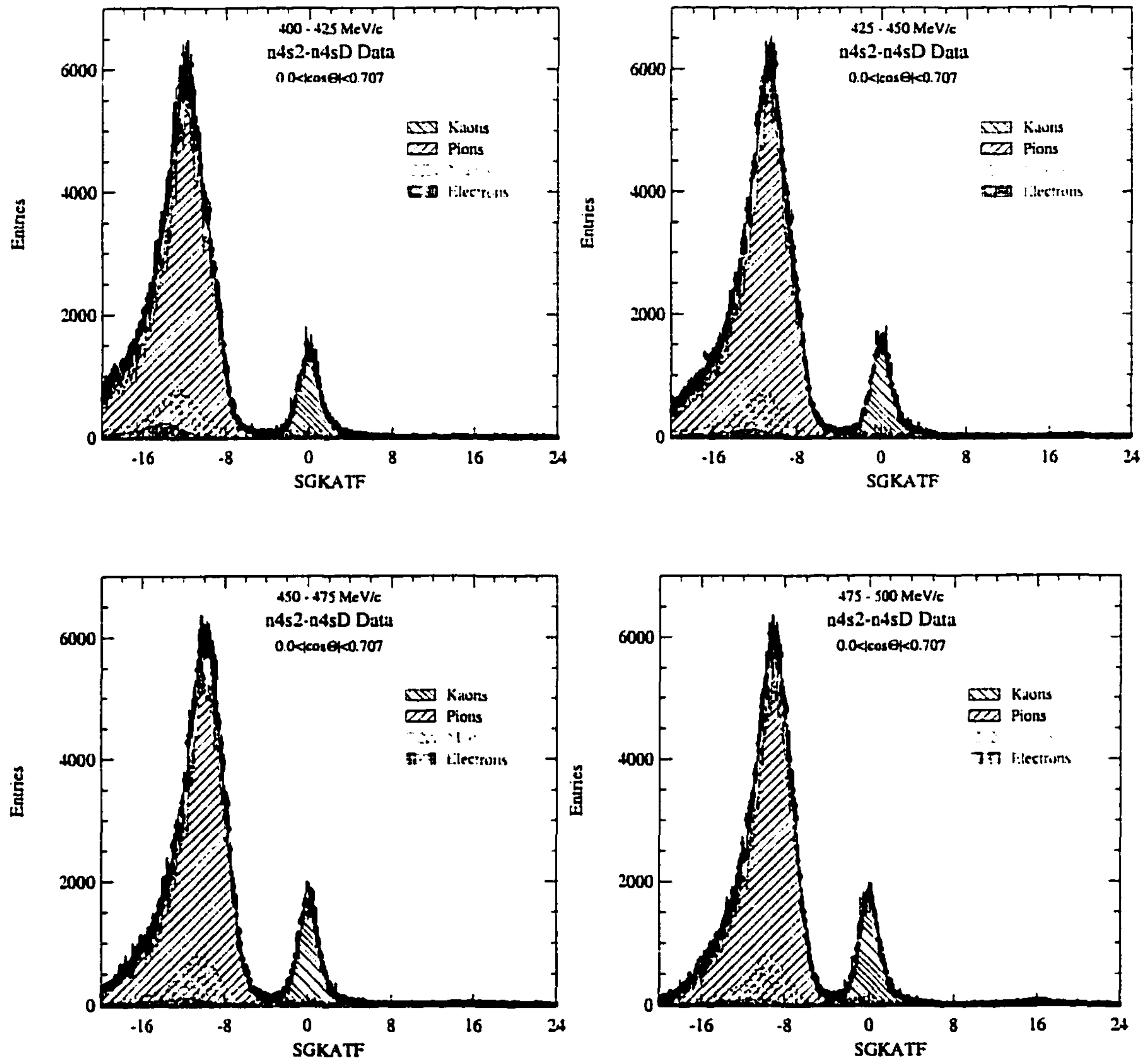

Figure 4.60: Fits to *ToF* data for 400–500 MeV/c in 25 MeV/c momentum bins, using control shapes described in the text as fitting functions. The solid line in each plot is the fit to the data (solid squares), with different hatchings representing the different control shape contributions.

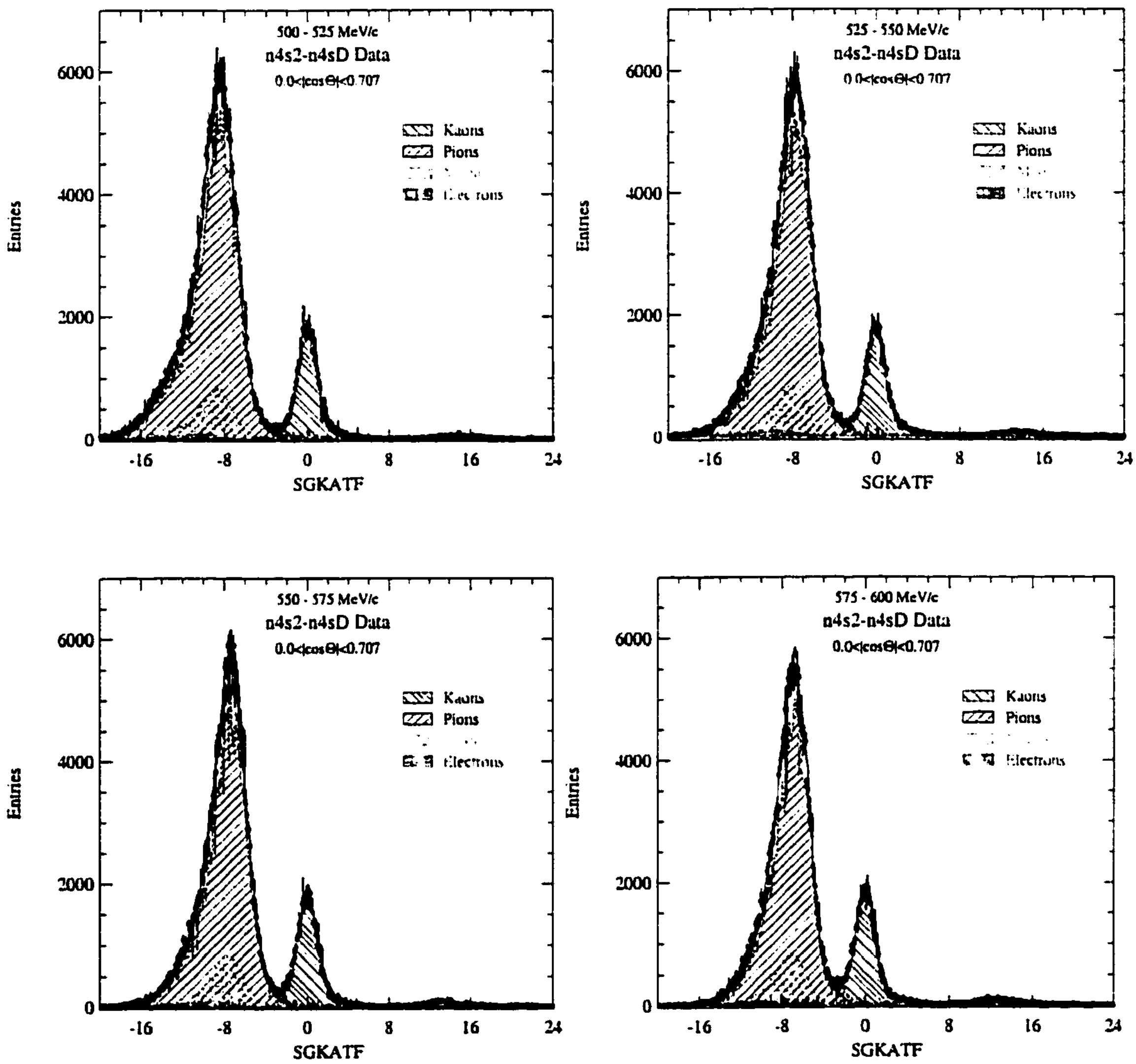

Figure 4.61: Fits to *ToF* data for 500–600 MeV/c in 25 MeV/c momentum bins, using control shapes described in the text as fitting functions. The solid line in each plot is the fit to the data (solid squares), with different hatchings representing the different control shape contributions.

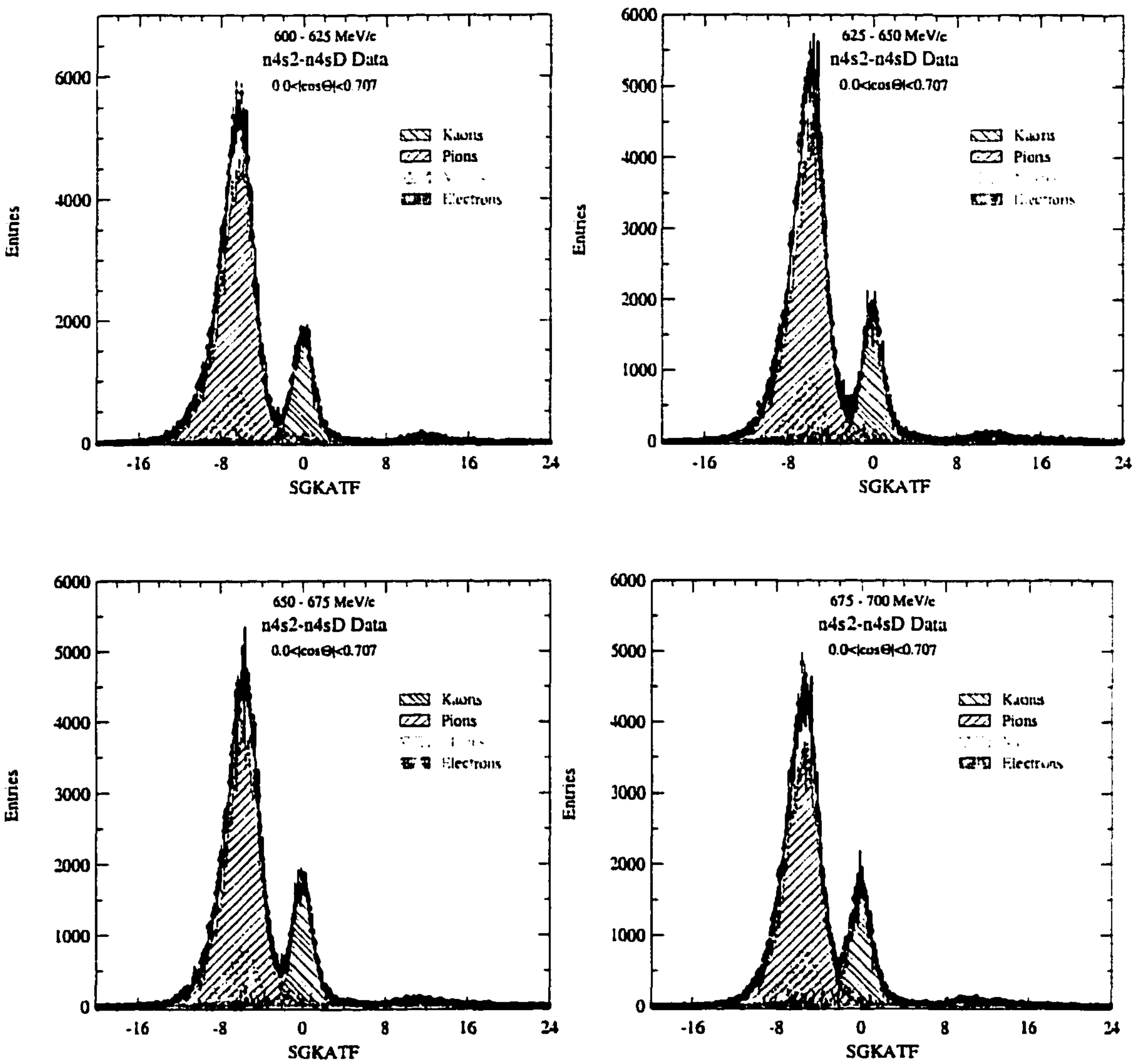

Figure 4.62: Fits to *ToF* data for 600–700 MeV/c in 25 MeV/c momentum bins, using control shapes described in the text as fitting functions. The solid line in each plot is the fit to the data (solid squares), with different hatchings representing the different control shape contributions.

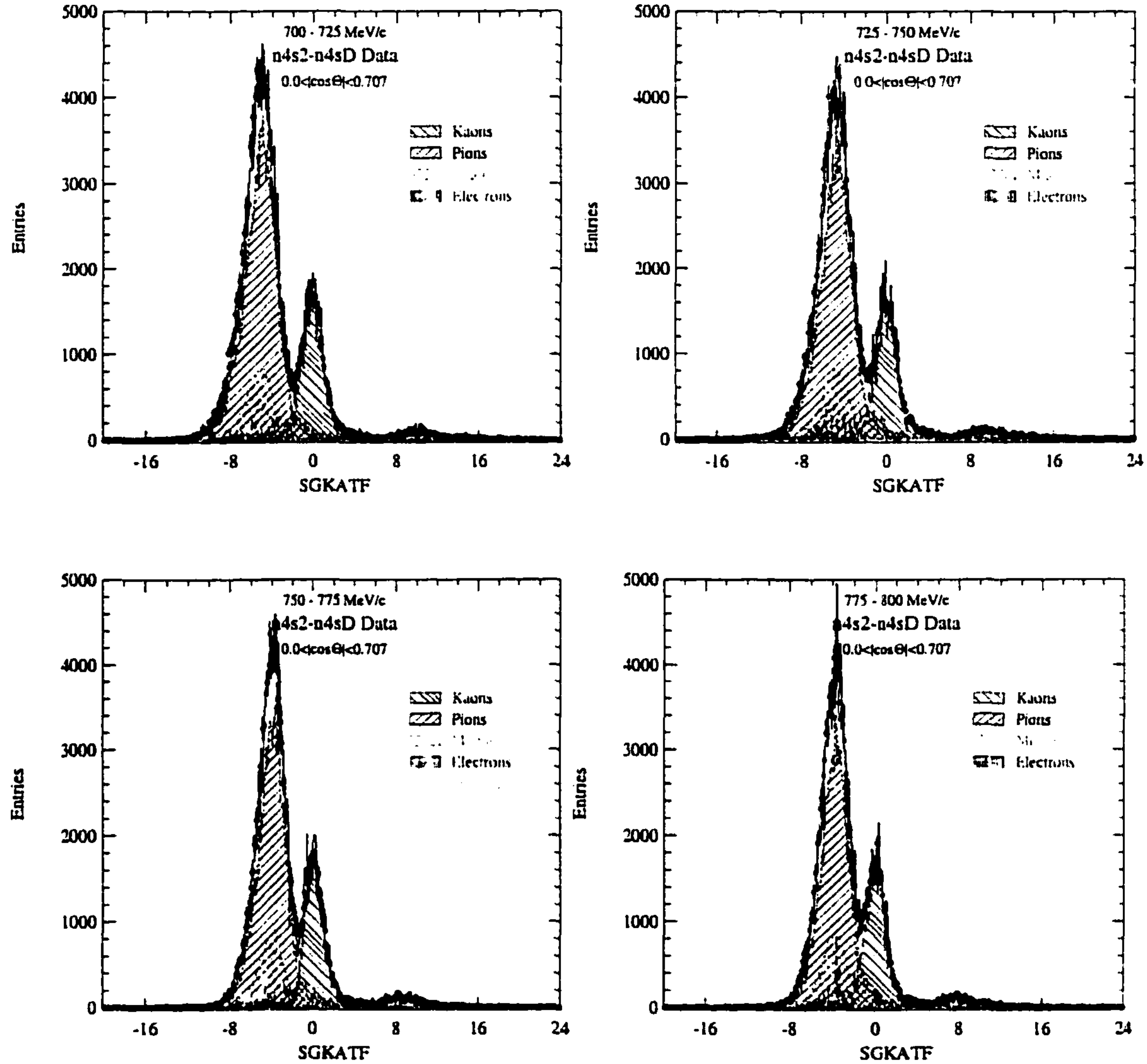

Figure 4.63: Fits to *ToF* data for 700–800 MeV/c in 25 MeV/c momentum bins, using control shapes described in the text as fitting functions. The solid line in each plot is the fit to the data (solid squares), with different hatchings representing the different control shape contributions.

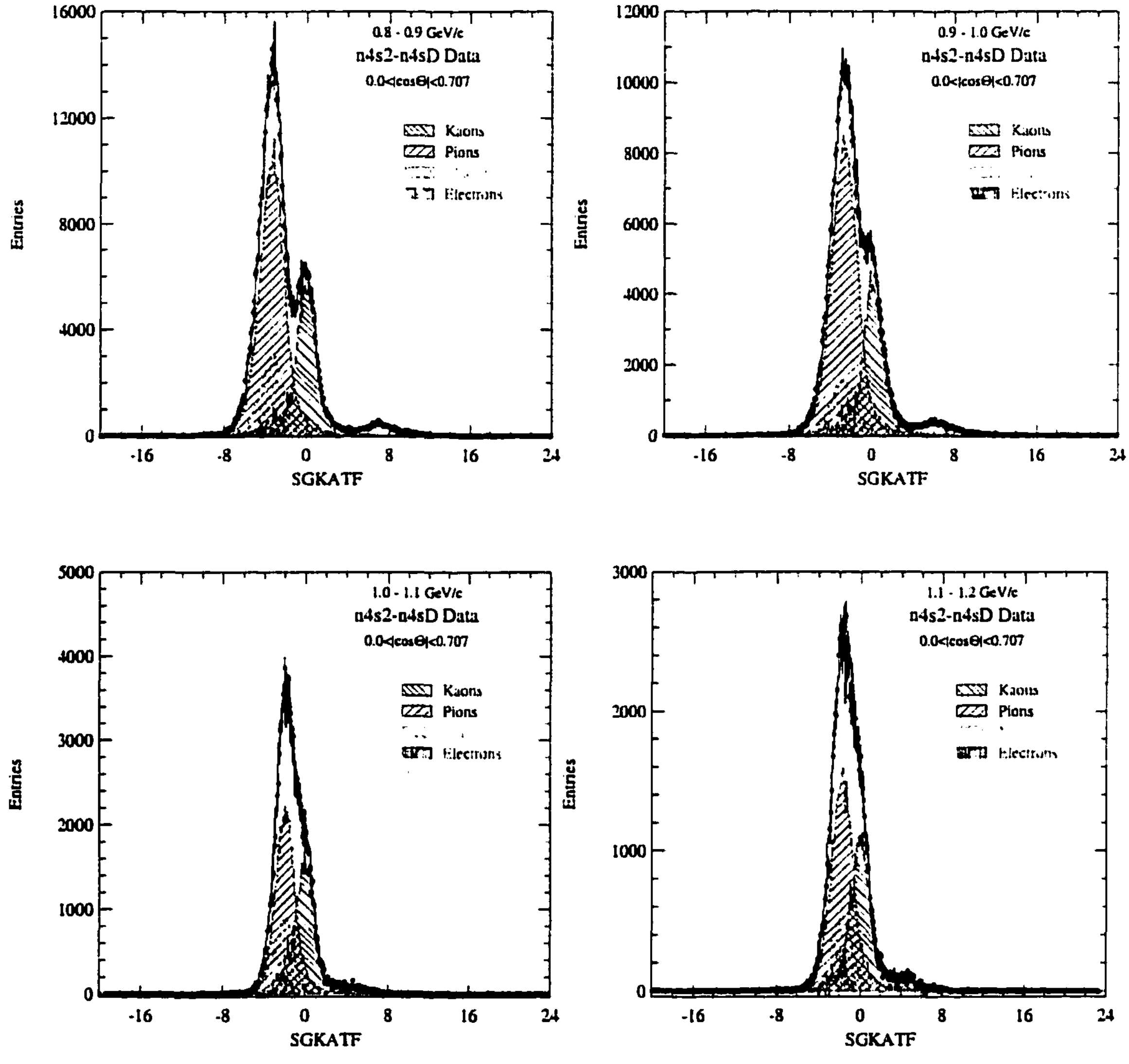

Figure 4.64: Fits to *ToF* data for 0.8–1.2 GeV/c in 0.1 GeV/c momentum bins, using control shapes described in the text as fitting functions. The solid line in each plot is the fit to the data (solid squares), with different hatchings representing the different control shape contributions.

device. After each fit for each PID device is performed, we set the kaon yield for that momentum bin and PID device to be the normalization scale factor of the kaon histogram from the fit times the area of the input kaon control shape histogram. We set the fractional error on the kaon yield to be the fractional error on the normalization scale factor from the fit plus the fractional error on the input area histogram (assumed to be one over the square root of the area) summed in quadrature. We fill the previously booked unbinned histogram with this raw kaon yield (plus its error) for each PID device, at the center of the appropriate momentum bin. We then project each unbinned histogram into a binned histogram (from 0 to 2.8 GeV/c in 112 bins for 25 MeV/c fits up to 800 MeV, and in 28 bins for 0.1 GeV/c fits above 0.8 GeV/c). This allows us to divide by the relevant efficiency bin-by-bin to get the corrected kaon yields for each PID device. Efficiency calculations for each PID device are detailed in the next section.

4.5 Determination of Efficiencies

4.5.1 Tracking Cuts from Monte Carlo

We compute the efficiency of our tracking, event shape and lepton suppression cuts from our sample of 4s2–4sD RECOMPRESS $B\overline{B}$ MC. CLEO Monte Carlo is produced in a three-step process: QQ is the Monte Carlo generator software program used by CLEO. It simulates data from B decays according to the latest published experimental results. Generated events are then propagated through a GEANT-based [57] simulation of the CLEO detector hardware, CLEOG. Finally, these raw events are processed through the PASS2 reconstruction code.

We fill two momentum spectrum histograms for tagged charged kaons from 0 to 2.8 GeV/c (one in 25 MeV/c bins for low momentum fits, and one in 0.1 GeV/c bins for high momentum fits). These momentum histograms are subject to all of our event shape, tracking and lepton suppression cuts as applied to our data shapes. We divide these histograms bin-by-bin by the appropriately binned QQ momentum spectrum for generated charged kaons in that momentum region. In this way, we obtain the tracking efficiency for each momentum bin. Figure 4.65 shows the momentum spectrum histograms which contribute to the numerator (*top*) and denominator (*bottom*) of the tracking efficiency calculation. Figure 4.66 shows the result. This efficiency is used to correct the raw charged kaon yields from our dE/dx fits.

4.5.2 *ToF* PID Cuts from Monte Carlo

We compute our *ToF* PID efficiency as follows: We fill two momentum spectrum histograms for tagged charged kaons from 0 to 2.8 GeV/c (one in 25 MeV/c bins for low momentum fits, and one in 0.1 GeV/c bins for high momentum fits). These momentum histograms are subject to all of our event shape, tracking, lepton suppression *and* ToF cuts, and become the numerator of the ToF efficiency calculation. We divide these histograms bin-by-bin by the appropriately binned momentum spectrum for charged kaons in that momentum region which pass all of our event shape, tracking and lepton suppression cuts only, the denominator of our ToF efficiency calculation. In this way, we obtain the ToF PID efficiency for each momentum bin. Figure 4.67 shows the momentum spectrum histograms which contribute to the numerator (*top*) and denominator (*bottom*) of the tracking efficiency calculation. Figure 4.68 shows the result. This efficiency is used with the tracking efficiency to correct the raw charged kaon yields from our ToF fits.

4.5.3 Combined Efficiency for *ToF* Fits

We multiply this ToF PID efficiency by the tracking efficiency described above to obtain the total efficiency for correcting our raw charged kaon yields from our ToF fits. Figure 4.69 indicates this process and displays the efficiency used for correcting fit yields from each of our PID devices.

4.6 Consistency Check with Monte Carlo

As a consistency check of our analysis methods, we ran our dE/dx and ToF analysis fitting scripts on our 4s2–4sD RECOMPRESS MC sample. Our goal here was to verify that our `Mn_Fit` scripts were working properly, exhibiting no unwanted *features*, thereby reconstructing the generated charged kaon momentum spectrum from `QQ`, when efficiency-corrected. We use our tagged MC samples of e, μ, π, K and p to fit the MC PID distribution for each momentum bin, which consists of all these MC tracks. We then obtain our efficiencies in the manner described above, using MC for PID efficiency, instead of ϕ data. The result from our previous analysis [51] appears in Figure 5.4.

4.7 Contributions to the Systematic Error

We concern ourselves here with quantifying the various contributions to our systematic errors. Our statistical errors are of order a few percent for the most populated momentum bins, so we have attempted to minimize our systematic errors as much as possible. We discuss the methods used to quantify these systematic errors in the following sections, or else quote a result from an independent study. Table 4.3 summarizes the results, including the effect when propagated to the extraction of our kaon yields. The total systematic error is the quadrature sum of these contributions.

4.7.1 Error on Number of $B\overline{B}$ Pairs

The number of $B\overline{B}$ pairs is the cross-section of the $\Upsilon(4S)$ peak (above the continuum) times the luminosity. The error on the number of $B\overline{B}$ pairs thus arises from the errors on measurements of the cross section and resonant and continuum luminosities. We quote the nominal CLEO value of 1.8% [58]. A discussion of the technique used to arrive at this number may be found in [59, 60].

4.7.2 Lepton Normalization Errors

We believe our electron normalization technique is valid to within about 20% percent. We arrived at this number by fitting for the electron yield in the momentum bins where the electrons are situated directly between the pion and kaon peaks, with the proton and muon contributions fixed and the pion and kaon yields also allowed to float.

Because the lepton contributions to the fits in the momentum regions where our suppression cuts are activated are relatively small, their effect on hadron yields due to errors in our normalization technique is somewhat reduced in these regions.

We believe that understanding the lepton contributions in the most populated momentum bins is our greatest systematic in this analysis, because it is there they (especially the electrons) can have the greatest impact on the kaon yields. The electron contribution begins to overlap with the kaon contribution around 400 MeV/c, just as our `R2ELEC`< 3.0 cut is activated. The muon contribution tends to remain under the pion contribution, but does begin to overlap with the kaon contribution before the `DPTHMU`< 3.0 cut is activated. Fortunately, this large systematic due to lepton normalizations has a greatly reduced effect on the kaon yields because of the relatively small contribution of leptons to the PID fits.

We allow these lepton norms to vary by 20%, and refit in each momentum bin with these high (+20%) and low (−20%) lepton yields. We observe the following effects on our raw kaon yields: 0.23% for electrons and 0.1% for muons.

4.7.3 Sideband Subtraction Errors for Control Shapes

We allow the vertex cuts which identify our control shape parent particles to vary, and observe the effect on the statistical error of the scale factor for that sideband subtraction. We take the largest statistical error divided by the smallest value that arises, and quote this as the systematic error for that sideband subtraction. We compute *LoSB* and *HiSB* contributions to our control shapes by using our nominal scale factor plus or minus its systematic error, respectively. We then process these systematic control shapes through our fitting routine, keeping everything else identical, and observe the effect on the raw kaon yields.

ϕ Sideband Subtraction Error

The largest statistical error (0.0055) divided by the smallest value of our ϕ scale factor (0.5455) gives a value of 1.0% for the ϕ sideband subtraction error. Because the ϕ background is much more complicated than those from our other control shape particle contributions, however, we will take this error to be 2.0%. With this error contribution, we observe a difference in our raw kaon yields of <0.03%. This contribution to the systematic error is negligible.

K_s^0 Sideband Subtraction Error

The pion control shapes are the most statistically significant contribution to the fits. The largest statistical error is 0.0035 and the smallest value of our K_s^0 scale factor is 1.0085. Dividing these two numbers and rounding up, this gives a value for the K_s^0 sideband subtraction error of 0.4%. With this error contribution, we observe a difference in our raw kaon yields of <0.01%. This contribution to the systematic error is also negligible.

Λ Sideband Subtraction Error

By varying our Λ vertex quality cuts, we find the largest statistical error to be 0.0102 and the smallest value of our Λ scale factor to be 0.5869. Dividing these two numbers gives a value of 1.7% for the Λ sideband subtraction error. With this error contribution, we observe a difference in our raw kaon yields of <0.02%. This contribution to the systematic error is again negligible.

4.7.4 Track Finding Errors

We quote the nominal CLEO value of 1% per track [61].

Table 4.3: Contributions to the Systematic Error. The total effect on our raw kaon yields is the quadrature sum of the non-negligible contributions.

Systematic Effect	% Error	$\%\Delta(N_K^{raw})$
Electron Normalization Error	20	0.23
Muon Normalization Error	20	0.1
ϕ Sideband Subtraction Error	2.0	*negligible*
K_s^0 Sideband Subtraction Error	0.4	*negligible*
Λ Sideband Subtraction Error	1.7	*negligible*
ToF Efficiency	1.3	1.3
Number of $B\overline{B}$ Pairs	1.8	1.8
Track Finding Errors	1	1
Total (Summed in Quadrature)		2.4

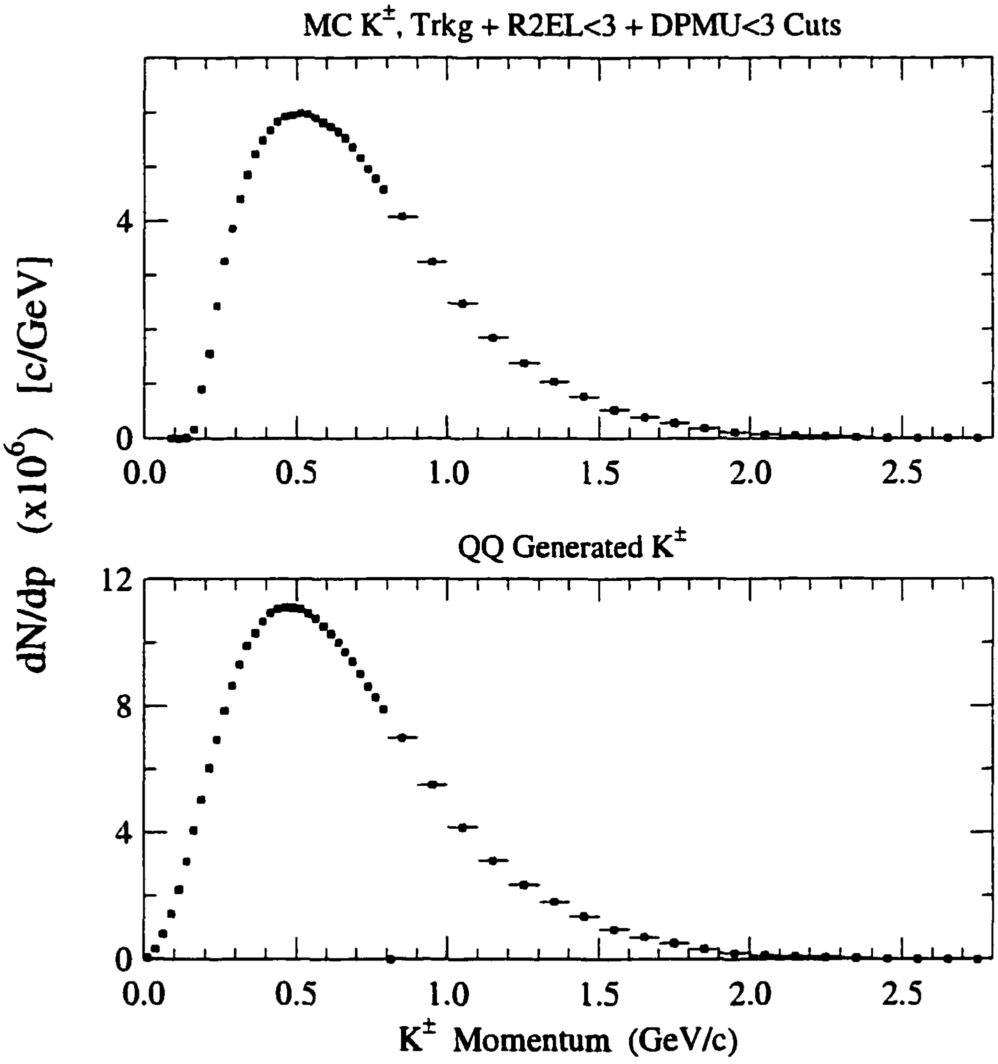

Figure 4.65: Momentum spectra for Monte Carlo kaons which contribute to our tracking efficiency. The top plot shows the spectrum of kaons which pass all of our tracking, event shape, and lepton suppression cuts and becomes the numerator of our efficiency calculation. The bottom plot shows the spectrum of kaons which were generated by QQ and becomes the denominator of our efficiency calculation. These spectra are scaled by momentum bin width.

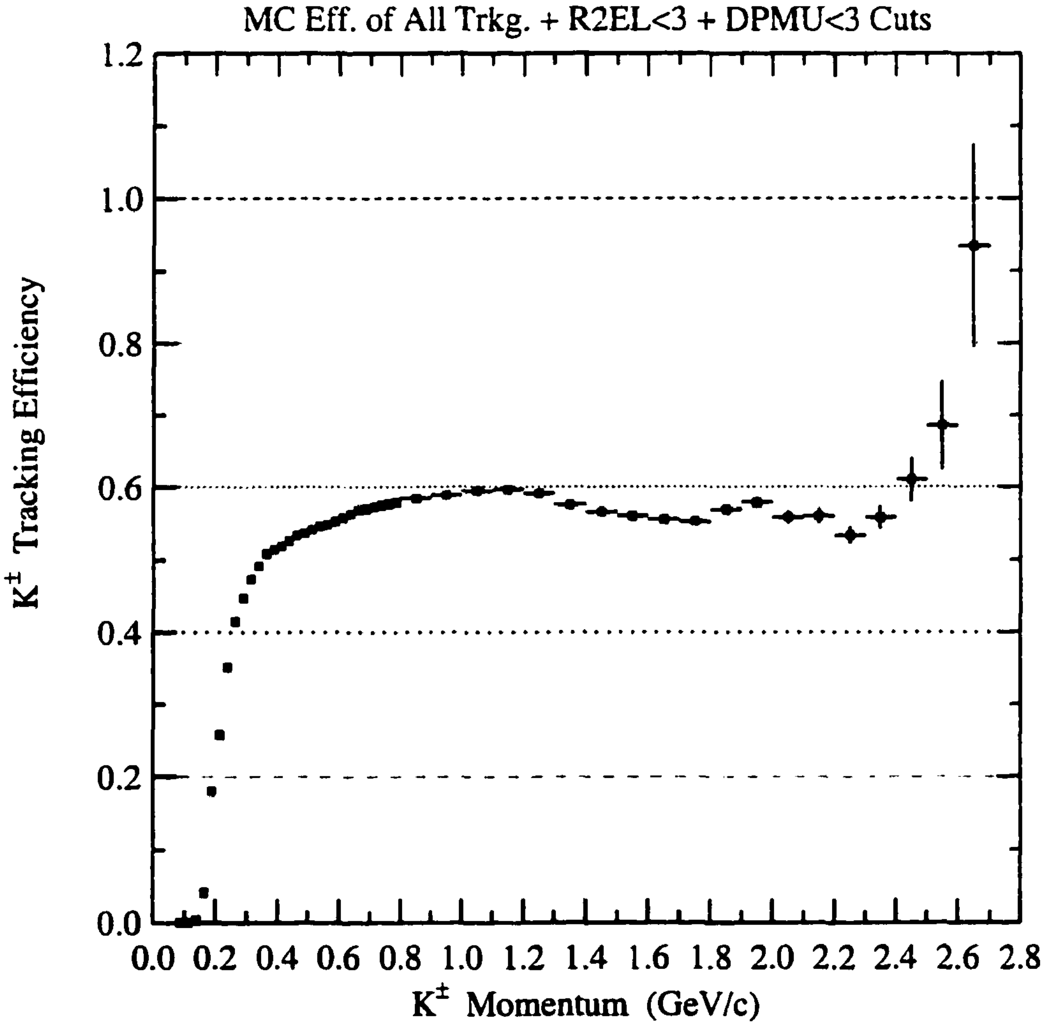

Figure 4.66: Monte Carlo efficiency of our tracking, event shape, CZCD and lepton suppression cuts.

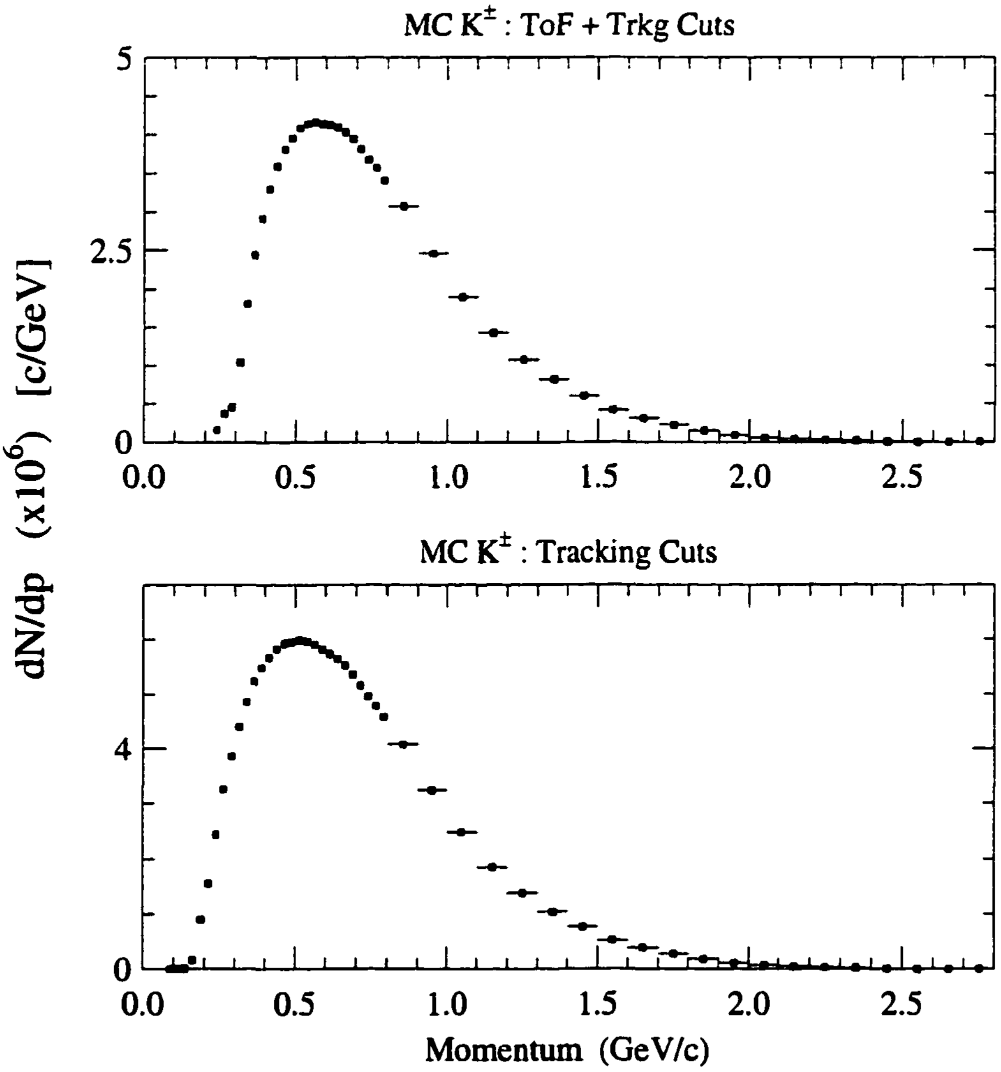

Figure 4.67: Momentum spectra for tracks identified as kaons from $B\overline{B}$ MC, which contribute to our *ToF* PID efficiency. The top plot shows the spectrum of MC kaons with *ToF* and tracking cuts. The bottom plot shows the same for kaons with tracking cuts *only*. The efficiency of our *ToF* PID cuts is computed by dividing the top histogram by the bottom histogram. These spectra are scaled by momentum bin width.

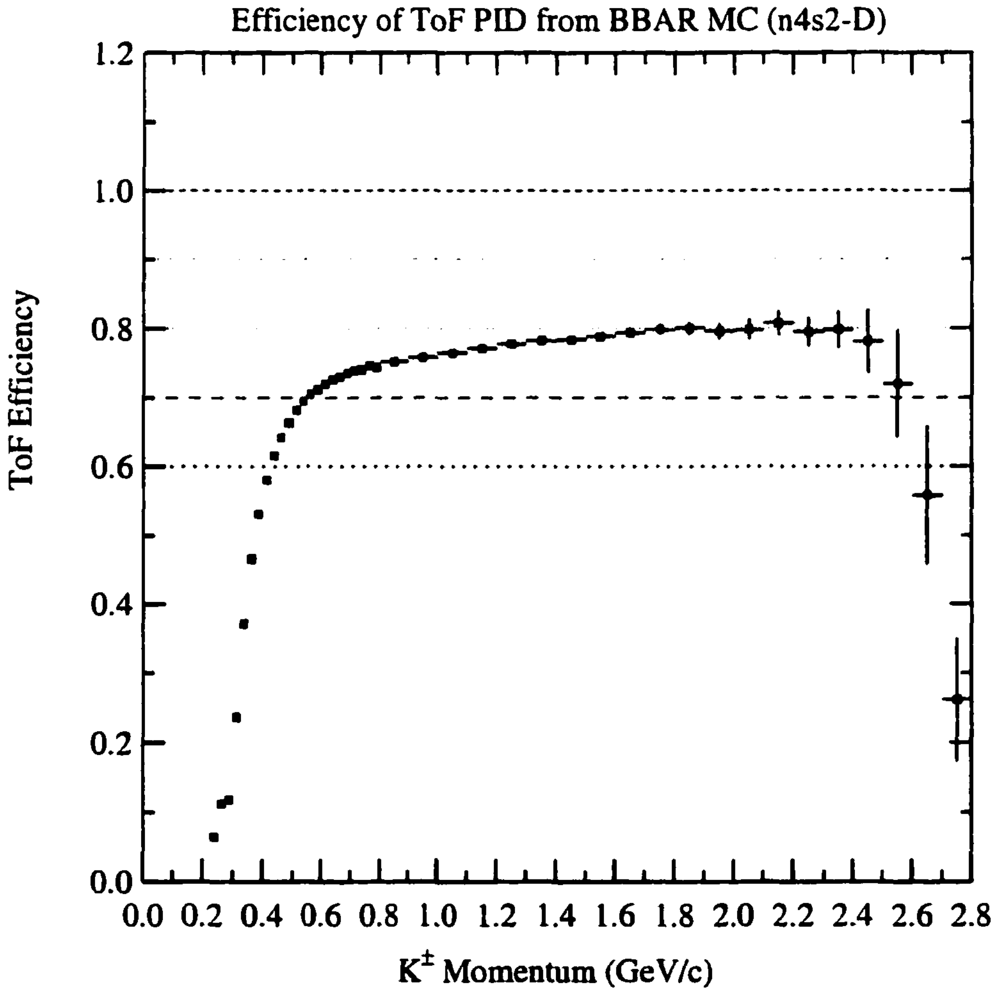

Figure 4.68: Efficiency of our *ToF* PID cuts as computed from our $B\overline{B}$ MC sample.

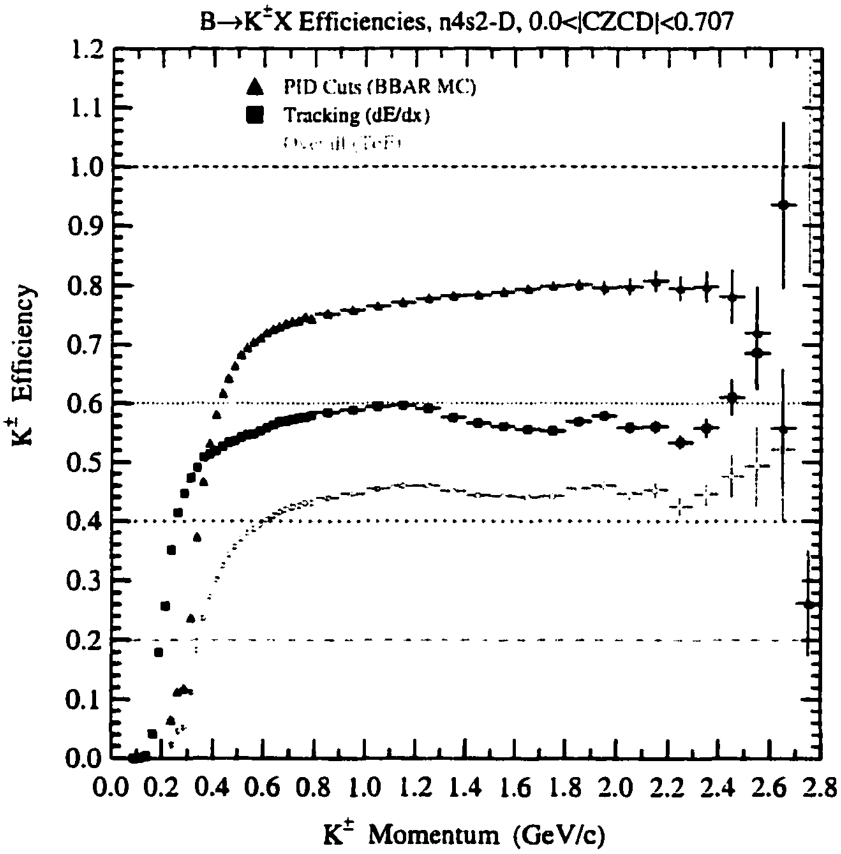

Figure 4.69: Efficiencies used for correcting our raw kaon yields from our dE/dx and ToF fit yields. The tracking efficiency corrects our dE/dx fit yields. The overall efficiency is the tracking efficiency multiplied by the PID efficiency and corrects our ToF fit yields.

Chapter 5

Presentation of Results

5.1 PID Momentum Spectra for Data and MC

Figure 5.1 shows our raw kaon yields from each PID device, before correcting for efficiency. These results are scaled by momentum bin and number of $\Upsilon(4S)$ events. Figure 5.2 displays the efficiency used for correcting fit yields from each of our PID devices. Figure 5.3 shows our efficiency-corrected kaon yields from each PID device, scaled by momentum bin and number of $\Upsilon(4S)$ events. The MC overlay is the QQ-generated spectrum for tagged charged kaons, also scaled by momentum bin and number of $\Upsilon(4S)$ events.

5.2 Tables of Results

Table 5.1 shows the efficiency used in each 25 MeV/c momentum bin from 75 to 800 MeV/c, for each PID device. Table 5.2 shows the efficiency used in each 0.1 GeV/c momentum bin from 0.8 to 2.8 GeV/c, for each PID device.

5.3 Branching Fraction and Average Multiplicity

We take a weighted average of our corrected spectra for dE/dx and ToF to obtain the momentum spectra for that charged kaon type. We sum over the momentum bins to obtain the total number of efficiency-corrected charged kaons. Table 5.3 lists these yields, scaled by momentum and number of $\Upsilon(4S)$ events, in 25 MeV/c from 175 to 800 MeV/c.

We discuss the average multiplicity and compute the charged kaon branching fraction as outlined in the following sections.

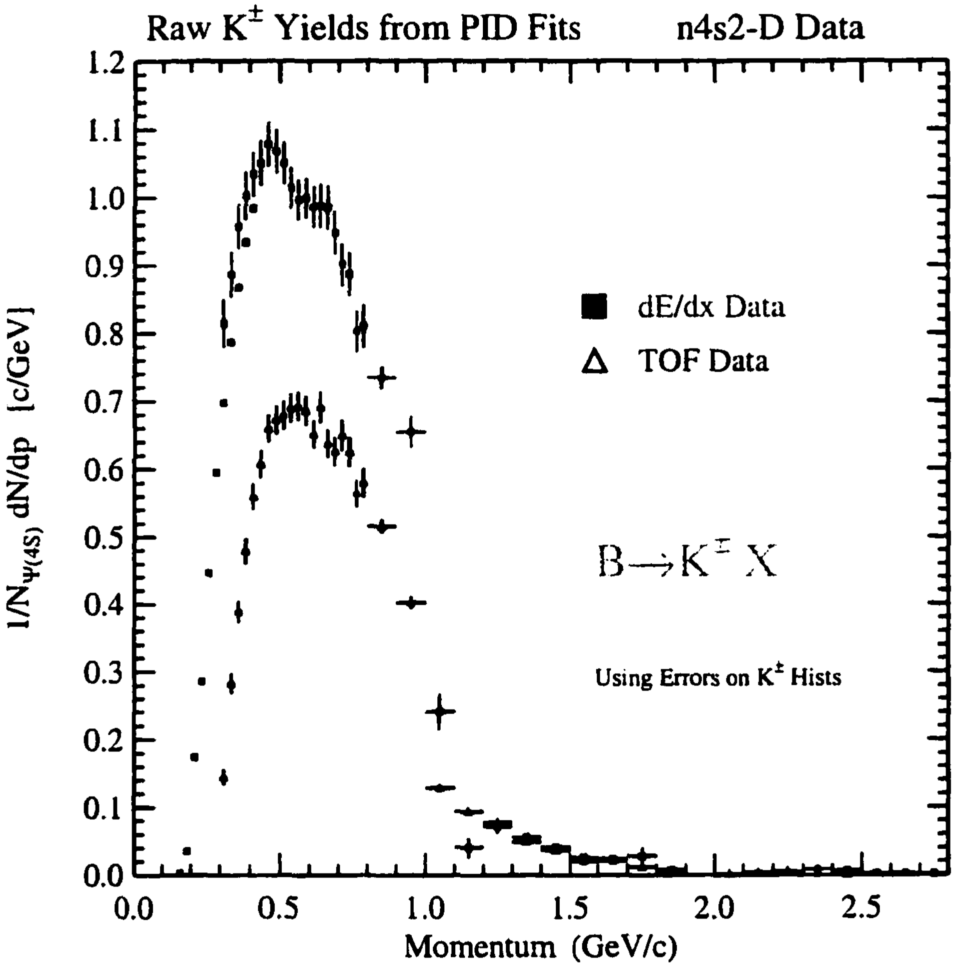

Figure 5.1: Uncorrected kaon yields from our dE/dx and ToF fits. These results are scaled by momentum bin and number of $\Upsilon(4S)$ events.

5.3.1 Charged Kaon Multiplicity at the $\Upsilon(4S)$

We divide the corrected yields momentum spectra by the number of $\Upsilon(4S)$ events and by the momentum bin width to obtain the number of charged kaons per $\Upsilon(4S)$ decay. That is:

$$N_K = \frac{1}{N_{\Upsilon(4S)}} \int_{p_{min}}^{p_{max}} \frac{dN}{dp} dp \tag{5.1}$$

where for the datasets used in this analysis:

$$N_{\Upsilon(4S)} = 2863094 \text{ events.} \tag{5.2}$$

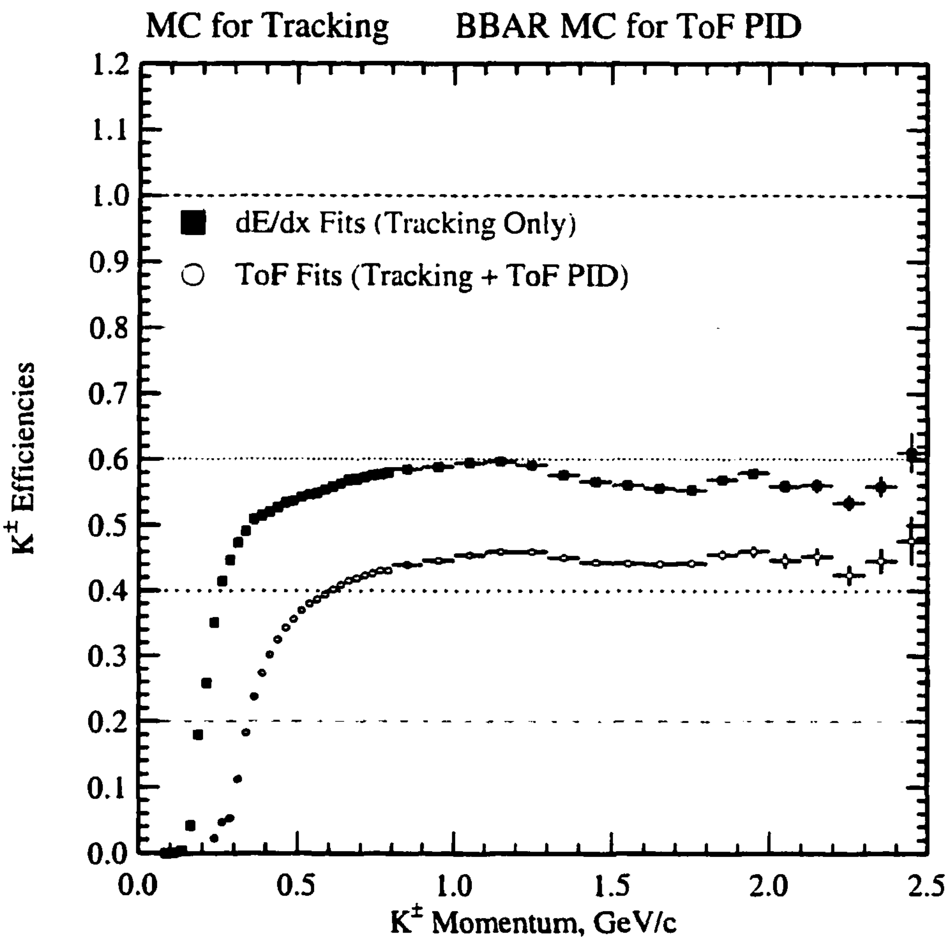

Figure 5.2: Efficiencies which correct the raw yields from our dE/dx and ToF fits.

Integrating over the data points on our average corrected spectrum from 0.2-0.8 GeV/c, we obtain an average kaon multiplicity at the $\Upsilon(4S)$ of:

$$N_K(CLEO) = 1.48 \pm 0.006 \pm 0.036 \tag{5.3}$$

Using dE/dx only, we get:

$$N_K = 1.51 \pm 0.009 \pm 0.031 \tag{5.4}$$

compared to:

$$N_K(ARGUS) = 1.55 \pm 0.03 \pm 0.05 \tag{5.5}$$

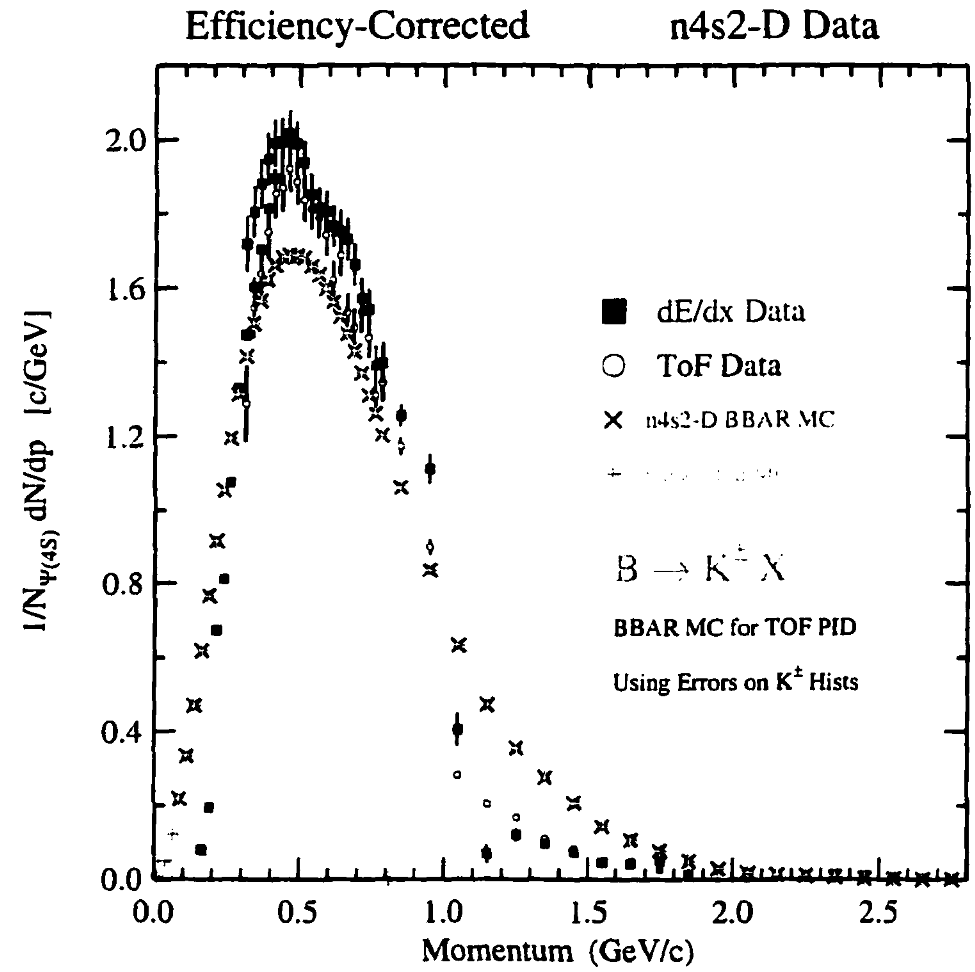

Figure 5.3: Efficiency-corrected kaon yields from our dE/dx and ToF fits. The MC overlay is the QQ-generated spectrum for tagged charged kaons. These results are all scaled by momentum bin and number of $\Upsilon(4S)$ events.

where, in each case, the first error is statistical and the second is systematic.

5.3.2 Inclusive Charged Kaon Branching Fraction

The inclusive branching fraction for a particle of type P is defined to be:

$$\begin{aligned} \mathcal{B}(B \to P X) &= \frac{N_P^{corr}}{2 \cdot N_{B\overline{B}}} \\ &= \frac{N_P^{obs}/\varepsilon}{2 \cdot \sigma_{B\overline{B}} \mathcal{L}_{\Upsilon(4S)}} \end{aligned} \tag{5.6}$$

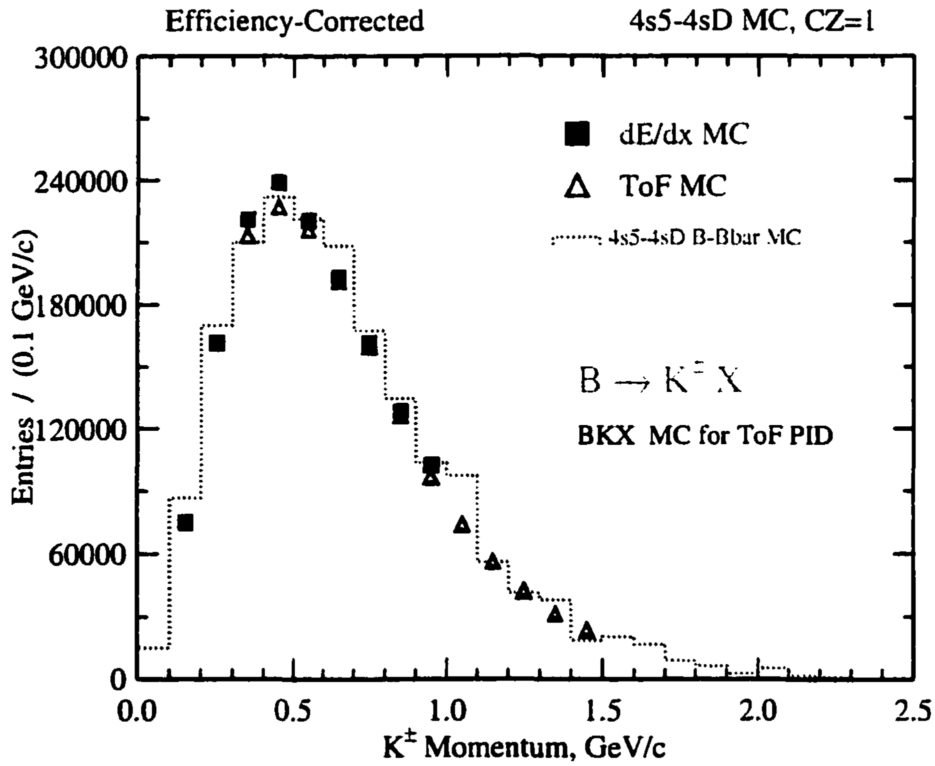

Figure 5.4: Efficiency-corrected MC kaon yields from our previous dE/dx and ToF fit yields, using tagged kaons from $B\overline{B}$ MC for PID efficiency. The MC overlay is the QQ-generated spectrum for tagged charged kaons, scaled to match the data.

where:

- N_P^{corr} is the acceptance-corrected number of observed particles of type P,
- N_P^{obs} is the raw number of observed particles of type P,
- ε is the efficiency or acceptance correction,
- $N_{B\overline{B}}$ is the number of $B\overline{B}$ pairs,
- $\sigma_{B\overline{B}}$ is the $B\overline{B}$ cross section, and
- $\mathcal{L}_{\Upsilon(4S)}$ is the luminosity taken on the $\Upsilon(4S)$ resonance peak.

Using this formula with the value for the $B\overline{B}$ cross-section listed below and the resonance luminosity given in section 4.1, we compute the charged kaon branching fraction. With:

$$\sigma_{B\overline{B}} = 1.072 \pm 0.0019\ nb \tag{5.7}$$

We obtain:

$$\mathcal{B}(B \to K^{\pm}X) = (74.0 \pm 0.3 \pm 1.8)\% \tag{5.8}$$

The branching fraction formula listed above assumes (as does the PDG) that $\mathcal{B}(\Upsilon(4S) \to B\overline{B}) = 100\%$. This assumption implies that the number of $\Upsilon(4S)$ events equals the number of $B\overline{B}$ pairs. The charged kaon branching fraction is thus essentially half of the average charged kaon multiplicity at the $\Upsilon(4S)$, since there are 2 B mesons per $\Upsilon(4S)$ decay.

Also according to the PDG, what are referred to as inclusive branching fractions for heavy state particles are often referred to as average multiplicities for light particles. This is a matter of convention, since there is a possibility to exceed a branching fraction of 100% for light particles when there is more than one such particle per B decay.

Table 5.1: Efficiencies used for correcting raw kaon yields from each PID device, in 25 MeV/c bins from 75–800 MeV/c.

Momentum (MeV/c)	Efficiency ε (dE/dx)	Efficiency ε (ToF)
75–100	0.0001 ± 0.0000	0.0000 ± 0.0000
100–125	0.0003 ± 0.0001	0.0000 ± 0.0000
125–150	0.0033 ± 0.0002	0.0000 ± 0.0000
150–175	0.0413 ± 0.0007	0.0000 ± 0.0000
175–200	0.1799 ± 0.0013	0.0000 ± 0.0000
200–225	0.2580 ± 0.0015	0.0000 ± 0.0000
225–250	0.3513 ± 0.0017	0.0226 ± 0.0004
250–275	0.4147 ± 0.0017	0.0466 ± 0.0005
275–300	0.4472 ± 0.0017	0.0527 ± 0.0006
300–325	0.4735 ± 0.0017	0.1121 ± 0.0009
325–350	0.4910 ± 0.0017	0.1825 ± 0.0012
350–375	0.5086 ± 0.0017	0.2371 ± 0.0014
375–400	0.5145 ± 0.0017	0.2733 ± 0.0015
400–425	0.5196 ± 0.0017	0.3017 ± 0.0016
425–450	0.5269 ± 0.0017	0.3247 ± 0.0017
450–475	0.5343 ± 0.0017	0.3432 ± 0.0018
475–500	0.5369 ± 0.0017	0.3564 ± 0.0019
500–525	0.5422 ± 0.0017	0.3697 ± 0.0019
525–550	0.5468 ± 0.0018	0.3798 ± 0.0020
550–575	0.5490 ± 0.0018	0.3869 ± 0.0020
575–600	0.5537 ± 0.0018	0.3938 ± 0.0021
600–625	0.5584 ± 0.0018	0.4018 ± 0.0021
625–650	0.5637 ± 0.0019	0.4092 ± 0.0022
650–675	0.5689 ± 0.0019	0.4152 ± 0.0022
675–700	0.5702 ± 0.0020	0.4192 ± 0.0023
700–725	0.5730 ± 0.0020	0.4233 ± 0.0023
725–750	0.5755 ± 0.0021	0.4262 ± 0.0024
750–775	0.5772 ± 0.0021	0.4308 ± 0.0025
775–800	0.5796 ± 0.0022	0.4307 ± 0.0025

Table 5.2: Efficiencies used for correcting raw kaon yields from each PID device, in 0.1 GeV/c bins from 0.8–2.8 GeV/c.

Momentum (GeV/c)	Efficiency $\varepsilon\,(dE/dx)$	Efficiency $\varepsilon\,(ToF)$
0.8–0.9	0.5846 ± 0.0012	0.4396 ± 0.0014
0.9–1.0	0.5892 ± 0.0013	0.4466 ± 0.0016
1.0–1.1	0.5949 ± 0.0015	0.4548 ± 0.0018
1.1–1.2	0.5964 ± 0.0018	0.4597 ± 0.0021
1.2–1.3	0.5913 ± 0.0020	0.4597 ± 0.0024
1.3–1.4	0.5761 ± 0.0022	0.4506 ± 0.0027
1.4–1.5	0.5661 ± 0.0026	0.4435 ± 0.0031
1.5–1.6	0.5607 ± 0.0030	0.4420 ± 0.0038
1.6–1.7	0.5557 ± 0.0035	0.4410 ± 0.0044
1.7–1.8	0.5533 ± 0.0041	0.4420 ± 0.0051
1.8–1.9	0.5693 ± 0.0053	0.4557 ± 0.0066
1.9–2.0	0.5787 ± 0.0070	0.4605 ± 0.0086
2.0–2.1	0.5589 ± 0.0086	0.4461 ± 0.0107
2.1–2.2	0.5605 ± 0.0104	0.4525 ± 0.0131
2.2–2.3	0.5341 ± 0.0117	0.4246 ± 0.0146
2.3–2.4	0.5586 ± 0.0154	0.4458 ± 0.0193
2.4–2.5	0.6100 ± 0.0302	0.4763 ± 0.0367
2.5–2.6	0.6854 ± 0.0618	0.4934 ± 0.0692
2.6–2.7	0.9348 ± 0.1402	0.5217 ± 0.1223
2.7–2.8	7.0000 ± 3.0551	1.8333 ± 1.0128

Table 5.3: Efficiency Corrected Numbers of Kaons for each PID Device, in 25 MeV/c bins from 150 to 800 MeV/c. These results are scaled by momentum and the number of $B\overline{B}$ pairs.

Momentum (MeV/c)	N_K (dE/dx)	N_K (ToF)
150–175	0.0000 ± 0.0000	0.0000 ± 0.0000
175–200	0.0792 ± 0.0097	0.0000 ± 0.0000
200–225	0.1950 ± 0.0068	0.0000 ± 0.0000
225–250	0.6735 ± 0.0108	0.0000 ± 0.0000
250–275	0.8115 ± 0.0103	0.0000 ± 0.0000
275–300	1.0758 ± 0.0111	0.0000 ± 0.0000
300–325	1.7196 ± 0.0751	1.2889 ± 0.1032
325–350	1.8056 ± 0.0690	1.5475 ± 0.0815
350–375	1.8829 ± 0.0668	1.6387 ± 0.0695
375–400	1.9491 ± 0.0698	1.7518 ± 0.0700
400–425	1.9908 ± 0.0626	1.8548 ± 0.0656
425–450	1.9940 ± 0.0640	1.8704 ± 0.0636
450–475	2.0189 ± 0.0612	1.9222 ± 0.0612
475–500	1.9893 ± 0.0605	1.8862 ± 0.0603
500–525	1.9384 ± 0.0579	1.8377 ± 0.0581
525–550	1.8539 ± 0.0554	1.8145 ± 0.0558
550–575	1.8163 ± 0.0544	1.7900 ± 0.0552
575–600	1.8055 ± 0.0538	1.7420 ± 0.0552
600–625	1.7661 ± 0.0548	1.6205 ± 0.0515
625–650	1.7532 ± 0.0577	1.6882 ± 0.0562
650–675	1.7315 ± 0.0568	1.5344 ± 0.0510
675–700	1.6625 ± 0.0563	1.4928 ± 0.0509
700–725	1.5727 ± 0.0557	1.5350 ± 0.0544
725–750	1.5411 ± 0.0558	1.4660 ± 0.0522
750–775	1.3906 ± 0.0525	1.3095 ± 0.0471
775–800	1.3979 ± 0.0556	1.3450 ± 0.0503

Chapter 6

Summary and Conclusion

We have investigated the inclusive production of charged kaons from B meson in $\Upsilon(4S)$ decays. Using dE/dx and ToF PID quantities, we have obtained the momentum spectrum for these particles which cover the entire attainable momentum range.

Our comparisons of this charged kaon spectrum from data with those generated from Monte Carlo indicate that our Monte Carlo simulation fails to reproduce the kaon peak as exhibited in the data. This indicates there is a contribution in the data that the Monte Carlo does not model.

By integrating over the bins of these momentum spectra, we obtained the results for the $\Upsilon(4S)$ multiplicity and branching fraction of charged kaons listed in Table 6.1.

Table 6.1: Summary of results for charged kaons.

$N_K(CLEO)$	$1.48 \pm 0.006(stat.) \pm 0.036(syst.)$
$\mathcal{B}(B \to K^{\pm}X)$	$\{74.0 \pm 0.3(stat.) \pm 1.8(syst.)\}\%$

Our results are about $1\,\sigma$ below the values that ARGUS has published. We can also conclude that an $\mathcal{O}(10\%)$ $b \to s\,g$ contribution cannot be ruled out. CLEO has recently observed [62] evidence of a possible $b \to s\,g^*$ signal in $B \to \eta\prime X_s$ for $2.0 < p_{\eta\prime} < 2.7$ GeV/c.

There are many theoretical uncertainties which prevent a conversion of the upper limit on various inclusive channels containing strange quarks into an upper limit on $b \to sg$. Thus we cannot yet rule out certain extensions of the Standard Model, including Supersymmetry or Technicolor. A $b \to sg$ contribution of $\mathcal{O}(1\%)$ is predicted by the Standard Model. The higher $b \to sg$ contribution of $\mathcal{O}(10\%)$ is needed to explain the observed low B semileptonic branching fraction, $\mathcal{B}_\ell(B)$, as well as the observed low charm multiplicity in B decays, η_c [15].

Our Maximum Likelihood method should improve our results somewhat, especially at higher momenta, and also allow for simultaneous extraction of pion and proton yields. In the longer term the improved $\pi/K/p$ resolution of CLEO III's `RICH` detector may significantly improve inclusive measurements of charged light hadrons at the $\Upsilon(4S)$.

References

[1] Particle Data Group, C. Caso *et al.*, Euro. Phys. J. C **3**, 1-794 (1998).

[2] "Introduction to Elementary Particles", David Griffiths, John Wiley & Sons, 1987.

[3] "Subatomic Physics", Hans Frauenfelder and Ernest Henley, Prentice Hall, 1991.

[4] S. Weinberg, A. Salam, and S. Glashow, Rev. Mod. Phys. **52**, (1980) 515.

[5] N. Cabibbo, Phys. Rev. Lett. **10**, 531 (1963); M. Kobayashi and T. Maskawa, Prog. Theor. Phys. **49**, 653 (1973).

[6] G. Backenstoss *et al.*, Phys. Rev. Lett. **6**, 415 (1961).

[7] M. Bardon *et al.*, Phys. Rev. Lett. **7**, 23 (1961).

[8] M. Gell-Mann and A. Pais, Phys. Rev. **97**, 1387 (1955).

[9] K. Lande *et al.*, Phys. Rev. **103**, 1901 (1956).

[10] J.H. Christenson *et al.*, Phys. Rev. Lett. **13**, 138 (1964).

[11] H. Weyl, "Electron And Gravitation. 1. (In German)," Z. Phys. **56**, 330 (1929).

[12] C. S. Wu *et al.*, Phys Rev **105**, 1413 (1957).

[13] "Quantum Field Theory", Lewis Ryder, Cambridge University Press, 1985.

[14] *Recent Results on Hadronic B Decays from CLEO*, by Roy Briere, published in "Particles and the Universe: Proceedings of the Twelfth Lake Louise Winter Institute", World Scientific, 1998.

[15] A. Kagan and J. Rathsman, hep-ph/9701300 (1997).

[16] ARGUS Collaboration, H. Albrecht *et al.*, Z Phys. *C* **58** 191–198 (1993).

[17] M.S. Alam *et al.*, Phys. Rev. Lett. **58**, 1814 (1987).

[18] CLEO Collaboration, Y. Kubota *et.al.*, Nucl. Instr. and Meth. A **320**, pp 66-113 (1992).

[19] B.D. McDaniel, IEEE Trans. on Nucl. Sci., **NS-28**, 1984 (1981).

[20] "dE/dx Performance at CLEO", A. Gritsan, CLEO Internal Memorandum, *CBX* 99-15 (1999).

[21] "RECOMPRESS Fake Rates", T. Riehle, CLEO Internal Memorandum, *CBX* 99-XX (1999).

[22] "Fake Muons Study with DPTHMU > 3", A. Bellerive, CLEO Internal Memorandum, *CBX* 97-59 (1997).

[23] "Maintenance and Calibration of the CLEO MUON Detector", H. Severini, CLEO Internal Memorandum, *CBX* 96-99 (1996).

[24] CLEO Collaboration, C. Bebek *et.al.*, Nucl. Instr. and Meth. A **302**, pp 261-276 (1991).

[25] see `http://www.lns.cornell.edu/restricted/CLEO /buzzwords/cleosoft.doc`.

[26] S. Richichi and N. Hancock, "PASS2 for Beginners: V 5.0 – *Running on the Recompress Farm*", (see `http://www.lns.cornell.edu/restricted/CLEO/soft /cmprs2/cleoii/pass2_for_beginners_v5.ps`).

[27] Documentation on the `DUET` CLEVER processor code is located in the following documents:
"How and Why Wonder Book of DUET Conventions", R. Kutschke, CLEO Software Note, *CSN* 94/334 (1994) and
"DUET Flow Control", R. Kutschke, CLEO Software Note, *CSN* 94/335 (1994).

[28] Documentation on the `CCFC` CLEVER processor code is located on the Cornell Alpha workstations at: /cleo/doc/ccfc.doc.

[29] Documentation on the `XBAL` CLEVER processor code is located on the Cornell Alpha workstations at:
/cleo/doc/xbal.doc, /cleo/doc/xbal_new.doc, and /cleo/doc/xbal_fix.doc.

[30] "The KNVF Secondary Vertex Finding Package", C. Prescott, CLEO Software Note, *CSN* 97/353 (1997).

[31] "Proposal for New Track Bank Conventions", R. Kutschke, CLEO Software Note, *CSN* 95/340 (1995).

[32] "Tracking Update for Recompress and SVX", R. Kutschke, CLEO Software Note, *CSN* 96/348 (1996).

[33] "Tracking Common Blocks for the Kalman Era", A. Foland, CLEO Software Note, *CSN* 97/354 (1997).

[34] "Billoir fitter for CLEO II", R. Kutschke & A. Ryd, CLEO Internal Memorandum, *CBX* 96-20 (1996).

[35] "Calling the Kalman Filter from DUET", R. Kutschke, CLEO Software Note, *CSN* 96/349 (1996).

[36] "Applied Fitting Theory V: Track Fitting Using the Kalman Filter", P. Avery, CLEO Internal Memorandum, *CBX* 92-39 (1992).

[37] "Trkman the Next Generation: The quest for track quality", S. Roberts, CLEO Software Note, *CSN* 96/103 (1996).

[38] Documentation on the EVCL CLEVER processor code may be found in: "EVCLAS Event Classification", Alan Weinstein, CLEO Software Note, *CSN* 96/347 (1996).

[39] The *Nile Project* (A Scalable Solution for Distributed Processing of Independent Data) is documented at:
`http://www.nile.cornell.edu/`.

[40] "Applied Fitting Theory VI: Formulas for Kinematic Fitting", P. Avery, CLEO Software Note, *CSN* 98/37 (1998).

[41] "Applied Fitting Theory V: Track Fitting Using the Kalman Filter", P. Avery, CLEO Internal Memorandum, *CBX* 92-39 (1992).

[42] Dr. David Kreinick, Cornell University, private communication.

[43] Much of this and the next section is taken from the following Web Page:
`http://www.lns.cornell.edu/restricted/CLEO/soft`
`/cmprs2/recmprs/skim.html`.

[44] Documentation on the *dskm* code is located on the Cornell Alpha workstations at: /cleo/doc/dskm.doc, which is also accessible via the web at:
`http://www.lns.cornell.edu/restricted/CLEO/soft`
`/cmprs2/cleoii/hadron.html`.

[45] Documentation on user control flags is located on the Cornell Alpha workstations at: `/cleo/doc/rutil.doc`, which is also accessible via the web at:
`http://www.lns.cornell.edu/restricted/CLEO/soft`
`/cmprs2/cleoii/rutil.html`.

[46] Documentation on the tau skim selection criteria is located on the Cornell Alpha workstations at: /cleo/doc/tauskm.doc, which is also accessible via the web at: `http://www.lns.cornell.edu/restricted/CLEO/soft /cmprs2/cleoii/tau.html`.

[47] "Secondary Vertex Finding Performance and the CLEO II Recompress", C. Prescott, CLEO Internal Memorandum, *CBX* 97-69 (1997).

[48] More on the dE/dx-Fixing process may be found at the following Web Page: `http://www.lns.cornell.edu/restricted/CLEO/soft /pass2/cleo2_reroar_rededx/index.html`.

[49] "An Improved dE/dx Calibration for CLEO II/SVX", David Asner, Jeff Gronberg, Harry Nelson, CLEO Internal Memorandum, *CBX* 98-26 (1998).

[50] These details were gleaned from slides of a CLEO Lunch Talk on the *ToF* system, which is posted at: `http://www.lns.cornell.edu/restricted/CLEO/analysis/ac_help /lunchtalk_tof_oct98.ps`.

[51] "Inclusive Charged Kaon Production from B Decays", S. Richichi, P. Skubic, CLEO Internal Memorandum, *CBX* 98-35 (1998).

[52] MINUIT: Function Minimization and Error Analysis Reference Manual, F. James, *et.al.*, CERN Program Library Long Writeup D506 (1998).

[53] More on the `Mn_Fit` software package may be found at the following Web Page: `http://www-zeus.physik.uni-bonn.de/ brock/mn_fit.html`.

[54] HBOOK: Statistical Analysis and Histogramming Reference Manual, O. Couet, *et.al.*, CERN Program Library Long Writeup Y250 (1998).

[55] G.C. Fox and S. Wolfram, Phys. Rev. Lett. **41**, 1581 (1978).

[56] "Observation of the Cabbibo Suppressed Charm Baryon Decay $\Lambda_c^+ - > p\phi$", B. Nemati, CLEO Internal Memorandum, *CBX* 95-7 (1995).

[57] R. Brun, *et.al.*, CERN Program Library Long Writeup W5013 (1993).

[58] Professor David Besson, University of Kansas, private communication.

[59] "The $\Upsilon(4S)$ Cross-Section at CLEO", D. Besson, CLEO Internal Memorandum, *CBX* 92-23 (1992).

[60] "The $\Upsilon(4S)$ Cross-Section, Reprise", D. Besson, CLEO Internal Memorandum, *CBX* 92-75 (1992).

[61] "Charged Particle Tracking Systematic Errors in $B\overline{B}$ Events", D. Besson, CLEO Internal Memorandum, *CBX* 96-1 (1996).

[62] T. Browder, *et al.*, Phys. Rev. Lett. **81**, 1786-90 (1998).

Appendix A

CLEO II Dataset Summary

In the tables which follow, the luminosity taken from `cleoiirun.fil` is meant as a

ROUGH GUIDELINE ONLY!

The *ONLY* accurate way to obtain the luminosity for your analysis is to use the statistics gathered for the runs *YOU ACTUALLY USE!* This is done automatically in `DRIVER`'s End-of-Job Summary.

Table A.1: CLEO-II RECOMPRESS Non-4S Data Statistics.

Data Set	Input DLTs	Run Range	4-mm Tapes	No. Runs	No. Files	Lumi. (pb^{-1})	Output DLTs
1s1	1s1_CL01 - 1s1_CL02	34546 - 34889	2130 - 2155	160	26	14.7	1s1_FR01 - 1s1_FR02
1s2	1s2_CL01 - 1s2_CL04	48059 - 48761	3187 - 3243	505	57	48.1	1s2_NEW_FR01 - 1s2_NEW_FR05
1s3	1s3_CL01	66398 - 66535	4944 - 4954	73	11	15.4	1s3_FR01 - 1s3_FR02
2s1	2s1_CL01 - 2s1_CL04	65845 - 66393	4911 - 4943	318	33	70.6	2s1_FR01 - 2s1_FR05
3s1	3s1_CL01 - 3s1_CL09	31203 - 33496	0141 - 2077	1007	101	132.0	Not Re-ROARed OR Skimmed

Table A.2: CLEO-II RECOMPRESS 4S Data Statistics.

Data Set	Input DLTs	Run Range	4-mm Tapes	No. Runs	No. Files	Lumi. (pb^{-1})	Output DLTs
4s1	4s1_CL01 - 4s1_CL10	33607 - 36173	2081 - 2250	946	100	127.7	4s1_FR01 - 4s1_FR08
4s2	4s2_CL01 - 4s2_CL21	36233 - 40095	2251 - 2522	2045	272	672.0	4s2_FR01 - 4s2_FR22
4s3	4s3_CL01 - 4s3_CL21	41386 - 45969	2541 - 2917	2841	376	682.2	4s3_FR01 - 4s3_FR27
4s4	4s4_CL01 - 4s4_CL11	46035 - 48057	3000 - 3186	1411	186	317.5	4s4_FR01 - 4s4_FR13
4s5	4s5_CL01 - 4s5_CL14	48943 - 51406	3261 - 3475	1795	214	322.5	4s5_FR01 - 4s5_FR15
4s6	4s6_CL01 - 4s6_CL12	51431 - 53702	3476 - 3671	1638	195	316.5	4s6_FR01 - 4s6_FR13
4s7	4s7_CL01 - 4s7_CL19	53747 - 56976	3672 - 3989	2346	316	461.0	4s7_FR01 - 4s7_FR20
4s8	4s8_CL01 - 4s8_CL10	57038 - 58813	3990 - 4168	1265	179	281.9	4s8_FR01 - 4s8_FR12
4s9	4s9_CL01 - 4s9_CL07	58837 - 60576	4169 - 4388	1201	220	343.5	4s9_FR01 - 4s9_FR14
4sA	4sA_CL01 - 4sA_CL07	60770 - 61778	4410 - 4532	682	122	190.8	4sA_FR01 - 4sA_FR08
4sB	4sB_CL01 - 4sB_CL07	61826 - 62855	4533 - 4654	481	120	140.0	4sB_FR01 - 4sB_FR08
4sC	4sC_CL01 - 4sC_CL07	63086 - 64026	4660 - 4768	407	93	141.5	4sC_FR01 - 4sC_FR08
4sD	4sD_CL01 - 4sD_CL06	64085 - 64674	4769 - 4815	274	45	98.0	4sD_FR01 - 4sD_FR06
4sE	4sE_CL01 - 4sE_CL06	64675 - 65238	4815 - 4860	288	44	128.8	4sE_FR01 - 4sE_FR06
4sF	4sF_CL01 - 4sF_CL06	65252 - 65818	4861 - 4910	311	52	145.9	4sF_FR01 - 4sF_FR07
4sG	4sG_CL01 - 4sG_CL20	66539 - 68027	4955 - 5113	833	157	455.1	4sG_FR01 - 4sG_FR21

Appendix B

List of RECOMPRESS DLTs

```
*** FHD Skims contain all Full ROAR Fields ***
          *** for Hadronic Events ***

*ALL* other Skim Types have TREL, TRMU, CDRH, CCEL,
    TRHT, TRHI, *and* TFDT ROAR Fields deleted!

    *ALL* 1s2_NEW_* DLTs have Fixed dE/dx Info
```

```
***************************************************************
***************************************************************
  DLT Name      Type of Data     Runs on Tape  Files   Date
***************************************************************
***************************************************************
 1s1_FR01  RECOMPRESS Full Roar  34596-34740    15   08/04/97
 1s1_FR02  RECOMPRESS Full Roar  34742-34889    11   08/04/97
***************************************************************
 1s1_FHD1  RECOMPRESS FHD Skim   34546-34889    26   08/04/97
 1s1_HAD1  RECOMPRESS HAD Skim   34546-34889    26   08/04/97
 1s1_TAU1  RECOMPRESS TAU Skim   34546-34889    26   08/04/97
 1s1_2TK1  RECOMPRESS 2TK Skim   34546-34889    26   08/04/97
 1s1_4TK1  RECOMPRESS 4TK Skim   34546-34889    26   08/04/97
***************************************************************
***************************************************************
```

1s2_NEW_FR01	Re-PASS2	Full Roar	48059-48242	12	07/11/98
1s2_NEW_FR02	Re-PASS2	Full Roar	48243-48385	12	07/12/98
1s2_NEW_FR03	Re-PASS2	Full Roar	48386-48530	13	07/13/98
1s2_NEW_FR04	Re-PASS2	Full Roar	48531-48671	12	07/14/98
1s2_NEW_FR05	Re-PASS2	Full Roar	48673-48761	08	07/14/98
**					
1s2_NEW_FHD1	Re-PASS2	FHD Skim	48114-48372	22	07/14/98
1s2_NEW_FHD2	Re-PASS2	FHD Skim	48386-48632	22	07/14/98
1s2_NEW_FHD3	Re-PASS2	FHD Skim	48647-48761	10	07/14/98
1s2_NEW_HAD1	Re-PASS2	HAD Skim	48114-48761	56	07/14/98
1s2_NEW_TAU1	Re-PASS2	TAU Skim	48114-48761	56	07/14/98
1s2_NEW_2TK1	Re-PASS2	2TK Skim	48114-48761	56	07/14/98
1s2_NEW_4TK1	Re-PASS2	4TK Skim	48114-48761	56	07/14/98
**					
**					
1s3_FR01	RECOMPRESS	Full Roar	66398-66490	06	07/30/97
1s3_FR02	RECOMPRESS	Full Roar	66491-66535	05	07/30/97
**					
1s3_FHD1	RECOMPRESS	FHD Skim	66398-66535	11	07/30/97
1s3_HAD1	RECOMPRESS	HAD Skim	66398-66535	11	07/30/97
1s3_TAU1	RECOMPRESS	TAU Skim	66398-66535	11	07/30/97
1s3_2TK1	RECOMPRESS	2TK Skim	66398-66535	11	07/30/97
1s3_4TK1	RECOMPRESS	4TK Skim	66398-66535	11	07/30/97
**					
**					
2s1_FR01	RECOMPRESS	Full Roar	65845-65988	08	07/25/97
2s1_FR02	RECOMPRESS	Full Roar	65992-66094	07	07/25/97
2s1_FR03	RECOMPRESS	Full Roar	66095-66190	06	07/28/97
2s1_FR04	RECOMPRESS	Full Roar	66192-66290	05	07/28/97
2s1_FR05	RECOMPRESS	Full Roar	66291-66393	07	07/29/97
**					
2s1_FHD1	RECOMPRESS	FHD Skim	65845-66165	19	07/25/97
2s1_FHD2	RECOMPRESS	FHD Skim	66167-66393	14	07/29/97
2s1_HAD1	RECOMPRESS	HAD Skim	65845-66393	33	07/29/97
2s1_TAU1	RECOMPRESS	TAU Skim	65845-66393	33	07/29/97
2s1_2TK1	RECOMPRESS	2TK Skim	65845-66393	33	07/29/97
2s1_4TK1	RECOMPRESS	4TK Skim	65845-66393	33	07/29/97
**					
**					
4s1_FR01	RECOMPRESS	Full Roar	33607-33863	12	07/31/97
4s1_FR02	RECOMPRESS	Full Roar	33865-34113	12	07/31/97

4s1_FR03	RECOMPRESS Full Roar	34115-34338	12	07/31/97
4s1_FR04	RECOMPRESS Full Roar	34340-34517	12	07/31/97
4s1_FR05	RECOMPRESS Full Roar	34898-35211	15	08/01/97
4s1_FR06	RECOMPRESS Full Roar	35213-35511	13	08/02/97
4s1_FR07	RECOMPRESS Full Roar	35514-35880	17	08/03/97
4s1_FR08	RECOMPRESS Full Roar	35892-36173	07	08/03/97
**				
4s1_FHD1	RECOMPRESS FHD Skim	33607-35357	69	08/01/97
4s1_FHD2	RECOMPRESS FHD Skim	35360-36173	31	08/02/97
4s1_HAD1	RECOMPRESS HAD Skim	33607-36173	100	08/03/97
4s1_TAU1	RECOMPRESS TAU Skim	33607-36173	100	08/03/97
4s1_2TK1	RECOMPRESS 2TK Skim	33607-36173	100	08/02/97
4s1_4TK1	RECOMPRESS 4TK Skim	33607-36173	100	08/03/97
**				
**				
4s2_FR01	RECOMPRESS Full Roar	36233-36569	14	07/17/97
4s2_FR02	RECOMPRESS Full Roar	36571-36774	14	07/19/97
4s2_FR03	RECOMPRESS Full Roar	36776-37103	17	07/19/97
4s2_FR04	RECOMPRESS Full Roar	37105-37352	15	07/19/97
4s2_FR05	RECOMPRESS Full Roar	37354-37587	15	07/19/97
4s2_FR06	RECOMPRESS Full Roar	37590-37788	13	07/19/97
4s2_FR07	RECOMPRESS Full Roar	37789-37932	13	07/20/97
4s2_FR08	RECOMPRESS Full Roar	37934-38048	11	07/20/97
4s2_FR09	RECOMPRESS Full Roar	38050-38220	14	07/21/97
4s2_FR10	RECOMPRESS Full Roar	38222-38383	13	07/21/97
4s2_FR11	RECOMPRESS Full Roar	38385-38502	11	07/21/97
4s2_FR12	RECOMPRESS Full Roar	38547-38783	13	07/21/97
4s2_FR13	RECOMPRESS Full Roar	38784-38947	11	07/22/97
4s2_FR14	RECOMPRESS Full Roar	38948-39102	12	07/22/97
4s2_FR15	RECOMPRESS Full Roar	39103-39226	10	07/22/97
4s2_FR16	RECOMPRESS Full Roar	39227-39353	10	07/23/97
4s2_FR17	RECOMPRESS Full Roar	39354-39514	12	07/23/97
4s2_FR18	RECOMPRESS Full Roar	39515-39619	12	07/23/97
4s2_FR19	RECOMPRESS Full Roar	39620-39746	12	07/23/97
4s2_FR20	RECOMPRESS Full Roar	39747-39891	14	07/24/97
4s2_FR21	RECOMPRESS Full Roar	39892-40051	13	07/24/97
4s2_FR22	RECOMPRESS Full Roar	40052-40095	03	07/24/97
**				
4s2_FHD1	RECOMPRESS FHD Skim	36233-37225	52	07/18/97
4s2_FHD2	RECOMPRESS FHD Skim	37227-37910	47	07/20/97
4s2_FHD3	RECOMPRESS FHD Skim	37913-38383	40	07/21/97
4s2_FHD4	RECOMPRESS FHD Skim	38385-38959	36	07/22/97
4s2_FHD5	RECOMPRESS FHD Skim	38960-39365	32	07/23/97

4s2_FHD6	RECOMPRESS FHD Skim	39366-39764	37	07/24/97
4s2_FHD7	RECOMPRESS FHD Skim	39766-40095	28	07/24/97
4s2_HAD1	RECOMPRESS HAD Skim	36233-38732	160	07/24/97
4s2_HAD2	RECOMPRESS HAD Skim	38733-40095	112	07/24/97
4s2_TAU1	RECOMPRESS TAU Skim	36233-40095	272	07/24/97
4s2_2TK1	RECOMPRESS 2TK Skim	36233-40095	272	07/24/97
4s2_4TK1	RECOMPRESS 4TK Skim	36233-40095	272	07/24/97
***				
***				
4s3_FR01	RECOMPRESS Full Roar	41386-41616	16	07/10/97
4s3_FR02	RECOMPRESS Full Roar	41618-41799	16	07/10/97
4s3_FR03	RECOMPRESS Full Roar	41801-41904	14	07/10/97
4s3_FR04	RECOMPRESS Full Roar	41905-42152	16	07/10/97
4s3_FR05	RECOMPRESS Full Roar	42153-42254	15	07/11/97
4s3_FR06	RECOMPRESS Full Roar	42256-42401	15	07/11/97
4s3_FR07	RECOMPRESS Full Roar	42403-42509	13	07/11/97
4s3_FR08	RECOMPRESS Full Roar	42511-42672	14	07/11/97
4s3_FR09	RECOMPRESS Full Roar	42673-42881	14	07/12/97
4s3_FR10	RECOMPRESS Full Roar	42884-43128	13	07/12/97
4s3_FR11	RECOMPRESS Full Roar	43129-43486	14	07/12/97
4s3_FR12	RECOMPRESS Full Roar	43488-43652	13	07/12/97
4s3_FR13	RECOMPRESS Full Roar	43654-43821	13	07/13/97
4s3_FR14	RECOMPRESS Full Roar	43822-44017	13	07/13/97
4s3_FR15	RECOMPRESS Full Roar	44018-44176	13	07/13/97
4s3_FR16	RECOMPRESS Full Roar	44177-44317	13	07/13/97
4s3_FR17	RECOMPRESS Full Roar	44319-44472	13	07/14/97
4s3_FR18	RECOMPRESS Full Roar	44473-44625	13	07/14/97
4s3_FR19	RECOMPRESS Full Roar	44626-44783	14	07/14/97
4s3_FR20	RECOMPRESS Full Roar	44785-44966	14	07/14/97
4s3_FR21	RECOMPRESS Full Roar	44967-45112	13	07/15/97
4s3_FR22	RECOMPRESS Full Roar	45113-45261	15	07/15/97
4s3_FR23	RECOMPRESS Full Roar	45262-45462	14	07/15/97
4s3_FR24	RECOMPRESS Full Roar	45464-45620	13	07/16/97
4s3_FR25	RECOMPRESS Full Roar	45621-45741	13	07/16/97
4s3_FR26	RECOMPRESS Full Roar	45743-45867	17	07/16/97
4s3_FR27	RECOMPRESS Full Roar	45868-45969	12	07/16/97
***				
4s3_FHD1	RECOMPRESS FHD Skim	41386-42152	62	07/10/97
4s3_FHD2	RECOMPRESS FHD Skim	42153-42650	55	07/11/97
4s3_FHD3	RECOMPRESS FHD Skim	42653-43556	49	07/12/97
4s3_FHD4	RECOMPRESS FHD Skim	43557-44195	48	07/13/97
4s3_FHD5	RECOMPRESS FHD Skim	44197-44676	42	07/14/97
4s3_FHD6	RECOMPRESS FHD Skim	44677-45240	49	07/15/97

4s3_FHD7	RECOMPRESS FHD Skim	45241-45782	48	07/16/97
4s3_FHD8	RECOMPRESS FHD Skim	45784-45969	23	07/16/97
4s3_HAD1	RECOMPRESS HAD Skim	41386-43792	184	07/16/97
4s3_HAD2	RECOMPRESS HAD Skim	43793-45969	192	07/17/97
4s3_TAU1	RECOMPRESS TAU Skim	41386-45969	376	07/16/97
4s3_2TK1	RECOMPRESS 2TK Skim	41386-45151	295	07/15/97
4s3_2TK2	RECOMPRESS 2TK Skim	45152-45969	81	07/16/97
4s3_4TK1	RECOMPRESS 4TK Skim	41386-45969	376	07/16/97

****

****

4s4_FR01	RECOMPRESS Full Roar	46035-46227	15	06/27/97
4s4_FR02	RECOMPRESS Full Roar	46232-46390	15	06/27/97
4s4_FR03	RECOMPRESS Full Roar	46391-46558	15	06/27/97
4s4_FR04	RECOMPRESS Full Roar	46559-46716	14	06/27/97
4s4_FR05	RECOMPRESS Full Roar	46717-46873	15	06/28/97
4s4_FR06	RECOMPRESS Full Roar	46875-47023	15	06/28/97
4s4_FR07	RECOMPRESS Full Roar	47038-47176	15	06/29/97
4s4_FR08	RECOMPRESS Full Roar	47177-47348	15	06/29/97
4s4_FR09	RECOMPRESS Full Roar	47350-47509	15	06/29/97
4s4_FR10	RECOMPRESS Full Roar	47510-47669	16	06/29/97
4s4_FR11	RECOMPRESS Full Roar	47670-47826	15	06/29/97
4s4_FR12	RECOMPRESS Full Roar	47827-48003	16	06/30/97
4s4_FR13	RECOMPRESS Full Roar	48004-48057	05	06/30/97

****

4s4_FHD1	RECOMPRESS FHD Skim	46035-46695	57	06/27/97
4s4_FHD2	RECOMPRESS FHD Skim	46696-47238	53	06/29/97
4s4_FHD3	RECOMPRESS FHD Skim	47239-47826	55	06/29/97
4s4_FHD4	RECOMPRESS FHD Skim	47827-48057	21	06/30/97
4s4_HAD1	RECOMPRESS HAD Skim	46035-48057	186	06/30/97
4s4_TAU1	RECOMPRESS TAU Skim	46035-48057	186	06/30/97
4s4_2TK1	RECOMPRESS 2TK Skim	46035-48057	186	06/30/97
4s4_4TK1	RECOMPRESS 4TK Skim	46035-48057	186	06/30/97

****

****

4s5_FR01	RECOMPRESS Full Roar	48943-49134	15	06/19/97
4s5_FR02	RECOMPRESS Full Roar	49135-49343	16	06/20/97
4s5_FR03	RECOMPRESS Full Roar	49344-49522	15	06/20/97
4s5_FR04	RECOMPRESS Full Roar	49523-49698	16	06/20/97
4s5_FR05	RECOMPRESS Full Roar	49699-49850	13	06/20/97
4s5_FR06	RECOMPRESS Full Roar	49851-50034	14	06/23/97
4s5_FR07	RECOMPRESS Full Roar	50035-50176	15	06/23/97
4s5_FR08	RECOMPRESS Full Roar	50177-50357	15	06/23/97
4s5_FR09	RECOMPRESS Full Roar	50358-50511	15	06/24/97

4s5_FR10	RECOMPRESS Full Roar	50512-50660	15	06/24/97
4s5_FR11	RECOMPRESS Full Roar	50661-50812	15	06/24/97
4s5_FR12	RECOMPRESS Full Roar	50814-51008	16	06/24/97
4s5_FR13	RECOMPRESS Full Roar	51009-51187	15	06/25/97
4s5_FR14	RECOMPRESS Full Roar	51188-51372	15	06/25/97
4s5_FR15	RECOMPRESS Full Roar	51373-51406	04	06/25/97

****

4s5_FHD1	RECOMPRESS FHD Skim	48943-49761	68	06/20/97
4s5_FHD2	RECOMPRESS FHD Skim	49762-49850	07	06/20/97
4s5_FHD3	RECOMPRESS FHD Skim	49851-50475	55	06/23/97
4s5_FHD4	RECOMPRESS FHD Skim	50476-51120	59	06/25/97
4s5_FHD5	RECOMPRESS FHD Skim	51123-51406	25	06/25/97
4s5_HAD1	RECOMPRESS HAD Skim	48943-51406	214	06/25/97
4s5_TAU1	RECOMPRESS TAU Skim	48943-51406	214	06/25/97
4s5_2TK1	RECOMPRESS 2TK Skim	48943-49850	75	06/20/97
4s5_2TK2	RECOMPRESS 2TK Skim	49851-51406	139	06/25/97
4s5_4TK1	RECOMPRESS 4TK Skim	48943-51406	214	06/25/97

****

****

4s6_FR01	RECOMPRESS Full Roar	51431-51614	15	06/13/97
4s6_FR02	RECOMPRESS Full Roar	51615-51815	16	06/13/97
4s6_FR03	RECOMPRESS Full Roar	51816-51986	14	06/13/97
4s6_FR04	RECOMPRESS Full Roar	51989-52160	15	06/14/97
4s6_FR05	RECOMPRESS Full Roar	52161-52318	15	06/14/97
4s6_FR06	RECOMPRESS Full Roar	52320-52508	16	06/14/97
4s6_FR07	RECOMPRESS Full Roar	52509-52681	15	06/15/97
4s6_FR08	RECOMPRESS Full Roar	52682-52851	16	06/15/97
4s6_FR09	RECOMPRESS Full Roar	52852-53038	16	06/15/97
4s6_FR10	RECOMPRESS Full Roar	53040-53208	15	06/16/97
4s6_FR11	RECOMPRESS Full Roar	53210-53357	15	06/16/97
4s6_FR12	RECOMPRESS Full Roar	53358-53577	16	06/16/97
4s6_FR13	RECOMPRESS Full Roar	53578-53702	11	06/17/97

****

4s6_FHD1	RECOMPRESS FHD Skim	51431-52089	55	06/13/97
4s6_FHD2	RECOMPRESS FHD Skim	52091-52783	61	06/15/97
4s6_FHD3	RECOMPRESS FHD Skim	52785-53370	53	06/16/97
4s6_FHD4	RECOMPRESS FHD Skim	53371-53702	26	06/17/97
4s6_HAD1	RECOMPRESS HAD Skim	51431-53702	195	06/17/97
4s6_TAU1	RECOMPRESS TAU Skim	51431-53702	195	06/17/97
4s6_2TK1	RECOMPRESS 2TK Skim	51431-53702	195	06/17/97
4s6_4TK1	RECOMPRESS 4TK Skim	51431-53702	195	06/17/97

****

****

4s7_FR01	RECOMPRESS	Full Roar	53747-53996	18	06/05/97
4s7_FR02	RECOMPRESS	Full Roar	53997-54167	16	06/05/97
4s7_FR03	RECOMPRESS	Full Roar	54171-54385	16	06/06/97
4s7_FR04	RECOMPRESS	Full Roar	54386-54520	15	06/06/97
4s7_FR05	RECOMPRESS	Full Roar	54524-54656	15	06/06/97
4s7_FR06	RECOMPRESS	Full Roar	54657-54801	16	06/06/97
4s7_FR07	RECOMPRESS	Full Roar	54802-54952	17	06/07/97
4s7_FR08	RECOMPRESS	Full Roar	54954-55102	18	06/07/97
4s7_FR09	RECOMPRESS	Full Roar	55103-55264	16	06/08/97
4s7_FR10	RECOMPRESS	Full Roar	55265-55402	16	06/08/97
4s7_FR11	RECOMPRESS	Full Roar	55403-55527	15	06/08/97
4s7_FR12	RECOMPRESS	Full Roar	55528-55657	16	06/08/97
4s7_FR13	RECOMPRESS	Full Roar	55658-55825	17	06/09/97
4s7_FR14	RECOMPRESS	Full Roar	55827-56012	16	06/09/97
4s7_FR15	RECOMPRESS	Full Roar	56013-56169	16	06/09/97
4s7_FR16	RECOMPRESS	Full Roar	56172-56349	16	06/10/97
4s7_FR17	RECOMPRESS	Full Roar	56350-56529	17	06/10/97
4s7_FR18	RECOMPRESS	Full Roar	56530-56720	17	06/10/97
4s7_FR19	RECOMPRESS	Full Roar	56721-56916	17	06/11/97
4s7_FR20	RECOMPRESS	Full Roar	56918-56976	06	06/11/97
**					
4s7_FHD1	RECOMPRESS	FHD Skim	53747-54520	65	06/06/97
4s7_FHD2	RECOMPRESS	FHD Skim	54524-55075	64	06/07/97
4s7_FHD3	RECOMPRESS	FHD Skim	55081-55603	58	06/08/97
4s7_FHD4	RECOMPRESS	FHD Skim	55604-56240	63	06/10/97
4s7_FHD5	RECOMPRESS	FHD Skim	56242-56976	66	06/11/97
4s7_HAD1	RECOMPRESS	HAD Skim	53747-55835	212	06/11/97
4s7_HAD2	RECOMPRESS	HAD Skim	55837-56976	104	06/11/97
4s7_TAU1	RECOMPRESS	TAU Skim	53747-56976	316	06/11/97
4s7_2TK1	RECOMPRESS	2TK Skim	53747-56373	261	06/10/97
4s7_2TK2	RECOMPRESS	2TK Skim	56374-56976	55	06/11/97
4s7_4TK1	RECOMPRESS	4TK Skim	53747-56976	316	06/11/97
**					
**					
4s8_FR01	RECOMPRESS	Full Roar	57038-57259	18	06/01/97
4s8_FR02	RECOMPRESS	Full Roar	57260-57422	16	06/01/97
4s8_FR03	RECOMPRESS	Full Roar	57423-57577	16	06/01/97
4s8_FR04	RECOMPRESS	Full Roar	57578-57706	16	06/01/97
4s8_FR05	RECOMPRESS	Full Roar	57707-57872	16	06/02/97
4s8_FR06	RECOMPRESS	Full Roar	57873-58027	16	06/02/97
4s8_FR07	RECOMPRESS	Full Roar	58028-58191	16	06/02/97
4s8_FR08	RECOMPRESS	Full Roar	58194-58360	16	06/03/97
4s8_FR09	RECOMPRESS	Full Roar	58361-58507	16	06/03/97

4s8_FR10	RECOMPRESS Full Roar	58508-58686	16	06/03/97
4s8_FR11	RECOMPRESS Full Roar	58687-58801	15	06/04/97
4s8_FR12	RECOMPRESS Full Roar	58802-58813	02	06/04/97
**				
4s8_FHD1	RECOMPRESS FHD Skim	57038-57664	61	06/01/97
4s8_FHD2	RECOMPRESS FHD Skim	57665-58266	59	06/02/97
4s8_FHD3	RECOMPRESS FHD Skim	58267-58813	59	06/04/97
4s8_HAD1	RECOMPRESS HAD Skim	57038-58813	179	06/04/97
4s8_TAU1	RECOMPRESS TAU Skim	57038-58813	179	06/04/97
4s8_2TK1	RECOMPRESS 2TK Skim	57038-58813	179	06/04/97
4s8_4TK1	RECOMPRESS 4TK Skim	57038-58813	179	06/04/97
**				
**				
4s9_FR01	RECOMPRESS Full Roar	58837-58981	15	05/22/97
4s9_FR02	RECOMPRESS Full Roar	58982-59100	15	05/22/97
4s9_FR03	RECOMPRESS Full Roar	59101-59216	15	05/22/97
4s9_FR04	RECOMPRESS Full Roar	59218-59345	15	05/23/97
4s9_FR05	RECOMPRESS Full Roar	59346-59507	16	05/23/97
4s9_FR06	RECOMPRESS Full Roar	59508-59637	16	05/23/97
4s9_FR07	RECOMPRESS Full Roar	59638-59754	15	05/24/97
4s9_FR08	RECOMPRESS Full Roar	59755-59878	16	05/24/97
4s9_FR09	RECOMPRESS Full Roar	59883-60007	16	05/24/97
4s9_FR10	RECOMPRESS Full Roar	60008-60108	16	05/25/97
4s9_FR11	RECOMPRESS Full Roar	60109-60214	16	05/26/97
4s9_FR12	RECOMPRESS Full Roar	60218-60323	16	05/26/97
4s9_FR13	RECOMPRESS Full Roar	60324-60432	17	05/26/97
4s9_FR14	RECOMPRESS Full Roar	60435-60576	16	05/27/97
**				
4s9_FHD1	RECOMPRESS FHD Skim	58837-59306	55	05/23/97
4s9_FHD2	RECOMPRESS FHD Skim	59307-59872	67	05/24/97
4s9_FHD3	RECOMPRESS FHD Skim	59873-60262	56	05/26/97
4s9_FHD4	RECOMPRESS FHD Skim	60263-60576	42	05/27/97
4s9_HAD1	RECOMPRESS HAD Skim	58837-60576	220	05/27/97
4s9_TAU1	RECOMPRESS TAU Skim	58837-60576	220	05/27/97
4s9_2TK1	RECOMPRESS 2TK Skim	58837-60576	220	05/27/97
4s9_4TK1	RECOMPRESS 4TK Skim	58837-60576	220	05/27/97
**				
**				
4sA_FR01	RECOMPRESS Full Roar	60770-60886	15	05/28/97
4sA_FR02	RECOMPRESS Full Roar	60887-61014	16	05/28/97
4sA_FR03	RECOMPRESS Full Roar	61015-61171	16	05/28/97
4sA_FR04	RECOMPRESS Full Roar	61187-61316	15	05/29/97
4sA_FR05	RECOMPRESS Full Roar	61317-61436	14	05/29/97

4sA_FR06	RECOMPRESS Full Roar	61437-61562	15	05/29/97
4sA_FR07	RECOMPRESS Full Roar	61563-61703	16	05/30/97
4sA_FR08	RECOMPRESS Full Roar	61705-61778	15	05/30/97

****

4sA_FHD1	RECOMPRESS FHD Skim	60770-61299	60	05/29/97
4sA_FHD2	RECOMPRESS FHD Skim	61300-61778	62	05/30/97
4sA_HAD1	RECOMPRESS HAD Skim	60770-61778	122	05/30/97
4sA_TAU1	RECOMPRESS TAU Skim	60770-61778	122	05/30/97
4sA_2TK1	RECOMPRESS 2TK Skim	60770-61778	122	05/30/97
4sA_4TK1	RECOMPRESS 4TK Skim	60770-61778	122	05/30/97

****
****

4sB_FR01	RECOMPRESS Full Roar	61826-62013	16	05/13/97
4sB_FR02	RECOMPRESS Full Roar	62014-62107	11	05/13/97
4sB_FR03	RECOMPRESS Full Roar	62108-62204	16	05/14/97
4sB_FR04	RECOMPRESS Full Roar	62206-62307	15	05/15/97
4sB_FR05	RECOMPRESS Full Roar	62308-62418	16	05/15/97
4sB_FR06	RECOMPRESS Full Roar	62422-62553	16	05/15/97
4sB_FR07	RECOMPRESS Full Roar	62556-62664	15	05/15/97
4sB_FR08	RECOMPRESS Full Roar	62665-62855	15	05/15/97

****

4sB_FHD1	RECOMPRESS FHD Skim	61826-62494	82	05/14/97
4sB_FHD2	RECOMPRESS FHD Skim	62495-62855	38	05/15/97
4sB_HAD1	RECOMPRESS HAD Skim	61826-62855	120	05/16/97
4sB_TAU1	RECOMPRESS TAU Skim	61826-62855	120	05/15/97
4sB_2TK1	RECOMPRESS 2TK Skim	61826-62855	120	05/15/97
4sB_4TK1	RECOMPRESS 4TK Skim	61826-62855	120	05/15/97

****
****

4sC_FR01	RECOMPRESS Full Roar	63086-63370	15	04/28/97
4sC_FR02	RECOMPRESS Full Roar	63371-63485	13	04/29/97
4sC_FR03	RECOMPRESS Full Roar	63487-63574	12	04/29/97
4sC_FR04	RECOMPRESS Full Roar	63576-63692	13	04/29/97
4sC_FR05	RECOMPRESS Full Roar	63693-63771	13	04/29/97
4sC_FR06	RECOMPRESS Full Roar	63773-63856	08	04/29/97
4sC_FR07	RECOMPRESS Full Roar	63857-63957	10	04/29/97
4sC_FR08	RECOMPRESS Full Roar	63959-64026	09	04/30/97

****

4sC_FHD1	RECOMPRESS FHD Skim	63086-63737	62	04/29/97
4sC_FHD2	RECOMPRESS FHD Skim	63738-64026	31	04/30/97
4sC_HAD1	RECOMPRESS HAD Skim	63086-64026	93	04/30/97
4sC_TAU1	RECOMPRESS TAU Skim	63086-64026	93	04/30/97
4sC_2TK1	RECOMPRESS 2TK Skim	63086-64026	93	04/30/97

```
4sC_4TK1  RECOMPRESS 4TK Skim   63086-64026   93   04/30/97
**************************************************************
**************************************************************
4sD_FR01  RECOMPRESS Full Roar  64085-64176   08   04/27/97
4sD_FR02  RECOMPRESS Full Roar  64177-64290   08   04/27/97
4sD_FR03  RECOMPRESS Full Roar  64291-64357   07   04/27/97
4sD_FR04  RECOMPRESS Full Roar  64358-64493   07   04/27/97
4sD_FR05  RECOMPRESS Full Roar  64494-64603   08   04/28/97
4sD_FR06  RECOMPRESS Full Roar  64605-64674   07   04/28/97
**************************************************************
4sD_FHD1  RECOMPRESS FHD Skim   64085-64674   45   04/28/97
4sD_HAD1  RECOMPRESS HAD Skim   64085-64674   45   04/28/97
4sD_TAU1  RECOMPRESS TAU Skim   64085-64674   45   04/28/97
4sD_2TK1  RECOMPRESS 2TK Skim   64085-64674   45   04/27/97
4sD_4TK1  RECOMPRESS 4TK Skim   64085-64674   45   04/27/97
**************************************************************
**************************************************************
4sE_FR01  RECOMPRESS Full Roar  64675-64814   11   05/01/97
4sE_FR02  RECOMPRESS Full Roar  64815-64909   07   05/01/97
4sE_FR03  RECOMPRESS Full Roar  64911-65022   07   05/01/97
4sE_FR04  RECOMPRESS Full Roar  65024-65101   06   05/01/97
4sE_FR05  RECOMPRESS Full Roar  65102-65179   07   05/02/97
4sE_FR06  RECOMPRESS Full Roar  65181-65238   06   05/02/97
**************************************************************
4sE_FHD1  RECOMPRESS FHD Skim   64675-65133   34   05/01/97
4sE_FHD2  RECOMPRESS FHD Skim   65134-65238   10   05/01/97
4sE_HAD1  RECOMPRESS HAD Skim   64675-65238   44   05/02/97
4sE_TAU1  RECOMPRESS TAU Skim   64675-65238   44   05/02/97
4sE_2TK1  RECOMPRESS 2TK Skim   64675-65238   44   05/01/97
4sE_4TK1  RECOMPRESS 4TK Skim   64675-65238   44   05/02/97
**************************************************************
**************************************************************
4sF_FR01  RECOMPRESS Full Roar  65252-65309   07   07/03/97
4sF_FR02  RECOMPRESS Full Roar  65310-65369   08   07/03/97
4sF_FR03  RECOMPRESS Full Roar  65371-65454   07   07/04/97
4sF_FR04  RECOMPRESS Full Roar  65455-65532   07   07/04/97
4sF_FR05  RECOMPRESS Full Roar  65533-65638   07   07/04/97
4sF_FR06  RECOMPRESS Full Roar  65639-65750   08   07/04/97
4sF_FR07  RECOMPRESS Full Roar  65752-65818   06   07/04/97
**************************************************************
4sF_FHD1  RECOMPRESS FHD Skim   65252-65546   31   07/04/97
4sF_FHD2  RECOMPRESS FHD Skim   65553-65818   19   07/04/97
4sF_HAD1  RECOMPRESS HAD Skim   65252-65818   50   07/04/97
```

4sF_TAU1	RECOMPRESS TAU Skim	65252-65818	50	07/04/97
4sF_2TK1	RECOMPRESS 2TK Skim	65252-65818	50	07/04/97
4sF_4TK1	RECOMPRESS 4TK Skim	65252-65818	50	07/04/97

****

****

4sG_FR01	RECOMPRESS Full Roar	66539-66664	07	07/06/97
4sG_FR02	RECOMPRESS Full Roar	66665-66741	08	07/06/97
4sG_FR03	RECOMPRESS Full Roar	66745-66813	07	07/06/97
4sG_FR04	RECOMPRESS Full Roar	66815-66907	07	07/06/97
4sG_FR05	RECOMPRESS Full Roar	66908-66971	07	07/06/97
4sG_FR06	RECOMPRESS Full Roar	66973-67030	07	07/06/97
4sG_FR07	RECOMPRESS Full Roar	67032-67089	07	07/07/97
4sG_FR08	RECOMPRESS Full Roar	67090-67180	08	07/07/97
4sG_FR09	RECOMPRESS Full Roar	67181-67254	09	07/07/97
4sG_FR10	RECOMPRESS Full Roar	67256-67306	07	07/07/97
4sG_FR11	RECOMPRESS Full Roar	67309-67359	07	07/07/97
4sG_FR12	RECOMPRESS Full Roar	67360-67433	09	07/08/97
4sG_FR13	RECOMPRESS Full Roar	67434-67502	07	07/08/97
4sG_FR14	RECOMPRESS Full Roar	67504-67566	07	07/08/97
4sG_FR15	RECOMPRESS Full Roar	67568-67636	09	07/08/97
4sG_FR16	RECOMPRESS Full Roar	67640-67722	08	07/08/97
4sG_FR17	RECOMPRESS Full Roar	67723-67796	08	07/08/97
4sG_FR18	RECOMPRESS Full Roar	67798-67875	09	07/09/97
4sG_FR19	RECOMPRESS Full Roar	67877-67954	08	07/09/97
4sG_FR20	RECOMPRESS Full Roar	67956-68011	08	07/09/97
4sG_FR21	RECOMPRESS Full Roar	68012-68027	03	07/09/97

****

4sG_FHD1	RECOMPRESS FHD Skim	66539-66937	32	07/06/97
4sG_FHD2	RECOMPRESS FHD Skim	66946-67245	33	07/07/97
4sG_FHD3	RECOMPRESS FHD Skim	67250-67491	29	07/08/97
4sG_FHD4	RECOMPRESS FHD Skim	67492-67819	37	07/08/97
4sG_FHD5	RECOMPRESS FHD Skim	67821-68027	25	07/09/97
4sG_HAD1	RECOMPRESS HAD Skim	66539-67523	100	07/09/97
4sG_HAD2	RECOMPRESS HAD Skim	67525-68027	57	07/09/97
4sG_TAU1	RECOMPRESS TAU Skim	66539-68027	157	07/09/97
4sG_2TK1	RECOMPRESS 2TK Skim	66539-67729	122	07/08/97
4sG_2TK2	RECOMPRESS 2TK Skim	67731-68027	35	07/09/97
4sG_4TK1	RECOMPRESS 4TK Skim	66539-68027	157	07/09/97

****

****

Appendix C

Analysis Variables

This Appendix details the meaning of various CLEO analysis variables and lists some of their allowed values. This information is taken from the include files which declare the CLEO common blocks, most of which are located on the Cornell Alphas in /cleo/clib/cvssrc/seq/clinc.

```
CCCCCCCCCCCCCC
C
C KINCD  - Track Classification
C      ( = 0 for good primary track
C      (   2 for good secondary track
C      (  -1 no z information, only r-phi. Do not use.
C      (  -2 KINCD=0 but identified as the inward
C                      going half of a curler. Do not use.
C      (  -3 KINCD=-1 but identified as the inward
C                       going half of a curler. Do not use.
C         -4 ... -8 These are created by the Kalman filter and
C                     are copies of KINCD=0 tracks which have been
C                     refitted using a different mass hypothesis.
C         -4 = electron hypothesis
C         -5 = muon hypothesis
C         -6 = kaon hypothesis
C         -7 = proton hypothesis
C         -8 = pion hypothesis, but at the outermost hit.
C             (The pion hypothesis at the origin
C               is stored as KINCD=0)
C

C    TNG(I) < 0
```

```
C               track I should be killed by user
C
C     TNG(I) >= 0
C               track I should be kept by user
C
C     INT( TNG(I)/100 )  =  N
C               track I was killed/kept for broad reason N.
C               If N is +1 then the track was kept because
C               it was a surviving ghost.  If N is -2 then
C               it was killed because it was a curler ...
C
C TNG           Explanation
C
C   0           not found in a subgroup, i.e. a good track
C 101           Tight ghost
C 111           Loose ghost, possible decay in flight
C 112           Loose ghost, both dbcd small
C 113           Loose ghost, both dbcd large
C 201           2 curler, 2 zfits, by far the most populous
C                 curler group
C 301           Wee (pronounced vee), i.e. decay in flight
C                 or scatter
C 401           dbcd/density regions
C 410           tails
C
C 501           miscleaneous (killed if cucd = 0 )
C 502           miscleaneous (killed if |pqcd| > 6.5 GeV)
C
CCCCCCCCCCCCCC
C
C-> DBCD        SIGNED IMPACT PARAMETER WRT BEAM SPOT
C-> CZCD        Z DIRECTION COSINE
C-> ZOCD   -    Z coordinate at the point of closest
C                                approach to the origin.
CCCCCCCCCCCCCC
C
C IQALDI - DE/DX QUALITY OF THE TRACK
C       IF =  0, NO DE/DX information
C       IF =  1, DE/DX information available with   NHITDI>10
C       IF = -2, DE/DX information available with 4<NHITDI<11

* DE50DI - MEAN OF THE LOWEST 40 PERCENT OF PULSE HEIGHTS
* RESDI  - EXPECTED RESOLUTION FOR THAT PULSE HEIGHT
```

```
*                                AND NUMBER OF HITS
*
* SGELDI - NUM. SIGMA AWAY FROM AN ELECTRON (DE50DI-ELDEDI) / RESDI
* SGMUDI -  "     "    "    "   A MUON          "    MUDEDI    "
* SGPIDI -  "     "    "    "   " PION          "    PIDEDI    "
* SGKADI -  "     "    "    "   " KAON          "    KADEDI    "
* SGPRDI -  "     "    "    "   " PROTRON       "    PRDEDI    "
*
CCCCCCCCCCCCCC
C
* ENTRSH(I)   - total CCFC calorimeter energy matched to track I
* EPTRSH(I)   - energy/momentum = ENTRSH(I)/PPTRSH(I)
* ENTRSH(I)   - total CCFC calorimeter energy matched to track I
*
C
CCCCCCCCCCCCCC
C
C TFSTAT - Status word: TFSTAT = 0 ----> no ToF measurement
C                       TFSTAT = 1 ----> Endcap ToF measurement
C                       TFSTAT = 2 ----> Barrel ToF measurement
C
C TFIDQL - Quality word: TFIDQL =  0 ----> good time measurement
C                        TFIDQL =  4 ----> T_east - T_west = 1 ns
C                        TFIDQL =  8 ----> ADC Saturated
C                        TFIDQL = 12 ----> Both 4 and 8 happened
C
C RESTF  - Estimated resolution for this measurement
C
C DTELTF - Difference from expected electron time in nanoseconds
C DTMUTF - Difference from expected     muon time in nanoseconds
C DTPITF - Difference from expected     pion time in nanoseconds
C DTKATF - Difference from expected     kaon time in nanoseconds
C DTPRTF - Difference from expected   proton time in nanoseconds
C
C SGXXTF - Same, but in units of sigma (DTXXTF/RESTF).
C BETATF - Relativistic Beta of the particle
C

CCCCCCCCCCCCCC
C
*  DPTHMU         - maximal depth in absorption lenghts at which
*                   CD track MUTRDR(IMUTR) correlates to good quality
*                   hits in the MU detector.
```

```
*                    (roughly speaking, "good quality" = two of three
*                            layers hit in a MU chamber unit)
*
*  MUQUAL          - MU track quality flag :
*
*  MUQUAL .EQ. 0  - CD track MUTRDR(IMUTR) correlates with muon hits
*                   everywhere expected.
*  MUQUAL .NE. 0  - CD track MUTRDR(IMUTR) fails to correlate to any
*                   hits in at least one of iron gaps where it was
*                   expected to hit MU chambers.
C
CCCCCCCCCCCCCC
C
C R2ELEC - Log-Likelihood that the track is an electron.
C
C      The variables that the Electron ID package uses are:
C
C          1.  SGELDI
C          2.  EPTRSH
C          3.  Distance of track-to-shower match
C          4.  LP2SH  RMS shower width (meters)
C          5.  LP4SH  (shower shape, E9/E25 = Sum of  9 crystals
C                      about highest divided by Sum of 25 crystals
C                      around highest)
C          6.  LP3SH  (theta width / phi width)
C          7.  SGELTF
C
CCCCCCCCCCCCCC
```

Appendix D

Maximum Likelihood

We maximize the following Likelihood Equation for our fit of charged tracks in each momentum bin:

$$
\begin{aligned}
&\mathcal{L}(n_\pi,\, n_K,\, n_p,\, n_e,\, n_\mu) \\
&= \prod_{i=1}^{N} \left(\sum_{j=\pi,\,K,\,p,\,e,\,\mu} \frac{n_j}{\sum n_k} \cdot f_j(<\mathrm{d}E/\mathrm{dx}>_i \mid \mathbf{p}_i) \cdot g_j(<\mathrm{TOF}>_i \mid \mathbf{p}_i) \right) \\
&\cdot \exp\left(-\frac{[n_\mu - h_\mu(p)]^2}{2\,\sigma_\mu^2(p)} - \frac{[n_e - h_e(p)]^2}{2\,\sigma_e^2(p)} \right) \\
&\cdot \exp(-\textstyle\sum n_k) \cdot (\sum n_k)^N
\end{aligned}
\tag{D.1}
$$

where:

$f_j(<\mathrm{d}E/\mathrm{dx}>_i \mid \mathbf{p}_i)$ is the PDF[1] for dE/dx,

$g_j(<\mathrm{ToF}>_i \mid \mathbf{p}_i)$ is the PDF for ToF,

p_i is the momentum measured in the drift chamber,

N is the total number of observed charged tracks in the momentum bin,

n_j is the number of particles of type j to be fitted,

h_e and h_μ are momentum-dependent lepton distributions derived from fits of MC to the data,

σ_e and σ_μ are the statistical errors on those distributions, and

$\sum n_k$ is the total number of (charged) π, K, p, e, μ tracks for this bin.

[1] Probability Distribution Function

The factors containing h_e and h_μ are used to constrain the number of leptons in each interval to float about those values determined from our fits of tracks in the MC which pass the complement of our lepton suppression cuts to those corresponding tracks in the data. See section 4.4.1 in the main text for details.

The last two factors containing $\sum n_k$ take into account the Poisson distribution of the total number of tracks in that bin.

We actually minimize the value of $-2\ln\mathcal{L}$, which turns the product term above into a sum and reduces the exponential terms to just their arguments.

This resulting sum on the number of tracks in each momentum bin is obtained using a two-step process: we sum over the number of SGKAXX bins in our data shape histograms and add the number of tracks in each SGKAXX bin to obtain the total number of tracks for that momentum bin.

We divide each particle type's control shape SGKAXX histogram by the total number of entries for that histogram to obtain the PDF for each species type. For each SGKAXX bin, the probability for each species type is then the (normalized) SGKAXX bin contents for that particle hypothesis. If the bin contents of a species are negative for that bin, the probability is set to zero in that bin for that species type.

We construct the fractional yield for each species type by taking the yield for that species divided by the sum of yields over the five species types (π, K, p, e, μ). These particle yields are allowed to float in the minimization process, subject to the lepton constraints described above. We multiply this fractional yield for each species type by the probability for that species type computed above and sum these terms over species type.

We construct the likelihood sum by multiplying the number of tracks in each data shape SGKAXX bin times the log of the probability sum described above. These probability sum factors are then computed for each SGKAXX bin, and the non-zero factors are added to the likelihood sum.

Once this sum over SGKAXX bins is computed, the (log) Likelihood Equation is then completed by adding the log of both the lepton constraint terms and the Poisson terms described above, using the total number of charged tracks for this momentum bin and the (floating) sum of yields over particle species.